INFORMATION TO USERS

This manuscript has been reproduced from the microfilm master. UMI films the text directly from the original or copy submitted. Thus, some thesis and dissertation copies are in typewriter face, while others may be from any type of computer printer.

The quality of this reproduction is dependent upon the quality of the copy submitted. Broken or indistinct print, colored or poor quality illustrations and photographs, print bleedthrough, substandard margins, and improper alignment can adversely affect reproduction.

In the unlikely event that the author did not send UMI a complete manuscript and there are missing pages, these will be noted. Also, if unauthorized copyright material had to be removed, a note will indicate the deletion.

Oversize materials (e.g., maps, drawings, charts) are reproduced by sectioning the original, beginning at the upper left-hand corner and continuing from left to right in equal sections with small overlaps.

Photographs included in the original manuscript have been reproduced xerographically in this copy. Higher quality 6" x 9" black and white photographic prints are available for any photographs or illustrations appearing in this copy for an additional charge. Contact UMI directly to order.

Bell & Howell Information and Learning
300 North Zeeb Road, Ann Arbor, MI 48106-1346 USA
800-521-0600

UMI®

Phase Stability and Processing of Sr and Mg Doped Lanthanum Gallate

Feng Zheng

A dissertation submitted in partial fulfillment of the requirements for the degree of

Doctor of Philosophy

University of Washington

2000

Materials Science & Engineering Department

UMI Number: 9976093

Bell & Howell Information and Learning Company
300 North Zeeb Road
P.O. Box 1346
Ann Arbor, MI 48106-1346

In presenting this dissertation in partial fulfillment of the requirements for the Doctoral degree at the University of Washington, I agree that the Library shall make its copies freely available for inspection. I further agree that extensive copying of this thesis is allowable only for scholarly purposes, consistent with "fair use" as prescribed in the U.S. Copyright Law. Requests for copying or reproduction of this dissertation may be referred to University Microfilms, 1490 Eisenhower Place, P.O. Box 975, Ann Arbor, MI 48106, to whom the author has granted "the right to reproduce and sell (a) copies of the manuscript in microform and/or (b) printed copies of the manuscript made from microform."

Signature 

Date: June 8, 2000

University of Washington
Graduate School

This is to certify that I have examined this copy of a doctoral dissertation by

Feng Zheng

and have found that this is complete and satisfactory in all respects,
and that any and all revisions required by
the final examining committee have been made.

Chair of Supervisory Committee

Rajendra K. Bordia

Reading Committee:

Rajendra K. Bordia

Guozhong Cao

Fatih Dogan

Date: June 8, 2000

University of Washington

Abstract

Phase Stability and Processing of Sr and Mg
Doped Lanthanum Gallate

by Feng Zheng

Chairperson of the Supervisory Committee: Professor Rajendra K. Bordia
Department of Materials Science and Engineering

Fuel Cells are one of the most promising energy transformers with respect to ecological and environmental issues. Solid Oxide Fuel Cells (SOFC) are all solid-state devices, which have higher overall energy efficiency compared to other type fuel cells. In addition, SOFCs can tolerate a variety of fuels (e.g. methane, natural gas, etc.) that would poison other types of fuel cells. Furthermore, co-generation of high quality heat and clean water is a technical reality and benefit of the SOFCs owing to their high operating temperature. However, the high operating temperature also has drawbacks. One of them is high maintenance cost; the other is relatively weak long-term service stability due to interdiffusion between fuel cell components. Thus, one of the challenges to improve a SOFC is to lower the operating temperature while maintaining or increasing its output voltage.

Undoped $LaGaO_3$ is an insulator, doping transforms it into an oxygen-ionic conductor. Sr and Mg doped $LaGaO_3$ (LSGM) perovskite is a new oxygen-ionic conductor with higher conductivity than yttria-stabilized zirconia (YSZ), the conventional solid electrolyte in electrochemical devices. Due to the high ionic conductivity, this material is a candidate for a wide variety of electrochemical devices such as SOFCs, oxygen pumps,

electrolysis, and oxygen sensors. In order to realize this potential, the phase stability and processing of this material needs to be investigated in detail.

In this study, a systematic investigation of the LSGM materials in terms of phase stability, phase transition, sintering, microstructure and electrical conductivity as functions of temperature, doping content and A/B cation ratio has been carried out. The generalized formula of the materials investigated is $(La_{1-x}Sr_x)_A(Ga_{1-y}Mg_y)_BO_{3-\delta}$. Where x and y were varied from 0.0 to 0.20 and A/B ratio was varied from 0.9 to 1.05. δ is oxygen deficiency which gives rise to electrical conduction and is governed by defect chemistry. Due to the electroneutrality condition, δ increases with doping content and off-stoichiometry (the derivation from A/B = 1). Room Temperature and High Temperature X-ray Powder Diffractometry (RT/HTXRPD) and Neutron Diffraction (ND) together with JADE and General Structure Analysis System (GSAS) software packages have been used to study the crystal structure and lattice constants with respect to doping content, A/B cation ratio and sintering temperature. Combining the results from thermal analysis [Differential Scanning Calorimetry (DSC), Differential Thermal Analysis (DTA) and ThermalGravimetric Analysis (TGA)] and X-ray diffraction, phase transitions and corresponding structure relationships have been investigated as functions of temperature and doping content. The densification behavior and microstructure evolution has been studied by Dilatometry and Scanning Electron Microscopy (SEM). Study has been conducted on materials with different doping content and A/B ratio at several different temperatures. The 4-point Probe DC Technique has been employed to measure the oxygen-ionic conductivity. Optimized processing parameters have been obtained by

investigating their impact on density change and microstructure. Consequently, a suitable compositional window of the LSGM perovskite has been identified for SOFC electrolyte applications. Based on detailed diffraction analysis, it is found that the undoped $LaGaO_3$ takes on the orthorhombic (Pbnm) symmetry at room temperature. This structure changes to rhombohedral (R3c) at 147 ± 2°C or changes to monoclinic (I2/a) when the doping level increases from 0.1 to 0.2 moles. Doping creates defects, so does variation in A/B cation ratio (δ). Upon doping, the LSGM perovskite is stabilized (does not undergo high temperature phase transitions) and shows very high oxygen ionic conductivity. Varying A/B cation ratio does not affect perovskite structure or phase transition but promotes the formation of minor phases. Small amounts of minor phases help in inhibiting grain growth, but large volume fractions of secondary phases degrade the structural stability and lower the conductivity. Due to this dual effect, the overall influence of A/B ratio on oxygen-ionic conductivity is not significant.

We have optimized the compositional window to make the single perovskite phase with high oxygen ionic conductivity (x = 0.10 to 0.20 with A/B ratio between 0.98 to 1.02). The best processing condition, starting from glycine nitrate process (GNP) combustion synthesized ultra-fine LSGM powder, is sintering in air at 1500°C for 2 hours. The doped material has higher oxygen ionic conductivity than YSZ at all temperatures. In addition, based on the structure and phase relations, a high temperature phase diagram for this system has been proposed. Finally, a model has been proposed to account for the high ionic conductivity of this material and to explain the effect of the doping content and the stoichiometry on the ionic conductivity.

TABLE OF CONTENTS

LIST OF FIGUERS

LIST OF TABLES

ACKNOWLEDGMENTS

It is my greatest pleasant to express my sincere thanks to Professor Rajendra K. Bordia of University of Washington (UW) and Dr. Larry R. Pederson of Pacific Northwest National Laboratory (PNNL) for their guidance during the course of this study. I also thank Professors Tomikazu Sasaki, E. James Davis, Guozhong Cao, Fatih Dogen and James M. Meyer for serving on my Ph.D. supervisory committee.

Thanks are extended to Drs. Larry Chick, Timothy Armstrong and Jeffry Stevenson of PNNL for many interesting discussions on SOFC materials with close relevance to the present study. Special thanks go to Mr. David E. McCready (PNNL) for discussions on X-ray powder diffraction analysis, and to Professor Brian Flinn (UW) for help on thermal analysis. Thanks are due to Dr. R.B.V. Dreele of Los Alamos National Laboratory (LANL) for providing the General Structure Analysis System (GSAS) for crystal structure refinement. Dr. E. Andrew Payzant, Dr. Claudia Rawn and Mr. Wallace D. Porter of High Temperature Materials Laboratory (HTML) in Oak Ridge National Laboratory (ORNL) are due special thanks for their support on high temperature characterization.

Fellow students in Roberts Hall, particular Mairead Stackpoole, Don Ellerby, Sam Salamone, Jung-Min Kwon, Kyle Flanigan, Hanson Fong, Hang Tian, Tom Graham, Jeff Reding, Gregory St. Pierre, Tao Shu, Xiuhong Han and David Wood deserve special thanks for making my study most fruitful and enjoyable.

Partial support for this research was from NSF under grants DMR 9257027, 9410981 and Netzsch Instruments. In addition, research was sponsored by the Assistant Secretary for Energy Efficiency and Renewable Energy, Office of Transportation Technologies, as part of the High Temperature Materials Laboratory User Program, Oak Ridge National Laboratory, managed by Lockheed Martin Energy Research Corp. for the U.S. Department of Energy under contract number DE-AC05-96OR22464. Associated Western Universities, Inc., Northwest Division (AWU-NW) Fellowship is recognized which enabled this study to be performed.

Finally my family deserve special acknowledgment. Without their long-term support I could not accomplish this. My wife Tao and son Lawrence (Yanghao) watched and supported me working through this every day.

CHAPTER 1

INTRODUCTION

The ever-increasing ecological awareness, triggered in part by the threat of global warming from fossil fuels and clean-up challenges from using nuclear power, has led us to seek alternative power sources. The fuel cell is one attractive alternative which can produce clean and efficient electricity to meet the environmental challenges. It is a widely accepted fact that the fuel cell was invented in 1839 by Sir William R. Grove, and it was predicted as a better energy transformation device compared to the electric motor, the dynamo and the steam turbine. However, there were many technical difficulties, which delayed its commercialization. Since early 1960s fuel cell technology has developed rapidly in part due to its successful use in space programs. Recently, there have been significant developments in fuel cell applications for power generation and use in automobiles.

A fuel cell is a device which continuously converts chemical energy into electrical energy (like a battery), but differs from the battery in its electrochemical process. The output from a fuel cell is a stable direct current (DC) of about one-volt. To operate a fuel cell, fuel (gaseous fuels) and oxidant (air or oxygen) are required. The most desirable fuel source is hydrogen or a hydrogen carrier such as natural gas (CH_4) or methanol (CH_3OH). The fuel gas is fed into the fuel electrode (porous anode in solid state) where the

hydrogen is oxidized ($H_2 \rightarrow 2H^+ + 2e^-$). Oxidant (pure oxygen or oxygen in air) is fed into the oxidant electrode (porous cathode in solid state) where it is reduced ($O_2 + 2e^- \rightarrow O^{-2}$). Ions of hydrogen or oxygen are conducted by an electrolyte layer (liquid or dense solid) which is sandwiched between the two electrodes. Water is formed at one interface between the electrode and electrolyte, depending on the mechanism of ion conduction through the electrolyte. For proton (hydrogen ion, H^+) conducting electrolyte fuel cells, water is formed at the cathode/electrolyte side according to the equation

$$2H^+ + \tfrac{1}{2}O_2 + 2e^- \rightarrow H_2O \qquad (1.1).$$

For oxygen ion (O^{-2}) conducting electrolyte fuel cells, water is formed at the anode/electrolyte side

$$H_2 + O^{-2} \rightarrow H_2O + 2e^- \qquad (1.2).$$

The overall reaction in the fuel cell is:

$$H_2 + \tfrac{1}{2}O_2 \rightarrow H_2O \qquad (1.3).$$

The free-energy change of this reaction is

$$\Delta G^o = -nFE_r^o \qquad (1.4).$$

where n is the number of electrons being transferred during the reaction, F is the Faraday constant (F = 96489 C/mol), E_r^o is the reversible cell potential (V). Under standard conditions [*where temperature T = 298 K, partial pressure* $p(H_2) = p(O_2) = 1$ *atm, and* H_2O *is in liquid state*], $n = 2$, ΔG^o = -237 kJ/mol for Eq. (1.3), the reversible potential of Eq. (1.4) is E_r^o= 1.228 V. The variations of the reversible potential (E_r) with temperature and pressure are:

$$E_r = E_r^o + \left(\frac{\partial E}{\partial T}\right)_p (T - 298) = E_r^o + \frac{\Delta S}{nF}(T - 298) \qquad (1.5)$$

and

$$E_r = E_r^o - \frac{\nu RT}{nF} \ln P \qquad (1.6)$$

where ΔS is the entropy change and R is the gas constant (R = 8.314 J/Kmol), T is the absolute temperature in Kelvin (K). For Eq. (1.3), both the entropy and gas molecules mole change is negative such that the reversible potential (E_r) of a fuel cell decreases with temperature [Eq. (1.5)] but increases with pressure [Eq. (1.6)]. The effect of

temperature and pressure on the fuel cell potential (E_r) will be less when water is vaporized.

According to the electrolyte material used. fuel cells can be characterized as five different types. Alkaline Fuel Cell (AFC), Solid Polymer Fuel Cell (SPFC) and Phosphoric Acid Fuel Cell (PAFC) are operated at low temperatures (< 200°C). Molten Carbonate Fuel Cell (MCFC) is operated at about 650°C and Solid Oxide Fuel Cell (SOFC) operates between 650 and 1000°C. These fuel cells are in different stages of commercialization. In a real application, hundreds to thousands unit fuel cells are packed and linked together to build the needed voltage and electrical current density.

This dissertation is organized as follows. In Chapter 2, the history of each type of fuel cells is briefly outlined and, they are compared from the view points of materials science and engineering. Focus will be on the choice and evolution of cell materials with special emphasis on those for SOFC. The goals of this study are presented in Chapter 3. The experimental details are given in Chapter 4. The experimental results are presented in Chapter 5 with two appendixes. The diffraction patterns are included in Appendix I. The phase relationships in La-Sr-Ga-Mg-O system are given in Appendix II. Chapter 6 is reserved for data analysis and discussion. Detailed illustration on thermodynamics and defect chemistry for Sr and Mg doped $LaGaO_3$ (LSGM) perovskite is presented in Appendix III. Finally, the suggestions for future work are presented in Chapter 7.

CHAPTER 2

BACKGROUND

Fuel cells have had a very long development history without reaching large-scale commercialization. Sir William Grove invented the first fuel cell in 1839. In his letter of December 1838 to the Philosophical Magazine,[1] Grove described the idea of a dilute sulfuric acid fuel cell. That cell consisted of two platinum strips with closed tubes surrounding them, which were filled with electrolyzed hydrogen and oxygen. Grove was well aware of the principle of fuel cell operation — the action could only take place at so called three-phase region, where the liquid, gas and 'platina foil' contact each other. He had also noticed that the three-phase contact[2,3] could be extended by coating electrodes with 'spongy platina.'

Using 4-cell and 26-cell series batteries, Grove electrolyzed the potassium iodide solution and water in 1842, as shown in Fig. 2.1. Oxygen and hydrogen is represented by OX and HY respectively. They are sunk into the sulfuric acid bath where electrons are produced and transferred through an external wire. He observed the fact that the hydrogen was consumed twice as fast as the oxygen in that set-up. To overcome this problem, a stronger sulfuric acid where hydrogen came from zinc sulfuric acid reaction and oxygen from air, was tried later. On a hydrogen-chlorine fuel cell, Grove found that other volatile bodies such as camphor, essential oils, ether and alcohol associated with oxygen gave a continuous current.

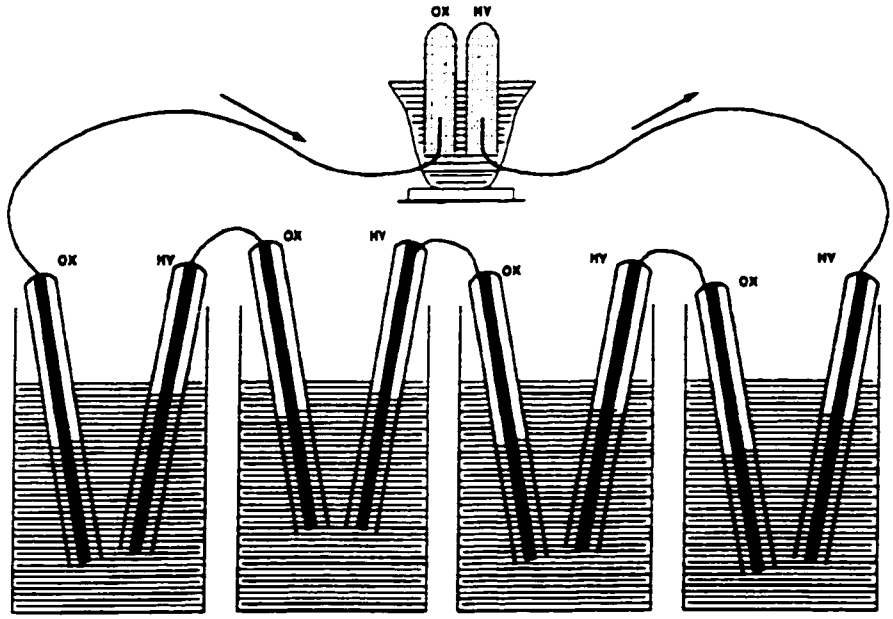

Fig. 2.1 Gove's First Fuel Cell,[2] 1842

Grove had also foreseen, almost 160 years ago, the fuel cell as a source of commercial electricity if hydrogen could be replaced by coal, wood, and other combustible materials. Modern fuel cell developments have proved Grove's hypothesis. For instance, the phosphoric acid fuel cell (PAFC) is a direct successor of Grove's first fuel cell.

In 1896, W.W. Jacques[4] thought the direct coal fuel cell (DCFC) would make the dynamo (invented in 1867) an obsolete device when he described a large ship powered with DCFC. His idea drew much publicity owing to the desire to find better use for coal — the primary fuel in the nineteenth century. His fuel cell, however, never achieved satisfactory performance due to the chemical reaction between carbon and the electrolyte. As a result, DCFC was the only type of fuel cell being completely abandoned (in 1939).

The alkaline fuel cell (AFC), using aqueous KOH as electrolyte was initiated by J.H. Reid[5] in 1902 and by P.G.L. Noel[6] in 1904. There was no significant improvement in AFC until F.T. Bacon started his fuel cell research in late 30s. Bacon's work finally established the reputation for fuel cell and found first application in space program in early 60s. Another significant contributor was E.W. Justi who started his AFC research from later 40s and established Siemens leadership in fuel cell development.[3]

F. Haber *et al.*[7,8] studied the thermodynamics of the reversible electromotive force (EMF) of the H_2-O_2 fuel cell in 1906 and 1907. As the electrolyte, they used a thin glass disk which was covered by platinum or gold on both sides and joined to tubes where gases were provided. Their measured open circuit voltage (OCV) matches the theoretical values very well and their cell was considered the prototype of the solid polymer fuel cell (SPFC).

Molten carbonate fuel cell (MCFC) has its roots in the work of E. Baur's group in Germany in early 1900s. One of his students, I. Taitelbaum[9] was the first person to add a diaphragm of porous MgO to a fuel cell with molten NaOH (380°C) as electrolyte in 1910.

It was W. Nernst[10] who discovered the 'Nernst mass' — the yttria stabilized zirconia (85% ZrO_2-15% Y_2O_3) — in 1897. He had used 'Nernst mass' as electrolyte to make a solid oxide fuel cell (SOFC) in 1900.[3] A theoretical treatment on the SOFC using 'Nernst

mass' was published much later by one of his students, W. Schottky[11] in 1935. Inspired by Schottky's paper, E. Baur and H. Preis[12] studied fuel cells with many solid electrolytes. However, only the 'Nernst mass' fuel cells had sufficiently high electrical conductance.

Fig. 2.2 shows one fuel cell designed by Baur and Preis.[12] The thin tubes, made from 'Nernst mass', had served as electrolyte. One end of the tube was closed and surrounded by the oxygen electrode — coarse coke (C) or iron powder (Fe). Coarse magnetite powders (Fe_3O_4) were filled into the tube as the anode. The fuel gases (e.g. H_2, CO or town gas) were allowed to circulate inside the tube and led to electrochemical reactions to produce electricity.

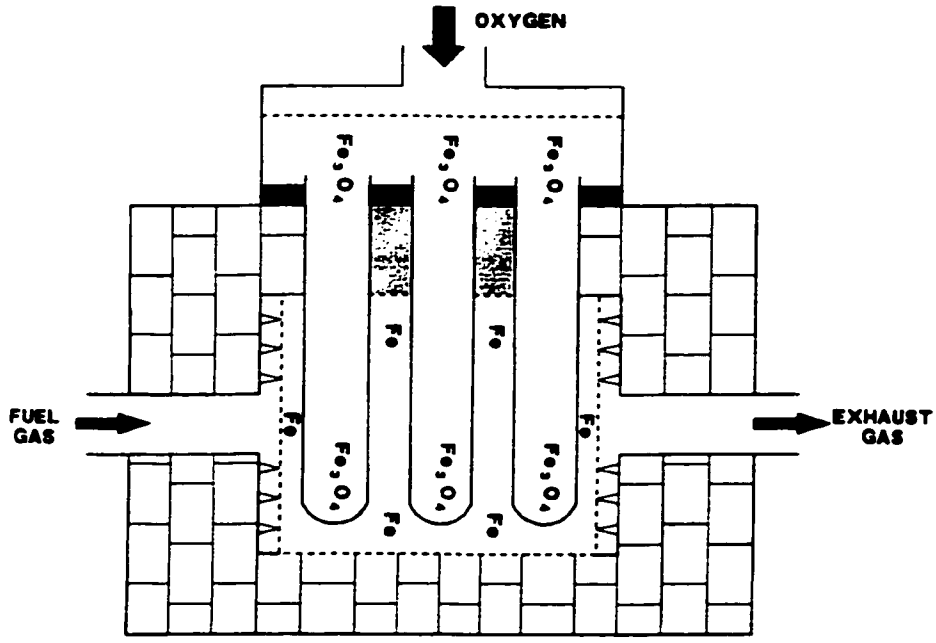

Fig. 2.2 Solid Electrolyte Fuel Cell Made by Baur and Preis[12] in 1937

2.1 ALKALINE FUEL CELL (AFC)

Alkaline fuel cell (AFC) operates at low temperature (65 ~ 100 or 220°C). The first major leap in cell development was due to the work of Francis T. Bacon. Bacon[13] used alkaline (KOH of different concentration) as electrolyte, sintered nickel metal of dual porosity as anode, and lithiated nickel oxide as cathode. His alkaline fuel cells (AFCs) were operated at various temperatures and pressures to achieve the best performance. In one cell using 30% KOH as the electrolyte, a cell voltage of 0.78 V at 800 mA/cm^2 was obtained at 200°C and at 45 atm. The choice of material for anode and cathode depends mainly on the use of catalysts. AFC can use either precious metal (Pt) or normal metal catalysts (Ni or Ag). In each case, good electric conductivity, suitable porosity, adequate mechanical, chemical and electrochemical stability needs to be assured. It was the space program that led to major developments in this type of fuel cells.

The half-cell reactions in the AFC are:

Anode: $$H_2 + 2OH^- \rightarrow 2H_2O + 2e^- \quad (2.1)$$

Cathode: $$0.5O_2 + H_2O + 2e^- \rightarrow 2OH^- \quad (2.2)$$

The overall cell reaction is: $$H_2 + 0.5O_2 \rightarrow H_2O + DC + Heat \quad (2.3)$$

The hydroxyl ions are the conducting species in the electrolyte. Water is produced at the anode. Water migration towards the cathode can dilute the electrolyte which reduces cell

conductivity and therefore degrades cell performance. There are two different methods to solve this problem. One is to circulate the electrolyte such that the water can be vaporized and the heat can be removed. Another is to circulate hydrogen gas so that the water vapor can be carried away. In the latter case, the heat is removed by circulating coolant. Fig. 2.3 and 2.4 show the schematic of these two concepts respectively.[14] In Fig. 2.3 and 2.4, arrows are used to point out the direction of gas supply, electron transfer and heat flow. The basic cell reaction is given in the diagram also. Fuel cell components (anode, electrolyte and cathode) are labeled. One real model of Siemens' AFC,[15] with captions showing gas flow, electrolyte flow, cell support, etc., is illustrated in Fig. 2.5 for comparison.

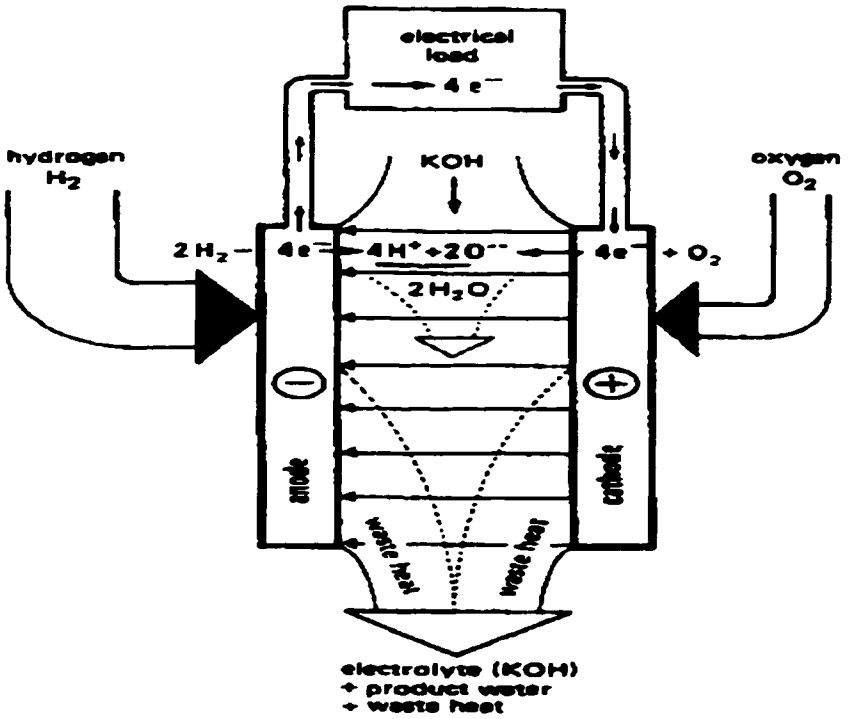

Fig. 2.3 Principles of the AFC with Mobile Electrolyte[14]

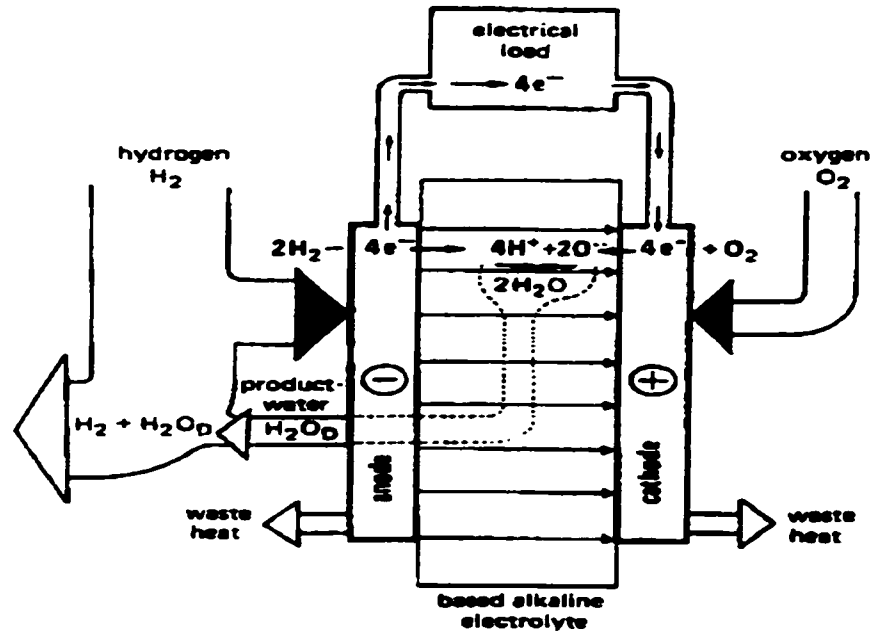

Fig. 2.4 Principles of the AFC with Matrix[14]

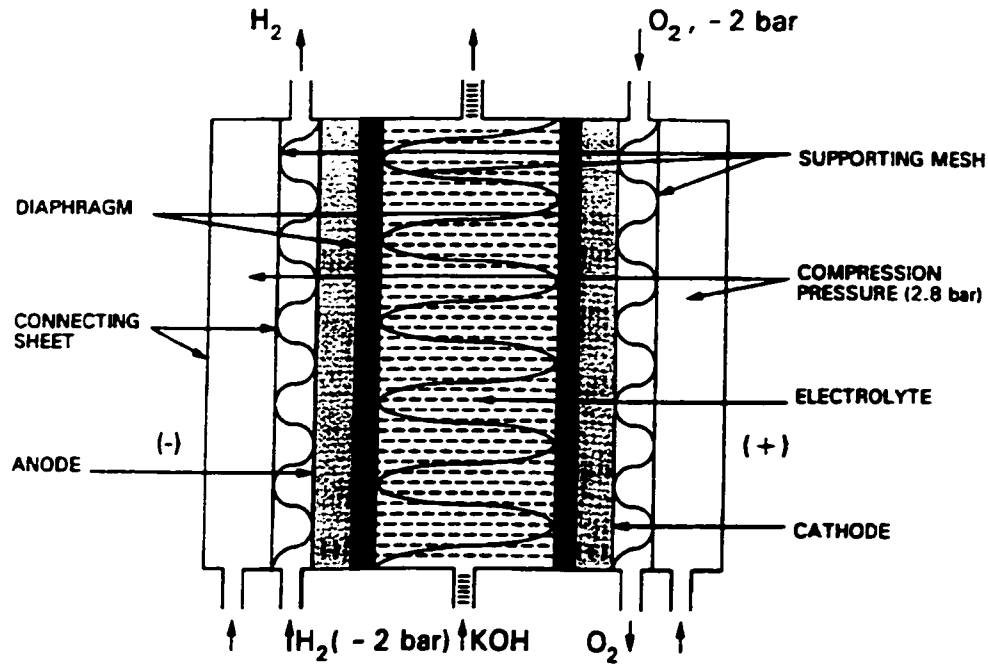

Fig. 2.5 Operation Principle of Siemens' AFC[15]

The major challenge for improving AFC is the complete removal of CO_2 from the gas streams in electrodes. The CO_2 in the air (~ 350 ppm) is sufficient to carbonate the electrolyte according to the reaction:

$$CO_2 + 2KOH \rightarrow K_2CO_3 + H_2O \qquad (2.4)$$

and form solid deposits on porous electrodes. To eliminate the effects of CO_2, fuel pretreatment must be performed so that the CO_2 level can be reduced to the level of a few ppm, which is within the tolerance of the AFC. One common technique to accomplish this is to pass CO_2-containing gaseous fuel through a thermally regenerable solvent:

$$2RNH_2 + CO_2 \Leftrightarrow RNH{\bullet}CO{\bullet}HNR + H_2O \qquad (2.5).$$

RNH_2 is an organic amine and it can react with CO_2 to produce water. With this technique, the CO_2 level can be reduced to 50 ppm in the first pass. Usually two more passes are sufficient to lower the CO_2 concentration to the AFC tolerance limit. Besides the removal of the CO_2, safe and efficient hydrogen storage methods are required for terrestrial applications where cost is the predominate issue. Storage of hydrogen in fiber-wound aluminum cylinders or in certain metal alloys (Ti-Ni) where hydrides can be formed are viable options for purpose of transportation.

2.2 SOLID POLYMER FUEL CELL (SPFC)

Solid polymer fuel cell (SPFC) operates between 25 ~ 120°C. With respect to design and operation, SPFC is the most elegant fuel cell. The first SPFC was developed by General Electric (GE)[16] for NASA in the 1960s. A solid polymer electrolyte membrane is sandwiched between two platinum-catalyzed porous electrodes. Fig. 2.6 schematically shows the operating principle of the SPFC with captions for cell components, water production, direction of gas flow and proton (H^+) transfer.[15] A cross section[16] of SPFC is given in Fig. 2.7 where more detailed captions are provided and a more detailed structural view of the SPFC[14] is given in Fig. 2.8. The flow paths of relevant species[17] are presented in Fig. 2.9 with cell reactions showing how protons (H^+) are transferred from anode to cathode. Historically, several names have been used to refer to the SPFC. These include Ion Exchange Membrane (IEM), Solid Polymer Electrolyte (SPE), and Proton Exchange Membrane (PEM). All of them indicate the fact that they use a solid polymer membrane as electrolyte.

The electrochemical reactions in SPFC are as the follows:

Anode: $$H_2 \rightarrow 2H^+ + 2e^- \quad (2.6)$$

Cathode: $$0.5O_2 + 2H^+ + 2e^- \rightarrow H_2O \quad (2.7)$$

The overall cell reaction is: $$H_2 + 0.5O_2 \rightarrow H_2O + DC + Heat \quad (2.8)$$

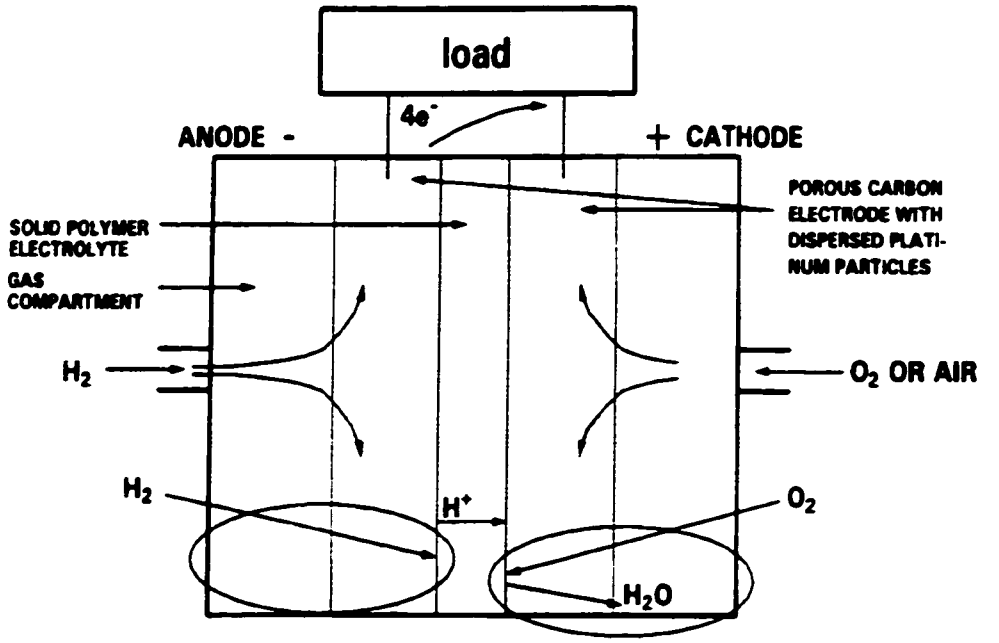

Fig. 2.6 The Operation Principle of the SPFC[15]

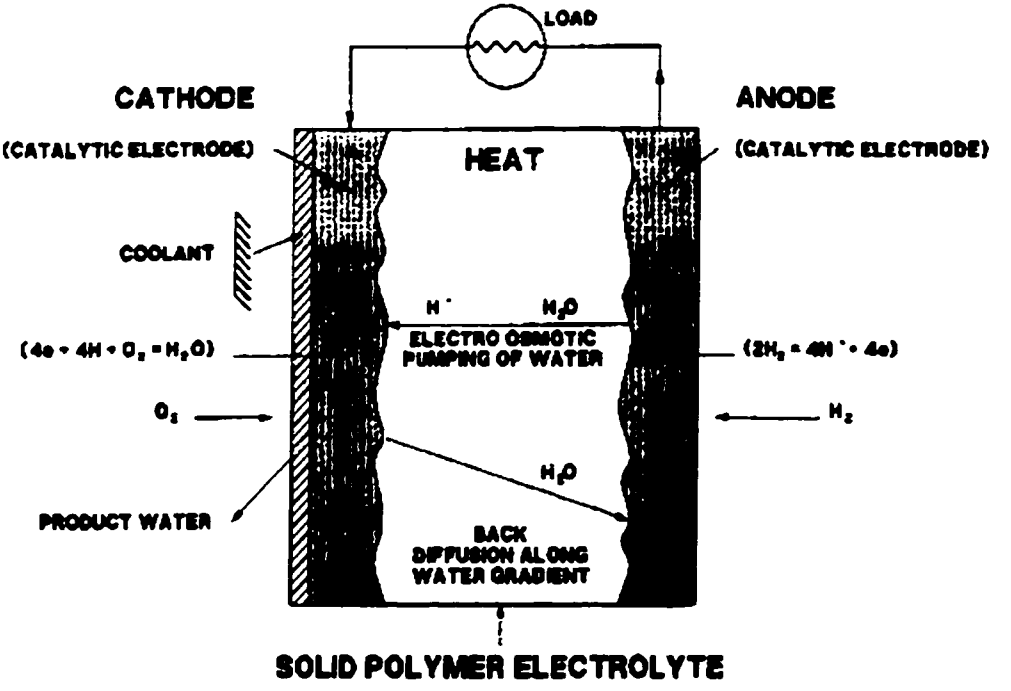

Fig. 2.7 Schematic Cross Section of a SPFC[16]

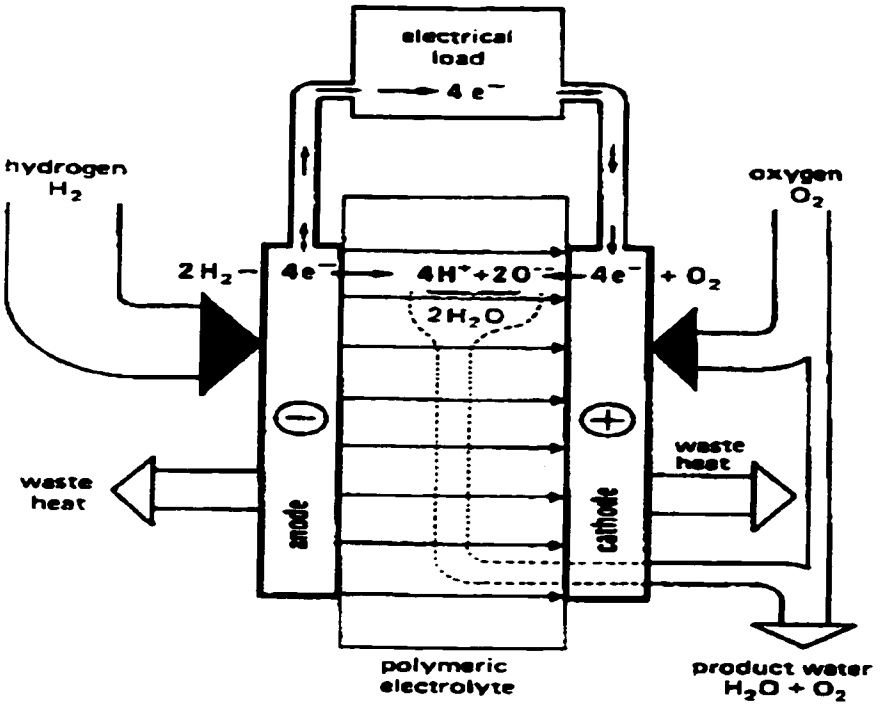

Fig. 2.8 Principles of the SPFC/PEM Fuel Cell[14]

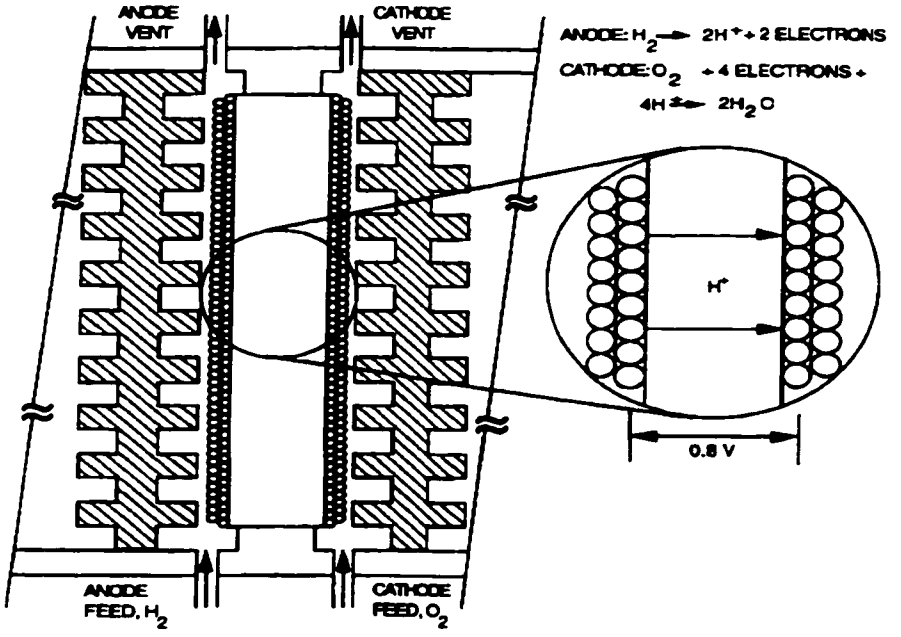

Fig. 2.9 Detail of the SPFC[17]

In these cells, hydrogen ions are conducted through the electrolyte. The state-of-the-art electrolyte materials are perfluorinated sulfonic membranes. These polymers have the following desired properties for a fuel cell:

(1) High oxygen stability

(2) High proton conductivity

(3) High chemical stability

(4) High mechanical strength and low density

These polymers are completely fluorinated and have a Teflon-like backbone. The fluorocarbon chain is connected by means of an ether linkage to a sulfonic acid group. These polymers have been synthesized over a wide range of equivalent weights (ratio of the weight of the polymer to the number of sulfonic acid groups). Fig. 2.10 shows the DuPont's Nafion and Dow Chemical Company's Perfluorosulfonate Ionomers.[16]

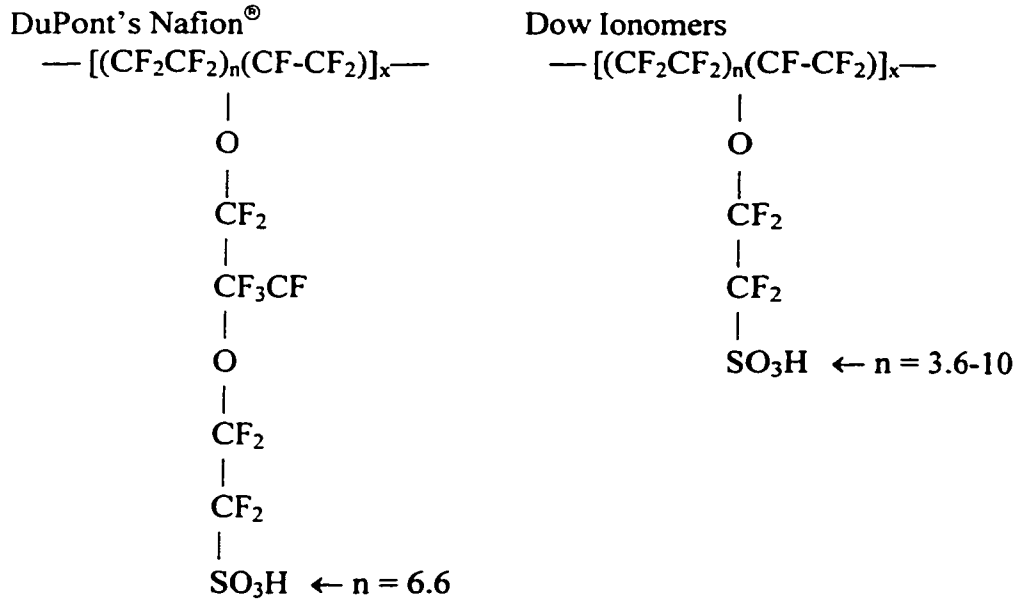

Fig. 2.10 Two Common Electrolyte Compositions Used for SPFC[16]

The acid concentration of the membrane is fixed and fuel cell product (i.e., water) can not dilute it. The acid concentration is given by the equivalent weight (EW) of the particular membrane (g dry polymer/mole of ion exchange sites). This number is the reciprocal of the ion exchange capacity in mole per gram. Lower EW and thinner membrane results in higher cell performance due to lower cell resistance. However, the thickness is limited by the need to avoid the cross-diffusion of the reactant gases.

The gas-diffusion electrodes contain unsupported or supported platinum electrocatalyst. The electrodes have a carbon backing (cloth or paper). A Teflon emulsion is used to bond the fine platinum particles to the carbon layer. The active layer is deposited a few microns thick on the substrate layer (about 10 μm for unsupported and 50 μm for supported electrocatalyst). Gas flow paths are provided by the graphite support structures allowing gas flow across the electrodes.

The applications for SPFC are diverse, varying from spacecraft to automobile. SPFC could be the only type of fuel cells for applications that require small size. For example, it has the potential to power small electronic products such as laptop computers.

2.3 PHOSPHORIC ACID FUEL CELL (PAFC)

Phosphoric acid fuel cell (PAFC), operates between 180 ~ 210°C and provides both electricity and heat. Currently, they are the second (after AFC) in term of commercial use. The half-cell reactions for this fuel cell are:

Anode: $H_2 \rightarrow 2H^+ + 2e^-$ (2.9)

Cathode: $0.5O_2 + 2H^+ + 2e^- \rightarrow H_2O$ (2.10)

The overall cell reaction is: $H_2 + 0.5O_2 \rightarrow H_2O + DC + Heat$ (2.11)

Fig. 2.11 shows the operating principle of the PAFC[15] showing the cell reactions, the paths of each species (gas, electron, protons) and cell components. The PAFC uses phosphoric acid as the electrolyte and is tolerant to CO_2. Phosphoric acid is a colorless, viscous, and hygroscopic liquid. Fig. 2.12 shows the phase diagram for the H_2O-P_2O_5 system.[18] Note the melting temperature variation with P_2O_5 content. The phosphoric acid

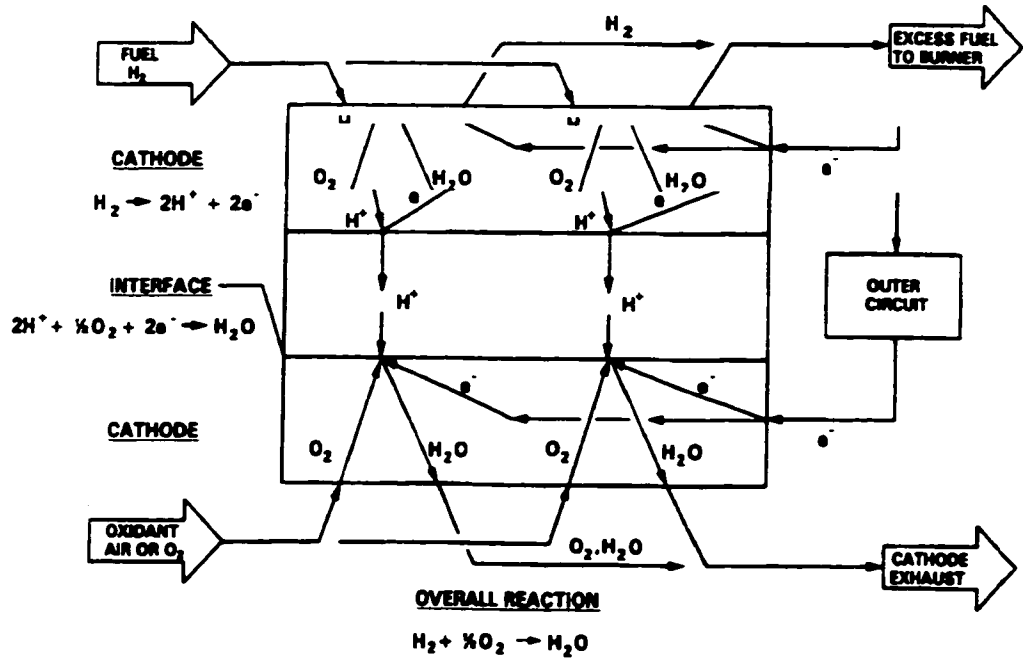

Fig. 2.11 The Operation Principle of the PAFC[15]

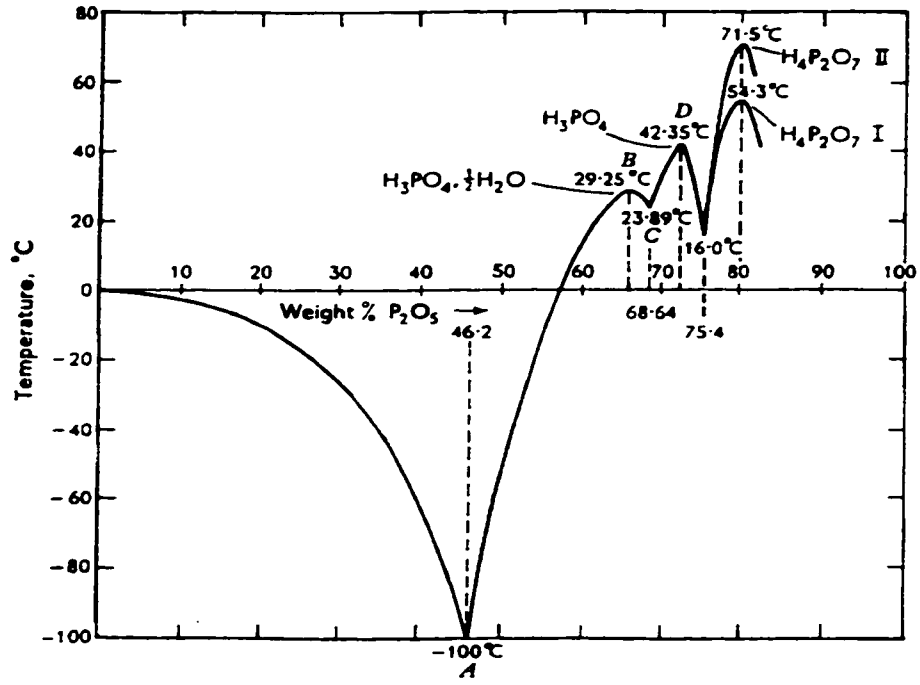

Fig. 2.12 Phases Diagram of the Phospheric Acid H_3PO_4[18]

of composition H_3PO_4 with the freezing point of 42°C is used in PAFC. The acid is contained in a porous matrix made from SiC. The phosphoric acid will be a solid at ambient temperature (< 42°C), and if the electrolyte freezes, the volume change would damage the electrodes and the SiC matrix. It is therefore necessary to keep the PAFC above the freezing point even when the cell is not operating. This requirement imposes some limitations on its applications.

The phosphoric acid is superior to other acids as an electrolyte for the following reasons:

(1) Workability under high temperature

(2) High CO_2 tolerance

(3) Low vapor pressure

(4) High O_2 solubility

(5) Good ionic conductivity at high temperature (with no electronic conductivity)

(6) Low corrosion rate at high temperature

(7) Large contact angle (> 90°) with electrodes

Inside a PAFC, the phosphoric acid is held in a matrix made from fine SiC powder bound with polytetrafluoroethylene (PTFE). Due to capillary force, the phosphoric acid fills the pores of the porous matrix. The thickness of porous SiC matrix is in the range of 0.1 ~ 0.2 mm to minimize internal cell resistance. The requirements for matrix material are:

(1) High capillary force to retain acid

(2) Electronic insulator

(3) Prevent the crossover of reactant gases within the cell structure

(4) High thermal conductivity

(5) Chemical stability at high temperature

(6) Sufficient mechanical strength

Considering the fuel cost, it is more economical to use reformed gas instead of pure hydrogen. The typical compositions of the reformed gas is about 78% H_2 and 20% CO_2. The remaining are impurities (CO < 1%, H_2S, Cl, NH_3, HCN, NO_x < 1 ppm). Fig. 2.13 shows the reactions with approximate gas compositions that occur in the PAFC[19] when reformed gas at pressure of 1 to several atms is used. Although PAFC can tolerate CO_2,

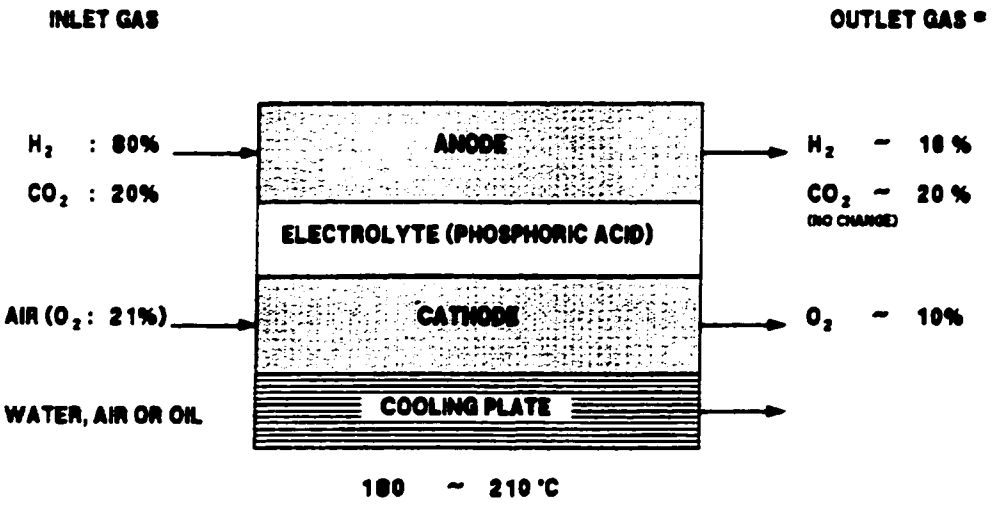

Fig. 2.13 Reactions in the PAFC[19]

other impurities all have negative effects. For instance, the existence of the CO decreases the activity of the Pt catalyst and the cell performance. For better cell performance, the electrode is composed of a porous carbon substrate and a Pt catalyst layer with some hydrophobic agents such as PTFE (Teflon). The function of the carbon substrate is to:

(1) Disperse and support the Pt catalyst

(2) Provide micropores in the electrode

(3) Increase the electrical conductivity of the catalyst layer.

To achieve this, the carbon substrate must satisfy the following requirements:

(1) Stable and mechanically rigid in phosphoric acid under working conditions

(2) Good electronic and thermal conductivity

(3) Porous, allowing efficient reactant gas diffusion

The activity of Pt catalyst depends on its particle size. Small particles with large specific surface area have high catalyst activity. Electrochemical reactions occur at the electrode surface where the three-phase zone (electrode, electrolyte and gas) is located. The current density of fuel cell is proportional to the number of reaction sites, the partial pressure of reactant gases, and the electric conductivity of the catalyst layer. Furthermore, the electrochemical properties of the electrode effects gas diffusion and wettability in the electrolyte. In order to maintain high cell performance, the electrode material must be porous but very fine to provide networks for maximum contact between reactant gas and the Pt catalyst while minimizing gas diffusion through electrolyte.

Electrode performance may decay with time under operating conditions. This is attributed to the sintering of the Pt catalyst and the obstruction to gas diffusion, which is due to the so-called "flooding" in the catalyst layer. Electrode flooding occurs when the pores of electrode are filled or partial filled with electrolyte such that the gas diffusion becomes difficult. Fig. 2.14 shows typical cell structure in the PAFC[15] and an exploded view of the three-phase zone is presented in Fig. 2.15[19] where captions are also provided. The mechanism of Pt sintering and carbon substrate corrosion[19] that cause cell performance decay are illustrated in Fig. 2.16. The requirements for electrode materials are such that they have:

(1) Good electronic conductivity to reduce ohmic losses

(2) Adequate mechanical stability and suitable porosity

(3) Chemical stability in the acidic electrolyte environment

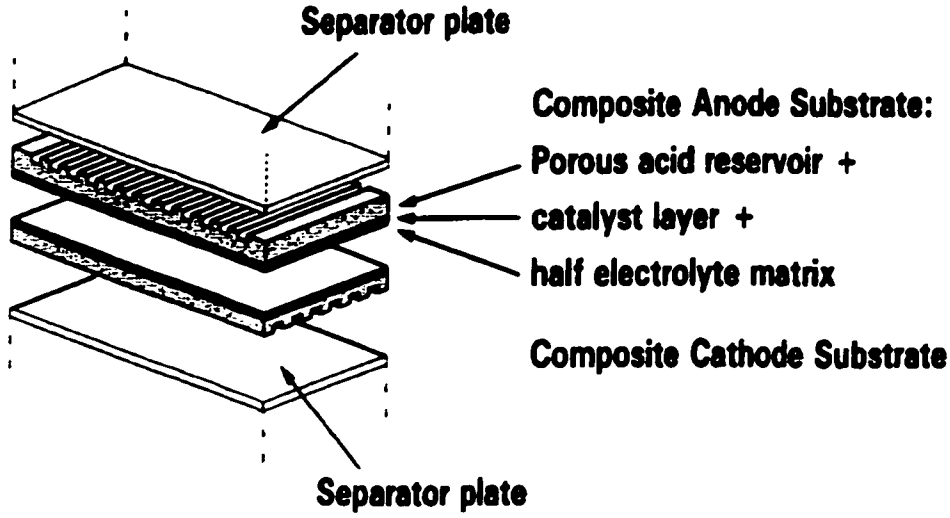

Fig. 2.14 Typical Cell Structure of the PAFC[15]

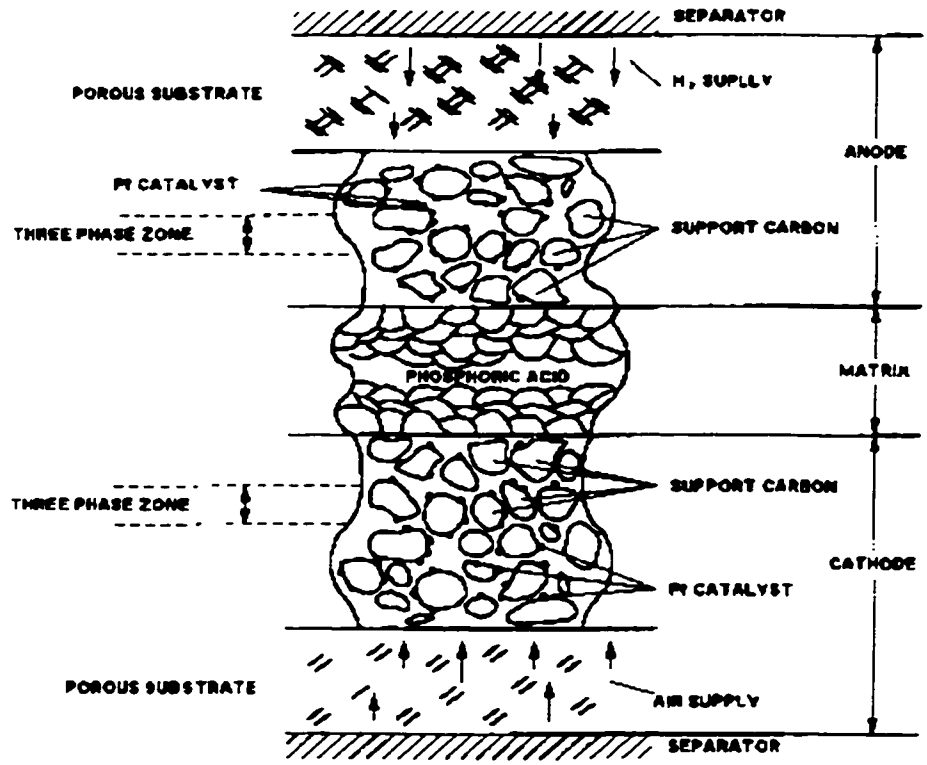

Fig. 2.15 Detailed Schematic View of the Three-phase Zone in Cell Structure[19]

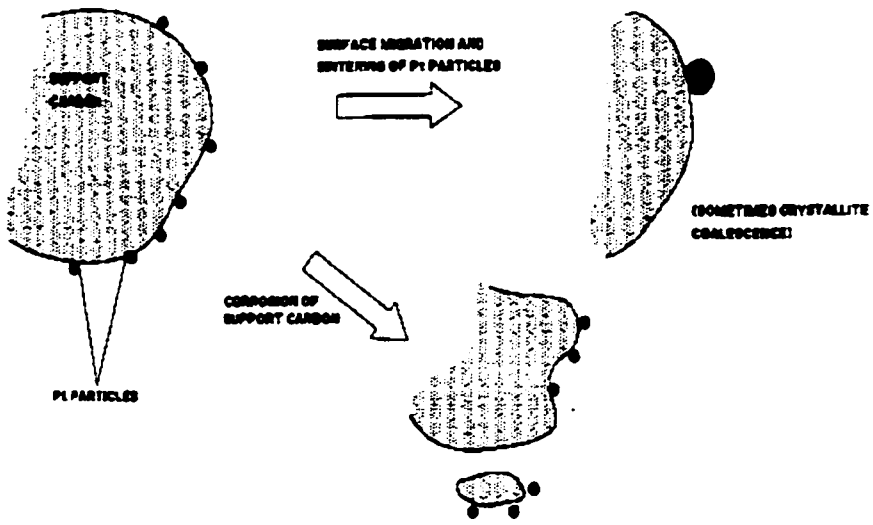

Fig. 2.16 Mechanisms of Pt Sintering and Support Carbon Corrosion[19]

(4) Long-term electrochemical stability.

Two distinct electrode materials are currently in use. Hydrophobic electrodes are partially wetted due to the hydrophobic PTFE used in carbon-based electrodes. Hydrophilic electrodes are metallic electrodes. In both cases, carbon is the vital material for the electrochemical cell stack. Normally carbon powder of high surface area is used for the electrocatalyst support, whereas porous carbon paper is used as the electrode substrate, and graphitic carbon for the bipolar plate.

To summarize, the main characteristics of the PAFC are the follows:

(1) Can operate with CO_2

(2) Can tolerate 1 ~ 2% CO at operating temperature of 200°C

(3) Can utilize the waste heat from the electrochemical cell stack efficiently for

the endothermic steam-reforming reaction to provide space heat or hot water.

The capability of using the waste heat leads to higher overall energy efficiency for PAFC than that of the AFC and SPFC where high-grade heat is not available.

2.4 MOLTEN CARBONATE FUEL CELL (MCFC)

The concept of molten carbonate fuel cell (MCFC) was introduced by O.K. Davtyan[3] in 1940s. Typically, the MCFC is operated at a temperature of about 650°C, at a pressure of 1 to 10 atms. Nobel metal catalyst is not required. The first MCFC was demonstrated by J. A. A. Ketelaar and G. H. J. Broers[3,20] in the late 1950s. The first pressurized MCFC stacks[20] were operated in the early 1980s. Starting in early 1950s, Ketelaar and Broers used thin layers of metal powder as electrode, which were covered by metal gauze. Silver was used as cathode (O_2, CO_2), and nickel as anode (fuel). Porous sintered MgO disks, impregnated with a low melting mixture of Li_2-K_2CO_3 or Li_2-Na_2-K_2CO_3, were used as the electrolyte. Perforated stainless steel disks were employed as supports. Fig. 2.17 shows their MCFC[3] developed in 1958.

Due to the electrochemical combustion of hydrogen and carbon monoxide, carbonates are the only electrolyte materials that satisfy the operating conditions to maintain the performance of MCFC. The state-of-the-art cell materials are porous Ni anode, porous Li-doped NiO cathode, and a molten carbonate (62%Li_2CO_3-38%K_2CO_3) electrolyte. The fuel used for MCFC is a mixture of H_2 and CO. The oxidant is a mixture of O_2 and CO_2.

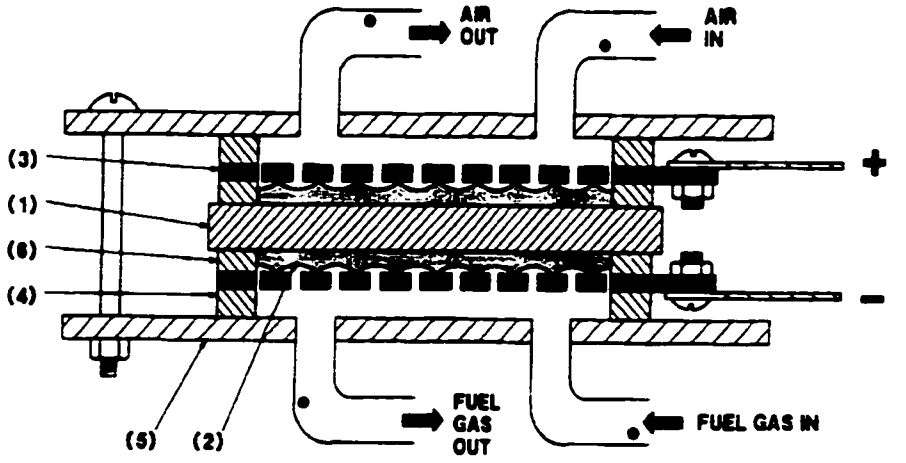

Fig. 2.17 MCFC Developed in 1958[3]
(1) Electrolyte disk, (2) Fine metal powder and metal gauze support
(3) Perforated stainless steel plate, (4) Asbestos gasket
(5) Steel cover plates, (6) Mica ring gaskets
(The bolts clamping the cell together are also isolated by mica rings)

The electrochemical reactions in MCFC are as follows:

Anode: $H_2 + CO_3^{2-} \rightarrow H_2O + CO_2 + 2e^-$ (2.12)

$CO + CO_3^{2-} \rightarrow 2CO_2 + 2e-$ (2.13)

Cathode: $0.5O_2 + CO_2 + 2e^- \rightarrow CO_3^{2-}$ (2.14)

The overall cell reactions are: $H_2 + 0.5O_2 \rightarrow H_2O + DC + Heat$ (2.15)

$CO + 0.5O_2 \rightarrow CO_2 + DC + Heat$ (2.16)

Fig. 2.18 shows schematically where the reaction takes place in MCFC[21] with flow directions for each species in different cell components. Fig. 2.19 schematically shows the operating principle of MCFC[22] with captions indicating cell reactions and components. Fig. 2.20 shows the detailed cell components[23] of MCFC.

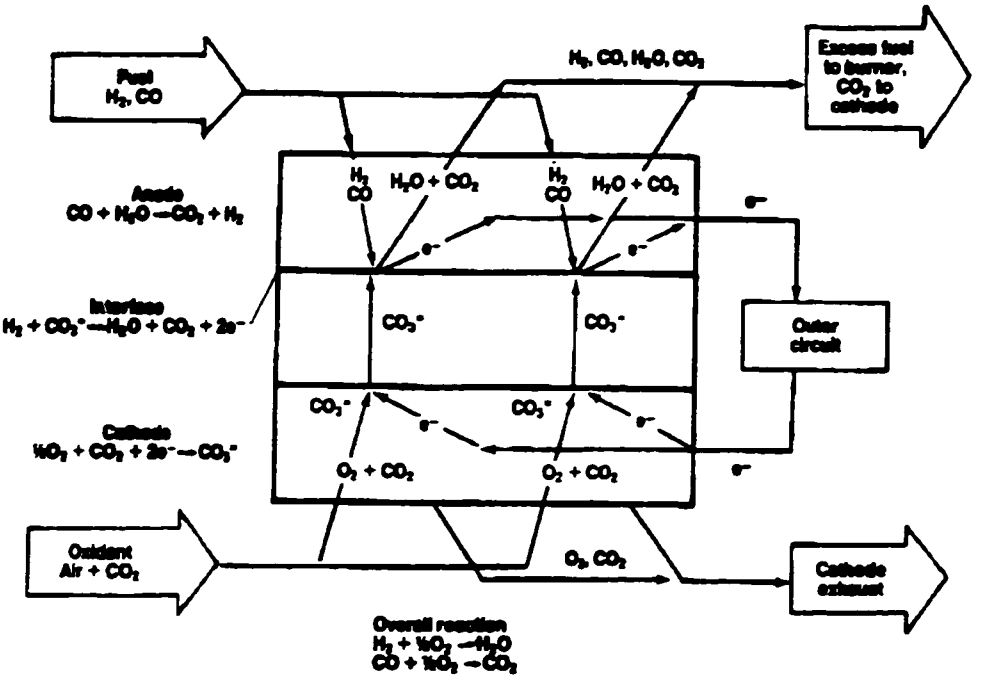

Fig. 2.18 Schematic Diagram of MCFC Reactions[21]

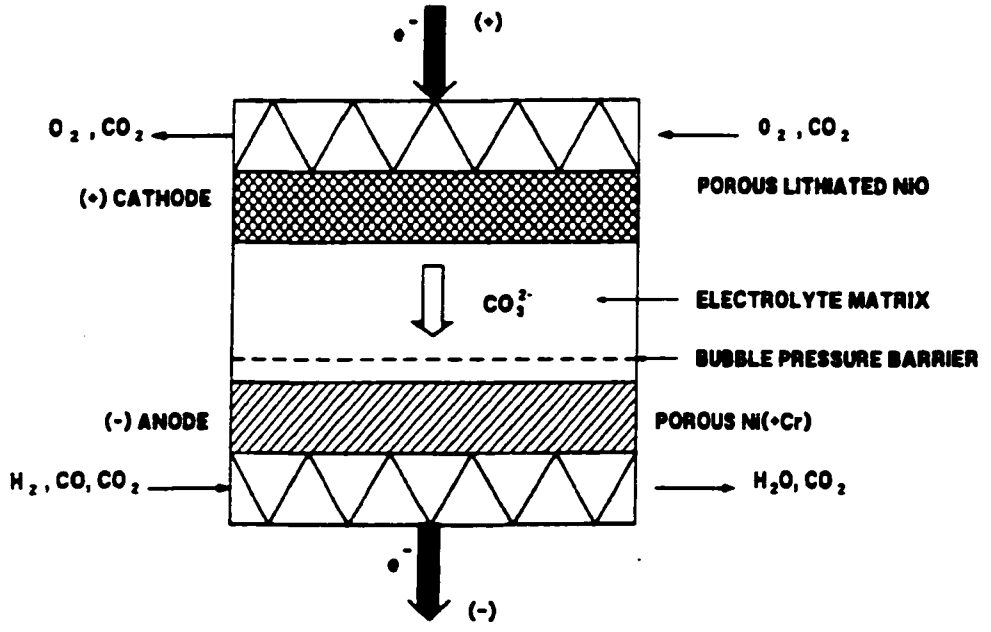

Fig. 2.19 Operating Principle of the MCFC[22]

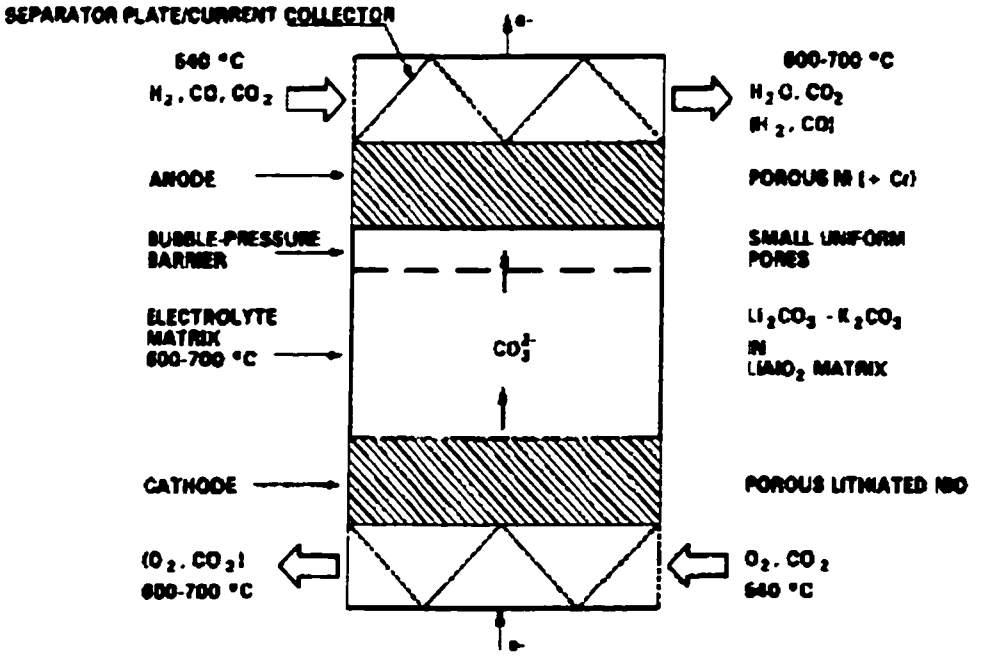

Fig. 2.20 The Cell Components in the MCFC[23]

Molten carbonates are extremely corrosive. In order to minimize the effects of corrosion, the carbonates are contained in a lithium aluminate $LiAlO_2$ matrix or support. The molten carbonates are retained in the ceramic matrix by capillary forces. At the cell operating temperature, the structure (carbonates and support) of the electrolyte is a thick paste. This paste provides gas seals (wet seal) at the edges of the cell[20] (see Fig. 2.21). The wet-seal area, especially on the anode side, is vulnerable to corrosive attack from carbonates. Fig. 2.22 shows the electrochemical reactions which can occur in the gas seals area, where the electrochemical reactions are listed in the diagram with labels for the cell components. Systematic study revealed that 310S stainless steel, Avesta 600 (Fe-28Cr-4Ni-2Mo) and Inconel 601 alloy have the best corrosion resistance against carbonates.[20] Fig. 2.23 shows

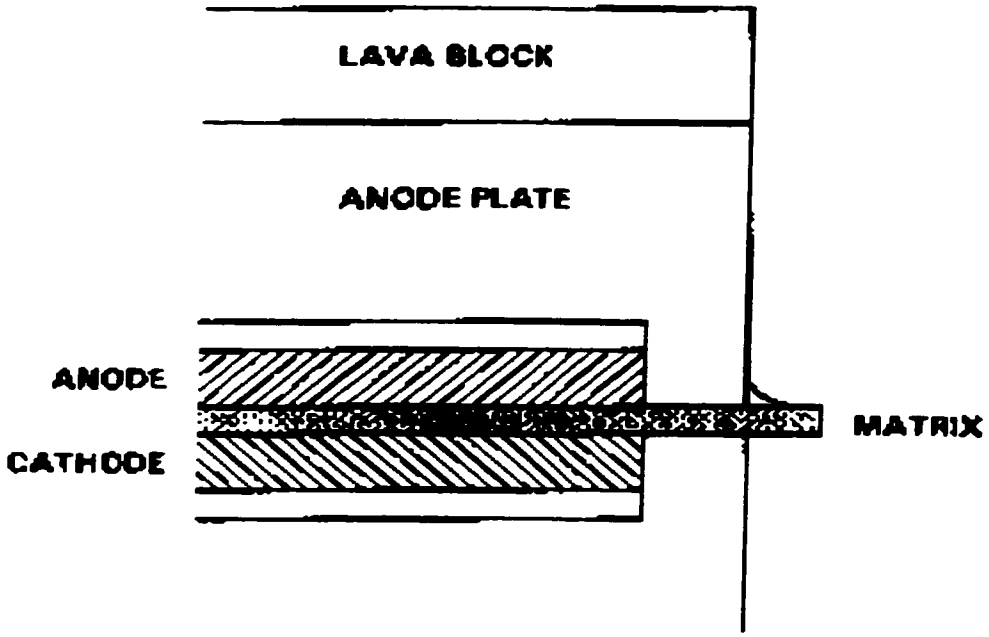

Fig. 2.21 Schematic of the Gas Seals (Wet Seal) in MCFC[20]

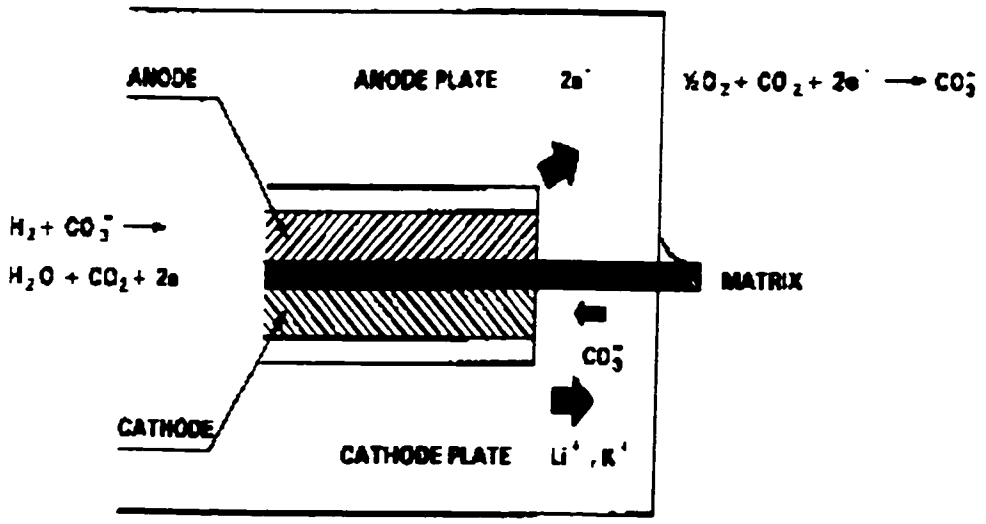

Fig. 2.22 Schematic of Ion and Current Flows in Wet-seal Corrosion[20]

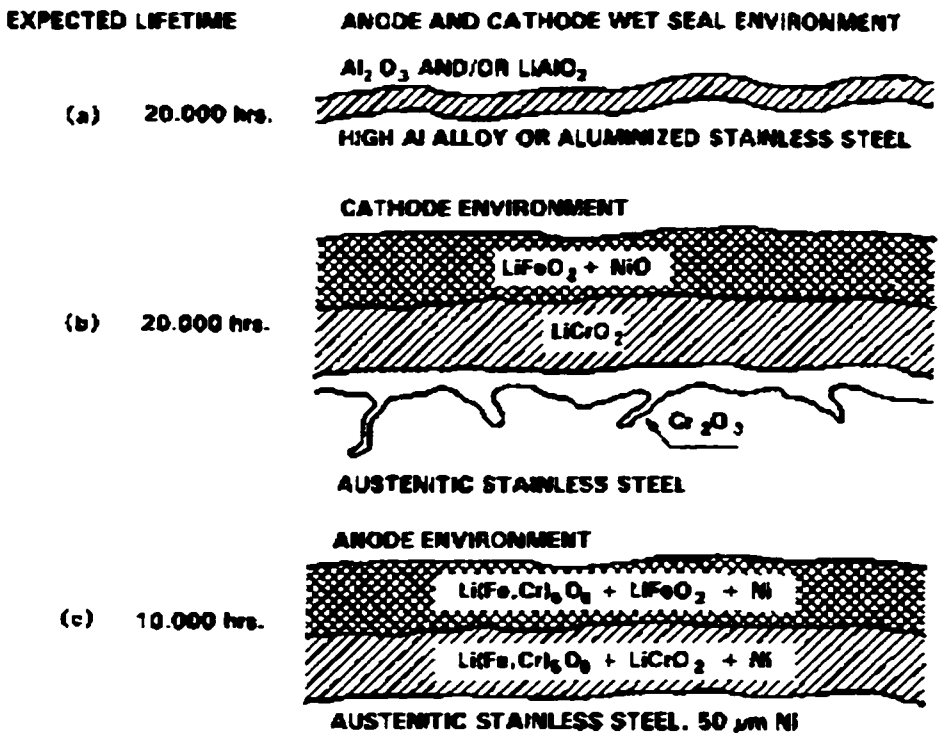

(a) Wet-seal Area (b) Cathode Environment (c) Anode Environment
Fig. 2.23 Formation of Protective Layers on SS 310 in MCFC[20]

the formation of protective layers on 310S stainless steel used in MCFC.[20] The compositions for the protective layers developed at different areas in the fuel cell are shown with expected lifetimes. Operating under a reducing atmosphere, the anode is more negative in potential than the cathode. Thus, the porous Ni metal structure is stable electrochemically. However, Ni powders are subject to sintering and creep at high temperature and pressure. In order to increase long-term stability, Cr or Al is added to the Ni anode to form dispersed oxides which reduce sintering and creep. Cathode material NiO is slightly soluble in carbonates and this reduces cell lifetime. The dissolved NiO may diffuse in the electrolyte and move toward the Ni anode. The metallic Ni from NiO

may electrodeposit in the electrolyte matrix due to the relatively negative potential. This Ni deposition can cause electronic conduction and therefore short-circuit the cell. It is understood that the partial pressure of CO_2 and the basicity of the electrolyte have effects on NiO dissolution according to the following reaction:

$$NiO + CO_2 \rightarrow Ni^{2+} + CO_3^{2-} \qquad (2.17).$$

To solve the problem of NiO dissolution, alternative cathode materials are under development. Optimizing the electrolyte composition is also under consideration. Characteristics of the current MCFC components[20] are given in table 2.1, where the composition, pore and grain size, and thickness are listed.

Table 2.1 Characteristics of the Cell Components of MCFC[20]

Component	Current status
Anode	Composition: Ni-10 wt% Cr Pore size: 3 ~ 6 μm with 50 ~ 70 vol% porosity Thickness: 0.5 ~ 1.5 mm Surface area: 0.1 ~ 1 m^2/g
Cathode	Composition: Lithiated NiO ($Li_xNi_{1-x}O$, $0.022 < x < 0.04$) Pore size: 7 ~ 15 μm with 70-80 vol% porosity Thickness: 0.5 ~ 0.75 mm Surface area: 0.5 m^2/g
Electrolyte support	Composition: γ-$LiAlO_2$ Surface area: 0.1 ~ 12 m^2/g
Electrolyte	Composition: 62%Li_2CO_3-38%K_2CO_3 70%Li_2CO_3-30%K_2CO_3 50%Li_2CO_3-50%Na_2CO_3
Fabrication process	Tape cast Thickness: 0.5 mm

Like PAFC, in addition to the generation of the electricity, high-quality heat is the by-product of MCFC. However, the temperature of the waste-heat coming from MCFC is much higher that that produced in PAFC. Higher energy conversion efficiency is therefore expected for MCFC.

2.5 SOLID OXIDE FUEL CELL (SOFC)

Operating between 600 ~ 1000°C, solid oxide fuel cell (SOFC) is an all-solid device. In contrast to other types of fuel cells, where the electrochemical reactions occur at the gas-liquid-solid three-phase-zone, reactions in SOFC occur at the gas-solid two-phase contact. The corrosive electrolyte is no longer a problem in SOFC, where two porous ceramic electrodes are separated by a dense oxide-ion conducting ceramic electrolyte. Fuel (H_2 or CO) is fed to the anode and reacts with oxygen ions to form water (or CO_2) while releasing electrons to the external circuit. Oxygen is fed to the cathode and accepts electrons from the external circuit to form oxygen ions. Electrons flow from the anode through the external circuit to the cathode. The electrochemical reactions in SOFC are as the follows:

Anode:
$$H_2 + O^{2-} \rightarrow H_2O + 2e^- \quad (2.18)$$
$$(CO + O^{2-} \rightarrow CO_2 + 2e^-) \quad (2.19)$$
$$(CH_4 + 4O^{2-} \rightarrow 2H_2O + CO_2 + 8e^-) \quad (2.20)$$

Cathode:
$$0.5O_2 + 2e^- \rightarrow O^{2-} \quad (2.21)$$

The overall cell reaction is: $H_2 + 0.5O_2 \rightarrow H_2O + DC + Heat$ (2.22)

$(CO + 0.5O_2 \rightarrow CO_2 + DC + Heat)$ (2.23)

$(CH_4 + 2O_2 \rightarrow 2H_2O + CO_2 + DC + Heat)$ (2.24)

Note that SOFC can operate with a variety of fuels (e.g., H_2, CO, CH_4). Fig. 2.24 shows the operating principles of SOFC[24] with cell reactions and flow directions for each species and with captions for each cell components. There are two current versions of SOFC[25] based on whether it is oxygen-ion (O^{2-}) or proton (H^+) conduction through the electrolyte. The detailed cell reactions and species flows for these two types of fuel cells are presented schematic in Fig. 2.25.

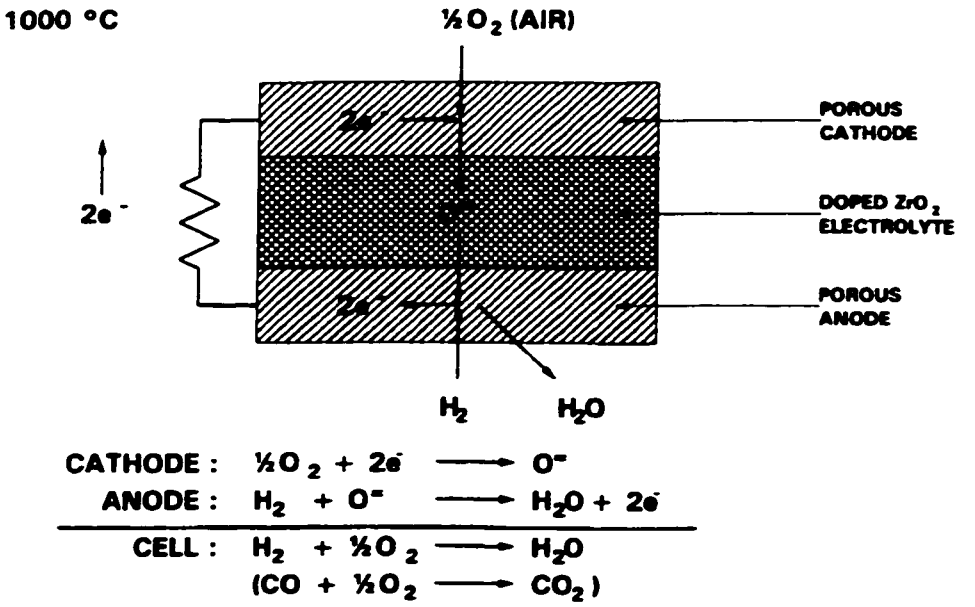

Fig. 2.24 Operating Principles of the SOFC[24]

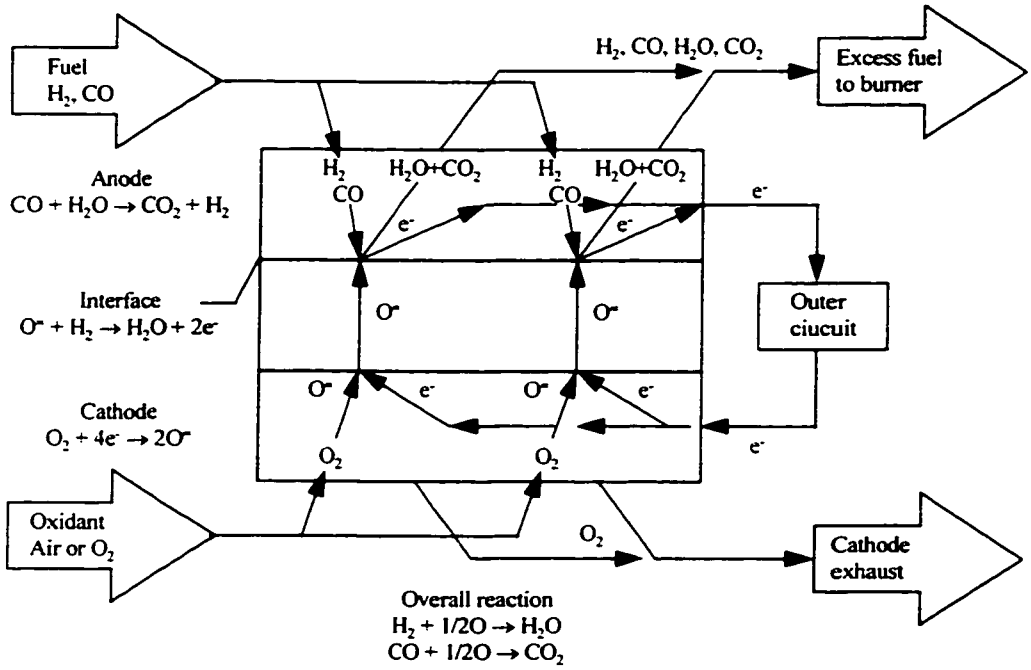

a) Oxygen-ion Conductor SOFC

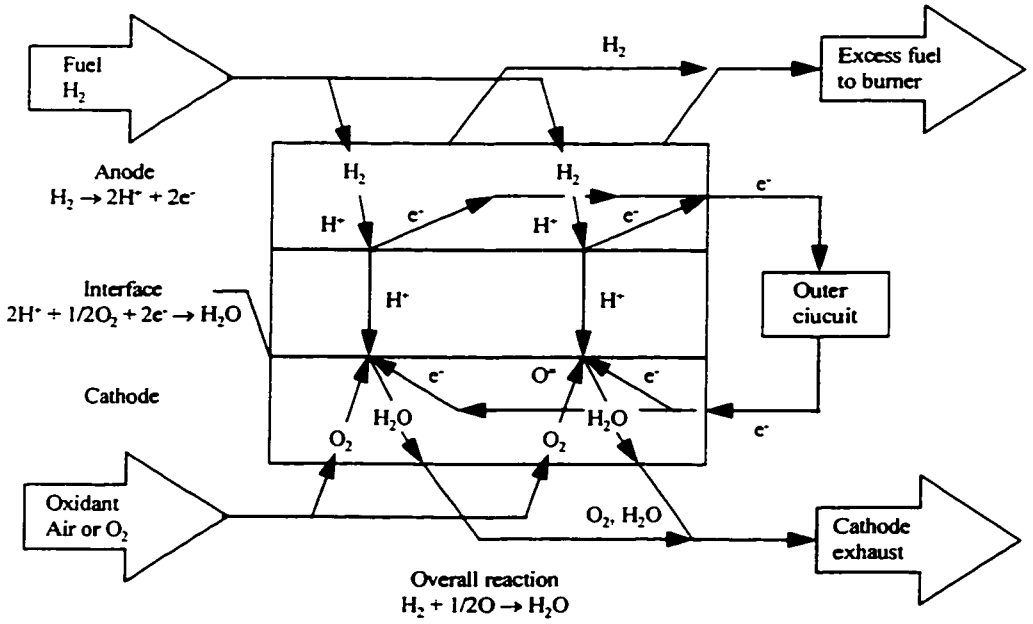

b) Proton Conductor SOFC

Fig. 2.25 Schematic Diagram of SOFC Reactions[25]

The focus of this research is on oxygen-ion conducting electrolyte materials and hence only oxygen-ion conducting SOFC will be reviewed in this section.

The history of SOFC started with W. Nernst[10] who first discovered in 1899 the solid-state oxygen-ion conductor with the composition of $(ZrO_2)_{0.85}(Y_2O_3)_{0.15}$ ('Nernst mass') when he was studying a glower or lamp light source. The potential of this material as an electrolyte for a fuel cell was considered much later (1930s).

W. Schottky,[11] a student of Nernst, in 1935 initiated a proposal of a true solid electrochemical cell (first theoretical paper on SOFC) using 'Nernst mass' as electrolyte. Inspired by Schottky's work, E. Baur and H. Preis[12] made the first SOFC in 1937. Using hydrogen and air as reactants, Baur and Preis operated their cell (coke anode, iron oxide cathode and 'Nernst mass' electrolyte) at 1050°C. The cell yielded a current density of 1 mA/cm^2 at 650 mV. Since then a variety of materials have been tested as solid electrolytes by many researchers. Only doped zirconia has shown promising properties. J. Weissbart and R.J. Ruka[26] reported their cell using calcia-stabilized zirconia as electrolyte in 1962 and the cell performance was determined by the resistance of the thick electrolyte. Archer *et al.*[27] demonstrated a multicell SOFC generator first in 1965. They built a 100 W solid electrolyte SOFC using calcia-stabilized zirconia as the electrolyte and sintered platinum as the electrodes. Later nickel-zirconia cermet (for the anode) and electronic conductive oxides (for the cathode) were used to replace the expensive platinum.[27]

2.5.1 Cathode Materials for SOFC

To be considered as a SOFC component, many specific material requirements need to be satisfied. High operating temperature and the combined oxidizing/reducing environments in SOFC has ruled out many candidates. The criteria for the cathode material are:

(1) High electrocatalytic activity for oxygen reduction

(2) High electronic conductivity

(3) Stability in the oxidizing atmosphere and at high-temperature

(4) Thermal expansion compatible with other cell components

(5) Porous for efficient oxygen transport

The high operating temperature and oxidizing atmosphere place severe material problems on the cathode. In the early stages of SOFC development, metals were considered as possible cathode materials where they serve as both electrocatalyst and current collector. Only noble metals (Pt, Pd, Au and Ag) can survive in oxidizing atmosphere. Considering the high operating temperature of SOFC, Au and Ag can not be used as cathode materials due to their low melting points. Pd has a considerable vapor pressure at high temperature, which degrades long-term cell performance. Thus the only reasonable choice is Pt. Indeed, Pt is the most suitable metallic electrode (cathode and anode) material for SOFC application. Pt is stable under both oxidizing and reducing environments and its coefficient of thermal expansion (CTE) is similar to that of the YSZ electrolyte. Although Pt is good, it is very expensive. Alternative cathode materials such as iron oxide[12] were used in 1937. Since then many other oxides and composites (oxide with a metallic wire

grid) have been proposed and examined. However, all of them fail to meet one or more of the requirements for cathode material except some doped p-type ABO_3 perovskites.[24] Substitution of donor- or acceptor-type cations in A or B sites of the perovskites increases their electrical conductivity. For example, the electrical conductivity of $LaMnO_3$ is contributed from the 3d electrons of Mn. Substitution of lower valence ions in the La^{3+} and Mn^{3+} sites may increase the conductivity. The state-of-the-art cathode material is Sr-doped $LaMnO_3$ (LSM).[28,29] Compared to many other oxides, LSM has an unusually large single phase region such that the Sr doping level can be varied to tailor its properties and meet the cathode requirements for SOFC.

The details of LSM materials can be found in Ref. 28 and 29. Only the important results are summarized here. Strontium doping enhances the electronic conductivity of $LaMnO_3$ by increasing the Mn^{4+} content owing to the substitution of La^{3+} by Sr^{2+} on the A-site,

$$LaMnO_3 \xrightarrow{SrO} La^{3+}_{1-x}Sr^{2+}_{x}\, Mn^{3+}_{1-x}Mn^{4+}_{x}O_3. \qquad (2.25)$$

The electronic conductivity of LSM takes place via the small polaron conduction mechanism. The temperature dependence of the conductivity is given by:

$$\sigma = (A/T)\exp(-E_a/kT) \qquad (2.26)$$

where A is the preexponential factor, k is the Boltzmann constant, and E_a is the activation

energy for conduction. For $LaMnO_3$ doped with less than 50 mol% Sr, the conductivity shows negative temperature dependence at temperatures above 1000°C, suggesting a semiconducting-to-metallic transition. Metallic-type conduction is observed for doping level of 50 to 60 mol% Sr at lower temperatures (200 to 1000°C). Oxygen activity and cation deficiency significantly influences the electrical behavior of doped $LaMnO_3$. At 1000°C, the conductivity of LSM material shows little dependence on $p(O_2)$ in the high oxygen partial pressure region, and this region becomes narrower with increasing temperature. As the $p(O_2)$ is reduced, the conductivity decreases in proportion to $[p(O_2)]^{1/4}$. At a critical $p(O_2)$, an abrupt decrease of the conductivity is observed due to the decomposition of the $LaMnO_3$. This critical $p(O_2)$ shifts to higher values when the temperature and/or the Sr content are increased.

Vacancies at the lanthanum site influence the phases and electrical properties of doped $LaMnO_3$. $(La_{1-x}Sr_x)_{1-y}MnO_{3-d}$ undergoes a phase transition at about 700°C in air where the conductivity behavior of the material changes. Below 700°C, the small polaron hopping mechanism well describes trends in conductivity. Above 700°C, the conductivity shows little dependence on the temperature.

The CTE of undoped $LaMnO_3$ is about $11.2*10^{-6}$ (cm/cm·K). Doping $LaMnO_3$ with Sr increases the value of CTE. Table 2.2 lists the CTE of some LSM materials. It is possible to match the thermal expansion of LSM cathode with others fuel cell components such as YSZ electrolyte by tailoring the Sr-doping concentration. LSM is also stable at SOFC

Table 2.2 Coefficient of Thermal Expansion (CTE) of $La_{0.99-x}Sr_xMnO_3$[28]

Composition	Coefficient of Thermal Expansion (CTE) ($*10^{-6}$ cm/cm·K)
$La_{0.99}MnO_3$	11.2
$La_{0.94}Sr_{0.05}MnO_3$	11.7
$La_{0.9}Sr_{0.1}MnO_3$	12.0
$La_{0.89}Sr_{0.10}MnO_3$	12.0
$La_{0.79}Sr_{0.20}MnO_3$	12.4
$La_{0.69}Sr_{0.30}MnO_3$	12.8
$La_{0.5}Sr_{0.5}MnO_3$	13.2

operating temperature. Fig. 2.26 shows the phase reactions between LSM and ZrO_2, the electrolyte material.[30] It is found that LSM perovskite doping with 0.3 to 0.4 mole Sr achieves the highest thermal stability without the formation of secondary phases ($La_2Zr_2O_7$ and $SrZrO_3$). An optimized doping window is clearly observed. Based on these results, it can be concluded that Sr doped $LaMnO_3$ is an attractive candidate as a cathode material.

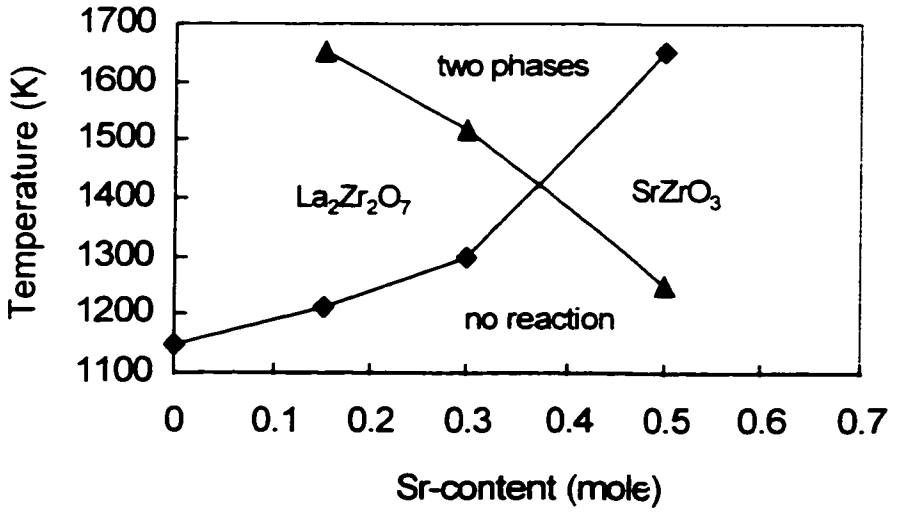

Fig. 2.26 Phase Reactions between $La_{1-x}Sr_xMnO_3$ and ZrO_2[30]

2.5.2 Anode Materials for SOFC

For the anode material, the criteria are:

(1) Effective oxidation catalysis

(2) High electronic conductivity

(3) Stability in the reducing anodic environment and at high-temperature

(4) Thermal expansion compatible with other cell components

(5) Porosity for easy fuel transport

(6) Tolerance to sulfur contaminants and hydrocarbon fuels

Coke was used as the anode material in the early stage of SOFC development. Later platinum was chosen as anode material and many other materials have also been examined. The current anode material is nickel-zirconia cermet (porous mixture of Ni and ZrO_2-Y_2O_3). The doped zirconia in the cermet functions as porous support and sintering inhibitor for the Ni particles, and behaves like an ionic conductor. In addition, it increases the effective surface area for fuel (H_2 and CO) oxidation. The electrical properties of the cermet depend strongly on the content and particle size of Ni. The electronic conductivity is dominated when Ni content is great than 30 vol% due to the formation of the Ni percolation network by particle-to-particle contact. When Ni content is less than 30 vol%, ionic conduction becomes predominant. Considering the thermal expansion behavior, Ni content has to be lowered (Ni is the only metal used in SOFC materials). The optimized Ni content of 35 vol% is then chosen to maintain the required electronic conductivity while maintaining acceptable CTE.

2.5.3 Electrolyte Materials for SOFC

Criteria for electrolyte materials are:

(1) High oxygen ion conductivity and negligible electronic conductivity

(2) High stability under both oxidizing and reducing atmospheres

(3) Stability at high-temperature

(4) Thermal expansion compatibility with electrode materials

(5) High density to prevent fuel transport to the cathode

Since the time of Nernst, Yittria Stabilized Zirconia (YSZ) was and still is the preferred electrolyte used in SOFC (and many other electrochemical devices), because of its high oxygen-ion conductivity and desirable stability in both oxidizing and reducing atmospheres. The ion transport number (ratio of ionic conductivity to total conductivity) of YSZ is close to unity and, it can be sintered to very high density to prevent fuel transport. The above-mentioned properties make it a very good choice for SOFC electrolyte. The only drawback of using YSZ is its relative low conductivity at lower temperatures and therefore the YSZ SOFC has to be operated at about 1000°C to achieve sufficient conduction. At such high temperature, the thermal and chemical stabilities of various SOFC components are significant problems.

Doped zirconia is stable in the fluorite structure. Doping aliovalent cations such as Y^{3+} can stabilize the zirconia structure while creating oxygen vacancies. The concentration of vacancies is proportional to the doping content according to the charge neutrality

requirement for ionic materials. Fig. 2.27 schematically illustrates the crystal structure and the mechanism of oxygen vacancy conduction in fluorite structure.[24] Oxygen occupies the tetrahedral sites formed by four nearest-neighbor cations (Y^{3+} or Zr^{4+}). Oxygen ion conduction occurs between vacant sites via an unoccupied octahedron. At 1000°C, the oxygen ion conductivity of YSZ can be maintained at 0.1 S/cm.

Only two oxides, Bi_2O_3 and CeO_2, have been reported to show ionic conductivities superior to that of YSZ.[31] However, Bi_2O_3 undergoes phase transitions (it is bcc γ–Bi_2O_3 and tetragonal β–Bi_2O_3 at $T < 650°C$; monoclinic α–Bi_2O_3 at 650 ~ 730°C; fluorite structure δ–Bi_2O_3 at 730 ~ 825°C). The volume change associated with these phase transitions leads to cracking and severe deterioration, which makes it unacceptable for SOFC applications. CeO_2, on the other hand, undergoes large departures from

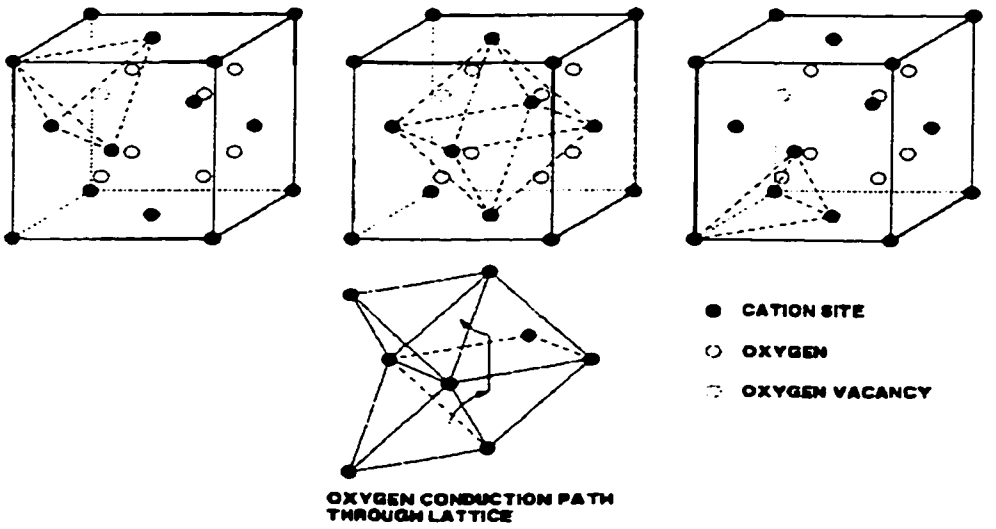

Fig. 2.27 Oxygen Vacancy Conduction Path in Stabilized Zirconia[24]

stoichiometry at elevated temperature which leads to appreciable electronic conduction and, is therefore not suitable for SOFC.

Table 2.3 summarizes the most important material requirements for each component of SOFC[32] in terms of electrical conductivity, stability, compatibility and porosity.

2.6 COMPARISONS OF FUEL CELLS

Owing to its long time success in space programs and military missions, Alkaline Fuel Cell (AFC) is the most developed class of fuel cells. The major challenge for AFC is its low tolerance to CO_2. Even the CO_2 in air (about 350 ppm) is sufficient to carbonate the electrolyte and form solid deposits in the porous electrode. In order to maintain cell performance, it is necessary to remove the CO_2 completely from the gas stream. Combination of this low CO_2 tolerance and high Pt catalyst loading makes AFC very expensive. Recent application in automobile industry may help develop new techniques to overcome the low CO_2 tolerance limit and reduce the Pt loading so its success can be expanded to wider applications.

Compared to AFC, Solid Polymer Fuel Cell (SPFC) is insensitive to CO_2, but it is sensitive to CO which can poison the cell and decrease cell performance. The tolerance limit to CO is about 100 ppm. SPFC also requires high Pt loading to promote cell reactions, which limits their wide usage. SPFC are currently being used in transportation applications. In the future, SPFC may find new applications because of their small sizes

Table 2.3 Requirements for SOFC Components[32]

	Requirements				
Component	Conductivity	Stability	Compatibility	Porosity	Thermal Expansion
Anode	High electrical conductivity	Chemical, phase, morphological, and dimensional stability in fuel environment	No undesirable chemical interactions or interdiffusion with adjoining cell components	Porous	Thermal expansion match with adjoining components
Electrolyte	High ionic conductivity. Negligible electrical conductivity	Chemical, phase, morphological, and dimensional stability in fuel and oxidant environments	No damaging chemical interactions or interdiffusion with adjoining cell components	Fully dense	Thermal expansion match with adjoining components
Cathode	High electrical conductivity	Chemical, phase, morphological, and dimensional stability in oxidant environment	No damaging chemical interactions or interdiffusion with adjoining cell components	Porous	Thermal expansion match with adjoining components
Interconnect	High ionic conductivity. Negligible electrical conductivity	Chemical, phase, morphological, and dimensional stability in fuel and oxidant environments	No damaging chemical interactions or interdiffusion with adjoining cell components	Fully dense	Thermal expansion match with adjoining components

in mini electronic application such as powering computers.

When cell operating temperature increases, it is possible and more economical to use natural gas rather than high purity hydrogen as fuel. However, the reaction of the hydrocarbon-to-hydrogen conversion is often incomplete during the gas reforming process, leaving carbon monoxide in the fuel stream.

Phosphoric Acids Fuel Cell (PAFC) is also sensitive to CO. Even more serious is PAFC sensitivity to H_2S, another leftover from gas reforming process. Both CO and H_2S are present in the reformed fuels. The tolerance of PAFC to CO is about 3%. The CO level can be reduced to less than 1-2% if more Pt is used. The tolerance level for H_2S is much lower, which is in the range of a few ppm.

While using reformed gases, both SPFC and PAFC have limited lifetimes because of the cell degradation due to carbon monoxide. However, neither CO_2 nor CO is a problem for Molten Carbon Fuel Cell (MCFC). The main issue with MCFC is the corrosive-electrolyte which attacks the electrodes. The sintering of its constituent components at operating temperature (650°C) is another issue that deserves to be considered. Furthermore, it still requires a high level of noble metal (Pt) loading for MCFC that increases the cost.

The low ionic conductivity of electrolyte material at lower temperature seems to be the

only problem with Solid Oxide Fuel Cell (SOFC). To maintain cell performance, it is therefore necessary to operate SOFC at elevated temperature. Consequently, many material compatibility problems are induced at high temperature. For SOFC, its long-term thermal-mechanical-chemical stability is of special concerns.

Table 2.4 lists the main characteristics and applications of each fuel cell, in term of operating temperature. For a particular fuel cell, the application fields are based on its properties and performance. The chemical reactions for different type of cell are summarized in table 2.5, with respect to anodic and cathodic reactions. The thermodynamic data for various cell reactions[22,32] are given in table 2.6, where T is temperature in Kelvin, ΔG° is the standard Gibbs free energy of formation (reaction), ΔH° is the standard enthalpy energy of formation (reaction), ΔS° is the standard entropy of formation (reaction), n is the number of electrons being transferred, υ is the volume change of the reaction in mole, E°_{r} is the reversible cell potential in volt, η_{rev} is the efficiency of cell reaction and l represents liquid, g represents gas.

Based on this comparison, it is clear that the overall properties of SOFC can be superior than other type of fuel cell if its high operating temperature can be reduced. To realize this possibility, new electrolyte materials with higher ionic conduction than the conventional YSZ are required.

Table 2.4 Type of Fuel Cell and Their Characteristics and Applications

Type	T_{op} (°C)	Characteristics	Applications
Alkaline Fuel Cell (AFC)	50 ~ 100	♥ High-power density (A/m^2) ♥ High Pt loadings ♥ $KOH + CO_2 \rightarrow K_2CO_3$ ♥ Pure O_2, no CO_2, no CO ♥ Very expensive	♥ Space vehicles ♥ Automobile
Solid Polymer Fuel Cell (PEM)	50 ~ 100	♥ Easy design ♥ High Pt loading ♥ Pure H_2 (> 99.99%), no CO ♥ Moderate current density	♥ Space and military ♥ Automobile
Phosphoric Acid Fuel Cell (PAFC)	~ 200	♥ Commercially successful ♥ Available in a few to 300 kW ♥ Tolerant to CO_2 but low CO ♥ High reliability ♥ High cost ($2000 to $3000 per kW)	♥ Electricity-heat cogeneration ♥ Power in remote areas (near natural gas supply lines) ♥ Automobile
Molten Carbonate Fuel Cell (MCFC)	600 ~ 700	♥ Corrosive Li_2CO_3-K_2CO_3 ♥ Internal natural gas-reforming ♥ need CO_2 for cathode ♥ CO is usable fuel ♥ No Pt but Ni catalyst ♥ High-grade heat available	♥ Medium to large (2 kW ~ 2 MW) cogeneration power systems ♥ Load levelers in electric utilities ♥ Not suitable for small power plants or for transportation use
Solid Oxide Fuel Cell (SOFC)	~ 1,000	♥ Very high temperature ♥ Simple in design ♥ Internal natural gas-reforming ♥ No catalyst needed ♥ CO is usable fuel ♥ Cell are difficult to produce ♥ High-grade heat available	♥ Cogeneration plant ♥ Potential use in transportation sector if the operating temperature can be reduced

Table 2.5 Typical Electrochemical Reactions in Fuel Cells

Fuel Cell	Anode Reaction	Cathode Reaction
AFC	$H_2 + 2(OH)^- \rightarrow 2\ H_2O + 2e^-$	$1/2\ O_2 + H_2O + 2e^- \rightarrow 2(OH)^-$
SPFC	$H_2 \rightarrow 2H^+ + 2e^-$	$1/2\ O_2 + 2H^+ + 2e^- \rightarrow H_2O$
PAFC	$H_2 \rightarrow 2H^+ + 2e^-$	$1/2\ O_2 + 2H^+ + 2e^- \rightarrow H_2O$
MCFC	$H_2 + CO_3^{-2} \rightarrow H_2O + CO_2 + 2e^-$ $CO + CO_3^{-2} \rightarrow CO_2 + 2e^-$	$1/2\ O_2 + CO_2 + 2e^- \rightarrow CO_3^{-2}$
SOFC	$H_2 + O^{-2} \rightarrow H_2O + 2e^-$ $CO + O^{-2} \rightarrow CO_2 + 2e^-$ $CH_4 + 4O^{-2} \rightarrow 2H_2O + CO_2 + 8e^-$	$1/2\ O_2 + 2e^- \rightarrow O^{-2}$

Table 2.6 Thermodynamic Data for Several Cell Reactions[22,32]

Reaction	T (K)	ΔG° (kJ)	ΔH° (kJ)	ΔS° (J/K)	n	ν (mole)	E_r^o (V)	η_{rev} ($\Delta G^\circ / \Delta H^\circ$)
$H_2 + 1/2O_2 \rightarrow H_2O(l)$	298	- 237	- 285	- 162	2	- 1.5	1.23	0.83
$H_2 + 1/2O_2 \rightarrow H_2O(g)$	298	- 229	- 242	- 44	2	- 0.5	1.18	0.95
$H_2 + 1/2O_2 \rightarrow H_2O(g)$	378				2	- 0.5		
$H_2 + 1/2O_2 \rightarrow H_2O(g)$	1273				2	- 0.5		
$NH_3 + 3/4O_2 \rightarrow 1/2N_2 + 3/2H_2O(l)$	298	- 226	- 225	- 97	3	- 1.25	1.17	0.89
$N_2H_4 + O_2 \rightarrow N_2 + 2H_2O(l)$	298	- 312	- 311	+ 2	4	- 1.0	1.61	1.00
$C + 1/2O_2 \rightarrow CO(g)$	298	- 137	- 110	+ 89	2	+ 0.5	0.71	1.24
$C + 1/2O_2 \rightarrow CO(g)$	773	- 180	- 110	+ 90	2	+ 0.5	0.93	1.63
$C + 1/2O_2 \rightarrow CO(g)$	1273	- 224	- 113	+ 87	2	+ 0.5	1.16	1.97
$C + O_2 \rightarrow CO_2(g)$	298	- 394	- 384	+ 33	4	0	1.02	1.00
$C + O_2 \rightarrow CO_2(g)$	773	- 396	- 394	+ 2	4	0	1.03	1.00
$C + O_2 \rightarrow CO_2(g)$	1273	- 396	- 395	+ 1	4	0	1.03	1.00
$C + 1/2O_2 \rightarrow CO_2(g)$	298	- 257	- 283	- 86	2	- 0.5	1.33	0.91
$C + 1/2O_2 \rightarrow CO_2(g)$	923				2	- 0.5	1.00	
$C + 1/2O_2 \rightarrow CO_2(g)$	1273	- 172	- 281	- 86	2	- 0.5	0.89	0.61
$CH_3OH(l) + 3/2O_2 \rightarrow CO_2 + 2H_2O(l)$	298	- 704	- 727	- 77	6	- 0.5	1.21	0.97
$CH_4 + 2O_2 \rightarrow CO_2 + 2H_2O(l)$	298	- 802	- 804	- 6	8	- 2.0	1.04	1.00
$CH_4 + 2O_2 \rightarrow CO_2 + 2H_2O(g)$	923				8	0		
$CH_4 + 2O_2 \rightarrow CO_2 + 2H_2O(g)$	1273				8	0		

2.7 NEW ELECTROLYTE MATERIAL FOR SOFC

An ideal electrolyte should be an electronic insulator but ionic conductor. There are four criteria for judging an electrolyte material:[33]

1. The working-ion conductivity σ_i: it must be high enough ($\sigma_i > 10^{-2}$ S/cm) to tolerate ohmic losses under load conditions
2. The transport (transference) number t_i: it should approach unity, $t_i = \sigma_i/\sigma \sim 1$, where $\sigma \equiv \sigma_e + \sum_i \sigma_i$ is the total electronic and ionic conductivity
3. The reaction window: the electrolyte must be chemically inert under load conditions (under both oxidizing and reducing environments);
4. Ease of fabrication: forming thin, homogeneous membranes of high mechanical strength and density to separate fuel and air from mixing.

The ionic conductivity is generally a tensor, σ, relating the applied electric field $\boldsymbol{E}$ to the current density $\boldsymbol{j}$. In the absence of any charge-carrier gradients, Ohm's law gives

$$\boldsymbol{j} = \sigma * \boldsymbol{E} \qquad (2.27)$$

and a different tensor components σ_{ij} describes the conductivity for each principal crystallographic direction. For polycrystalline ceramic electrolytes, a single scalar σ is sufficient and it often obeys an Arrhenius-type expression:

$$\sigma = (A/T)\exp(-E_a/kT) \qquad (2.28)$$

where A is a pre-exponential factor, E_a is the activation energy, k is Boltzmann's constant and T is the absolute temperature. From Eq. (2.28), it is clear that σ increases as T increases.

The operating temperature of a fuel cell is determined by the temperature dependence of the conductivity of its electrolyte. For a conventional yttria stabilized zirconia (YSZ) electrolyte, an operating temperature of about 1000°C is required to achieve adequate oxygen ionic conductivity. This high operating temperature challenges the choice of electrode materials. Electrode reactions at such high temperatures tend to degrade fuel cell performance and shorten cell lifetime. The maintenance cost of a fuel cell system is likely to be proportional to its operating temperature, and so becomes an important economic factor at elevated temperature. Therefore, alternative electrolyte materials with sufficient ionic conductivity and high stability at lower temperatures are essential to further improve the SOFC technology.

If an intermediate temperature (500 ~ 800°C) oxide ion conductor is available, then some of the constraints on electrode materials can be removed. Furthermore, fuel cell lifetime reliability will improve significantly. Lower temperature will also lead to cell designs with less expensive fabrication process. Stimulated by this possibility, many potential electrolyte materials have been studied, and the search for new electrolyte materials is an ongoing research effort. In general, the electrolyte materials possess one of the following lattice structures: fluorite (or fluorite-type), perovskite (or perovskite-type),

brownmillerite and pyrochlore. In this section, important results on some of these materials are reviewed.

Pure perovskite-type $LaGaO_3$ is an insulator. Doping $LaGaO_3$ with alkaline-earth elements turns it into a fast ion conductor. The conductivity of this perovskite varies with dopants and changes with doping concentrations. The Sr and Mg doped $LaGaO_3$ (LSGM) perovskites are the fastest ionic conductors (second to B_2O_3 and CeO_2-based oxides at temperature above and below 700°C, respectively). Their conductivity is higher than that of the YSZ in all tested temperature regions.[34-37]

Oxides with higher ionic conductivity than that of YSZ are presented in Fig. 2.28[36] with decreasing conductivity from material number 1 (δ-Bi_2O_3) to 5 $(ZrO_2)_{0.9}(Y_2O_3)_{0.1}$. The conductivity of LSGM material is placed in the middle. The desired σ-T window for SOFC application is located in the top-right quadrant of Fig. 2.28. Although bismuth oxide (no. 1) and ceria (no. 2) have highest conductivity, they are not stable under reducing environment.[38,39] This leaves LSGM perovskite as the most promising candidate to replace the well-established YSZ. In addition to high conductivity, the thermal expansion behavior of LSGM perovskite is similar to that of other SOFC components, namely, the Sr doped $LaMnO_3$ (LSM)[28,29] perovskite — the cathode and, the Ca doped $LaCrO_3$ (LCC)[28] perovskite — the interconnect. They all adopt the same structure — they belong to the perovskite family. The overall properties of LSGM materials are then very attractive and they have been considered the best candidates for SOFC electrolytes.

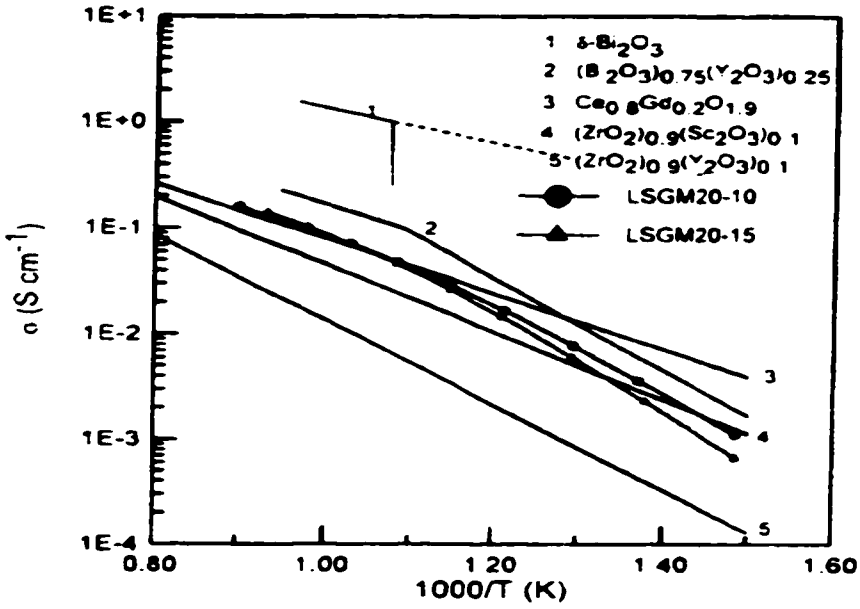

Fig. 2.28 Comparison of Solid Electrolyte Materials[36]

However, to establish their use as an electrolyte, many other properties such as phase, mechanical and chemical stability, optimum processing conditions and microstructure have to be evaluated and well understood. With all these in mind, the literature on pure and doped $LaGaO_3$ is reviewed thoroughly in this section.

2.7.1 Pure $LaGaO_3$

Naray-Szabo[40] investigated $LaGaO_3$ in 1947 and considered its structure to be cubic with cell edge of 3.89 kX (1 kX = 1.00202 Å), however, the composition of the samples were not reported and this cast a shadow of doubt on the quality of this work. It was Geller[41] who reported the early structure study of $LaGaO_3$ in detail. The room temperature structure of $LaGaO_3$ has reported as orthorhombic with a = 5.496, b = 5.524 and c =

7.787 Å, unit cell volume of 236.4 $(Å)^3$, volume per formula unit of 59.1 $(Å)^3$, X-ray density of 7.21 g/cm^3, minimum average interionic distances are: $d(La^{3+}\text{-}Ga^{3+})$ = 3.895, $d(La^{3+}\text{-}O^{2-})$ = 2.754 , and $d(Ga^{3+}\text{-}O^{2-})$ = 1.948 Å. Converting to pseudo-cell gave a = 3.896, b = 3.894 Å and $\beta = 90.3°$. This orthorhombic phase transfers to rhombohedral structure at 875°C and high temperature lattice constants at 900°C are: a = 5.544Å, α = 60°25', with simplest unit cell volume of 121.6 $(Å)^3$, volume per formula unit of 60.8 $(Å)^3$. Pseudo-cell dimensions are: a = 3.933 Å, α = 90°22'. There was a 2.9% thermal expansion in cell volume for temperature rise from 25 to 900°C.

In later papers, Geller and his coworkers[42,43] reported new data for $LaGaO_3$. Instead of 850°C, they suggested a higher orthorhombic to rhombohedral transition temperature of 877°C[42] and 875°C.[43] Lattice constants of rhombohedral phase at 880°C are: a = 5.567, c = 13.531Å, volume per formula unit of 60.53 $(Å)^3$; primitive cell lattice constant of a = 5.538 Å, $\alpha = 80°$. At 1100°C, these increased to a = 5.580, c = 13.589 Å, formula unit volume of 60.07 $(Å)^3$; primitive cell lattice constant of a = 5.558 Å, $\alpha = 76°$.

A tentative phase diagram of Ga_2O_3-La_2O_3 system at high temperatures in air was studied by Mizuno *et al.*[44] in 1985. The phase diagram obtained in this study is presented in Fig. 2.29. Two intermediate compounds were detected. One with mole ratio 1:1 (composition of $LaGaO_3$) is a perovskite-type phase. The other with mole ratio of 1:2 (composition of $La_4Ga_2O_9$) is a monoclinic compound. The lattice parameters were determined as a_o = 5.475, b_o = 5.524, c_o = 7.745 Å for the $LaGaO_3$ and a_o = 7.973, b_o = 10.968, c_o = 11.569

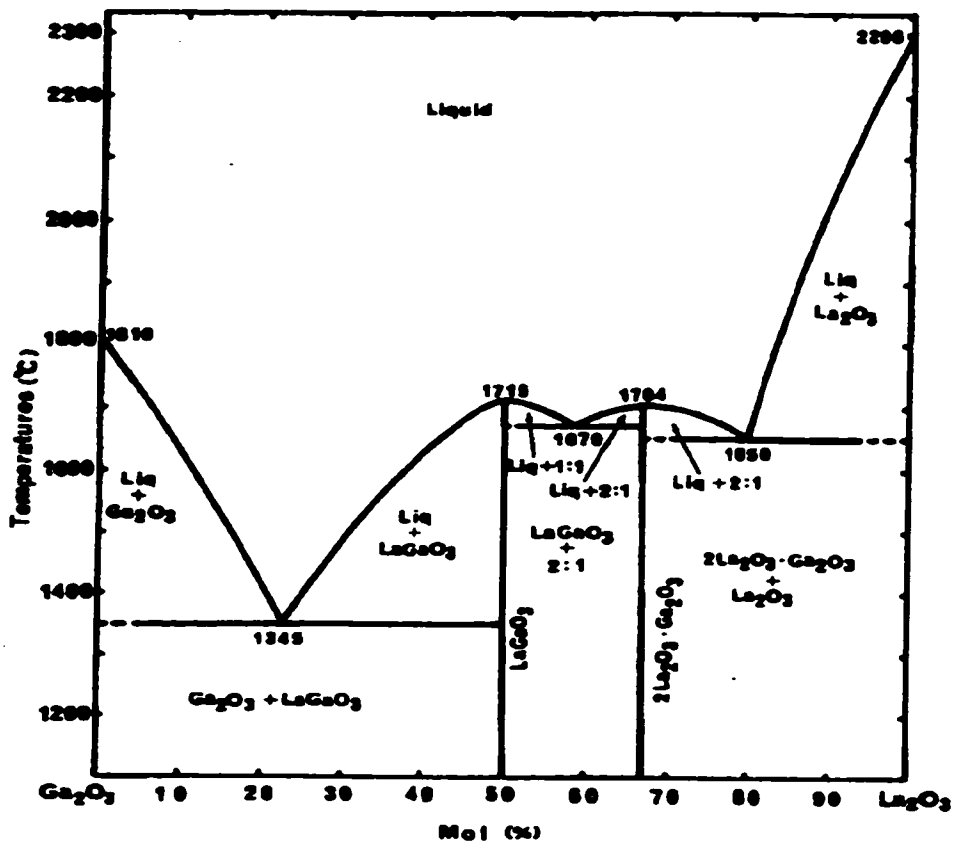

Fig. 2.29 Phase Diagram of the System Ga_2O_3-La_2O_3 at High Temperatures[44]

Å, β = 108.30° for the $La_4Ga_2O_9$. They have also confirmed that the reversible phase transition of $LaGaO_3$ between orthorhombic and rhombohedral structures occurred at about 900°C.[41-43] Both $LaGaO_3$ and $La_4Ga_2O_9$ melt congruently and the solidification point of $LaGaO_3$ was measured as 1715 ± 20°C and that of $La_4Ga_2O_9$ is 1704 ± 20°C. The eutectic points were determined at 23 mol% of La_2O_3 at 1345°C, and at 57 mol% of La_2O_3 at 1670°C.[45] Unfortunately, Mizuno *et al.*'s work has not received due recognition possibly because it was only published in Japanese.

Looking for a better substrate for $YBa_2Cu_3O_{7-x}$ (YBCO), the high-temperature superconducting thin film, Sandstrom and coworkers[46] first proposed $LaGaO_3$ because its lattice parameters and CTE are comparable to those of polycrystalline bulk YBCO. At 400°C, the CTE are α = 10.55 ppm/°C for $LaGaO_3$ and α = 11.60 ppm/°C for YBCO. At 700°C, they are 12.08 ppm/°C and 12.16 ppm/°C, respectively. Using dilatometry on single crystals, they did find the reported orthorhombic to rhombohedral transition in $LaGaO_3$,[41-43] but were not able to detect the transition at 875°C; instead they found an unexpected transition temperature near 150°C. Fig. 2.30 shows the dilatometric measurements on a single crystal of $LaGaO_3$.[46]

Using an optical microscope, Miyazawa[47] observed directly a ferroelastic-like transition at ~140°C in a single crystal of $LaGaO_3$. He pointed out that this transition is likely the source producing catastrophic surface irregularities and causing relatively low critical

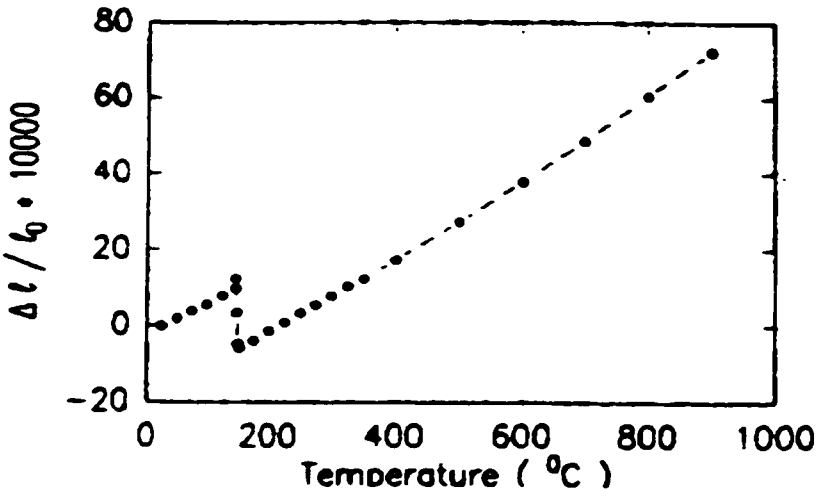

*Fig. 2.30 Thermal Expansion ($\Delta l/l_o$*10000) of Single Crystal $LaGaO_3$[46]*

current density in YBCO thin film grown on $LaGaO_3$ substrate. In addition, Miyazawa has also proposed that the substitution of Sr or Nd on the La site might *shift the 140°C transition* to lower temperature (below room temperature).

Belt and Uhrin[48] confirmed Mizuno's phase diagram study[44] and showed a slightly different lattice constants of a = 5.482, b = 5.526 and c = 7.780 Å. They found the structure of $LaGaO_3$ is orthorhombic at 25°C but rhombohedral at 780°C. Thermal expansion of $\alpha = 9*10^{-6}$ 1/°C and dielectric constant of $\varepsilon = 27$ at 9.3 GHz were also reported. In addition, they have shown that $LaGaO_3$ is insoluble in common mineral acids at 25°C but soluble in H_2SO_4, H_3PO_4, or their mixtures at 150 ~ 200°C.

Giess *et al.*[49] found $LaGaO_3$ single crystals are heavily twinned and shown a sharp (first-order) phase transition at 147°C. Similar thermal behavior, as reported in Ref. 46 (see Fig. 2.30), was observed. The dilation associated with this transition is about 0.3%. The CTE above the transition was determined to be $\alpha = 10.3*10^{-6}$ 1/°C. Nd substitution on a third of all La sites shifted the transition to about 710°C (Note this result is in disagreement to the proposal made by Miyazawa[47]). The transition was no longer sharp (710 ~ 715°C) and exhibited some hysteresis and the CTE dropped to $\alpha = 8.72*10^{-6}$ 1/°C. The hardness and toughness of $LaGaO_3$ was measured to be 9.4 GPa and 0.7 $MPa*m^{1/2}$, respectively.

An enthalpy change, ΔH = 355 J/mol associated with the first order phase transition at

145°C in $LaGaO_3$ was reported by O'Bryan *et al.*[50] Differential scanning calorimetry (DSC) study clearly indicated this phase transition as shown in Fig. 2.31. Dilatometric expansions along the <111> axis and its orthogonal direction are + 0.26% and - 0.37% respectively at the phase transition. Fig. 2.32 shows the observed thermal expansion behavior. High temperature X-ray diffractometry clearly indicated that the structure changes from orthorhombic to rhombohedral in the vicinity of phase transition temperature. The volume change associated with this phase transition is very small ($\Delta V/V$ < 0.01%). A second phase transition was detected at about 1180°C by differential thermal analysis (DTA). Extrapolating the high temperature XRD data, a cubic structure is predicted near 1900°C, though it is above the melting point of $LaGaO_3$ (~ 1715°C[44]).

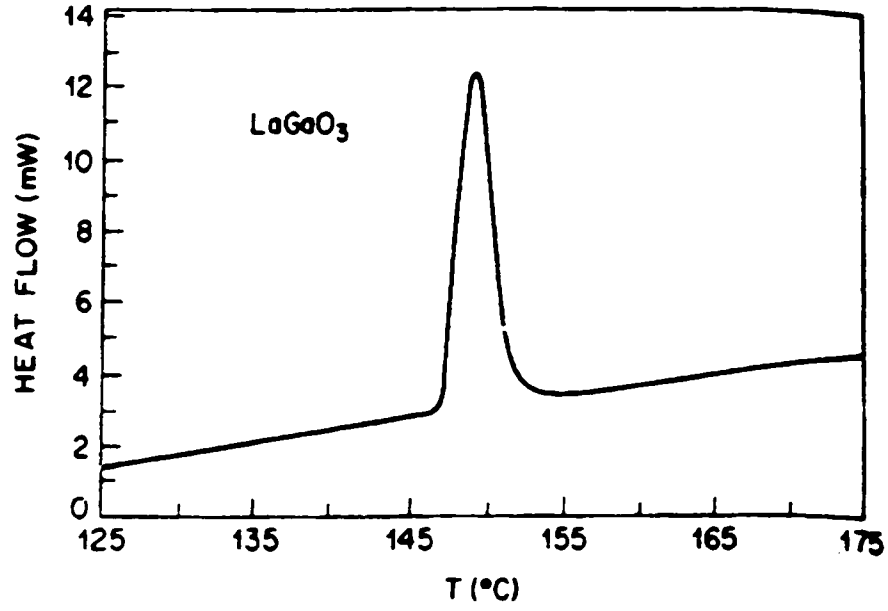

Fig. 2.31 DSC Data for $LaGaO_3$ on a Heating Rate of 10°/min[50]

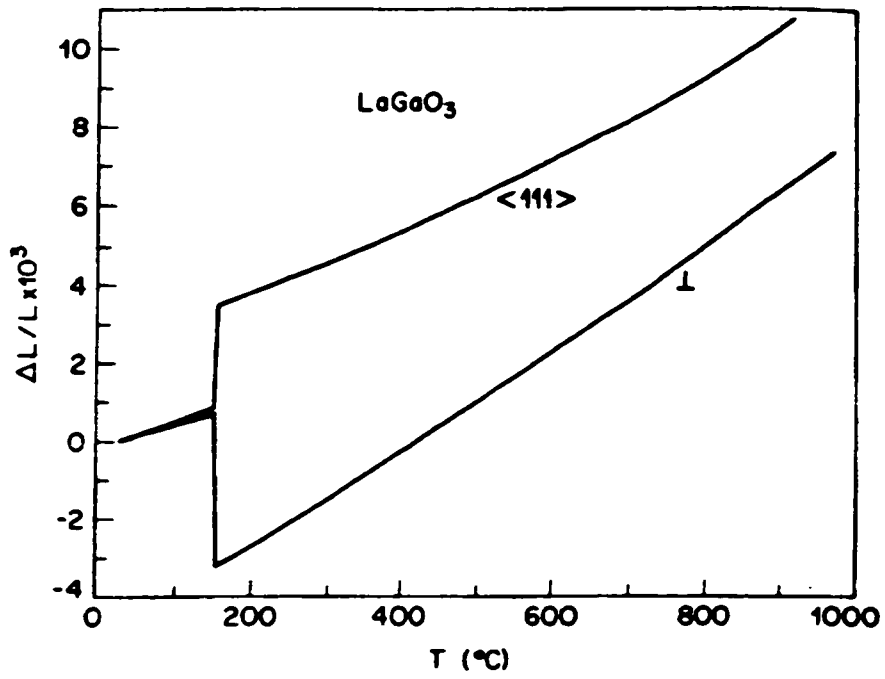

Fig. 2.32 Thermal Expansion of $LaGaO_3$ along <111> and an Orthogonal Direction (Heating-rate Is 4°/min)[50]

Theoretically, the valence bands of perovskite compound ABO_3 should be formed by the 2p electrons of oxygen, 4p electrons of B atom (Ga in $LaGaO_3$) and 6s, 5d, 4f electrons of A atom (La in $LaGaO_3$). G. Jasiolek and H. Dabkowska[51] have indeed found a weak overlap of the 5d electrons of La with the 2p electrons of oxygen experimentally by using X-ray emission spectroscopy (XES). The thermodynamic stability of $LaGaO_3$ was investigated by Azad and co-workors,[52] they found the standard Gibbs' energy of formation of the $LaGaO_3$ perovskite from its constituent sesquioxides is:

$$\Delta G^{\circ}_{f,ox} (\pm 0.34) = - 24.54 + 0.0049\ T/K\ (kJ/mol) \qquad (2.29)$$

over the temperature range of 840 to 1105 K. The standard enthalpy of formation of the $LaGaO_3$ at 298.15 K was estimated to be $\Delta H^{\circ}_{f,298}$ = -1458.8 kJ/mol using a modified electronegativity scale. The elastic constants of single crystal $LaGaO_3$ have been determined as c_{11} = (26.8 ± 5), c_{44} = (10.2 ± 2) and c_{12} = (11.4 ± 4)*10^{10} Nm^{-2}, from ultrasonic frequencies of thick plane-parallel plates in the range between 6 and 40 MHz by Haussuha and Mateika.[53]

A detailed structure analysis associated with the phase transition in $LaGaO_3$ was performed in situ by Wang and Yao *et al.*[54-56] up to 900°C, using transmission electron microscopy (TEM), X-ray powder diffraction (XRPD), and white-beam synchrotron X-ray topography (WBSXRT). A first order phase transition from orthorhombic (Pbnm) to rhombohedral (R-3c) at 145°C was confirmed. Table 2.7 lists the lattice parameter change as a function of temperature. Their structure refinement results are given in table 2.8.

Table 2.7 Unit-cell Parameters of $LaGaO_3$ as Function of Temperature[54]

T (°C)	Orthorhombic (Pbnm)			Hexagonal (R-3c)		Rhombohedral. (R-3c)*		V (Å³) per formula
	a (Å)	b (Å)	c (Å)	a (Å)	c (Å)	a (Å)	α	
25	5.496(1)	5.527(1)	7.781(2)					59.09(6)
100	5.497(2)	5.528(2)	7.781(3)					59.11(7)
150				5.5146(7)	13.3436(16)	5.4699	60°31'	58.57(2)
400				5.5493(9)	13.4534(22)	5.5115	60°28'	59.80(3)
700				5.5676(9)	13.5308(22)	5.5385	60°21'	60.54(3)
900				5.5712(8)	13.5501(22)	5.5450	60°19'	60.70(3)

** The symmetry of the high temperature phase R-3c can be indexed as both hexagonal and rhombohedral perovskite.*

Table 2.8 Structure Refinement Results of $LaGaO_3$*[54]

Atoms	Coordinates	25°C	150°C	900°C
La	x	0.9964(15)	0.0	0.0
	y	0.0163(7)	0.0	0.0
	z	0.25	0.25	0.25
Ga	x	0.0	0.0	0.0
	y	0.5	0.0	0.0
	z	0.0	0.0	0.0
O(1)	x	0.064(10)	0.445(4)	0.448(4)
	y	0.500(5)	0.0	0.0
	z	0.25	0.25	0.25
O(2)	x	0.708(6)		
	y	0.284(10)		
	z	0.033(6)		
Bond length (Å) Ga-O		1.977(7) 1.956(3) 2.020(3)	1.965(3)	1.987(3)
Bond angle (deg) O-Ga-O		88.97(5) 91.37(4) 88.99(4)	88.87(9) 91.13(9) 180.00	89.12(9) 90.88(9) 180.00

** The refined structure parameters have their usual means such that x, y, z shows the atom position in unit cell and bond length is the distance between two particular atoms, bond angle is the geometry of any three atoms. The number in bracket is the sigma of the measurement.*

Kobayashi *et al.*[57] found two phase transitions in $LaGaO_3$, using high temperature X-ray diffractometry (HT-XRD) and differential scanning calorimetry (DSC). A first order phase transition from orthorhombic to rhombohedral occurred at ~150°C. A second-order one from the rhombohedral to monoclinic starts at 750°C and completes by 1000°C. Their discoveries are best presented by a DSC curve shown in Fig. 2.33.

Morozov *et al.*[58] claimed the precise measurement of lattice parameters of single-crystal $LaGaO_3$ with a = 5.48545(3), b = 5.54018(3), and c = 7.74565(3) Å. They reported that there is a single-phase transition from orthorhombic to rhombohedral at about 160°C. In

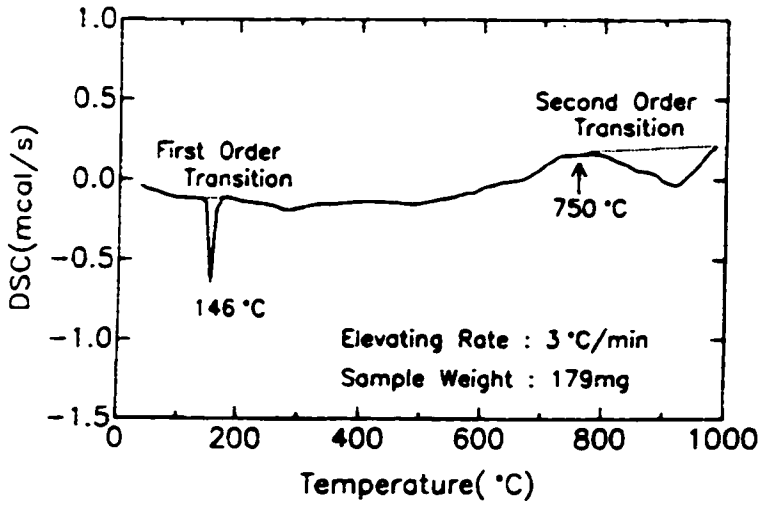

Fig. 2.33 DSC Curve of Single Crystal $LaGaO_3$ (Heating Rate, 3°C/min, in Air)[57]

addition, they argued that a triclinic structure of $LaGaO_3$ can also be indexed.[59] Using X-ray diffraction and X-ray topographic methods they found the triclinic lattice to be a = 5.44517, b = 5.49768, c = 7.70217 Å, α = 88.8045, β = 88.8876, and γ = 90.7448°. The coordinates of atoms in unit cell of $LaGaO_3$ are listed in table 2.9.

Studying the twinning of $LaGaO_3$ single crystals, Bdikin and Shmyt'ko[60] found that at 293 K these crystals adopt an orthorhombic structure with a = 5.520(2), b = 5.490(2), and

Table 2.9 Atom Coordinates in Single Crystal $LaGaO_3$*[59]

Atom	Position	x	y	Z
La	4 (c)	-0.01	0.03	0.25
Ga	4 (b)	0.5	0	0
O(1)	4 (c)	0.01	0.50	0.25
O(2)	8 (d)	-0.26	0.26	0.09

** 4(b), 4(c) and 8(d) are particular atom positions in crystal*

c = 7.770(1) Å. A first order phase transition from orthorhombic to rhombohedral was observed at 412.5 K. The lattice constants at 423 K are: a = 3.889 Å, α = 89.50°.

Using neutron powder diffraction, Marti *et al.*[61] studied the crystal structures and phase transitions of $LaGaO_3$ in the temperature range of 10 ~ 1673 K. They confirmed the orthorhombic (Pbnm) to rhombohedral (R3c) phase transition occurs at about 423 K. However, it is still questionable whether the high temperature phase is of centrosymmetry (R-3c) or non centrosymmetry (R3c). Their preference went to centrosymmetry.[62,63] The refined lattice constants and atom coordinates of $LaGaO_3$ perovskite are listed in table 2.10.

In-situ TEM study conducted by Dube *et al.*[64] shows there is a domain rearrangement at approximately 145°C in $LaGaO_3$, where a orthorhombic *(Pbnm = Pnma)* to rhombohedral (R3c) phase change takes place. Changes of heat flow and dielectric properties are associated with this phase transition. Fig. 2.34 shows the dielectric constant of a (001) single crystal $LaGaO_3$ as function of temperature in low frequency regions. A big jump in dielectric content is clearly observed from 140 to 150°C. DSC results are presented in Fig. 2.35, showing a distinct peak around 146°C.

High-temperature X-ray measurements of gallates have been reported by Utke *et al.*[65] $LaGaO_3$ is orthorhombic at room temperature and rhombohedral above 151°C where a jump in pseudo-cubic lattice parameter was observed.

Table 2.10 High Temperature Data of $LaGaO_3$[61]

Temperature		12 K	298 K	413 K	573 K	1353 K	1673 K
Space group		Pbnm	Pbnm	Pbnm	R3c	R3c	R3c
Constants							
a (Å)		5.5028(6)	5.5269(3)	5.5295(7)	5.5388(3)	5.5835(4)	5.6118(45)
b (Å)		5.4736(5)	5.4943(3)	5.4949(6)			
c (Å)		7.7507(10)	7.7774(4)	7.7850(11)	13.4090(9)	13.6016(4)	13.7472(45)
V ($Å^3$)		233.45(8)	236.17(4)	236.54(9)	356.25(7)	367.23(6)	374.93(31)
La	x	-0.0021(11)	-0.0030(7)	-0.0020(13)	0	0	0
	y	-0.0216(6)	-0.0179(5)	-0.0151(8)	0	0	0
	z	0.25	0.25	0.25	0.2507(12)	0.2507(14)	0.2422(15)
Ga	x	0.5	0.5	0.5	0	0	0
	y	0	0	0	0	0	0
	z	0	0	0	0	0	0
O(1)	x	0.0709(10)	0.0665(7)	0.0672(15)	0.1158(9)	0.1245(12)	0.2412(28)
	y	0.5056(12)	0.5033(9)	0.5007(17)	0.3426(16)	0.3439(21)	0.3905(33)
	z	0.25	0.25	0.25	0.0775(11)	0.0725(13)	0.0296(18)
O(2)	x	-0.2276(8)	-0.2305(6)	-0.2327(10)			
	y	0.2273(8)	0.2289(6)	0.2322(11)			
	z	0.0347(4)	0.0354(3)	0.0355(6)			
Bond angles							
Ga-O(1)-Ga		157.2(3)	158.6(2)	158.4(5)	161.4(5)	162.4(7)	135.6(11)
Ga-O(2)-Ga		161.2(2)	161.5(2)	162.0(3)			

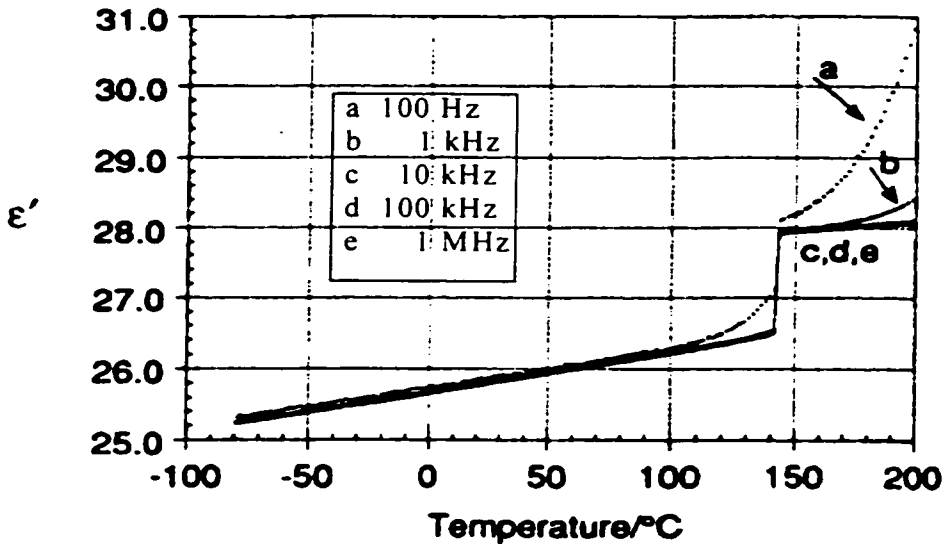

Fig. 2.34 Temperature Dependence of Permittivity in the Low Frequency Region for (001) $LaGaO_3$ Single Crystal[64]

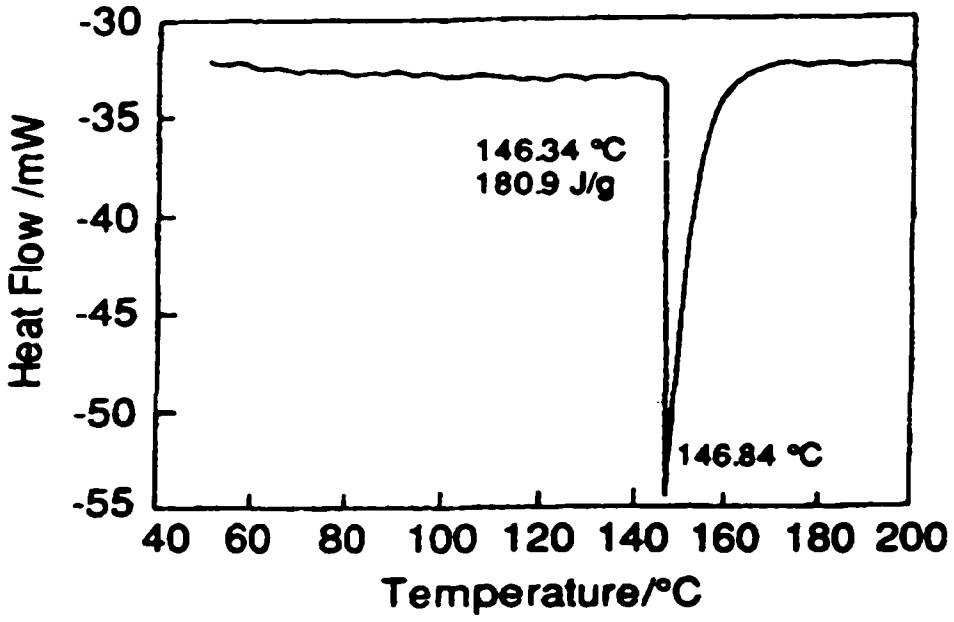

Fig. 2.35 DSC Analysis Indicates the Phase Transition Occurs at 146°C in $LaGaO_3$[64]

It can be concluded from this review that the structure and phase stability of pure $LaGaO_3$ is reasonably well established and understood. There is however some disagreement on the symmetry[61] and transition temperatures.[41-65] Fortunately, pure $LaGaO_3$ is an insulator and can not be a choice of SOFC electrolyte at all. The focus of our interest is then lies in the structure and properties of doped $LaGaO_3$.

2.7.2 Doped $LaGaO_3$

The studies by Ishihara and co-workers[34,66-69] can be regarded as the true beginning of doped $LaGaO_3$ as a possible fast ion conductor. They found that doping with alkaline earth cations effectively enhances electrical conductivity of $LaGaO_3$ perovskite. Among those alkaline earth elements, doping Sr on the La-site has the biggest impact. The

electrical conductivity increases with increased Sr-content and a maximum is reached at Sr = 0.1 mole. Several secondary phases (including $SrGaO_3$, La_4SrO_7[34] and at least two unknowns[66]) are detected by XRD when Sr > 0.1 mole. Further increase in conductivity can be achieved by Ga-site doping. Mg is the most effective element. The electrical conductivity is increased with Mg-content and a maximum occurs at Mg = 0.2 mole. The ion conductivity of $La_{0.9}Sr_{0.1}Ga_{0.8}Mg_{0.2}O_3$ (O should be 2.85) is higher than that of YSZ and is stable from $p(O_2) = 10^{-21}$ to 1 atm. In their test SOFC, the $La_{0.9}Sr_{0.1}Ga_{0.8}Mg_{0.2}O_3$ perovskite is the best electrolyte among doped $LaGaO_3$ family, where Ni and $La_{0.9}Sr_{0.1}CoO_3$ (O should be 2.95) are the desired anode and cathode materials respectively. The details are presented in table 2.11.[68]

Goodenough *et al.*[35,70-74] have also investigated Sr and Mg doped $LaGaO_3$ perovskite as oxygen ion conducting electrolyte. They found the structure of $La_{0.9}Sr_{0.1}Ga_{0.8}Mg_{0.2}O_{2.85}$ (LSGM) to be cubic with a = 3.911(3) Å at room temperature. At 600°C, a pure oxygen

Table 2.11 Effects of Electrode Materials on the Performance of LSGM SOFC[68]

Anode	Cathode	O.C.V. (V)	M.P.D. (W/cm^2)
Pt	Pt	1.098	0.09
Ni	Pt	1.099	0.15
Ni	LSM	1.098	0.31
Ni	LSC	1.099	0.71
Ru	LSC	1.051	0.01
Co	LSC	1.100	0.53

O.C.V.: open circuit voltage
M.P.D.: maximum power density
LSM: $(La_{0.6}Sr_{0.4})_{0.9}MnO_3$
LSC: $La_{0.6}Sr_{0.4}CoO_3$
LSGM: $La_{0.9}Sr_{0.1}Ga_{0.8}Mg_{0.2}O_{2.85}$ (0.5 mm thickness)

ion conductivity of $\sigma > 10^{-2}$ S/cm over wide oxygen partial pressure range ($10^{-20} < p(O_2) < 0.2$ atm) was determined. It was also reported that this perovskite does not absorb water. Its CTE ($\alpha \sim 10*10^{-6}\ K^{-1}$) is about the same as that of 9% YSZ ($\alpha = 10.5*10^{-6}\ K^{1}$). The activation energy for oxygen vacancies migration in the perovskite (E_a = 1.07 eV) was slightly higher than that in YSZ (E_a = 0.98 eV). The higher ion conductivity of the LSGM was attributed to a much bigger pre-exponential term (A = 24.84 Ks/cm) in $\sigma = (A/T)\exp(-E_a/kT)$. Table 2.12 lists the comparison of bulk properties of LSGM with those of YSZ. In addition, they always observed one secondary phase of composition $LaSrGaO_4$ at grain boundaries. They also found other trace compounds like SrO and MgO in LSGM. Furthermore, they investigated the interfacial diffusion between LSGM with several SOFC components. The diffusion in LSGM/LSM, fired at 1470°C for 36 hours, was less than that in LSGM/LSC, fired at 1050°C for only 2 hours. Where LSM = ($La_{0.84}Sr_{0.16}MnO_3$) and LSC = ($La_{0.5}Sr_{0.5}CoO_{3-\delta}$) respectively. In table 2.13, the properties of LSGM (electrolyte) are compared to those of two possible electrode materials.[71]

Table 2.12 Comparison between YSZ and LSGM[35]

Bulk property	9% YSZ	LSGM
c*(1-c)	0.043	0.0475
Ea (eV)	0.98	1.07
A (10^6 Ks/cm)	1.1	24.84
σ (10^{-2} S/cm) @ 571°C	0.279	1.09
σ (10^{-2} S/cm) @ 800°C	3.6	10.4
$P(O_2)$ (atm) for t ~ 1	$1\text{-}10^{-18}$	$0.4\text{-}10^{-20}$
α ($10^{-6}\ K^{-1}$)	10.5	10.0

** c is the normal vacancy concentration*
$p(O_2)$ range is at 1000°C for YSZ and 950°C for LSGM

Table 2.13 Comparisons of the Material Properties among LSGM, LSM and LSC[71]

Properties	LSGM	LSM	LSC
Composition	$La_{0.9}Sr_{0.1}Ga_{0.8}Mg_{0.2}O_{2.85}$	LSM-16	LSC-50
σ (S/cm)	~ 0.10 @ 800°C	~ 150 @ 1000°C	~ 1000 @ 1000°C
α ($*10^{-6}$/K)	12.47 (613 to 850°C)	12.0 (25 to 1000°C)	20.0 (25 to 1000°C)
Chemical stability	$10^{-22} < p(O_2) < 1$ atm @ 800°C	if $p(O_2) < 10^{-14}$ atm Decomposes @ 1000°C Sr doping ↓ stability	if $p(O_2) < 10^{-7}$ atm Decomposes @1000°C Sr doping ↓ stability

Comparing these data we can conclude that LSGM perovskite is more stable than LSM and LSC under reducing condition.

Most of the studies reported thus far utilize solid state reaction to prepare LSGM materials. Realizing that this method is time-consuming and does not always lead to complete reactions, Goodenough *et al.*[72] developed a new sol-gel synthesis route (using salt acetate solution) to make LSGM material. From this preparation technique, the final LSGM perovskite structure was reported as cubic and free of secondary phases. AC conductivity data measured from this 'pure cubic' perovskite was fitted to be $\sigma T = 7.42*10^{6}\exp[-0.99(eV)/kT]$ with $\sigma = 0.11$ S/cm at 800°C. The flow chat for the sol-gel procedure is given in Fig. 2.36.

Several fuel cells with LSGM electrolyte have been tested in the temperature regions of 600~800°C.[73] The cathode material is doped lanthanum cobaltite ($La_{0.6}Sr_{0.4}CoO_{3-\delta}$) and, a

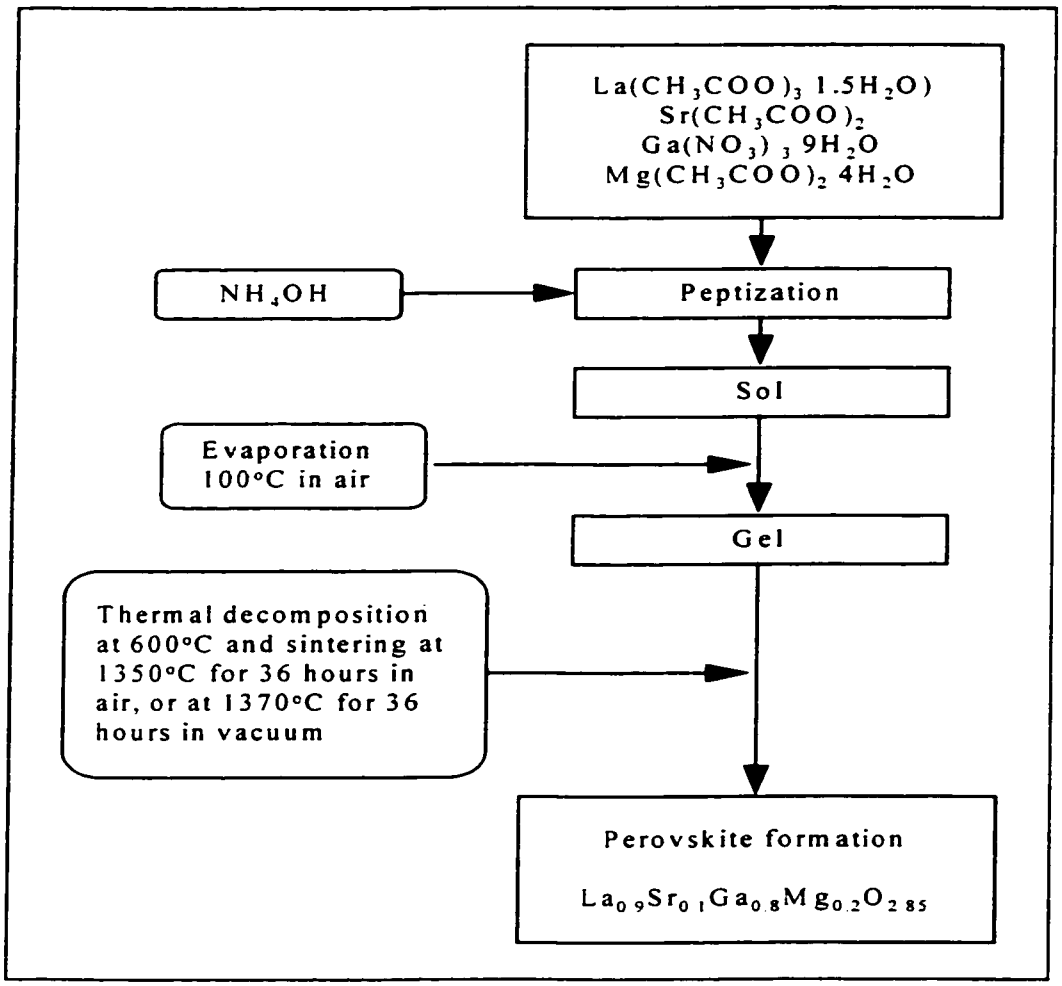

Fig. 2.36 Flow Chart for the Sol-gel Synthesis of LSGM[72]

mixture of NiO with either doped ceria or LSGM used as anode. The cell performance was limited by large overpotentials that occur at the anode (and the cathode). Better anode materials and processing methods are needed for LSGM SOFC.

Only doping Sr at La-site in $LaGaO_3$ limits the single perovskite phase region to less than 0.1 mole Sr. Huang and Petric[36,75] found that with the substitution of Sr for La, additional doping of Mg in the Ga-site increases the oxygen vacancies, and also the

solubility of Sr in $LaGaO_3$. When doping at both La- and Ga-cation sites, Sr solubility in LSGM can be increased to 0.25 mole. The solubility of Mg in LSGM depends on the Sr content. Fig. 2.37 shows the solubility ranges of Sr and Mg in LSGM. The solid-line in Fig. 2.37 represents maximum solubility of Sr and Mg in single LSGM perovskite phase while the dotted-line shows the region where the measured oxygen ion conductivity is identical and equals to the value (in unit of S/cm) shown in the figure. They also observed the structure change in LSGM. They found that the substitution of Sr for La only changes the cell constants; while doping Sr at La-site and Mg at Ga-site, both the lattice parameter and structure change systematically until cubic symmetry is achieved.

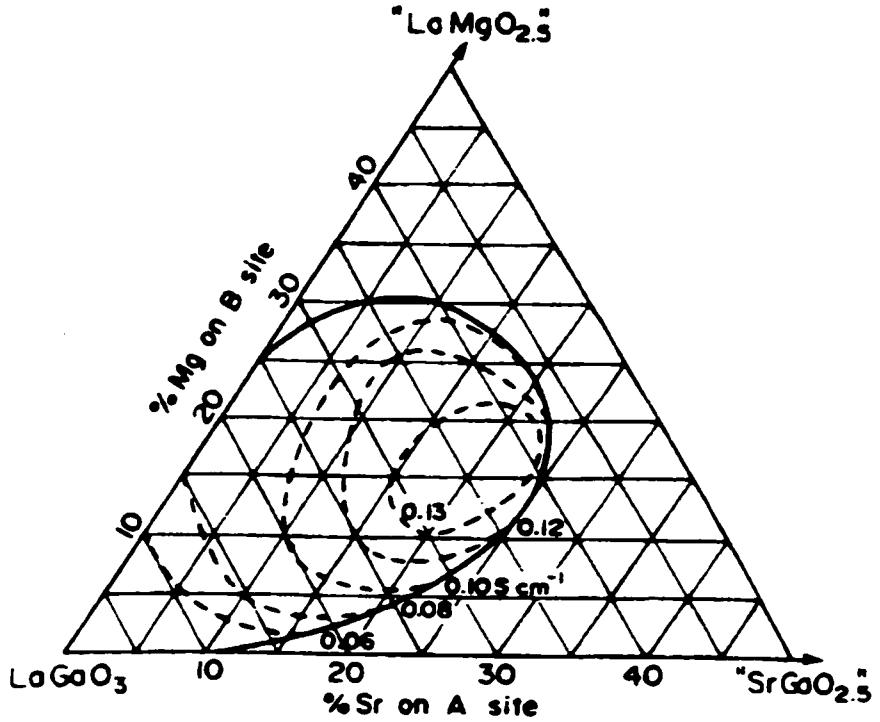

Fig. 2.37 The Solubility Regions and Isoconductivity Lines of LSGM[36]

In order to compare the stability of LSGM with that of YSZ, Wang and Hellstrom[76] investigated the chemical compatibility of the electrolyte materials LSGM and YSZ with several cathode materials including $(La_{0.6}Sr_{0.4})MnO_3$ (LSM), $(La_{0.6}Sr_{0.4})CoO_3$ (LSC), $(La_{1.7}Sr_{0.3})CuO_4$ (LSU) and $(La_{0.6}Sr_{0.4})(Co_{0.2}Fe_{0.8})O_3$ (LSCF). They found that the solid solution is formed at interfaces of LSGM and LSM, LSC and LSCF with no indication of new phase up to 1200°C. The only exception was with LSU where several new phases ($LaCuO_3$, for example) are formed. On the contrary, interfacial compounds ($La_2Zr_2O_7$ or $SrZrO_3$) were formed at all electrodes but LSM with YSZ electrolyte. The activation energy of the interfacial conduction are calculated (see Table 2.14). It can be concluded that the stability of LSGM with candidate electrodes is comparable to that for YSZ.

Using XRD, analytical transmission electron microscopy (ATEM), convergent-beam electron diffraction (CBED), differential thermal analysis (DTA) and high-temperature XRD, Drennan *et al.*[77] characterized one LSGM perovskite made by solid-state reaction. At room temperature, $La_{0.9}Sr_{0.1}Ga_{0.8}Mg_{0.2}O_{3-x}$ (LSGM-1020) is orthorhombic (Pnma 62) with a = 5.5391(7), b = 7.8236(12), c = 5.5224(7) Å. Its flexural strength is 162 ± 14

Table 2.14 Activation Energies for the Interfacial Reaction[76]

Activation Energy (kJ/mol)		
	Electrolytes	
Cathodes	With LSGM	withYSZ
LSM	125	137
LSC	120	102
LSCF	180 (T < 720°C); 130 (T > 720°C)	110
LSU	76	190

MPa (compared to the modulus of rupture of 158 MPa and the fracture toughness of 1.63 $MPam^{1/2}$ for $La_{0.8}Sr_{0.2}Ga_{1-x}Mg_xO_{3-\delta}$ where x = 0.02 to 0.2, reported by Sammes *et al.*[78]). It becomes rhombohedral (R3c) at 445 K and its strength is 55 ± 11 MPa at 1173 K. Atomic coordinate refinements are given in table 2.15. The 4-probe dc conductivity data were measured as σ = 0.121 S/cm at 1073 K and σ = 0.316 S/cm at 1273 K. The activation energy for conduction, E_a = 109 ± 3 kJ/mol at 673 ~ 723 K, and E_a = 64±2 kJ/mol at 1123 ~ 1273 K have also been calculated and reported.

Phase development of glycine-nitrate combustion synthesized $La_{0.9}Sr_{0.1}Ga_{0.8}Mg_{0.2}O_{3-\delta}$ (LSGM-1020) and $La_{0.8}Sr_{0.2}Ga_{0.8}Mg_{0.2}O_{3-\delta}$ (LSGM-2020) were reported by Stevenson *et al.*[37,79] The powder synthesized under fuel-rich condition was amorphous with a surface area of about 20 m^2/g. To get the perovskite phase, further heat treatment is required and the amount of perovskite phase increases with temperature at fixed time. The powder surface area decreases with increased temperature and the amount of perovskite phase. Two tetragonal compounds, $LaSrGaO_4$ and $LaSrGa_3O_7$, and trace amount of MgO may appear as secondary phases in LSGM, depending on the composition and heat treatment.

Table 2.15 Refined Fractional Atomic Coordinates with Estimated Standard Deviations[77]

Atom	10^3 x/a	10^3 y/b	10^3 z/c
La	9998(14)	2500	-18(36)
Sr	9998(14)	2500	-18(36)
Ga	0	0	5000
Mg	0	0	5000
O1	4380(119)	2500	584(129)
O2	2409(127)	504(32)	7522(174)

Contrary to the proposal made by Miyazawa,[47] that the substitution of Sr or Nd to La may shift the 140°C transition in $LaGaO_3$ to a lower temperature (below room temperature), *Giess et al.*[49] found that Nd substitution on a third of all La sites shifted the transition to about 710°C. The transition was no longer sharp (710 ~ 715°C) and exhibited some hysteresis, and the CTE dropped to $8.72*10^{-6}$ $°C^{-1}$.

Berthold and Jobst[80,81] found the transition temperature of rare earth doped $LaGaO_3$ increases linearly with doping concentration. With no doping, the phase transition occurs at 150°C. Doping with 35 mol% Nd, shifts the phase transition temperature as high as 855°C. Doping with 10 mol% Gd, the phase transition temperature shifts to 750°C. Peaks split are well resolved between $2\theta = 65$ to 70° due to the phase transition. The lattice constants decrease with doping concentration and a garnet phase of composition $Ga_5R_3O_{12}$ (R = Nd and Gd) starts to form with increased doping (Nd > 0.36, Gd > 0.1 mole). Fig. 2.38 shows the influence of rare earth doping on the transition temperature.

The latest report on the structure characterization of LSGM come from the studies of Irvine and co-workers.[82-84] Using powder neutron diffraction, Irvine *et al.* studied the structure of oxide ion conductor $La_{0.9}Sr_{0.1}Ga_{0.8}Mg_{0.2}O_{0.285}$ over a wide temperature range (25-1000°C). Rather than orthorhombic, the room temperature structure of their LSGM material is indexed as monoclinic (I2/a). There are two phase transitions between 250 and 1000°C: monoclinic (pseudo-orthorhombic) → monoclinic (pseudo-rhombohedral) → rhombohedral (R3c). The effects of impurities such as La_4SrO_7 are excluded from the

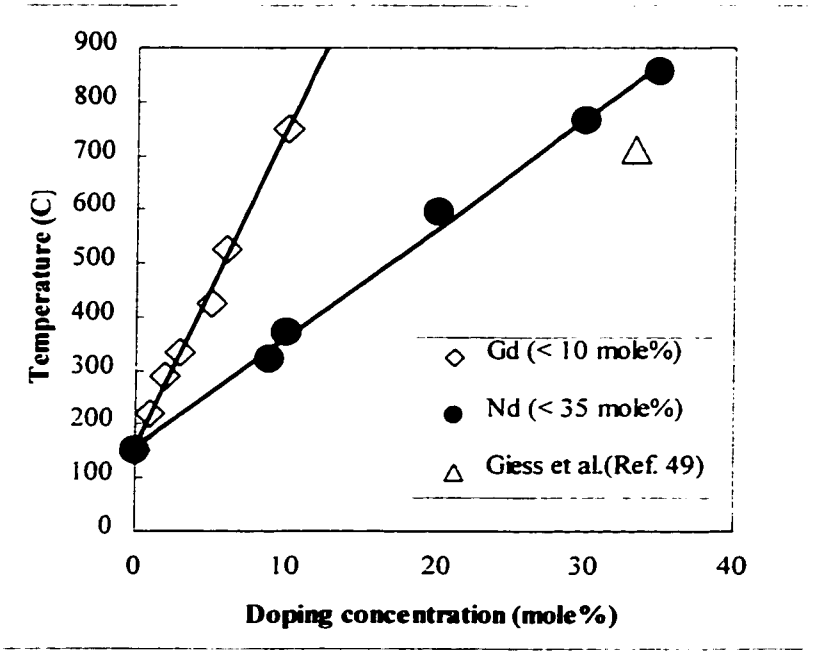

Fig. 2.38 Influence of Doping on Phase Transition Temperature of $LaGaO_3$[49,80,81]

structure refinements. The refined structural parameters of undoped and doped $LaGaO_3$ are presented in table 2.16 and 2.17, respectively.

2.7.3 Summary

Most of the interest in Sr and Mg doped $LaGaO_3$ perovskites is due to their high oxygen-ion conductivity (higher than that of YSZ at all test temperatures). There is limited work that has been devoted to crystal structure, mechanical properties and phase development of doped systems. However, only two or three compositions have been explored in detail, which is not sufficient to evaluate these materials as new electrolytes for SOFC. There is no explanation why these perovskites should exhibit significantly higher electrical conduction. Furthermore, different studies on phase transition and crystal structure have

Table 2. 16 Refined Structural Parameters of $LaGaO_3$[84]

Atom	Parameter	25 °C	250 °C	500 °C	750 °C	1000 °C
La	x	-0.0047(2)	0	0	0	0
	y	-0.0168(2)	0	0	0	0
	z	0.25	0.2508(3)	0.2512(3)	0.2513(3)	0.2517(2)
	Site	1.0	1.0	1.0	1.0	1.0
Ga	x	0.5	0	0	0	0
	y	0	0	0	0	0
	z	0	0	0	0	0
	Site occup.	1.0	1.0	1.0	1.0	1.0
O1	X	0.2705(2)	0.1137(2)	0.1163(3)	0.1192(3)	0.1224(3)
	Y	0.2714(2)	0.3420(4)	0.3439(4)	0.3457(4)	0.3473(4)
	Z	0.5365(1)	0.0772(2)	0.0768(3)	0.0756(3)	0.0747(2)
	Site occup.	1.0	1.0	1.0	1.0	1.0
O2	X	0.0681(2)				
	Y	0.5078(3)				
	Z	0.25				
	Site occup.	1.0				
	a (Å)	5.52432(2)	5.5358(7)	5.5472(8)	5.560(1)	5.5745(8)
	b (Å)	5.49246(2)	5.5358(7)	5.5472(8)	5.560(1)	5.5745(8)
	c (Å)	7.77448(4)	13.39797(6)	13.45131(6)	13.50672(6)	13.56587(7)
	Space gp.	Pbnm	R3c	R3c	R3c	R3c

not yielded consistent results. The present work is intended to fill some of these gaps by systematical studying phase stability and phase transition of LSGM materials as function of both composition (in term of doping concentration and A/B cation ratio variation) and temperature. It is hoped that the processing parameters for producing LSGM electrolyte will be optimized by evaluating the relationships between processing and properties of selected compositions. A self-consistent model for oxygen-ion conduction will then be proposed based on the structure-property relation observed in these materials.

Table 2. 17 Refined Structural Parameters of $La_{0.9}Sr_{0.1}Ga_{0.8}Mg_{0.2}O_{2.85}$[84]

Atom	Parameter	25 °C	250 °C	500 °C	750 °C	1000 °C
La/Sr	x	0.25	0.25	0.25	0	0
	y	-0.0003(6)	0.0028(4)	0.000(1)	0	0
	z	0	0	0	0.2544(6)	0.248(2)
	Site occup.	0.9/0.1	0.9/0.1	0.9/0.1	0.9/0.1	0.9/0.1
Ga/Sr	X	0	0	0	0	0
	Y	0.5	0.5	0.5	0	0
	Z	0	0	0	0	0
	Site occup.	0.80(1)/ 0.20(1)	0.78(1)/ 0.22(1)	0.79(1)/ 0.21(1)	0.79(1)/ 0.21(1)	0.77(1)/ 0.23(1)
O1	X	0.4713(3)	0.4736(3)	0.4780(8)	0.1354(9)	0.147(1)
	Y	0.7605(5)	0.7619(5)	0.7318(8)	0.346(1)	0.347(2)
	Z	0.2465(9)	0.246(1)	0.256(1)	0.084(1)	0.080(2)
	Site occup.	1.02(2)	1.00(2)	0.95	0.94(2)	0.96(2)
O2	X	0.25	0.25	0.25		
	Y	0.4378(5)	0.440(1)	0.443(1)		
	Z	0	0	0		
	Site occup.	0.87(2)	0.84(2)	0.95		
	a (Å)	7.81603(4)	7.83332(5)	7.85603(5)	5.57402(3)	5.59033(3)
	b (Å)	5.53930(2)	5.54993(3)	5.55965(3)	5.57402(3)	5.59033(3)
	c (Å)	5.51467(2)	5.52917(3)	5.54542(3)	13.61871(7)	13.67757(8)
	Space gp.	I2/a	I2/a	I2/a	R3c	R3c

CHAPTER 3

SCOPE OF THIS STUDY

The goal of this study is to systematically investigate Sr and Mg doped $LaGaO_3$ (LSGM) perovskites in terms of phase transition and phase stability as function of doping content, A/B cation ratio and temperature. An additional goal is to obtain optimum processing conditions and material properties for selected compositions. These perovskites are promising candidates as solid oxide fuel cell (SOFC) electrolyte to replace the conventional yttria-stabilized zirconia (YSZ). Limited studies have been conducted on these materials and most of them were focused on a few compositions which is not sufficient to understand their usage as oxygen-ion conductor in SOFC. In addition, it is essential to optimize processing conditions for these materials to further explore their potential as electrolyte materials.

This study consists of two parts:

(1) Investigate phase transition, phase stability, phase relation, microstructure and electrical conduction (oxygen ionic conductivity) in the La-Sr-Ga-Mg-O system as function of composition and temperature, and

(2) Optimization of processing parameters for making single phase LSGM perovskite.

All materials used in this study were prepared by the author, using the Glycine-nitrate combustion process (GNP) at Pacific Northwest National Laboratories (PNNL). The structure, phase transition and phase stability of ABO_3-type perovskite in LSGM system were investigated as function of Sr- and Mg-content, A/B cation ratio, and temperature. A quaternary phase diagram of La_2O_3-SrO-Ga_2O_3-MgO system was proposed based on the data from literature and the results from this study. Structure refinements of LSGM perovskite of selected compositions were performed by Rietveld method using General Structure Analysis System (GSAS). The effects of sintering temperature and doping content on microstructure were investigated by observing thermally etched sample surfaces with scanning electron microscopy (SEM). Electrical conductivity was measured by four-point probe (DC) method. An optimized processing method, based on the correlation found among various material properties and the microstructures, was established for producing the LSGM electrolyte for SOFC.

CHAPTER 4

EXPERIMENTAL PROCEDURE

Although it is well established that doping with alkaline-earth elements can turn electrical insulator $LaGaO_3$ into a fast ionic conductor, the knowledge of crystal structure and phase boundary of doped $LaGaO_3$ perovskites is far from complete. Investigation of Sr and Mg doped $LaGaO_3$ (LSGM) perovskites in the quaternary La_2O_3-SrO-Ga_2O_3-MgO system would permit the discovery of a suitable compositional window for new SOFC electrolyte-materials. With this goal, five 'standard' samples with various target compositions were chosen to map out the single perovskite phase region in the binary La_2O_3-Ga_2O_3 system, with respect to the change in A/B cation ratio (from La/Ga = 0.95 to 1.05). Starting from these standards, samples with several doping levels, on both La-site and Ga-site, were examined to explore the single LSGM phase region. The results were used to develop a tentative phase stability diagram for the quaternary system.

All samples were prepared by glycine-nitrate process (GNP), a combustion synthesis method, followed by calcination and sintering. Various amounts of glycine and appropriate heat treatments were examined to optimize processing parameters. Characterization of crystal structure at each stage of thermal treatment was performed by X-ray diffraction (for all samples) and neutron diffraction (for selected compositions). Electrical conductivity was measured by a 4-point dc method for selected samples.

Thermal analyses (TGA, DTA, DSC, and Dilatometry) were used to obtain additional information on energy evolution and phase change. The experimental methodology and instrumental details are presented in following sections.

4.1 POWDER SYNTHESIS AND SAMPLE PREPARATION

4.1.1 Glycine Nitrate Process (GNP)

The Glycine Nitrate Process (GNP),[85-87] best known for producing fine multicomponent ceramic powders, was employed for powder synthesis in this study. Metal nitrates, $La(NO_3)_3$, $Sr(NO_3)_2$, $Ga(NO_3)_3$ and $Mg(NO_3)_2$, were dissolved in deionized water and filtered to obtain precursor solution free of contaminants. The solutions were stored in high-density polyethylene containers to prevent reactions with air (absorbing moisture or evaporation). The gravimetric method[88] was used to characterize the concentration of metal cations in the solution, with the results presented in table 4.1.

The desired compositions of the ceramics (LSGM perovskites) were calculated and prepared based on the cation concentrations of metal nitrates (c.f. Table 4.1). Glycine

Table 4.1 Cation Concentration in Metal Nitrates

Metal Nitrate	Metal Concentration (*10^{-3} moles/gram solution)
$La(NO_3)_3$	0.83
$Sr(NO_3)_2$	1.55
$Ga(NO_3)_3$	0.839
$Mg(NO_3)_2$	1.396

($H_2NCH_2CO_2H$), an amino acid fuel, was added into metal nitrates. Glycine aids in avoiding selective precipitation during water evaporation by forming metal complexes.

The mixed precursor solution of nitrates and glycine was heated using a hot plate in a stainless steel beaker to a viscous liquid. Auto-ignition of the precursor solution occurred at about 180°C. Consequently, explosive combustion resulted and an amorphous oxide ash was produced. This combustion reaction was accompanied by self-sustained flame temperatures in the range of 1100° to 1450°C. The ashes produced by the combustion were ultra-fine with uniform particle size distribution and were compositionally homogeneous.[85-87]

Preliminary studies indicated that a glycine to excess oxygen ratio of 2 (adding 2 moles of glycine per mole of excess oxygen in the precursor solution of metal nitrates) achieved better synthesis efficiency (Glycine to excess oxygen ratio of 0.5, 1 and 2 were examined). Consequently, a glycine to excess oxygen ratio of 2 was used for most of the samples produced in this study.

4.1.2 Calcination

The main purpose of calcination was to burn out organic residues in the ashes and convert the amorphous ashes into crystalline powders. The ashes collected after GNP combustion synthesis were placed in an alumina boat and fired in air in an electric furnace. For the

LSGM materials, the calcination parameters used were 650°C for 0.5, 1 or 2 hours; 800°C, 1000°C, 1200°C, for 1 or 2 hours; 1250°C for 1 hour; and 1400°C, 1500°C for 1 or 2 hours.

For most compositions, there were several crystalline phases after early stages of calcination. However, the number of phases decreased to only one or two as the calcination time and temperature increased. The influence of calcination on phase development will be presented in Chapter 5.

4.1.3 Sintering

As-synthesized or calcined powders were uniaxially compacted (55 MPa) in a steel die prior to cold isostatically pressing at 138 MPa into cylindrical compacts. The pressed compacts were sintered in air in a $MoSi_2$ furnace under the following conditions: 1200°C, 1300°C, 1400°C, and 1500°C for 2 hours, and 1500°C for 9 hours (for phase equilibrium study). The heating and cooling rate used were 2 and/or 5°C per minute.

The methodology of sample preparation and characterization is given in Fig. 4.1. The compositional matrix of the Sr and Mg doped $LaGaO_3$ perovskites prepared by GPN method is listed in table 4.2. The bulk density of various compositions of interest was measured by the Archimedes method (using ethylene). The characterization methods are labeled with letters as the following:

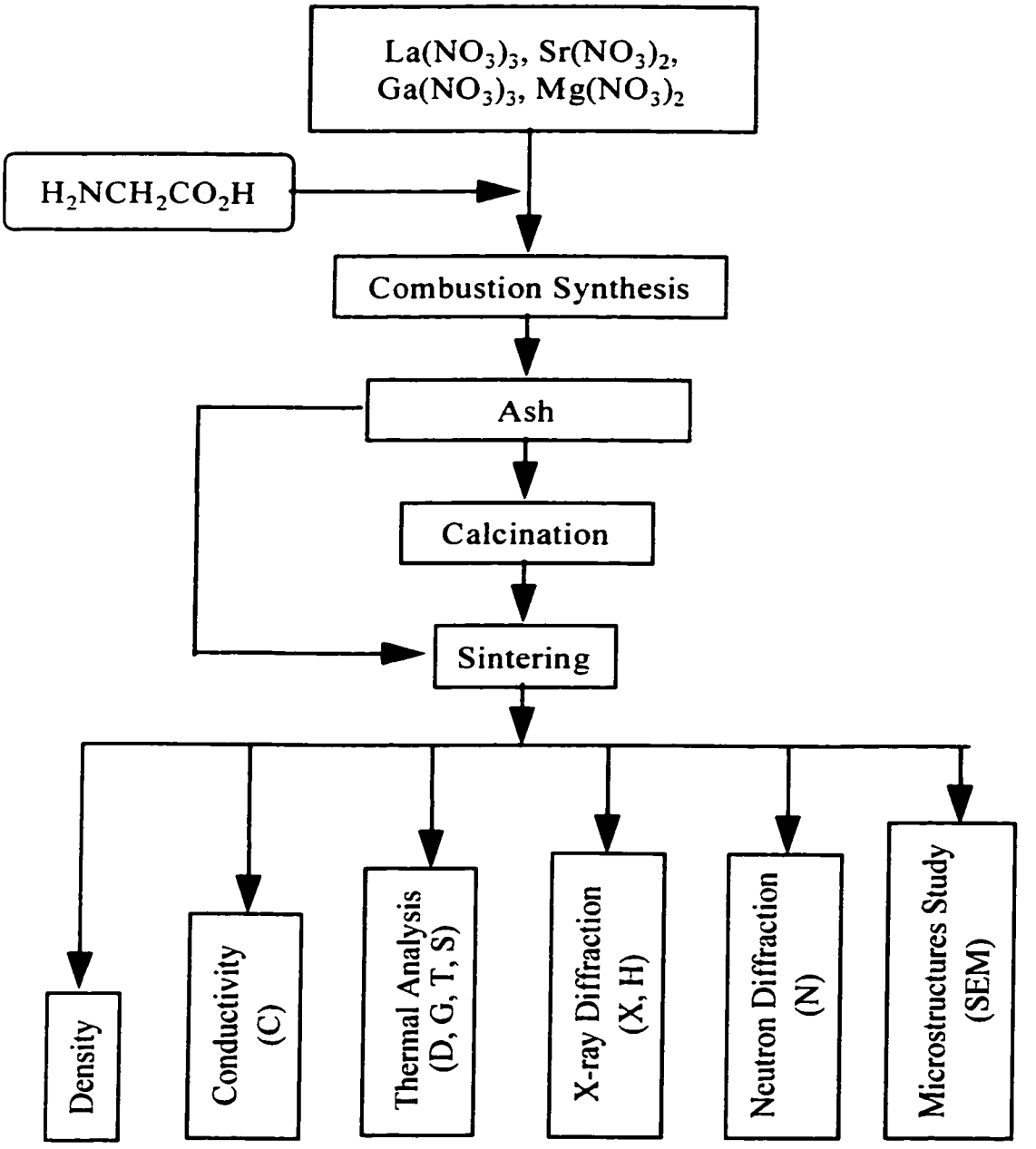

Fig. 4.1 Flow Chat of LSGM Sample Preparation and Characterization

Table 4.2 GNP Samples in LSGM System

LSGM	A/B Cation Ratio					
Perovskite*	0.90	0.95	0.98	1.00	1.02	1.05
LSGM-0000		GHTSX	GHTSX	GHNTSX	GHTSX	GHTSX
LSGM-1010		GHTSX	DGHTSX	DGHNTSX	DGHTSX	GHTSX
LSGM-1020	X	X	X	CX	X	
LSGM-2010				X		
LSGM-1520				CX		
LSGM-2015				CX		
LSGM-2020		CDGHTSX	CGHTSX	CDGHNTSX	GHTSX	DGHTSX
LSGM-2520				X		
LSGM-3020				X		
Secondary Phases in LSGM System						
$La_4Ga_2O_9$				X		
$SrLaGa_3O_7$				X		
$SrLaGaO_4$				X		

** The four digits numbers after LSGM represent the Sr (first two digits) and Mg (last two digits) doping level in mole percent.*

C: Electrical Conductivity Measurement

D: Dilatometry

G: Thermogravimetry Analysis (TGA)

H: High Temperature X-ray Diffraction (HTXRD) Analysis

N: Neutron Diffraction (ND) Study

T: Differential Thermal Analysis (DTA)

S: Differential Scanning Calorimetry (DSC)

X: Room Temperature X-ray Diffraction (XRD) Analysis

SEM: Scanning Electron Microscopy

4.2 TECHNIQUES OF CHARACTERIZATION

4.2.1 Room Temperature X-ray Diffraction

The sintered LSGM samples were crushed and ground with an agate mortar and pestle, followed by sieving to ~ 325 mesh (< 45 μm) particle size. Specimens were mounted in a front-loading, shallow-cavity holder fabricated from low-background, off-axis, single-crystal quartz supplied by Gem Dugout, State College, PA. Data collection was performed at room temperature (26 ± 2°C). The instrumental conditions and diffraction scan parameters used in this study are listed in table 4.3. Overnight slow-scan room temperature X-ray powder diffraction measurements were conducted using a Scintag PAD V vertical θ/2θ goniometer, with CuKα radiation (45 kV and 40mA) and a Si(Li) Peltier-cooled solid state detector. The data were collected between 15 and 135° (2θ) at a step size of 0.01° and 4 sec/step.

Table 4.3 X-ray Instrumental Conditions and Diffraction Scan Parameters

Instrumental Conditions		
Goniometer	Philips Type PN3550/00X, Vertical	
X-ray Source	Fixed-Anode LFF Cu Tube	
Power	40 kV, 45 mA (1800 W)	
Radiation, 1	Cu $K\alpha_1$, 1.54060 Å	
Monochromator	Graphite	
Counter	Scintillation	
Soller Slits	Employed on incident beam side only	
Divergence Slit	Variable	
Receiving Slit	Fixed, 0.2 mm	
Diffraction Scan Parameters		
2θ Range	Scan Rate	Comments
5 - 75°	0.04°/2s (normal)	No internal standard used
5 - 75°	0.02°/10s (slow)	no peaks observed below 15°

4.2.2 High Temperature X-ray Diffraction

High temperature x-ray diffraction (HTXRD) measurements were conducted using a Scintag PAD X vertical θ/θ goniometer equipped with a modified Buehler HDK-2 diffraction furnace. The diffractometer utilized CuKα radiation (45 kV and 40mA) and a Si(Li) Peltier-cooled solid state detector. The data were collected as step scans, with a step size of 0.02° and a count time of 1 sec/step between 20 and 70° (2θ). All data were collected in air. The temperature was monitored with a Pt/Pt-10%Rh thermocouple spot-welded to a Pt-30%Rh heater strip on which a thin layer of LSGM powders was dispersed. The calibration of the thermocouple was verified with an optical pyrometer.

Data for stoichiometric compositions (A/B = 1) were collected on both heating and cooling. Starting at room temperature, data collection were carried out at following temperatures: every 5°C from 140 to 155°C; every 50°C from 200 to 400°C; every 5°C from 400 to 425°C; every 25°C from 425 to 600°C; every 100°C from 600 to 1300°C; either 50 or 100°C increments from 1300°C back to room temperature. For off-stoichiometric compositions ($A/B \neq 1$), data were collected on heating only at the following temperatures: room temperature, 200, 400, 600, 800, 1000, and 1200°C.

4.2.3 Neutron Diffraction

Neutron diffraction measurements were conducted at the High Flux Isotope Reactor (HFIR) of Oak Ridge National Laboratory (ORNL) using the high-resolution neutron

powder diffractometer (HB-4) at room temperature, 300, 600, 900 and 1100°C. HB-4 is equipped with a Ge(115) monochromator and 32 equally spaced 3He detectors. The powder sample was contained in a spinning cylindrical vanadium can. Data were collected with constant monitor counts with a step size of 0.05° 2θ between 11 and 135° 2θ. The wavelength was calibrated using NIST SRM 640b (Si) (National Institute of Standards and Technology, Standard Reference Program, Gaithersburg, MD).

4.2.4 Thermal Analysis

In addition to X-ray and neutron diffraction, various thermal analysis techniques, i.e., Differential Thermal Analysis (DTA), Differential Scanning Calorimetry (DSC), ThermoGravimetric Analysis (TGA) and Dilatometry were used to detect the phenomena relevant to energy evolution, phase change and sinterability of LSGM perovskites. According to literature[46-65,81-84] there are two distinct phase transitions in $LaGaO_3$. Netzsch STA 409C DTA/TGA analyzer was used to take and record the differential heat flux and mass change of the samples up to temperature 1500°C with heating rate of 5°C per minute in air or simulated air (gas flow of N_2 and O_2 in volume ratio of 4:1). These studies were conducted to investigate phase changes and also to monitor LSGM electrolyte behavior in an environment similar to SOFC operating conditions. As-synthesized LSGM powders (30 mg) or fine-powders from crushing sintered LSGM disk (100 or 250 mg) were placed in an alumina crucible as test samples. 30 mg (for test of as-synthesized) or 100 or 200 mg (for test of sintered-powders) fine Al_2O_3 powders in an identical alumina crucible

were used as reference. Netzsch STA DSC 200 analyzer was used to detect and record energy evolution of the LSGM materials up to 500°C with heating rate of 5°C per minute in air or helium. Fine powders of crushed (sintered) LSGM of about 30 mg were contained in an aluminum pan as test sample. An empty aluminum pan was used as reference. Netzsch Dilatometry DIL 402C was used to study the sinterability of the LSGM materials up to 1500°C. Cylindrical samples (diameter of ~ 12 mm and thickness of ~ 6 mm), were first uniaxially pressed in double-action dies (with low green density of 20 to 30% theoretical density) followed by isostatic pressing (~ 135 MPa), were heated under flowing air at 5°C per minute to the desired temperature (between 1300 to 1500°C). These samples were held isothermally for 2 hours at the peak temperatures. The sintering shrinkage was monitored during the heating and the isothermal hold cycle. After the isothermal hold, the samples were cooled to room temperature at a rate of 5°C per minute in flowing air. The thermal expansion of nearly fully dense sintered LSGM materials was measured up to 1000°C with heating rate of 5°C per minute in air in the same instrument. The specimens were held isothermally at 1000°C for 15 minutes, allowing sufficient time to reach thermal equilibration.

4.2.5 Electrical Conductivity Measurement

The electrical conductivity (σ, in unit of S/cm), of nearly fully dense (> 96% of theoretical density) sintered LSGM bars (dimensions of 30 mm x 2 mm x 2 mm) of selected compositions, was measured as a function of temperature up to 1100°C in air by

the four-point probe technique (or 4-point dc method) using platinum electrodes at the Pacific Northwest National Laboratories (PNNL). A heating and cooling rate of 1.6°C/min was used. The output from the 4-point probe is the resistively (ρ, in unit Ω-cm) of the tested material which is inversely equal to its electrical conductivity ($\rho = 1/\sigma$). The 4-point probe technique is a well-developed characterization method which offers an absolute measurement with no required calibration.[89] The setup of the 4-point probe device consists of four collinear (or in-line) platinum probes (electrodes) of finite radius with equal probe spacing (s, in unit of mm and it is normally close to 1 mm). A direct current (dc) is used to supply current through the outer two probes while a voltmeter measures the voltage across the inner two probes (See Fig. 4.2).

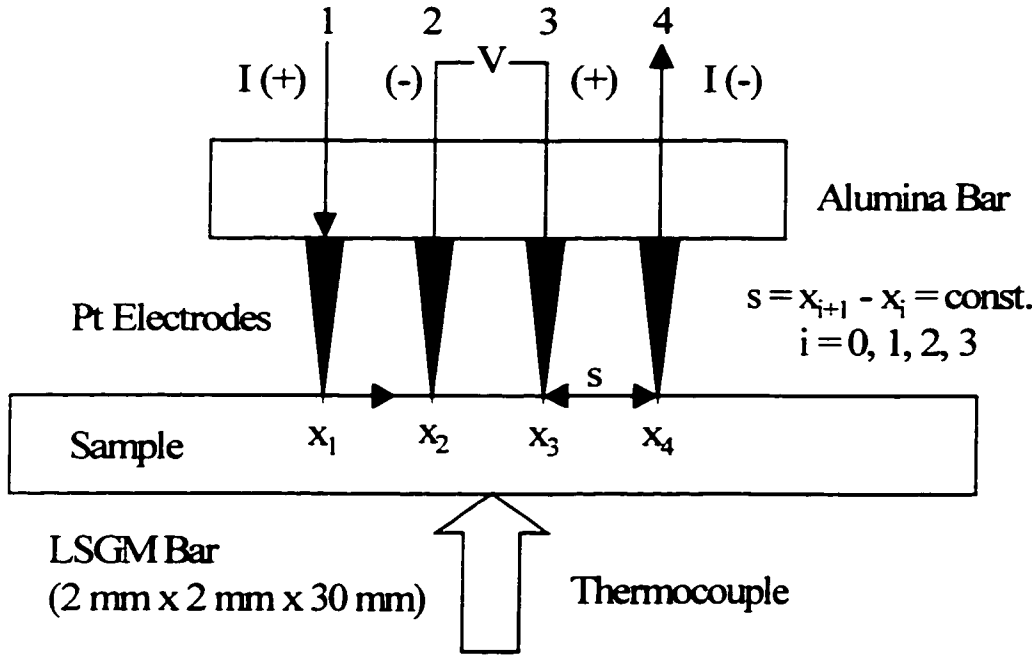

Fig. 4.2. Schematic of 4-point Probe Configuration

Assuming the size of the platinum probe is infinitesimal and the size of the sample is semi-infinite in lateral dimension with thickness larger than the probe space s. The floating potential V_f at a distance r from an electrode carrying a current I in the test material of ressistivity ρ is calculated as:

$$V_f = \frac{\rho I}{2\pi r} \tag{4.1}$$

There are two electrodes (1 and 4) carrying currents of equal magnitude but in opposite directions in Fig. 4.2, and the floating potential V_f at any point in the sample is therefore the superposition of the potential induced by each of the electrodes.

$$V_f = \frac{\rho I}{2\pi r}\left(\frac{1}{r_1} - \frac{1}{r_4}\right) \tag{4.2}$$

where r_1 = distance from probe number 1, r_4 = distance from probe number 4.

The floating potentials at probe 2, V_{f2} and at probe 3, V_{f3} can therefore be expressed as:

$$V_{f2} = \frac{\rho I}{2\pi}\left(\frac{1}{s_1} - \frac{1}{s_2 + s_3}\right) \tag{4.3}$$

and

$$V_{f3} = \frac{\rho I}{2\pi}\left(\frac{1}{s_1 + s_2} - \frac{1}{s_3}\right) \tag{4.4}$$

by substituting the proper distances to probe 1 and probe 4 respectively. The potential difference (voltage drop) V measured between the two inner probes becomes:

$$V = V_{f2} - V_{f3} = \frac{\rho I}{2\pi}\left(\frac{1}{s_1} - \frac{1}{s_2 + s_3} - \frac{1}{s_1 + s_2} + \frac{1}{s_3}\right) \tag{4.5}$$

Since $s_1 = s_2 = s_3 = s$, Eq. (4.5) simplified as:

$$V = V_2 - V_3 = \frac{\rho I}{2\pi s} \tag{4.6}$$

and the resistivity (Ω-cm) is given by:

$$\rho = 2\pi s\left(\frac{V}{I}\right) \tag{4.7}$$

with V measured in volts, I in amperes and s in cm. The typical probe radii are 30 to 500 μm and the probe spacings range from 0.5 to 1.5 mm. It is convinent to choose s = 1.588 mm such that $2\pi s = 1$. The final expression for specific conductivity (S/cm) becomes:

$$\sigma = \frac{I}{V} \tag{4.8}$$

CHAPTER 5

RESULTS

In order to characterize the structure and enhance our understanding of the new SOFC electrolytes — the Sr and Mg doped $LaGaO_3$ (LSGM) perovskites, several techniques were used to study the phase development and phase changes as function of doping concentration, A/B cation ratio and temperature. Many compositions of the LSGM materials were analyzed by thermal techniques (TGA, DTA, DSC, Dilatometry), and diffraction techniques (XRD, HTXRD and neutron diffraction). The change in lattice constants, space groups, and atom coordinates were measured and calculated using JADE and GSAS. Based on these results, the phase boundary of the LSGM perovskite in La_2O_3-SrO-Ga_2O_3-MgO quaternary system was defined. Microstructure of the main perovskite phase and that of minor phases were observed by SEM. Electrical conductivity of selected compositions of interest was measured as a function of temperature. These experimental results are presented in the following sections.

5.1 PHASE DEVELOPMENT AND STABILITY

This part is the major focus of this research. The effects of doping, A/B ratio and the temperature are summarized in separate sub-sections.

5.1.1 Effects of Doping

For $LaGaO_3$ perovskite, doping with Sr and Mg creates oxygen vacancies ($Sr'_{La} = Mg'_{Ga}$

and $V_O^{\bullet\bullet} = \frac{1}{2} Sr'_{La} = \frac{1}{2} Mg'_{Ga}$). By altering composition, doping also impacts crystal structures and promotes the formation of secondary phases. Fig. 5.1 shows a partial X-ray spectra of LSGM materials with LSGM-0000 ($LaGaO_3$) at the bottom, LSGM-1010 ($La_{0.9}Sr_{0.1}Ga_{0.9}Mg_{0.1}O_{2.9}$) in the middle and LSGM-2020 ($La_{0.8}Sr_{0.2}Ga_{0.8}Mg_{0.2}O_{2.8}$) on the top. These spectra were taken from samples sintered at 1500°C for 9 hours to achieve full equilibrium. Note that not only the peak position shifts towards lower 2θ angle (increase d-space), the peak shape also changed (from a triplet to a doublet) when the doping content was increased (from zero to 0.2 mole). The index for these peaks changed from (400/224/040) for LSGM-0000 and LSGM-1010 to (004/422) for LSGM-2020. A phase transition from an orthorhombic (Pbnm) to a monoclinic (I2/a) structure was indicated when the doping level increased from 0.1 to 0.2 mole. The crystallographic relation between I2/a and Pbnm is found to be $(001)_{Mon}//(100)_{Orth}$. Table 5.1 lists the observed and calculated diffraction data corresponding to these high θ-2θ angles. Where HKL is the Miller indices of the lattice; 2T is the diffraction angle with C representing the calculated values, O the observed values and (C-O) the difference between C and O. D is the inter-planar spacing; a, b (β) and c are lattice parameters with sigma in the parentheses. As can be seen, the calculated values match very closely with the observed data.

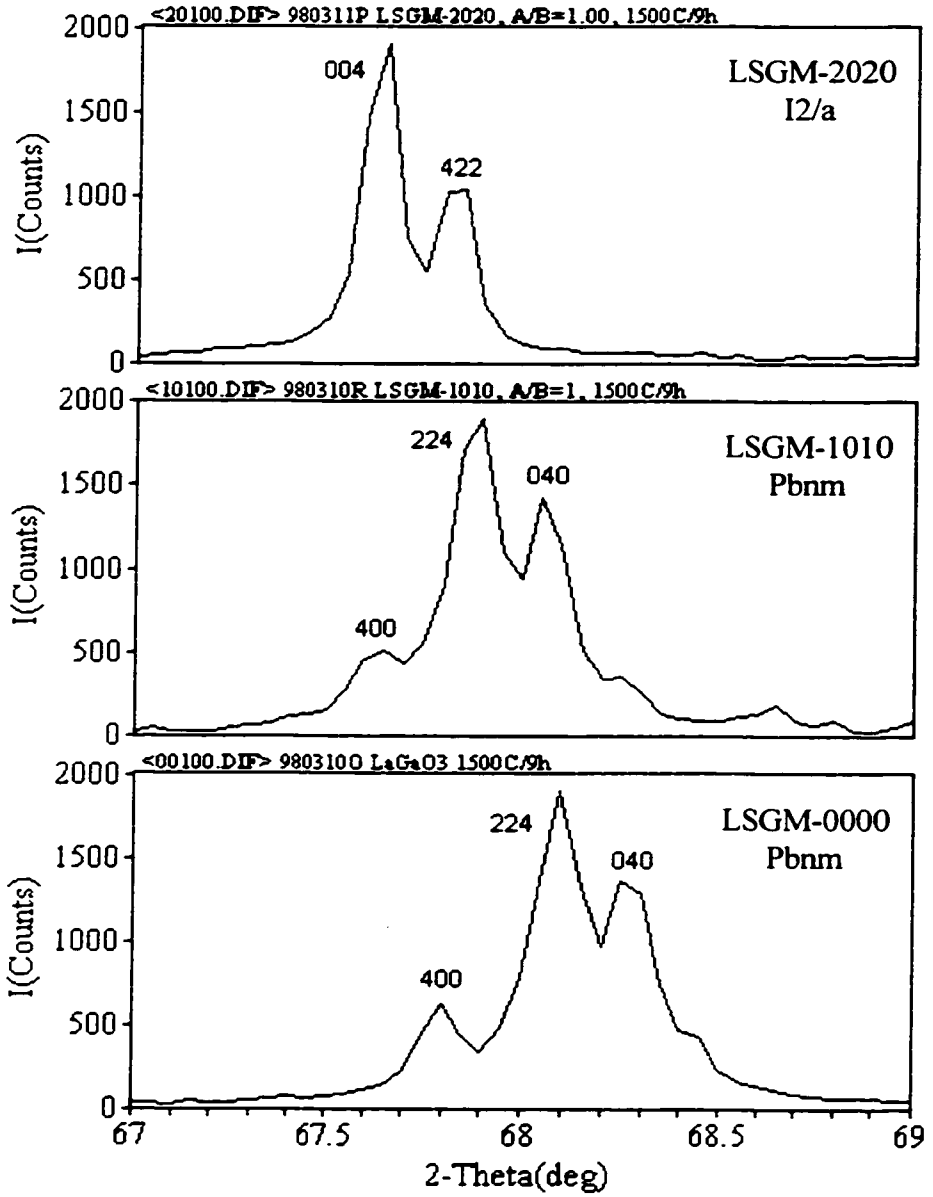

Fig. 5.1 High θ–2θ Angle X-ray Spectra of Stoichiometric LSGM Show Phase Transition between LSGM-1010 and LSGM-2020 (A/B = 1.0)

Table 5.1 High Angle 2θ X-ray Data Shows the Phase Transition as a Function of Doping Content (from Pbnm to I2/a)

LSGM	H K L	2T (C)	2T (O)	2T (C-O)	D (C)	D (O)	D (C-O)	Parameters (Å)
0000	4 0 0	67.831	67.832	-0.001	1.3805	1.3805	0.0000	a=5.5243(5)
	2 2 4	68.098	68.097	0.001	1.3757	1.3757	0.0000	b=5.4924(6)
Pbnm	0 4 0	68.274	68.273	0.001	1.3726	1.3726	0.0000	c=7.7748(9)
1010	4 0 0	67.680	67.680	0.000	1.3832	1.3797	0.0000	a=5.5372(7)
	2 2 4	67.876	67.876	0.000	1.3797	1.3797	0.0000	b=5.5066(8)
Pbnm	0 4 0	68.035	68.036	-0.001	1.3797	1.3797	0.0000	c=7.8038(11)
2020	0 0 4	67.620	67.619	0.001	1.3843	1.3843	0.0000	a=7.8172(6)
	4 2 2	67.659	67.658	0.001	1.3836	1.3836	0.0000	b=5.5349(8)
I2/a								c=5.5357(9)
								β=89.895(8)

5.1.2 Effects of A/B Cation Ratio

Similar to the effect of doping, the variation in A/B cation ratio also leads to the creation of oxygen vacancies and the formation of secondary phases. However, the impact of the A/B ratio on crystal structure of LSGM perovskite was negligible. The full scan room temperature X-ray spectra of LSGM materials with various A/B cation ratios are presented in Appendix I as Fig. A-1 to A-3 for LSGM-0000, LSGM-1010 and LSGM-2020, respectively. Note, in each Figure, there are five spectra corresponding to A/B ratio of 0.95, 0.98, 1.00, 1.02 and 1.05. At bottom of each figure, an indexed X-ray diffraction pattern for each doping level is attached for comparison. The X-ray detectable secondary phases are marked in Fig. A-1 to A-3, with corresponding powder diffraction file (PDF) number. Estimated results of secondary phase(s) are presented in table 5.2, as functions of the doping content and the A/B cation ratio. Note that the total amount of crystalline secondary phase(s) present is very small (~1 wt%) except for LSGM-1010 at A/B = 0.95, where the amount of $SrLaGa_3O_7$ was larger than 2 wt%, and for LSGM-2020 at A/B =

1.05, where $SrLaGaO_4$ was also larger than 2 wt%. Based on table 5.2, we can find the best LSGM compositional window for SOFC electrolytes.

5.1.3 Effects of Temperature

The as-synthesized LSGM powders by GNP combustion synthesis were amorphous. Upon heating, moisture and organic residues were vaporized and sublimed. The thermal behavior of LSGM materials was studied by DTA/TGA, with results shown in Fig. 5.2. Regardless of composition, there was 17 ± 2 % weight loss when the powders were heated from room temperature up to 1500°C. The weight loss started gradually at about 500°C (decomposition of metal nitrates) and was completed by about 800°C. Approximately 3 ± 1 wt% was lost rapidly at temperature of 780 ± 10°C. A sharp exothermal peak was observed by DTA corresponding to this weight loss. Decomposition of metal nitrides (SrN_2, MgN_2) is believed to be responsible for this weight loss. In addition, there was a slope change in the TG curves at 650 ± 20°C and X-ray analysis showed that the amorphous powders began crystallizing in this temperature region.

Table 5.2 X-ray Detectable Secondary Phases (%) in LSGM Perovskite

	A/B cation ration				
Doping	0.95	0.98	1.00	1.02	1.05
0 (mole)	Ga_2O_3 (< 1 wt%)	Ga_2O_3 (< 1 wt%)	None	None	$La_4Ga_2O_9$ (~ 1 wt%)
0.1 (mole)	$SrLaGa_3O_7$ (> 2 wt%)	$SrLaGa_3O_7$ (~ 1 wt%)	None	$La_4Ga_2O_9$ La_4SrO_7 (~ 1 wt%)	$La_4Ga_2O_9$ La_4SrO_7 (> 1 wt%)
0.2 (mole)	$SrLaGa_3O_7$ (~ 1 wt%)	None	$SrLaGaO_4$ (~ 1 wt%)	$SrLaGaO_4$ (> 1 wt%)	$SrLaGaO_4$ (> 2 wt%)

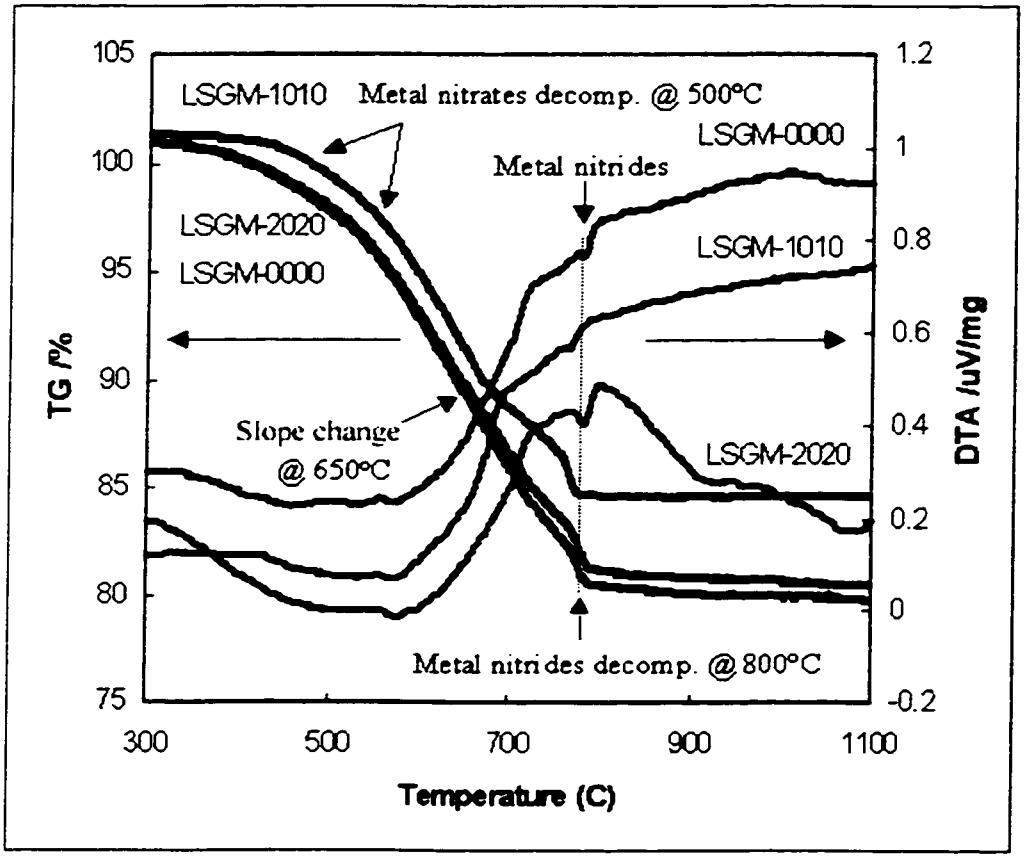

Fig. 5.2 Thermal Analysis Results of the LSGM Ashes

The transformation of amorphous powders into crystalline phases increased with temperature and holding time (at fixed temperature). The evolution of crystallization was very complicated. Usually there were several crystalline phases developed from amorphous powders and these phases competed with each other for the duration of the heating process. Most of these phases would convert to the final perovskite after high temperature treatment. However, in some cases, one or two impurity phases did remain in trace amounts as shown in table 5.2. The crystallization of LSGM materials synthesized under different conditions was evaluated in detail. Fig. 5.3 shows a typical X- ray

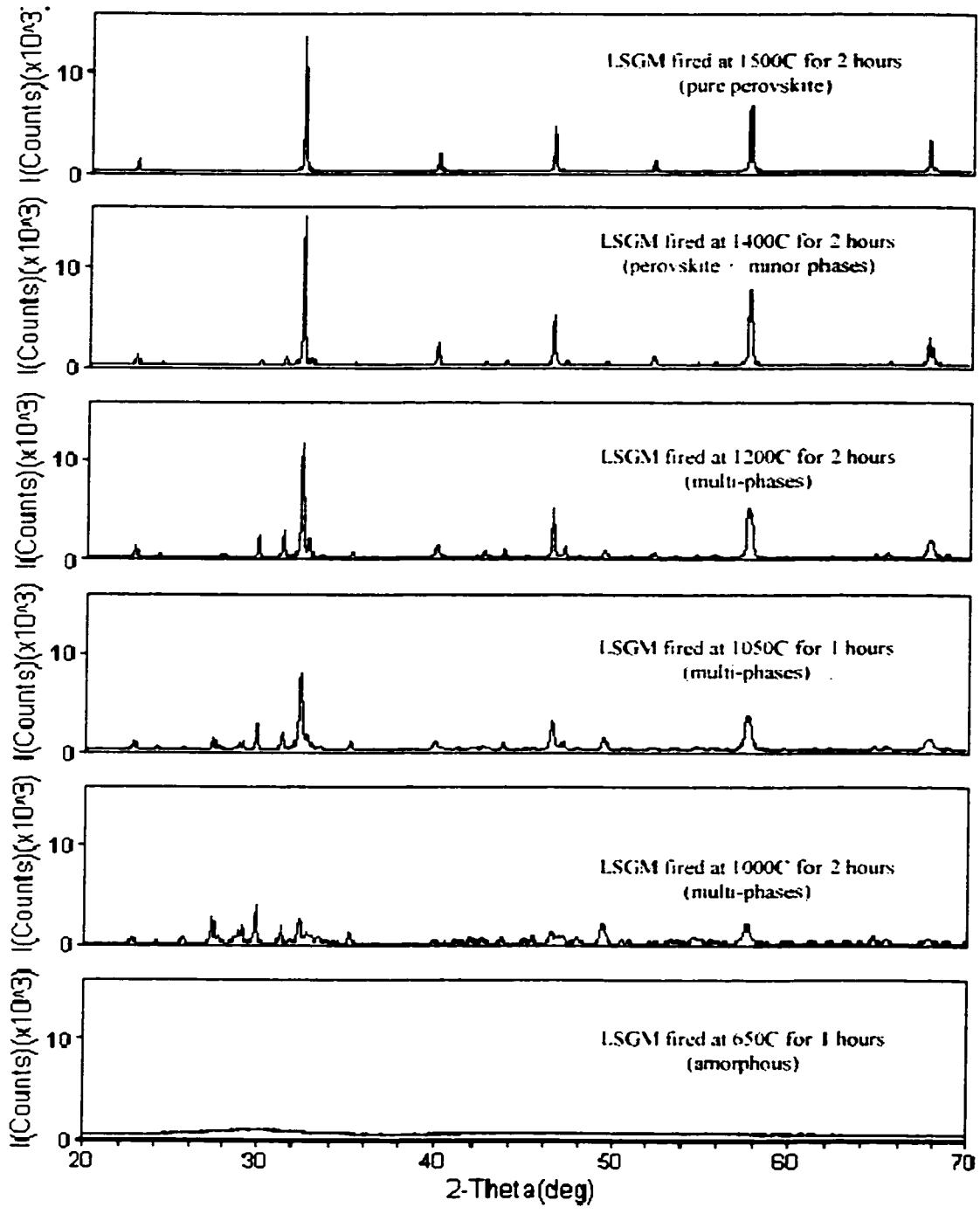

Fig. 5.3 X-ray Spectra of LSGM-1010 (A/B = 1.0) Observed at Various Temperatures.

diagram for stoichiometric LSGM-1010 (A/B = 1.0) heated at different temperatures. After 650°C for 1 hour, the majority of the material was amorphous with no detectable X-ray peak. When fired at 1000°C for 2 hours, several phases, including perovskite, were detected. However, the total amount of the perovskite phase was small. When the heating temperature was increased, the amount of perovskite phase increased with a decrease of other phases. For example, after being heated at 1050°C for 1 hour, the X-ray intensity (the peak-height) of the perovskite phase began to dominate the spectrum. When fired at 1200°C for 2 hours, the ratio of perovskite phase to other phases increased dramatically. After 1400°C for 2 hours, the majority of the material was perovskite with only trace minor phase(s) left. Finally, after heating at 1500°C for 2 hours, the product was essentially single phase perovskite. The characters of the X-ray spectra for remaining LSGM materials were similar with respect to the heat temperature. The effect of composition was negligible. There were always trace amounts of minor phases presented after heat treatment, which is thermodynamically favorable (see Fig. A-1 for LSGM-0000 at various A/B ratio, Fig. A-2 for LSGM-1010 at various A/B ratio and Fig A-3 for LAGM-2020 at various A/B ratio in Appendix I for detail).

After sintering at 1500°C for 2 or 9 hours, the LSGM materials were quite stable. The DTA/TG curves were flat for samples heated in air or simulated air (a mixture of 80 vol.% N_2 and 20 vol.% O_2) up to 1500°C. These results are shown in Fig. 5.4a). The DTA curves are plotted in the lower part with the TG curves on the top in Fig. 5.4a). Note that there was a small weight gain in the TG curves. The origin of this is not clear. The slight

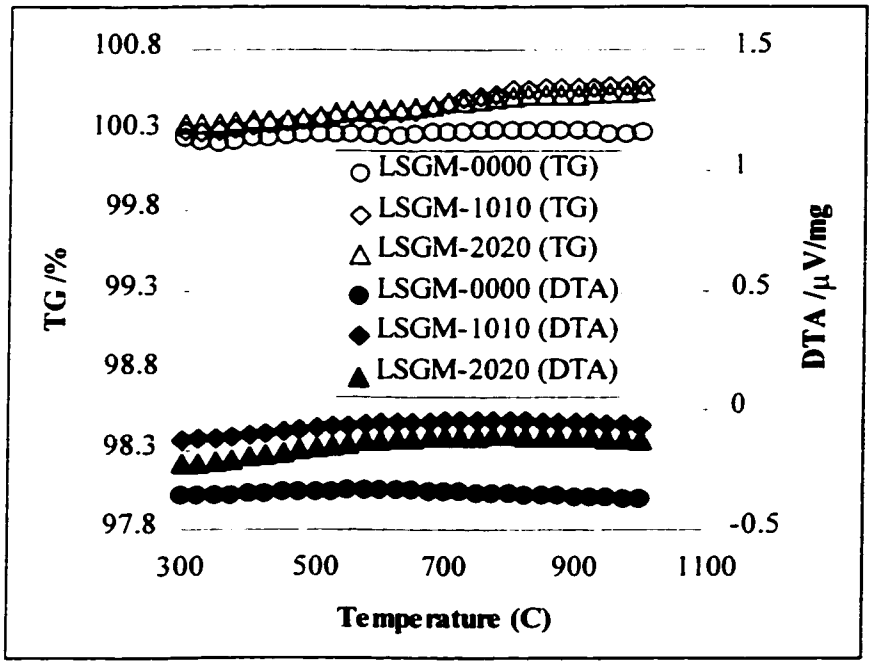

a) TG/DTA Curves

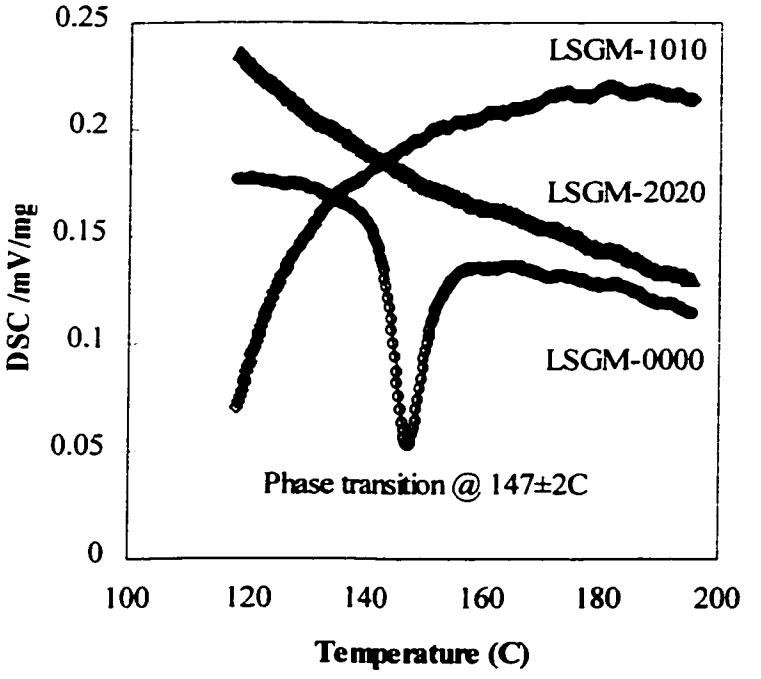

b) DSC Curves

Fig. 5.4 Thermal Analysis Results of the Sintered LSGM Powders (A/B = 1.0)

difference in DTA curves between undoped $LaGaO_3$ and doped LSGM-1010 and LSGM-2020 indicates that the specific heat of the perovskites changed upon doping. DSC studies showed that there was an endothermic peak in undoped $LaGaO_3$ at 147 ± 2°C, but no such peak was detected in doped LSGM. The data from DSC experiments is presented in Fig. 5.4b). These results confirmed the fact that there is a first-order phase transition at 147 ± 2°C in pure $LaGaO_3$. This is consistent with literature data.[46-65,81-84] The structure of $LaGaO_3$ changes from room temperature orthorhombic (Pbnm) to high temperature rhombohedral (R3c) upon heating.

Further HTXRD study showed that there were peak-splits occurring in LSGM-0000 (A/B = 0.95 to 1.05) perovskite as a function of temperature (results are presented in Fig. A-4 to A-8 in Appendix I). The high temperature X-ray scan temperatures were from room temperature to 1200°C and the data were collected for one hour at chosen temperatures. These temperatures were 27, 200, 400, 600, 800, 1000, and 1200°C. The diffraction spectra were plotted from low temperature scan to high temperature ones. The indexed room temperature X-ray diffraction patterns of the perovskite phase are attached on the bottom of the figures for comparison. The detectable secondary phases were marked at their highest peak positions with PDF number cited according to the database on JADE. The HTXRD data for LSGM-0000 at A/B = 0.95 is presented in Fig. A-4, data for A/B = 0.98 is in Fig. A-5, data for A/B = 1.00 is in Fig. A-6, data for A/B = 1.02 is in Fig. A-7, and data for A/B = 1.05 is in Fig. A-8. A typical X-ray diffraction spectra with peak shape change at expanded high θ–2θ angles for undoped $LaGaO_3$ (LSGM-0000 and A/B

= 1.0) is shown in Fig. 5.5. Where room temperature peaks (400/224 of Pbnm) split and changed to (220/208 of R3c) at high temperatures. The corresponding structure change in $LaGaO_3$ from orthorhombic (Pbnm, at room temperature) to rhombohedral (R3c, at 200 to 1200°C) is clearly indicated. The crystallographic relation in these two structures is such that the (110) of the high temperature phase (rhombohedral R3c) parallels the (100) of the room temperature phase (orthorhombic Pbnm). This peak-split phenomenon is the evidence of phase transition.

With these HTXRD data, the lattice constants and structure change with respect to temperature for undoped $LaGaO_3$ were calculated using JADE. The results are presented in Fig. 5.6. From this figure we can see very clearly that not only do the lattice constants increase with temperature, but also the crystal structure changes with temperature. In the low temperature region (< 200°C), the lattice constants a, b, and c are well separated which is an indication of a crystal with an orthorhombic symmetry (Pbnm or Pnma). The symmetry was broken when temperature increased above 200°C. In the new structure, a and b merged together while c jumped from ~ 7.7 to ~ 13.3 Å, as would be seen in a hexagonal-rhombohedral distortion of space group R3c. This R3c phase is stable in the temperature region tested (up to 1200°C).

The unit cell volumetric thermal expansion behavior of $LaGaO_3$ perovskite at various A/B cation ratios was calculated from high temperature X-ray data and the results are presented in Fig. 5.7. A pseudo-cubic method was used, in which the distorted perovskite

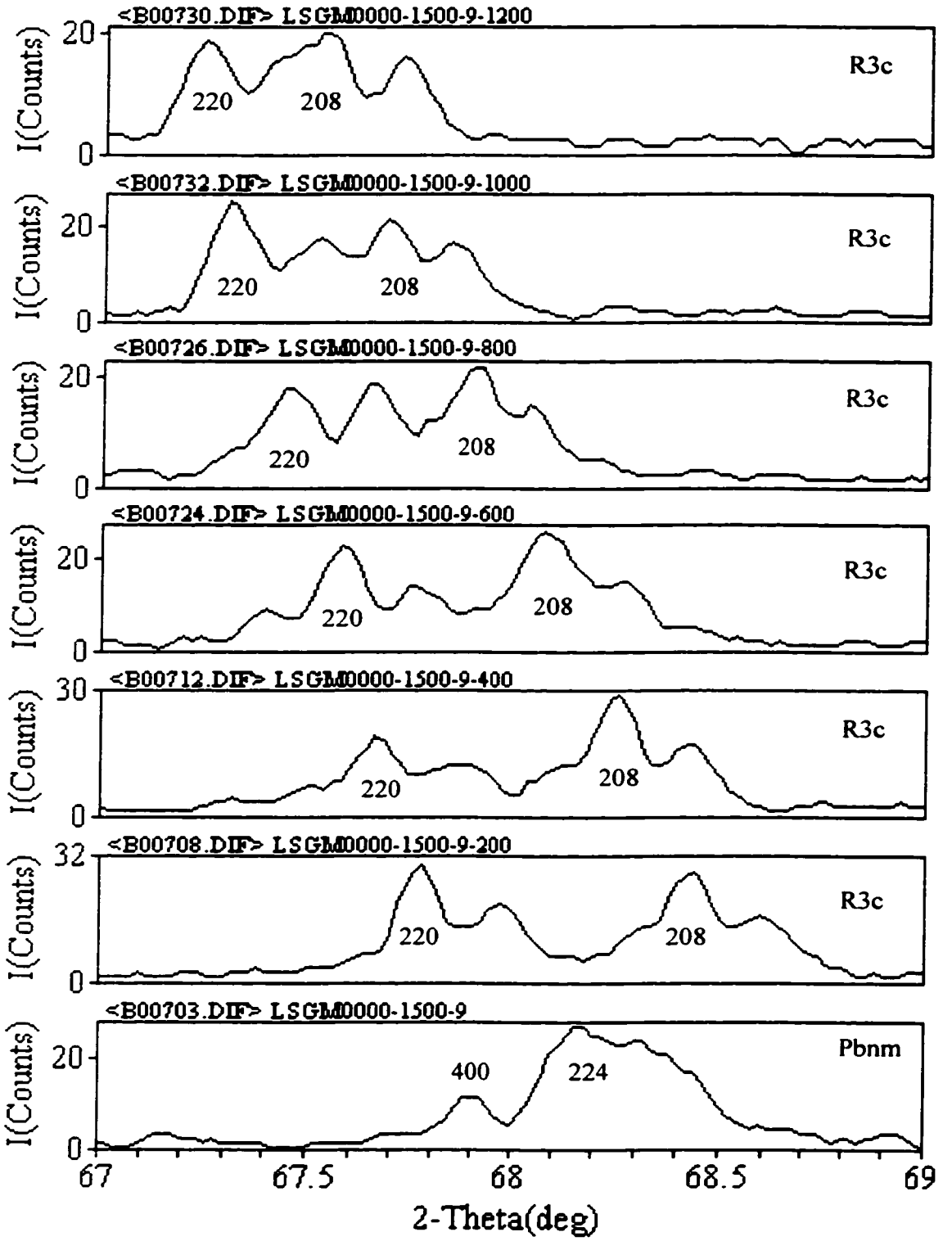

Fig. 5.5 Peak-split Corresponds to Phase Transition in $LaGaO_3$ Perovskite

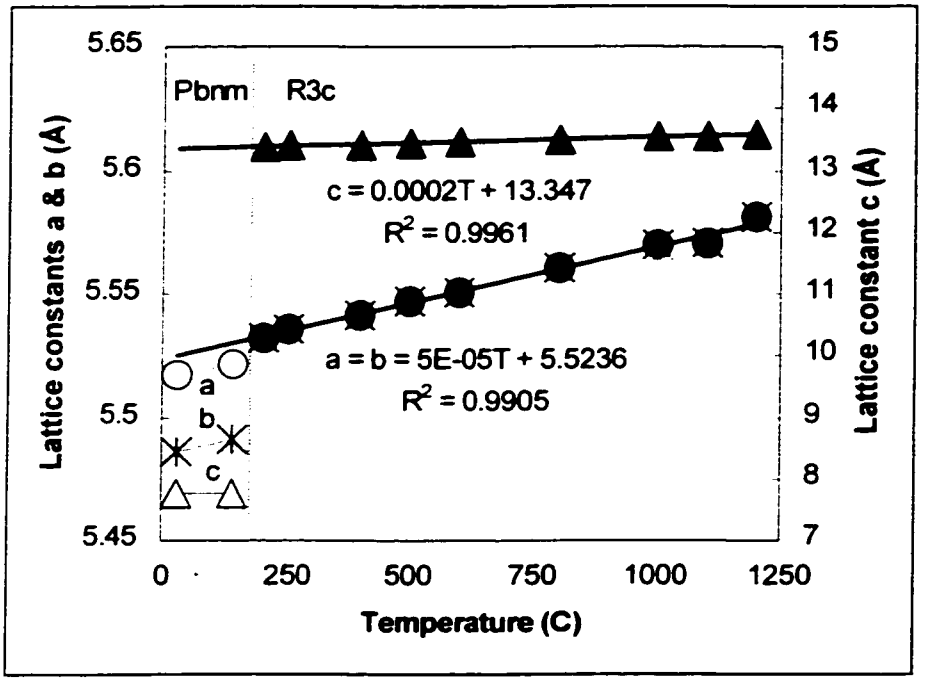

Fig. 5.6 Lattice Constants & Structure Change vs. Temp. in undoped $LaGaO_3$ (A/B = 1.0) Note Pbnm to R3c ($\alpha_a = 5*10^{-5}$ Å/K, $\alpha_c = 2*104^3$ Å/K) transition at ~ 150°C.

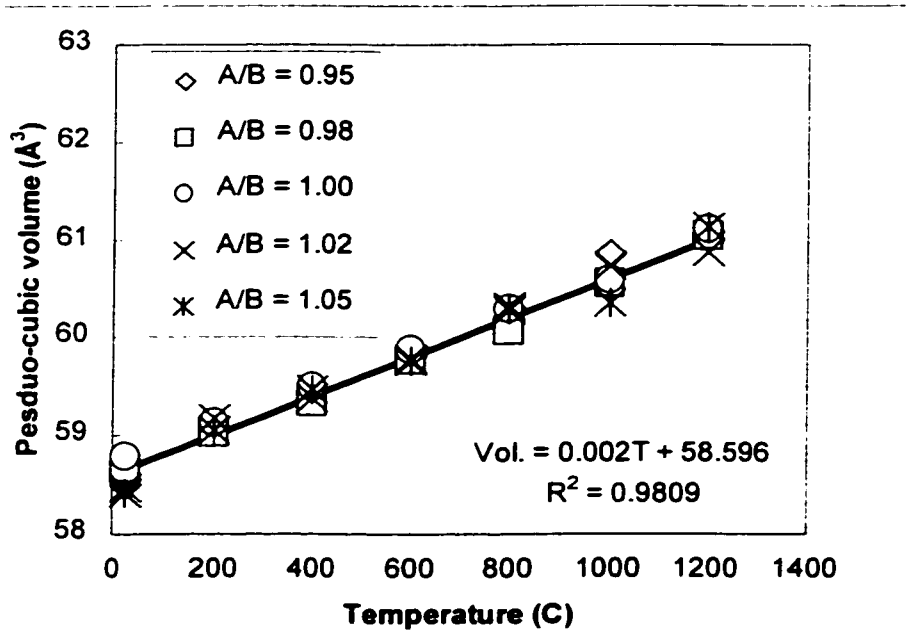

Fig. 5.7 Volumetric Thermal Expansion of LSGM-0000 ($\alpha_V = 2*10^{-3}$ Å³/K)

was converted to cubic structure in order to compare different structures. The expansion coefficient (α_i, where i is a, b, c or v for volume) is equal to the slope change of lattice constants and pseudo-cubic volume as a function of temperature and these values are reported in Fig. 5.6 and 5.7.

Note the difference between thermal expansion in lattice constants a, b, c and unit cell volume v that we reported here, based on high temperature X-ray diffraction data, with bulk thermal expansion (CTE), measured by dilatometry. The calculated lattice thermal expansion coefficients in Fig. 5.6 and 5.7 are only applicable to the change in lattice constants and unit cell volume with respect to temperature where the lattice orientation is important. We should not confuse these with bulk CTE where the lattice orientation effect is averaged due to the contribution from different grains. Further we should note difference in the dimensions (units) of these two thermal coefficients.

From these two plots we can conclude that even though there are large changes in the lattice constants and structure at the phase transition temperature (~150°C), the perovskite unit cell volume did not change abnormally. A linear volumetric expansion behavior is demonstrated through the entire temperature range, including the low temperature orthorhombic structure (Pbnm 62) and the high temperature rhombohedral symmetry (R3c 161).

For doped $LaGaO_3$ (LSGM), differences have been observed in both thermal analysis results and X-ray diffraction patterns. Upon doping, the first-order phase transition that was observed in pure $LaGaO_3$ disappeared. This was confirmed by thermal analysis where no endothermic peak in DSC curves was observed (see Fig. 5.4), and by diffraction analysis where no peak-split in HTXRD spectra was observed. Full scan HTXRD were performed on LSGM-1010 at each A/B cation ratio (A/B = 0.95 to 1.05) and the results are presented in Fig. A-9 to A-13 in Appendix I with PDF number cited for secondary phases (if present). No peak-split was detected in these spectra as function of temperature and A/B cation ratio. Structural analysis using neutron diffraction data, collected at HFIR of ORNL at room temperature, 300, 600, 900 and 1100°C was also performed and these results are shown in Fig A-14 to A-18 in Appendix I. Full-profile Rietveld refinement[90] was performed using the General Structure Analysis System (GSAS).[91] The observed data (cross), calculated spectrum (bulk line) with marks of peak positions and the difference profile are shown together in these figures. The lattice constants and volume change as a function of temperature for LSGM-1010 were calculated using both JADE and GSAS. The results are presented in Fig. 5.8 (with A/B = 1.0) and 5.9 (with various A/B ratios). The lattice constants a, b, and c calculated from HTXRD data are presented in Fig. 5.8 a), and those computed from data of neutron diffraction are presented in Fig. 5.8 b). Note that there is a small difference between these two sets of data due possibly to the detection limit of these techniques. It is believed that the results from neutron diffraction tend to have higher accuracy but the data collection is

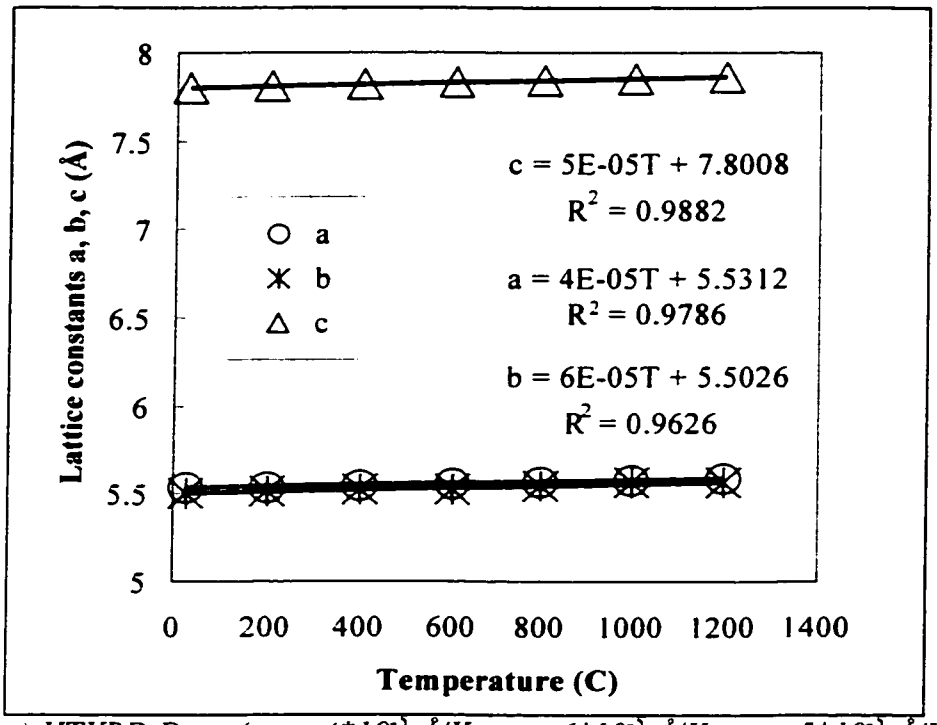

a) HTXRD Data ($\alpha_a = 4*10^{-5}$ Å/K, $\alpha_b = 6*10^{-5}$ Å/K, $\alpha_c = 5*10^{-5}$ Å/K)

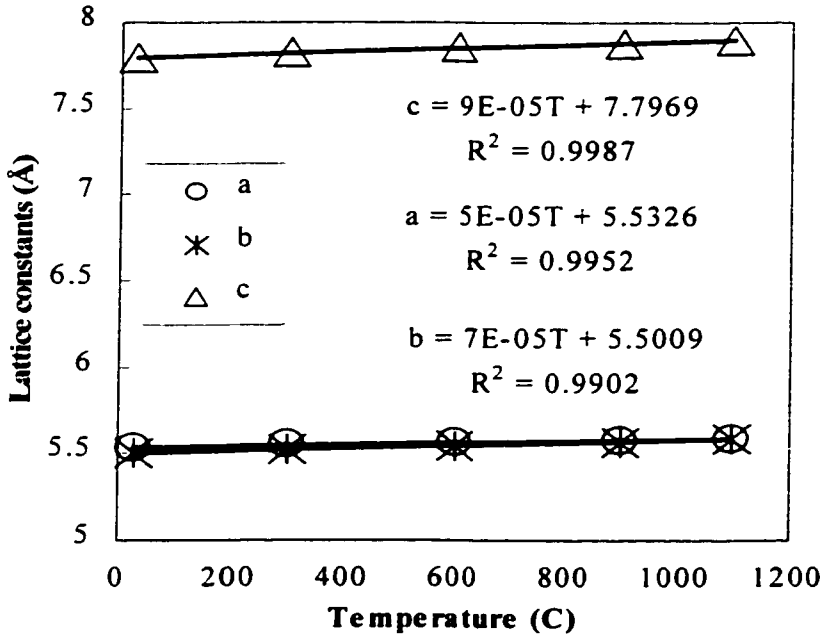

b) Neutron Diffraction Data ($\alpha_a = 5*10^{-5}$ Å/K, $\alpha_b = 7*10^{-5}$ Å/K, $\alpha_c = 9*10^{-5}$ Å/K)

Fig. 5.8 Lattice Constants Change vs. Temperature for LSGM-1010 (A/B = 1.0)

very expensive. The HTXRD data collection is relatively easier and cheaper to perform, but the data analysis is a time-consuming process. In addition, the sample holder for XRD, a Pt-Rh alloy strip, introduced one extra phase whose diffraction peaks heavily overlapped those of LSGM perovskite. This peak-overlap made structure analysis very difficult. The results presented in Fig. 5.9 are unit cell volumetric thermal expansion of LSGM-1010 calculated from HTXRD data (assuming a pseudo-cubic structure) at various A/B cation ratios. Note that there is certain degree of data scatter in Fig. 5.9. However, like that in undoped $LaGaO_3$, a linear volumetric thermal behavior is clearly demonstrated. It is clear from these results that 10 mol% doping at the La and Ga sites (by Sr and Mg respectively) stabilizes the room temperature Pbnm structure to high temperature.

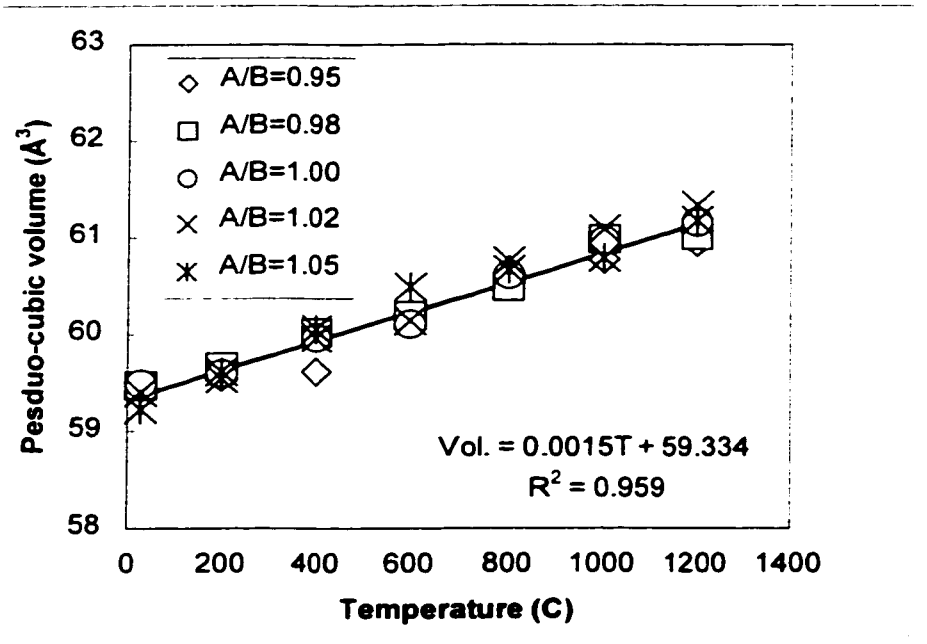

*Fig. 5.9 Volumetric Thermal Expansion of LSGM-1010 (α_V = 1.5*10^{-3} Å^3/K)*

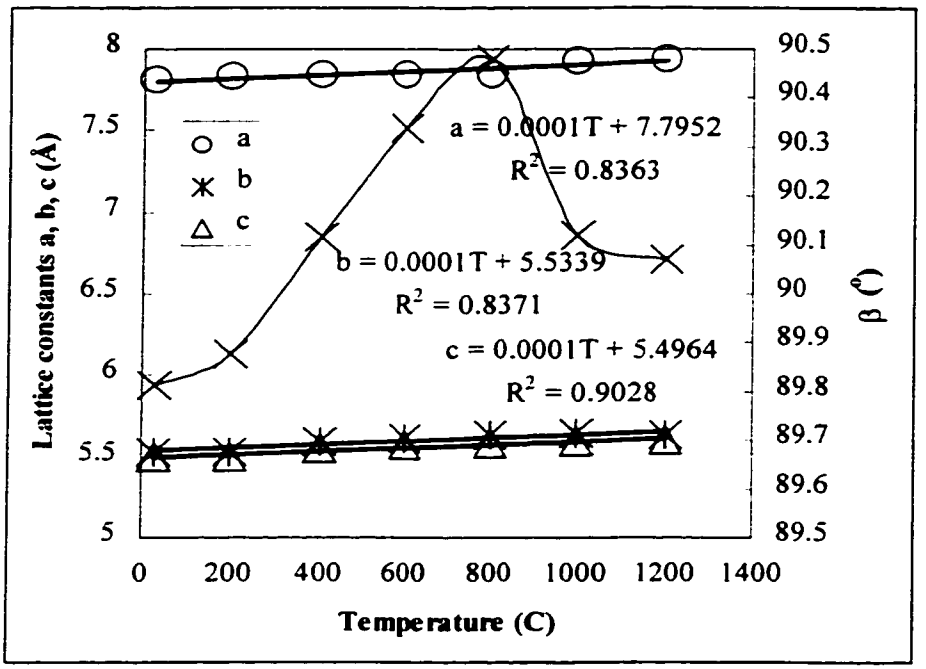

Fig. 5.10 Lattice Constants Change vs. Temperature in LSGM-2020 (A/B = 1.0)

For highly doped LSGM-2020, the HTXRD results for each A/B ratio (A/B = 0.95 to1.05) are presented in Fig A-19 to A.23 in Appendix I. The calculated lattice constant changes with respect to temperature are presented in Fig. 5.10. Where a, b, and c increased linearly with temperature and β varies around 90°. This non-linear behavior of the β angle must be due to the higher doping level that creates more lattice defects. Consequently, the volumetric thermal expansion of LSGM-2020 has large scatter and the calculated results are presented in Fig. 5.11 for various A/B cation ratios. By comparing the results from Fig. 5.11 for LSGM-2020 to Fig. 5.9 for LSGM-1010 and Fig. 5.7 for LSGM-0000, we can conclude that as the doping level increases, attempts to fit the data to a pseudo-cubic structure result in poorer fits (lower R^2 values). The average value of the volumetric cell expansion coefficient also increases with doping level. Based on

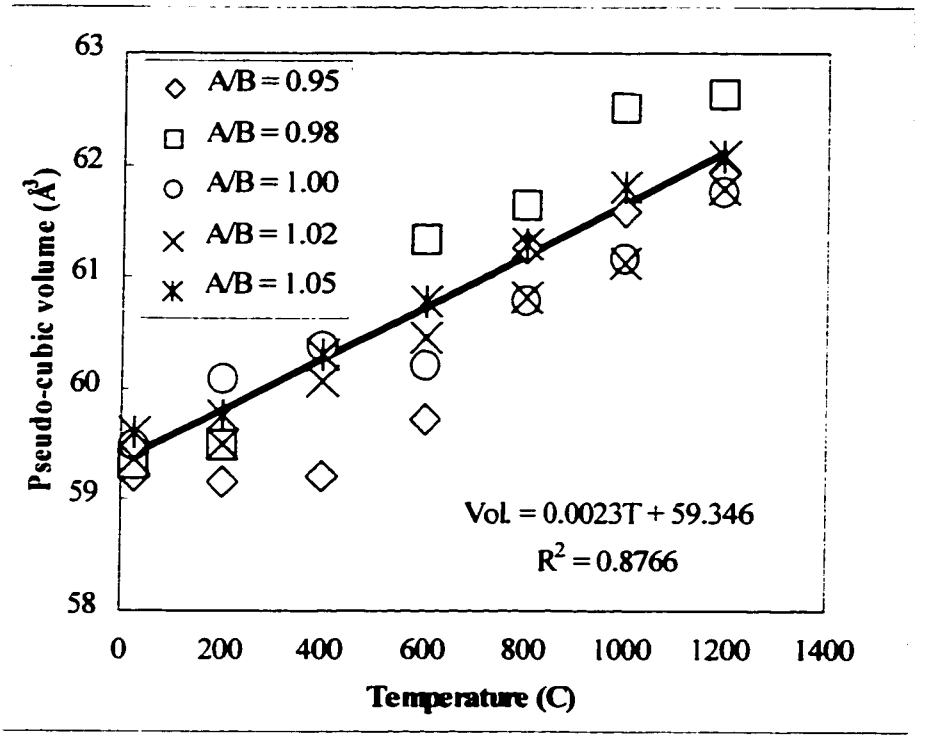

*Fig. 5.11 Volumetric Thermal Expansion of LSGM-2020 (α_v = 2.3*10^{-3} Å^3/K)*

thermal analysis (see Fig. 5.4) and diffraction study (see Fig. 5.8 to 5.11), we can conclude that there is no phase transition in LSGM-1010 and LSGM-2020 as temperature increases. In addition, the change in lattice constants and unit cell volume is a linear function of temperature and is dependent on the doping level.

We have also measured the CTE of selected LSGM compositions, using high temperature dilatometer, and the results showed linear thermal expansion behavior. The preliminary dilatometry study is summarized and presented in table 5.3. In this table, the inflection point is defined as the temperature where its first derivative in the thermal expansion curve is equal to zero. The CTE recorded at the inflection point is a real-time

Table 5.3 Linear Thermal Expansion Of LSGM Materials (Dilatometry Study)

Sample Composition	α (1/°C) at First Inflection Point (°C)	α (1/°C) at Second Inflection Point (°C)	Theoretical α (1/°C)
LSGM-1010 (A/B=0.98)	$7.687*10^{-6}$ (170.6)	$2.695*10^{-6}$ (427.1)	$4.0927*10^{-6}$ (477.0 - 909.3°C)
LSGM-1010 (A/B=1.00)	$7.622*10^{-6}$ (159.5)	$2.145*10^{-6}$ (398.5)	$4.0720*10^{-6}$ (483.0-903.0°C)
LSGM-1010 (A/B=1.02)	$7.701*10^{-6}$ (170.0)	$2.454*10^{-6}$ (397.4)	$3.8072*10^{-6}$ (530.0-903.0°C)
LSGM-2020 (A/B=0.95)	$8.010*10^{-6}$ (157.6)	$2.872*10^{-6}$ (414.5)	$4.6558*10^{-6}$ (600.0-903.0°C)
LSGM-2020 (A/B=1.00)	$8.688*10^{-6}$ (164.9)	$2.536*10^{-6}$ (454.9)	$5.8138*10^{-6}$ (625.0-925.0°C)
LSGM-2020 (A/B=1.05)	$8.856*10^{-6}$ (163.4)	$3.085*10^{-6}$ (454.0)	$5.5517*10^{-6}$ (625.0-925.0°C)

measurement while the theoretical thermal coefficient is calculated by averaging the 'real-time' data points over test temperature range (shown in parentheses).

5.1.4 Summary of Phase Development Study

The results from thermal analysis, X-ray and neutron diffraction have provided evidence that LSGM materials undergo structure changes as function of doping content and temperature. The variation in A/B cation ratio did not alter the lattice structure or induced phase transition, however, it does promote the formation of minor phases (see Table 5.2).

Pure $LaGaO_3$ perovskite changes from room temperature orthorhombic structure to distorted rhombohedral at 145 ± 2°C. Doping with Sr and Mg at a low level (LSGM-1010) stabilizes the orthorhombic structure to elevated temperatures. However, heavily

doped LSGM-2020 adopts monoclinic symmetry. In addition, secondary phases are developed and vary with the doping content and the A/B cation ratio.

Recall the X-ray detected secondary phases, presented in Table 5.2, with respect to the A/B cation ratio and the doping content. We found that the development of these phases is consistent with the binary La_2O_3-Ga_2O_3 phase diagram[45] for undoped $LaGaO_3$. For doped $LaGaO_3$ materials, no phase diagram is available in the literature. In order to evaluate our experimental results, a preliminary quaternary La_2O_3-SrO-Ga_2O_3-MgO phase diagram was proposed and constructed, based on available constituent binary phase diagrams and structure data on ternary compounds. Details of the process used are presented in Appendix II. The result of this study is shown in Fig. 5.12. The undoped $LaGaO_3$ is marked by a cross-circle in the diagram while the composition of doped $LaGaO_3$ (LSGM) perovskite is shown by an arrow. The unary (elemental) oxides (at the corners) are represented by squares. Ovals represent the binary (double) oxides (on the edges). The ternary (triple) oxides (at the planes) are represented by triangles. The phases found in this study are marked as open ovals (in undoped $LaGaO_3$) and/or open triangles (in doped $LaGaO_3$). Comparing the data presented in table 5.2 with this proposed quaternary system, we conclude that the phases identified in this study are consistent with the proposed phase diagram.

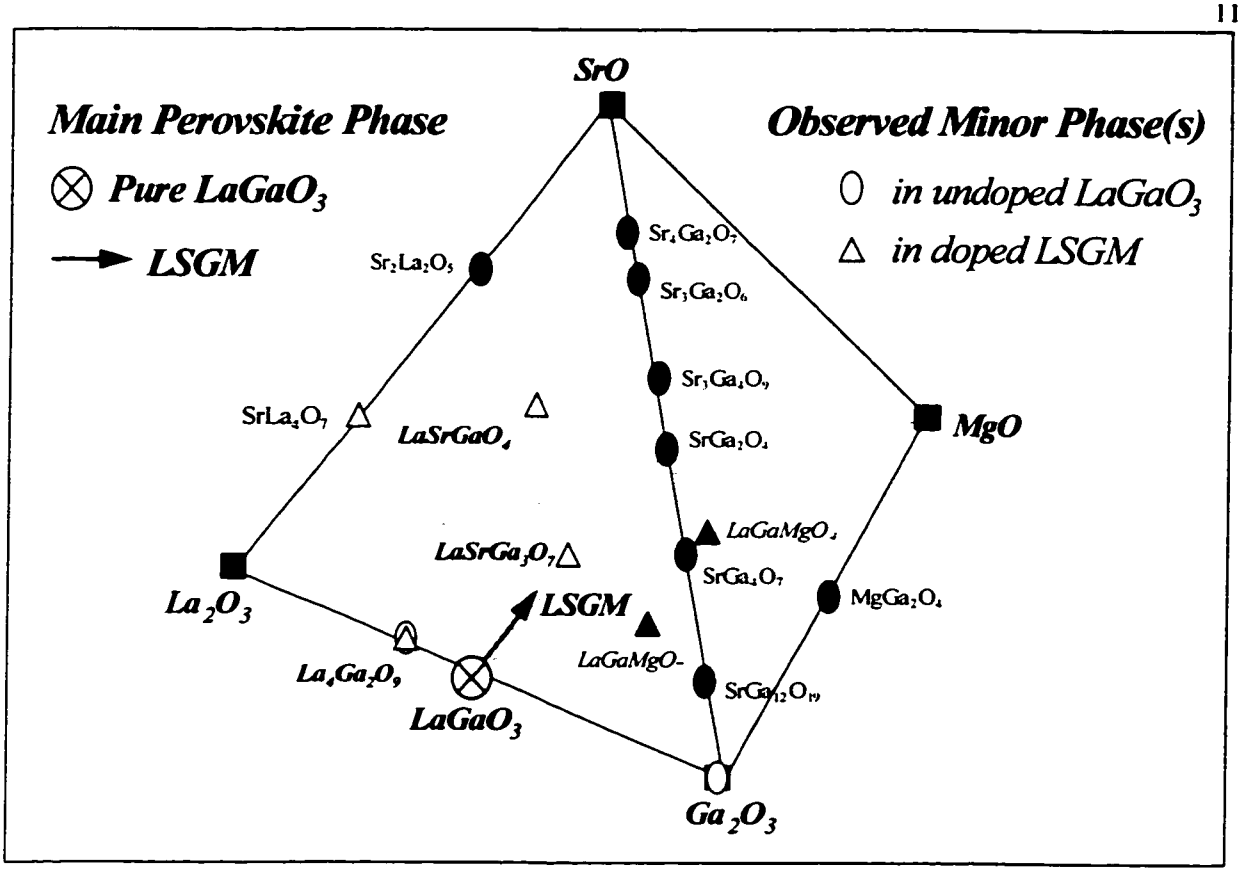

Fig. 5.12 The Predicted La_2O_3-SrO-Ga_2O_3-MgO Quaternary Phase Diagram (Samples Have Been Equilibrated at 1500°C for 9 Hours)

5.2 ELECTRICAL CONDUCTIVITY

The electrical conductivity of selected LSGM materials was measured by 4-point probe dc technique at PNNL. Some of the results are listed in table 5.4 (with YSZ data for comparison) and presented in Fig. 5.13. The effects of A/B ratio are shown in Fig. 5.14 and 5.15 for LSGM-1020 and LSGM-2020 respectively. The conductivity of all LSGM samples is higher than those of YSZ samples at all test temperatures (see Table 5.4). The conductivity for all LSGM materials increases when the test temperature is increased (see Figs. 5.13-15). Within the ranges explored in this study, the conductivity seems

independent of the doping content and the A/B ratio (see Table 5.4 & Figs. 5.13 to 5.15). The only exception is that at very high temperature (1000°C), the conductivity of the LSGM-1020 is less than the samples with higher level of doping.

Table 5.4 Electrical Conductivity of Selected LSGM Materials (c.f. Data of YSZ)

	Conductivity (S/cm) @ Indicated Temperatures			
Composition	400°C	600°C	800°C	1000°C
LSGM-1020	$3*10^{-4}$	$1.5*10^{-2}$	0.10	0.26
LSGM-1520	$4*10^{-4}$	$1.5*10^{-2}$	0.12	0.36
LSGM-2015	$5*10^{-4}$	$1.8*10^{-2}$	0.11	0.31
LSGM-2020	$4*10^{-4}$	$2.0*10^{-2}$	0.12	0.40
YSZ	$0.8*10^{-4}$	$0.6*10^{-2}$	0.05	0.18

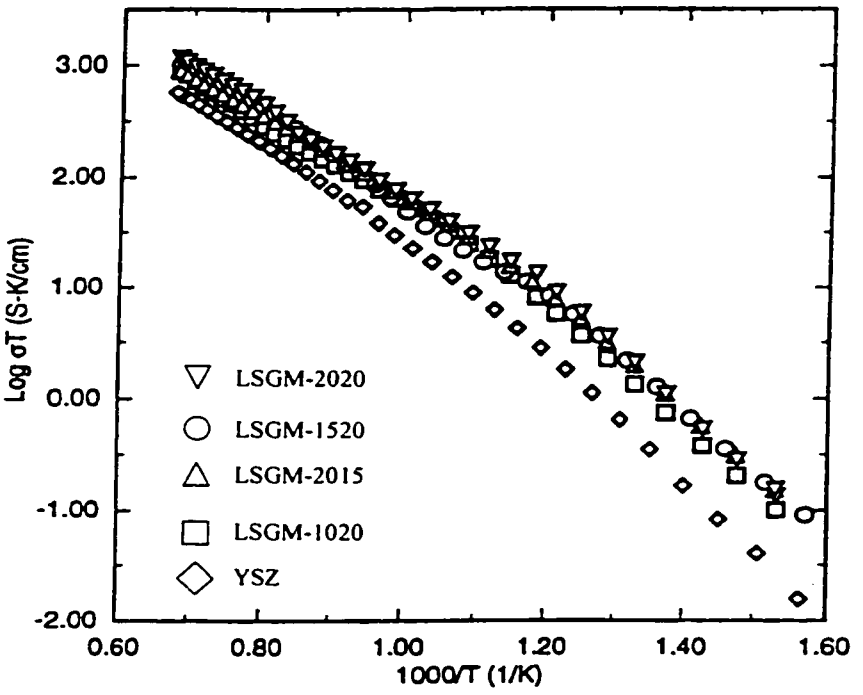

Fig. 5.13 Electrical Conductivity of LSGM Materials

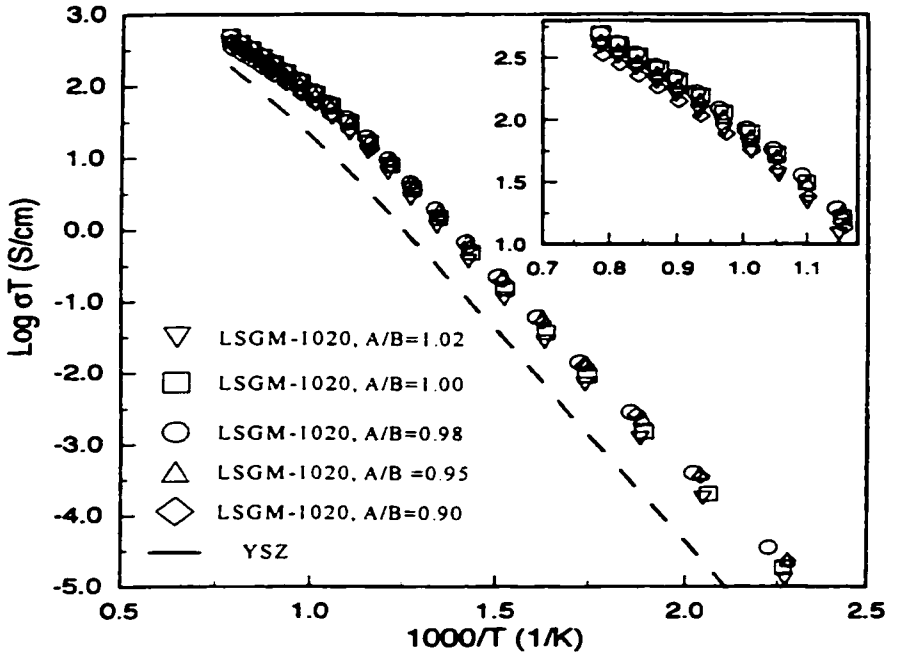

Fig. 5.14 Electrical Conductivity of LSGM-1020 as Functions of A/B Ratio and Temperature

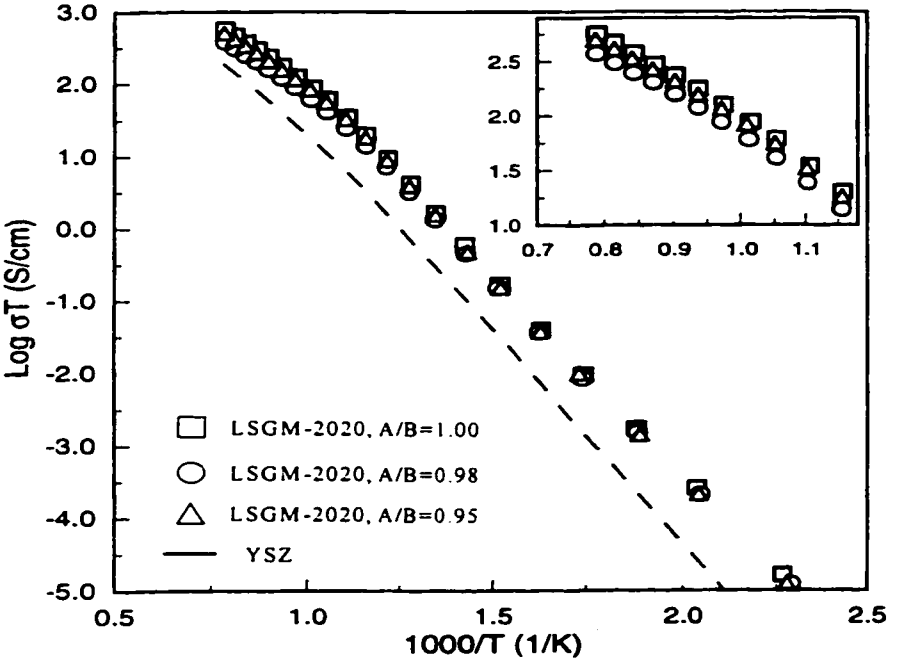

Fig. 5.15 Electrical Conductivity of LSGM-2020 as Functions of A/B Ratio and Temperature

5.3 SINTERING BEHAVIOUR

All LSGM materials made by GNP combustion synthesis could be sintered to very high densities (> 95% theoretical density with negligible porosity) at temperatures of 1400 to 1500°C for 2 hours. Thermal analysis showed that there is approximately 17% weight loss for as-received ash (c.f. section 5.1.3 and Fig. 5.2) during sintering above 1300°C for 2 h, while the weight loss of compacts made from calcined (@ 650°C for 1 h) powders is about 5%. The influence of sintering temperature and doping content on density is presented in Fig. 5.16. In general, the density increases with sintering temperature (up to 1500°C) but decreases with doping content. For each composition, the maximum sintered density is obtained at 1500°C. Undoped $LaGaO_3$ has the highest sintered density. Detailed morphology study shows that pores are less than 1 μm in diameter and found at

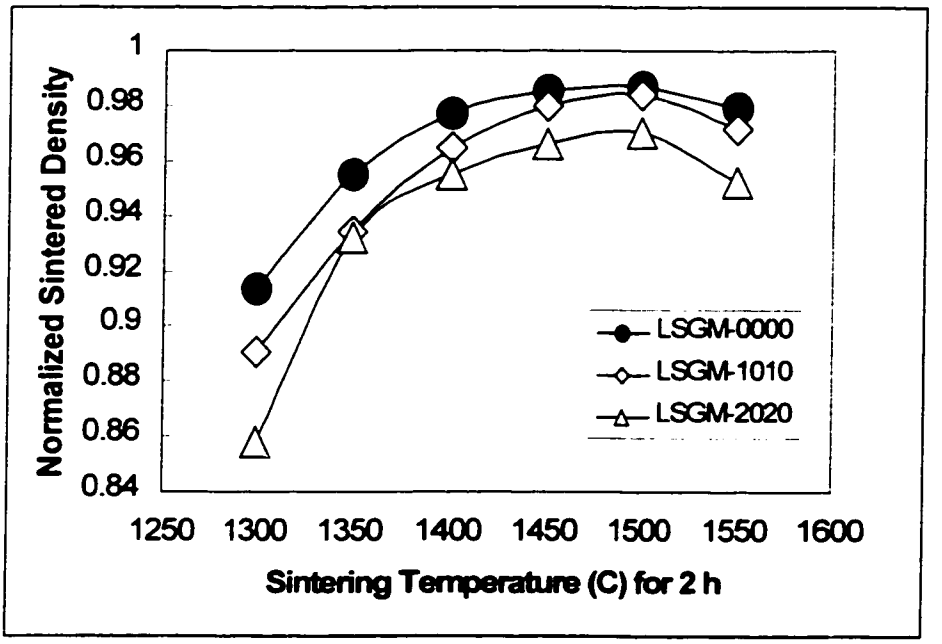

Fig. 5.16 Sintered Density of LSGM Materials as Function of Temperature

both the grain boundaries and inside the grains. The average grain sizes, estimated from SEM micrographs of polished and thermal etched samples, by using the linear intercept technique,[92] are less than 10 μm when sintering temperature is less than 1500°C, and less than 20 μm when sintering temperature is higher than 1500°C. The average grain size. as function of sintering temperature and A/B cation ratio is shown in Fig. 5.17. We have found two-correlation in these sintered samples: the average grain size increases with sintering temperature and the average grain size tends to be smaller as A/B ratio decreases below unity or increases above unity.

The effect of doping on grain size depends on the level of doping and sintering temperature. For low sintering temperatures (1400°C), the micrograph obtained from

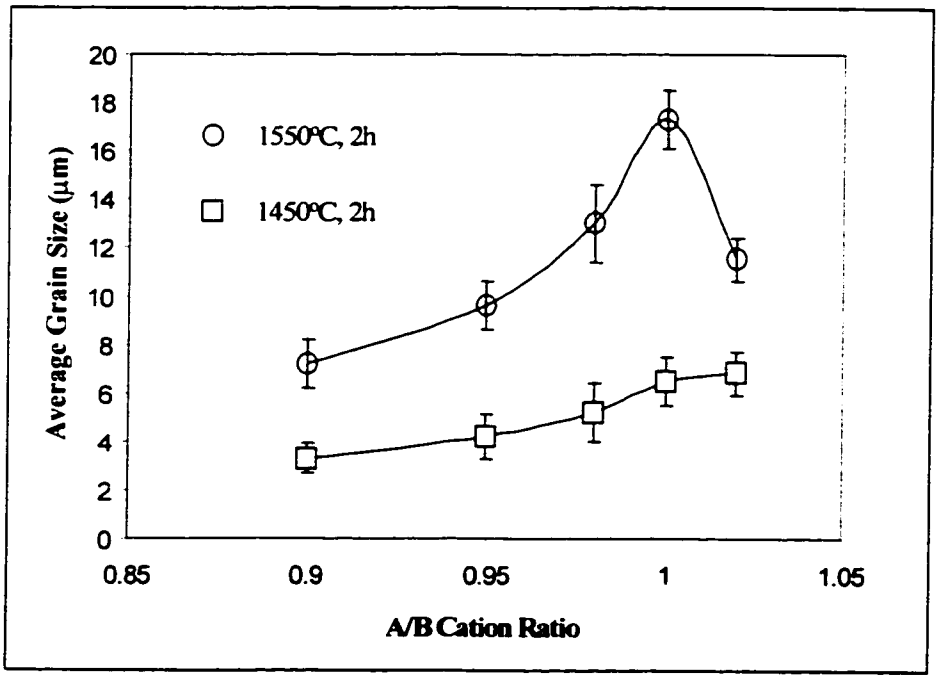

Fig. 5.17 Average Grain Size (μm) of sintered LSGM Perovskites

thermally etched samples are shown in Fig. 5.18. The top micrograph is for the undoped material, the middle one for the 10 mol% doped and the bottom one for 20 mol% doped. For this case, the undoped samples has the largest grain size and the 10 mol% doped the finest grain size. If the sintering temperature is increased to 1500°C, the undoped samples has the smallest grain size and the 20 mol% doped samples has the largest grain size (Fig. 5.19). We believe that these observations can be explained by noting that doping introduces both crystalline and amorphous secondary phases. For the 10 mol% doped samples, sintered at 1400°C, the effect of the crystalline secondary phases dominate and they pin the grain boundaries leading to finer grain size (compared to the undoped sample). However, when the doping level increases to 20 mol%, the volume of the liquid phase increases and these samples has a higher grain size than the 10 mol% doped samples but still less than the undoped samples. For samples sintered at 1500°C, the amorphous phases have a higher volume fraction (compared to 1400°C samples at any doping level) and as a result, the grain size increases as doping level increases. Evidence of crystalline secondary phases for the 1400°C sintered samples is provided in Fig. 5.20. We do not have direct evidence of amorphous secondary phases.

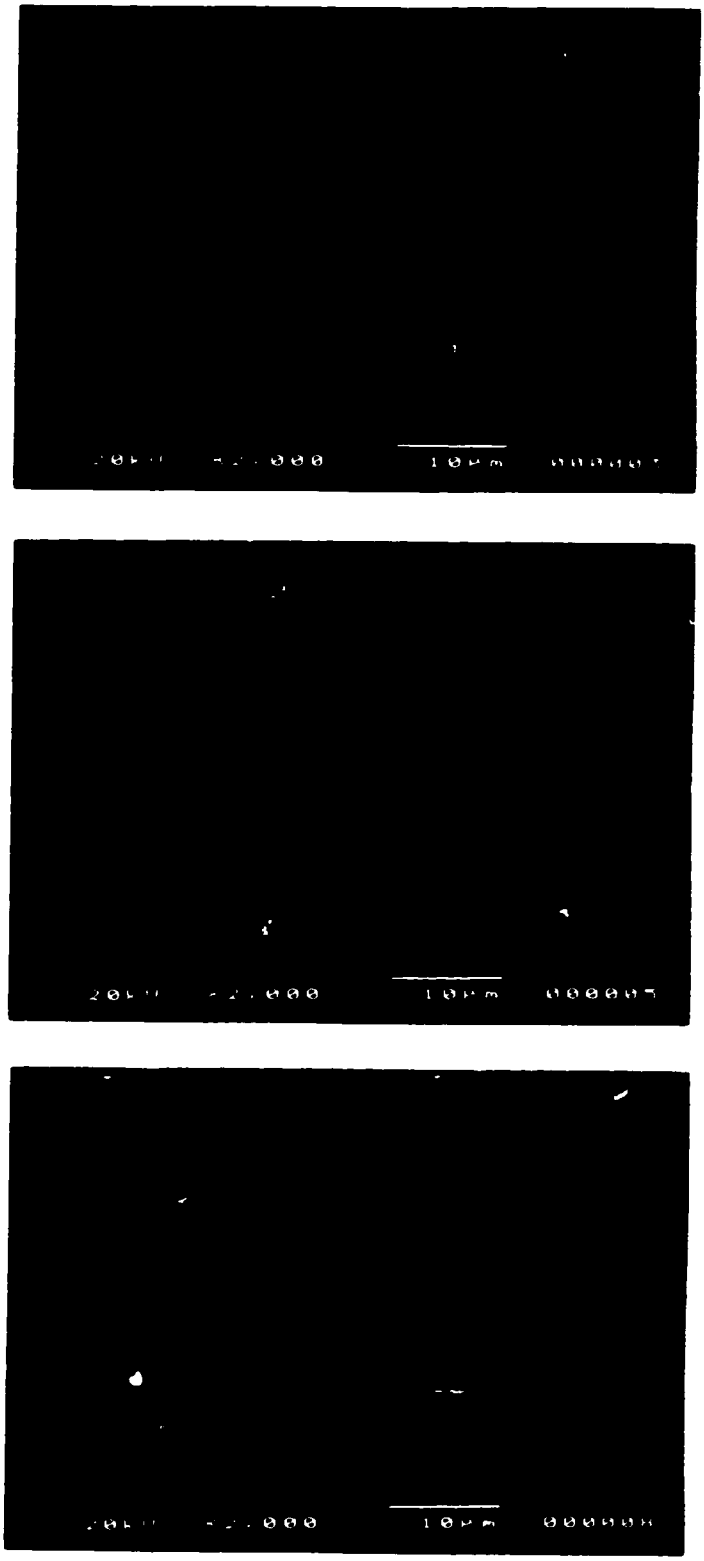

Fig. 5.18 Morphology of LSGM-0000 (top), 1010 and 2020 (bottom) at 1400°C/2h

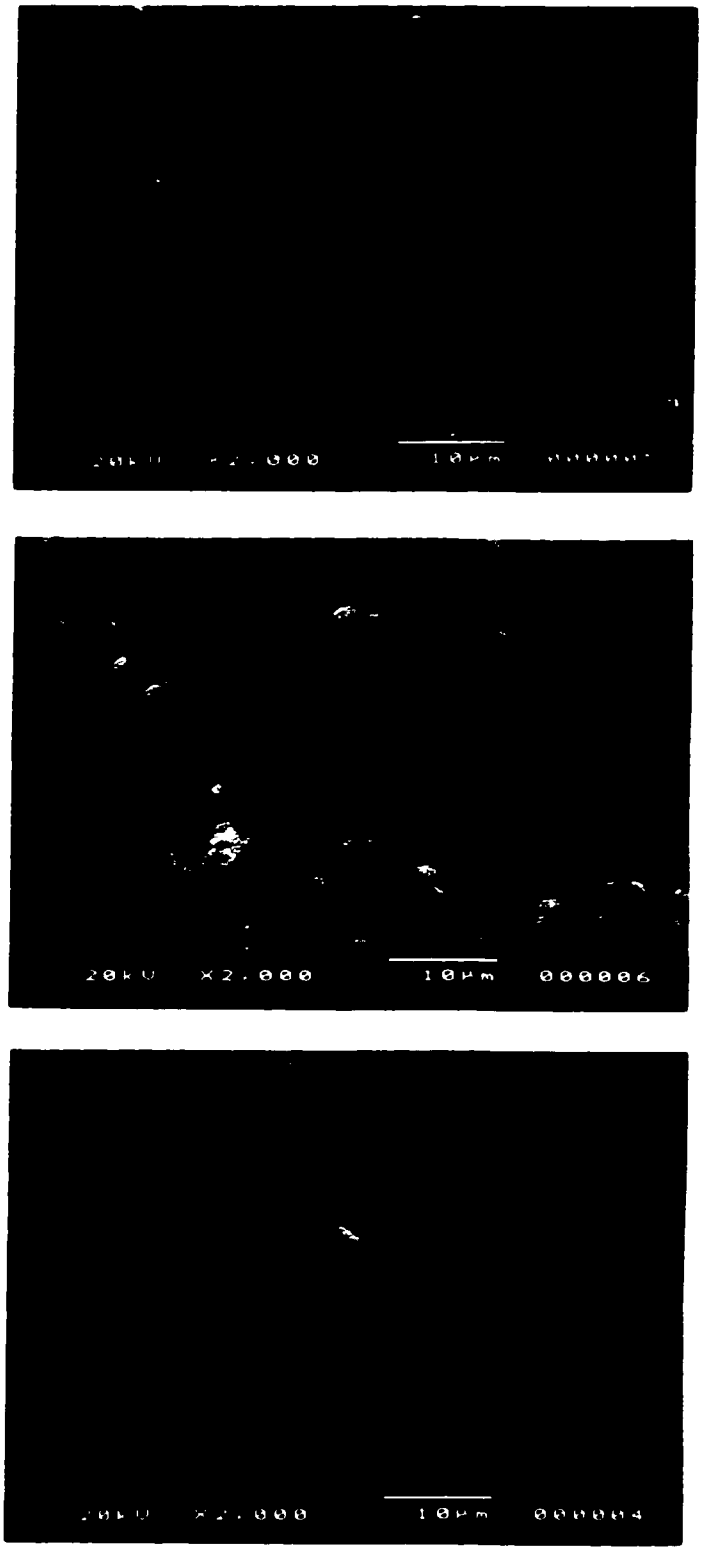

Fig. 5.19 Morphology of LSGM-0000 (top), 1010 and 2020 (bottom) at 1500°C/2h

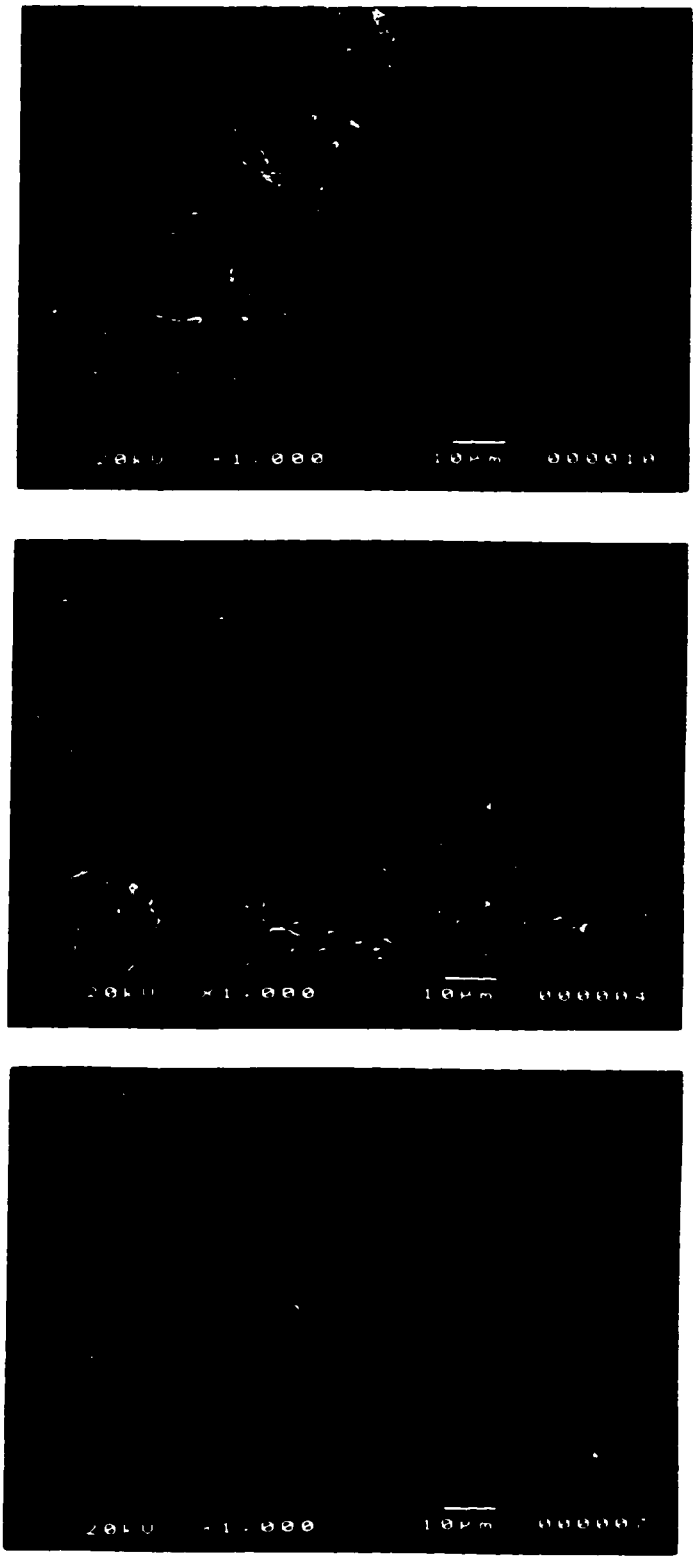

Fig. 5.20 Two-phase Region in LSGM-0000 (top), 1010 and 2020 (bottom) at 1400°C/2h

CHAPTER 6

DISCUSSION

The structure changes of LSGM perovskites have been studied systematically as functions of temperature, doping content, and A/B cation ratio. The experimental results were presented in the previous chapter. In this chapter, we will analyze the results in order to provide a reasonable hypothesis to answer the fundamental question as to why LSGM materials demonstrate superior oxygen-ion conductivity compared to the conventional YSZ electrolyte. Discussion will be focused on lattice structure change as a function of doping, A/B cation ratio and heat treatment. In the end, we will compare the electrical conduction mechanism dominating in LSGM perovskites and in YSZ. In addition, the effect of doping on the phase stability will also be considered.

6.1 PHASE STABILITY OF LSGM PEROVSKITES

Unlike porous electrode material (see section 2.5 and references cited thereby for detailed discussion), the electrolyte must be dense to prevent gas diffusion and crossover in SOFC. In addition, the operating conditions for the electrolyte are more severe than for electrode materials. The electrolyte has to function well under both oxidizing and reducing environment with no gas diffusion to assure that the conduction is only by oxygen-ion transfer from cathode to anode. Before the discovery of LSGM, cubic YSZ was the only known material to meet such requirements (see section 2.5.3). The commonly used YSZ electrolyte has a composition of 8 ~ 10 mol% Y_2O_3[28] and adopts a

fluorite structure (space group Fm-3m). The room temperature lattice constant of 10 mol% Y_2O_3 doped ZrO_2 (YSZ-10) is 5.1486 Å.[93] Oxygen vacancy (or O^{2-} ion) is transferred from one tetrahedron (formed by 4-nearest cations) to another tetrahedron via an octahedron (formed by 6-cation ions), as shown in Fig. 2.27. At 1000°C, the oxygen-ion conductivity is maintained at 0.1 S/cm, which is required for SOFC operation.[28,32,94,95]

The Sr and Mg doped perovskite $LaGaO_3$ (LSGM) has oxygen-ion conductivity superior to that of YSZ (c.f. Fig. 2.28 in section 2.7 and Table 5.4 and Figs. 5.18 to 5.20 in section 5.3). Due to the desire to lower the operating temperature of SOFC, substantial efforts have been put into the development of this potential electrolyte material. In spite of the fact that several studies have been focused on the electrical conductivity of LSGM and shown that the conductivity is indeed very high, there is no theoretical explanation available. To fill this gap, we propose a qualitative model to couple the measured electrical conduction data with crystal structures and try to depict why LSGM electrolyte should demonstrate high oxygen-ion conductivity.

6.1.1 Perovskite Structure Stability

Like fluorite, the perovskite structure is of cubic symmetry. For an ideal cubic perovskite, one can calculate its lattice parameter by adding the B-site cation and anion together, as they form the basic skeletal (B-O-B) of the octahedron (six anion ions occupying the corner positions with one B-cation at the center) which stabilizes the cubic structure. Fig. 6.1 shows the structure of an ideal cubic perovskite. For the LSGM perovskite, the atom positions in an ideal cubic structure and one of its common distortions, the

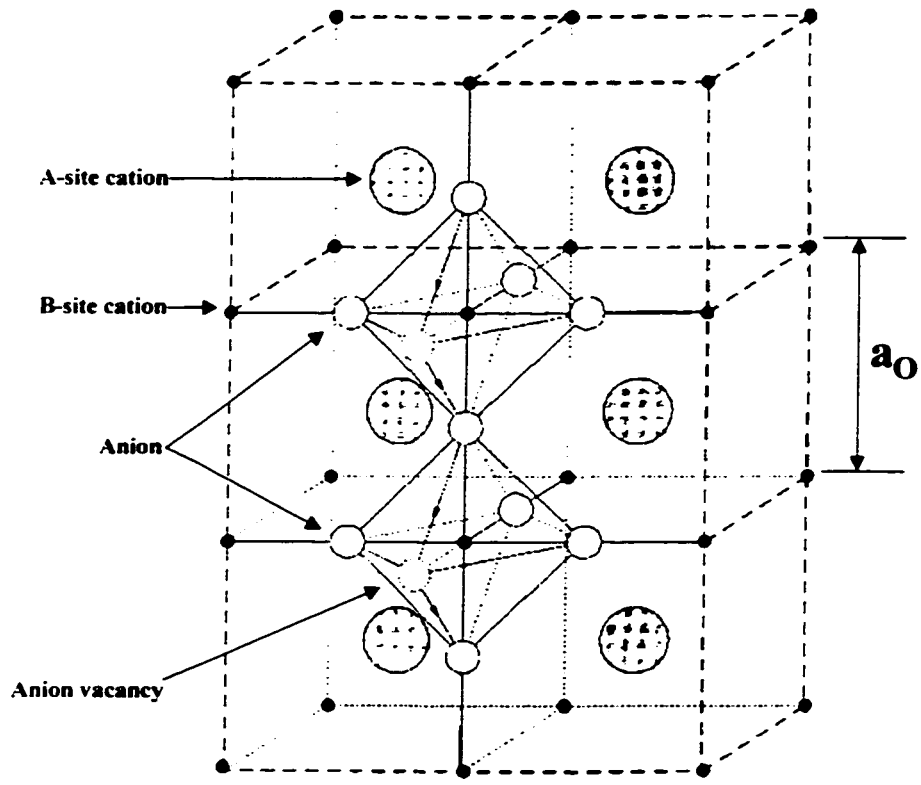

Fig. 6.1 The Ideal Perovskite Structure ABO_3

orthorhombic symmetry, are shown schematically in Fig. 6.2. Taking ionic radii into consideration, Goldschmid[96] defined the tolerance factor as:

$$t = \frac{(r_A + r_O)}{\sqrt{2}(r_B + r_O)} \tag{6.1}$$

where r_A, r_B and r_O are the ion radii of the A-, B-site cation and oxygen ion, respectively. For an ideal cubic perovskite, t = 1, as required by geometry. Any deviation from unity in Eq. (6.1) would cause structural distortion.

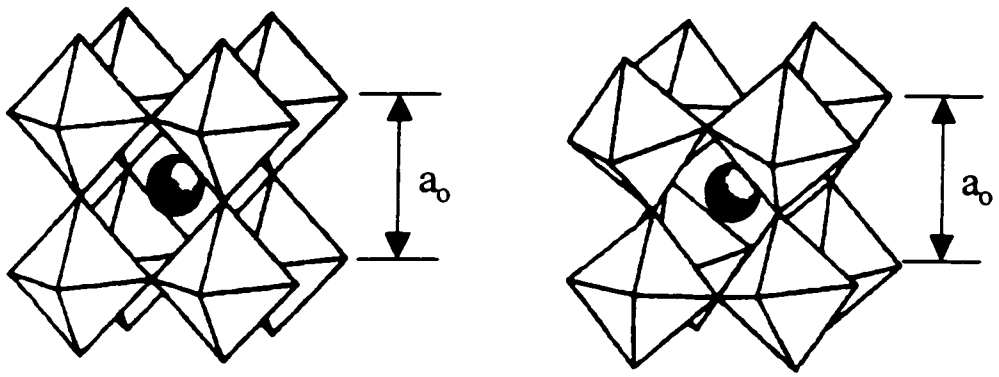

a) Cubic perovskite *b) Orthorhombic perovskite*

Fig. 6.2 Crystal Structure of the LSGM Perovskite. (The black dot represents the A-site cations (La^{3+} or Sr^{2+}). The anions (O^{2-}) occupy the corners of the octahedra while the B-site cations (Ga^{3+} or Mg^{2+}) are located in the center of the octahedra).

We can compute the tolerance factor for the LSGM perovskites using ionic radii of Shannon.[97] The data adopted and used in this study are listed in table 6.1. For pure $LaGaO_3$, t = 0.966. For doped LSGM, an averaged cation radius was used for this calculation. Consequently, t = 0.964 was computed for 0.1 mole doped LSGM-1010 and, similar, t = 0.962 for 0.2 mole doped LSGM-2020. Goodenough and Longo[98] have pointed out the perovskite structure may only occur within the range of $0.75 < t < 1.00$, providing $r_A > 0.90$ Å and $r_B > 0.51$ Å. For LSGM system, these three conditions are satisfied such that the perovskite structure is indeed a reality. However, since the tolerance factor is shifted away from unity with doping, more distortion is expected.

Table 6.1 Effective Ion Radius in LSGM System*

Species	La^{3+}	Sr^{2+}	Ga^{3+}	Mg^{2+}	O^{2-}
Radius (Å)	1.36 (XII)	1.44 (XII)	0.62 (VI)	0.72 (VI)	1.40 (VI)

** The coordination number of the ions of interest is given in Roman number*

6.1.2. Saddle Point Dimension Calculation

Earlier studies on fast ion conductors indicated the migration of the anions via a vacancy mechanism takes place along <110> edges of the anion octahedron in perovskite compounds.[99-101] The oxygen ion transfer paths in the LSGM perovskite are depicted in Fig. 6.3, showing that the edges of the octahedron are the optimized conduction path (c.f. Fig. 2.27 for YSZ). The two adjacent A-sites (occupying the body center positions) cations and one B-site (at the corner) cation produce a triangle on the (110) plane. When an anion migrates to a point midway between them, it fills the gap of size r_C which is confined by the three nearest neighbor cations as shown in Figure 6.4, and a saddle point configuration is established. This is the largest opening available between the cations in perovskite. The anion may pass along any of the <110> edges of the octahedron depending on where a vacancy is available. By migrating through the saddle-point opening, anions behave as charge carriers and provide the electrical conduction (with the desired fast ionic conductivity). The dimension of this saddle point, defined as the critical radius (r_C), relative to the size of the anion, is a measure of the ease of anion diffusion.

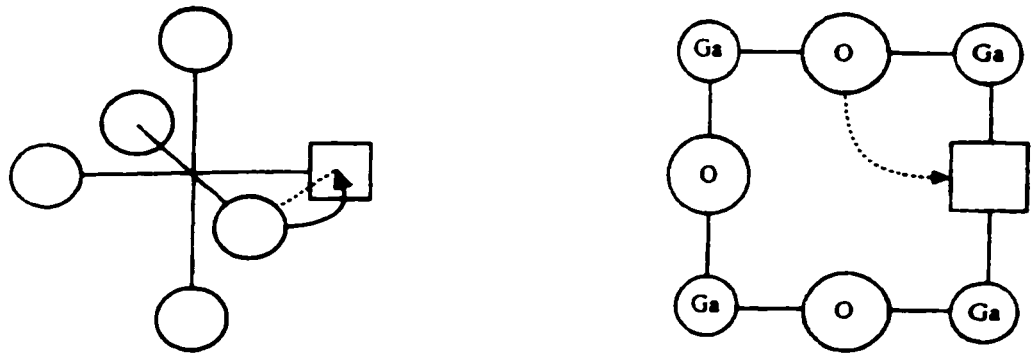

a) GaO_6 octahedron *b) [Ga-O] ab-plane*

Fig. 6.3 The Oxygen Migration Paths in Perovskite

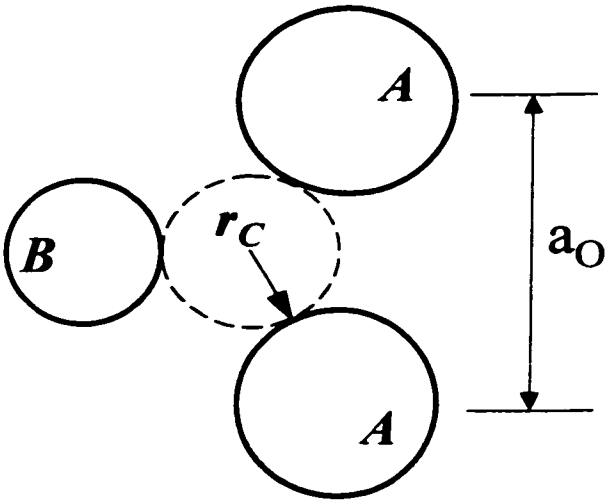

Fig. 6.4 Saddle-point Configuration of Anion Migration in Perovskite

The value of r_C will affect the activation energy of the diffusing species. From Fig. 6.4, using simple geometric relation, the critical radius r_C can be expressed as:

$$r_C = \frac{\left(\frac{3}{4}a_0 - \sqrt{2}r_B\right)a_0 - (r_A + r_B)(r_A - r_B)}{2(r_A - r_B) + \sqrt{2}a_0} \qquad (6.2)$$

with a_O, r_A, and r_B being the cubic (or pseudo-cubic) lattice constant, radius of A and B cation respectively.

In the LSGM system, the r_C is the opening between two La^{3+} (Sr^{2+}) cations and one Ga^{3+} (Mg^{2+}) cation along the <110> edge of the GaO_6 octahedron, as shown in Fig. 6.5. The value of r_C represents the available opening along the path of O^{2-} ion migration. Theoretically, regardless of the structure of the oxides, the bigger the opening, the easier the O^{2-} ion migration. The energy barrier for O^{2-} ion migration is expected to be inversely

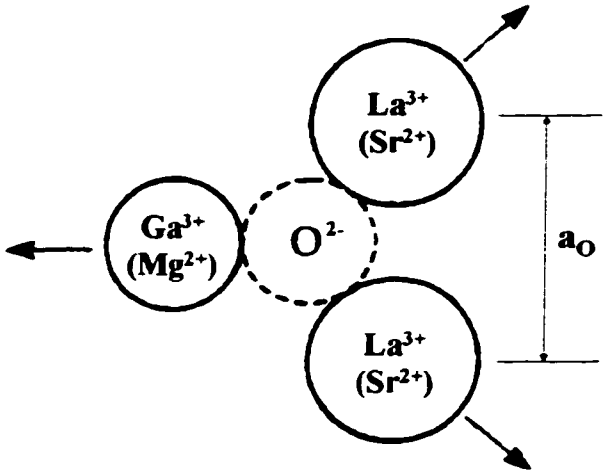

Fig. 6.5 Saddle-point Opening in LSGM Perovskite

proportional to the opening size (r_C). A higher O^{2-} ionic conduction maybe expected from a material with larger saddle-point opening. Based on an oxygen-ion radius, a saddle-point opening (diameter) of 2.80 Å should facilitate the highest oxygen-ion conduction for a material when other factors are equal. However, the r_C values of known ionic conductors are less then 1 Å (r_C = 0.9803 Å for YSZ-10[93], for example) while the oxygen ion radius is 1.40 Å.

6.1.3. Lattice Free Volume and Packing Factor Calculation

In addition to the saddle-point dimension, there must be a certain free space (volume) available in the lattice in order to conduct oxygen ions. We define the lattice free volume, V_f, as the unit cell volume minus the volume of each constituent ion.

$$V_f = V_C(\textit{unit cell volume}) - \sum V_i(\textit{volume of constituent ion}) \qquad (6.3)$$

Utilizing a vacancy mechanism, oxygen-ion migration takes place through the unoccupied volume in the unit cell such that the V_f ought to be another parameter to be considered in studying electrolyte materials and their ionic conductivity. In a similar fashion, packing factor may influence the oxygen-ion conductivity. We can define lattice packing factor, c_i, as the ratio of the summation of the volume of constituent ions to the volume of unit cell, i.e.,

$$c_i = \frac{\sum V_j}{V_C} = \frac{V_C - V_f}{V_C} \tag{6.4}$$

where j represents each individual ion, c represents unit cell. Note the relation between lattice free volume V_f and the packing factor c_i. The well-known YSZ-10[93] has a packing factor close to 0.74 with more than one quarter (26.32 vol%) of its unit lattice space being free. For pure $LaGaO_3$, if it is in an ideal condition of cubic symmetry such that $a_o = 2(r_{Ga}^{3+} + r_O^{2-}) = 2(0.62 + 1.40) = 4.04$ Å, the packing factor is about 0.69 which gives more than thirty percent of free lattice space (30.82 vol%). However, the measured data, from various sources (includes this study) with different sample preparation methods, showed a lower symmetry (than cubic) with a pseudo-cubic lattice value of approximation 3.89+ Å (c.f. Chapter 2 and Table 6.2 later). In this case, the corresponding packing factor is about 0.77 with less lattice free space (22.51 vol%). More detailed structure analysis showed that, in reality, the structure of the $LaGaO_3$ deviates from the cubic structure ($a_o < 4.04$ Å) by tilting and rotating the GaO_6

octahedra.[98] This is true for doped $LaGaO_3$ where the distortion is even bigger. Our X-ray and neutron diffraction study supports this understanding.

6.2. CRYSTAL STRUCTURE ANALYSIS OF THE PEROVSKITES

In order to calculate r_C, V_f, and c_i as a function of doping, A/B ratio and temperature, we need the lattice constants and structural information. This was done by analyzing the X-ray and Neutron diffraction data presented in Fig. A-1 to A-23 in Appendix I, using JADE and/or GSAS. The procedure used for analysis is the following.

In JADE, the X-ray diffraction intensities were determined from observed peak heights after background subtraction. In addition, the reported experimental intensities were corrected to the fixed-slit approximation using the $1/\sin\theta$ function resident in the X-ray powder diffraction pattern processing code JADE 2.1 & 3.1 (Materials Data, Inc., MDI, Livermore, CA). In its DOS version (JADE 2.1), the 2θ error-corrected experimental d-spacing was indexed using the Louer algorithm-based code included in Micro-INDEX, Ver. 2.0. The hkl-space search was limited to maximum lattice parameter of a = 10, b = 10 and c = 10 Å, with input unit cell volume of 4000 $(Å)^3$. The solutions from indexing were a ~ 5.5+, b ~ 5.4+ and c ~ 7.7+ Å for orthorhombic perovskite (cf. $LaGaO_3$, PDF 24-1102). The lattice parameters resulted from indexing and the 2θ error-corrected experimental d-spacings were input to the Appleman-Evans algorithm-based, auto-indexing cell refinement program resident in Micro-CELLREF, Ver. 2.0. The refinement code was executed in three least-squares cycles to reach convergence with an input 2θ-error limit of 0.03°. In Windows version (JADE 3.1), the above mentioned procedures

were incorporated into a main operating window, where all necessary calculations and refinements were performed in the program, provided correct structure data (compound, space group, and lattice constants) were available as input for the program. In GSAS, estimated lattice constants, atom positions and space group information are required as initial input into the program. The GSAS program can then refine these parameters gradually until converge is reached based on least square fitting.

The calculated room temperature lattice constants, space group and unit cell volume of the LSGM materials are given in table 6.2 as a function of doping content and A/B cation ratio. It is found that the effect of A/B ratio on lattice constants is negligible. However, doping has strong influence on structure changes. There is a phase transition from orthorhombic to monoclinic when doping level increased from 0.1 mole to 0.2 mole (see Fig. 5.1 for detail). Structural analysis shows the crystallographic relationship between the monoclinic structure and the orthorhombic symmetry is $(001)_{Mono}//(100)_{Orth}$ & $<001>_{Mono}//<100>_{Orth}$. Fig. 6.6 shows the geometrical relationships between different unit cells in perovskite. The ideal perovskite structure is shown by a shadowed cube in the upper-left corner of Fig. 6.6. The orthorhombic (Pbnm) and/or monoclinic (I2/a) perovskite is illustrated in the middle of the drawing by solid lines. The hexagonal-rhombohedral perovskite is presented in dash lines. The size and shape of orthorhombic or monoclinic cell are close to four times that of the ideal cubic, while the hexagonal-rhombohedral (R3c) perovskite is approximately six times the cubic cell size.

*Table 6.2 Lattice Parameters Change vs. Composition in LSGM Perovskite (in Å)**

LSGM		A/B Cation Ratio				
Doping	Parameters	0.95	0.98	1.00	1.02	1.05
0.0	a	5.524311(52)				
	b	5.492413(62)				
	c	7.774804(91) Å				
	vol.	235.902(4) $Å^3$				
	a_0	3.8924 Å				
	space gp	Pbnm				
0.1	a	5.537241(71)				
	b	5.506648(80)				
	c	7.803778(114) Å				
	vol.	237.950(5) $Å^3$				
	a_0	3.9037 Å				
	space gp	Pbnm				
0.2	a	7.817197(617)				
	b	5.534872(840)				
	c	5.535661(936) Å				
	β	89.89530(86)				
	vol.	239.512(18) $Å^3$				
	a_0	3.9122 Å				
	space gp	I2/a				

** Samples were sintered at 1500°C in air for 9 hours (a_0 is pusdo-cubic lattice constant)*

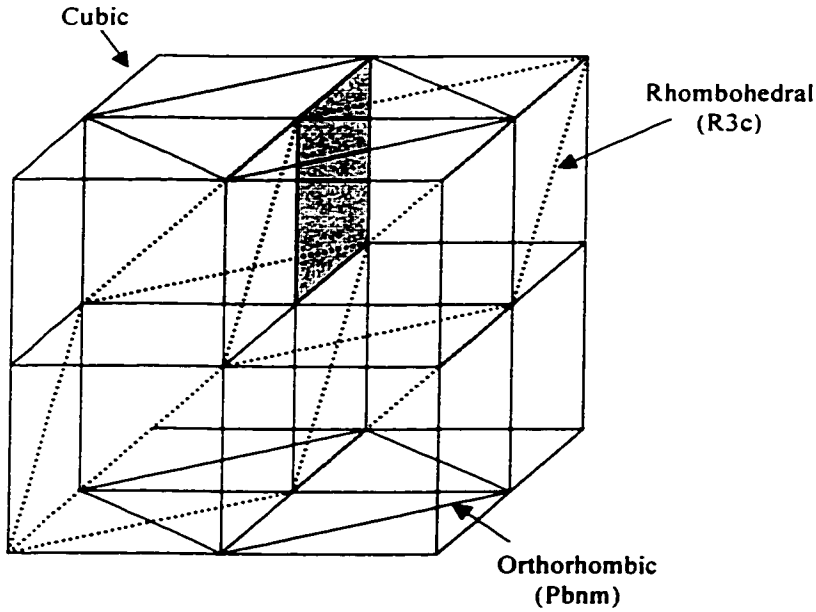

Fig. 6.6 Schematic View of the Geometry for Various Unit-cells in Perovskite

For the sake of comparison and saddle point dimension calculation, the pseudo-cubic lattice constant a_0 has been computed by converting the orthorhombic and monoclinic perovskite into cubic structure. The results are reported in table 6.2. From table 6.2 we see clearly that the pseudo-cubic lattice constant increases with doping content, which is a desirable fact in LSGM system as the saddle-point size is less than the size of oxygen ion, the conducting species. We want to reduce the size difference between O^{2-} ion and the available conduction path opening by increasing doping level. Based on the data presented in table 6.2 and the ionic radii in table 6.1, the value of the saddle-point dimension (Eq. 6.2) and lattice free volume (Eq. 6.3) with respect to the change in the A/B cation and doping content can be calculated. The results are summarized in table 6.3 and presented in Fig. 6.7 and 6.8 respectively. The saddle-point size (r_C) increases with doping but it is independent of non-stoichiometry. The lattice free volume (V_f) increases with doping and off-stoichiometry. The undoped stoichiometric $LaGaO_3$ has a minimum lattice free volume.

It is of interest to discuss the computation of the saddle-point size. If only the host cations

*Table 6.3 Saddle-point (r_C, Å) and Lattice Free Volume (V_f, Å^3) in LSGM Material**

LSGM		A/B cation ratio				
Doping	Opening	0.95	0.98	1.00	1.02	1.05
0.0 (mole)	r_C	0.928				
	V_f	56.886	53.553	51.331	52.771	54.829
0.1 (mole)	r_C	0.934				
	V_f	62.868	59.580	57.388	58.779	60.767
0.2 (mole)	r_C	0.939				
	V_f	68.364	65.121	62.959	64.302	66.219

** The cell volume values are taken from table 6.2*

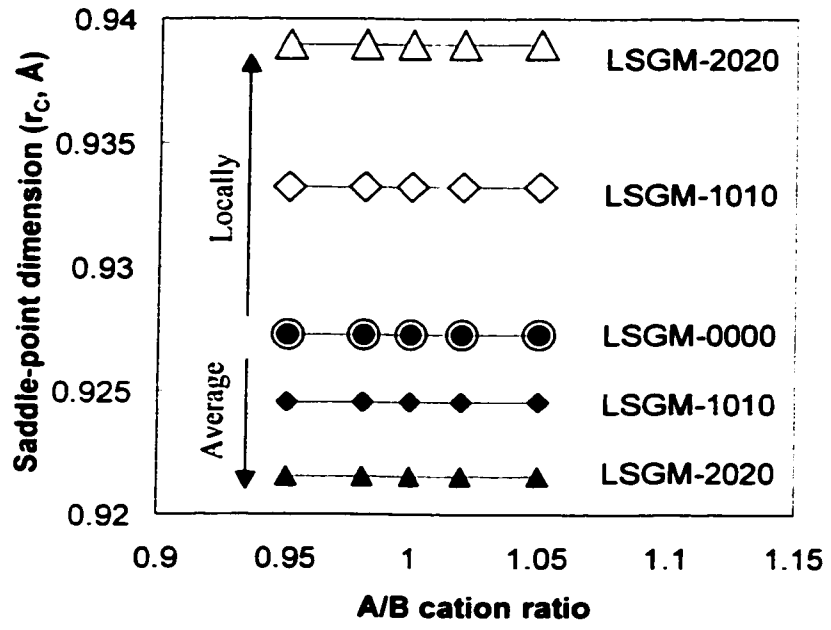

Fig. 6.7 The Calculated Saddle-point Dimension (r_C) in the LSGM Perovskite

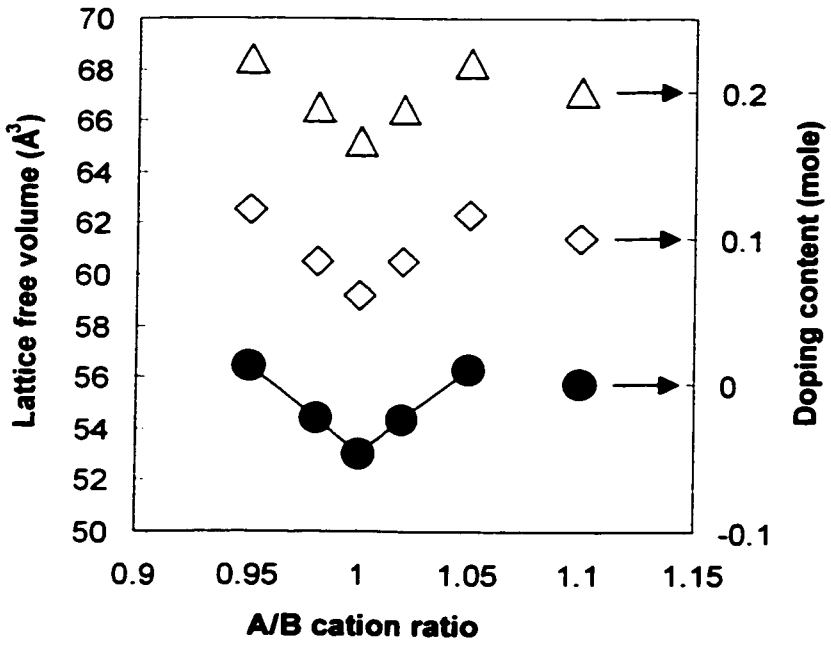

Fig. 6.8 The Calculated Lattice Free Volume (V_f) in the LSGM Perovskites

(La^{3+} and Ga^{3+}) are considered for saddle-point configuration (designated as locally in Fig. 6.7), then the saddle-point size increases with doping (Sr^{2+} and Mg^{2+}). This can be explained by noting that the lattice will undergo expansion when the sizes of dopants are bigger than that of hosts (this is the case in the LSGM system). Consequently the size of the saddle-point is increased. However, if we average the host cation sizes with those of the dopants and use them in Eq. 6.2 for r_A and r_B to calculate r_C (saddle-point size), the opposite result is obtained. The saddle-point size decreases as the doping level increases. This is shown in Fig. 6.7 by the data points labeled "average". Being a first approximation based on statistical study, the effect of doping on saddle-point size is negligible if doping level is low. Table 6.4 summarizes the probability of forming the cation-triangle from various combinations of cations. In reality, since the majority of cations are those of the host matrix, it is reasonable to only use the host cation sizes (indicated as locally) for low doping systems used in this study. The saddle-point sizes calculated by both methods are presented together in Fig. 6.7 for comparison. The lattice free volume behaves rather simply and the trend is very clear. Both the doping and the off-stoichiometry (A/B ratio different than 1) increase the lattice free volume as shown in

Table 6.4 Probability of Forming Saddle-point from Cations by Statistical Data

Probability			
Doping level (mole)	0	0.1	0.2
All cations from host	1	0.729	0.512
One cation from doping	0	0.243	0.384
Two cations from doping	0	0.027	0.096
Three cations from doping	0	0.001	0.008
Total	1	1	1

Fig. 6.8. Using the data in table 6.2 we can calculate packing coefficients for LSGM perovskites as a function of doping and A/B cation ratio (using Eq. 6.3). The data is listed in table 6.5 and plotted in Fig. 6.9. The packing factor decreases as doping level increases and the composition deviates from stoichiometry.

*Table 6.5 Packing Factor Change in the LSGM Material**

LSGM	A/B Cation Ratio				
Doping (mole)	0.95	0.98	1.00	1.02	1.05
0.0	0.759	0.773	0.782	0.776	0.768
0.1	0.736	0.749	0.759	0.753	0.745
0.2	0.715	0.728	0.737	0.732	0.724

** The cell volume values are taken from table 6.2.*

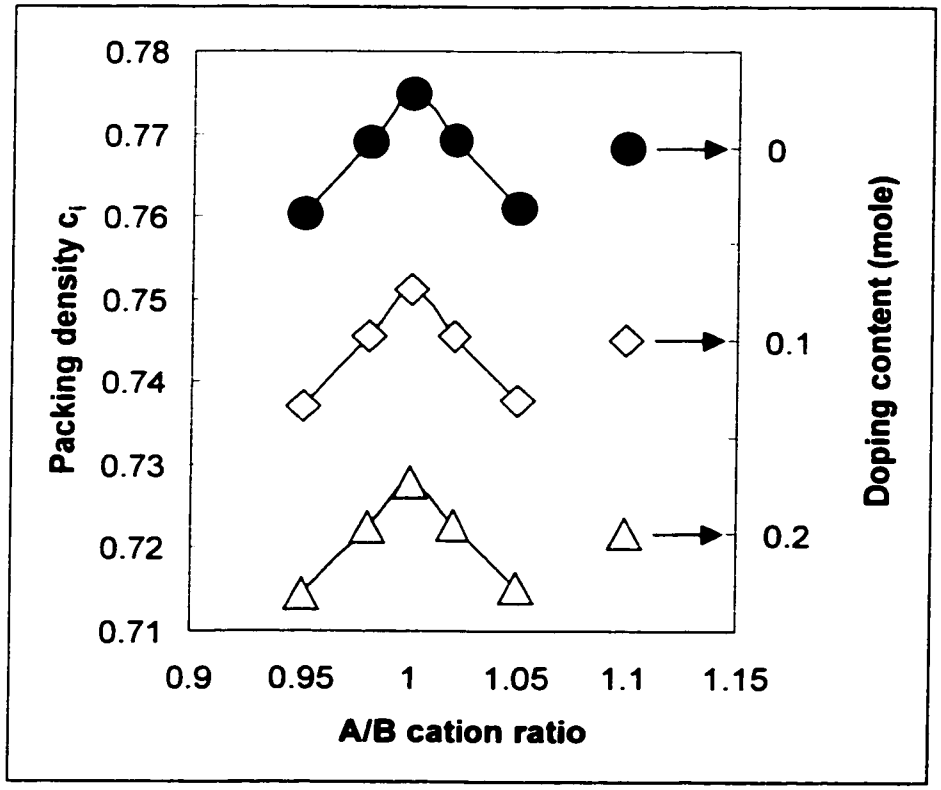

Fig. 6.9 The Calculated Packing Factor (c_i) in the LSGM Perovskites

Note, it is possible to tailor the lattice parameters (V_f and c_i) for LSGM perovskites such that the conditions for oxygen-ion conduction is close to or even more favorable than that in YSZ by changing doping content and varying A/B cation ratio.

Upon heating, undoped $LaGaO_3$ undergoes a phase transition from orthorhombic (Pbnm 62) to rhombohedral symmetry (R3c 161) at 147 ± 2°C (see Fig. 2.30 to 2.35 and section 5.1.3 for details). The crystallographic relationship between hexagonal- rhombohedral (R3c) and orthorhombic (Pbnm) perovskite is $(110)_{Rhom}//(100)_{Orth}$ & $<110>_{Rhom}//<100>_{Orth}$. The pictorial views and explanation can be found in Fig. 6.6. The structure of doped LSGM materials is stable from room temperature to elevated temperature (Pbnm for LSGM-1010, I2/a for LSGM-2020). For the purpose of examining the effect of temperature on oxygen-ion conduction, we have calculated the pseudo-cubic lattice constant (a_O) followed by the saddle-point dimension (r_C) as a function of temperature, doping and A/B ratio. Table 6.6 and Fig. 6.10 present the pseudo-cubic lattice constant (based on data from Fig. A-4 to A-23 in Appendix I). Using data from table 6.6 and Eq. 6.2, the "local value" of r_C has been calculated as a function of temperature and doping level. The results are presented in Fig. 6.11. Note that the saddle-point size increases as temperature increases for all compositions.

Table 6.6 The Pseudo-cubic Constant (a_O) Varies with Doping Content and Temperature

LSGM	Temperature (°C)						
Doping (mole)	27	200	400	600	800	1000	1200
0.0	3.8924	3.8931	3.8959	3.8989	3.9021	3.9052	3.9082
0.1	3.9037	3.9046	3.9079	3.9110	3.9145	3.9182	3.9218
0.2	3.9122	3.9153	3.9188	3.9218	3.9248	3.9278	3.9306

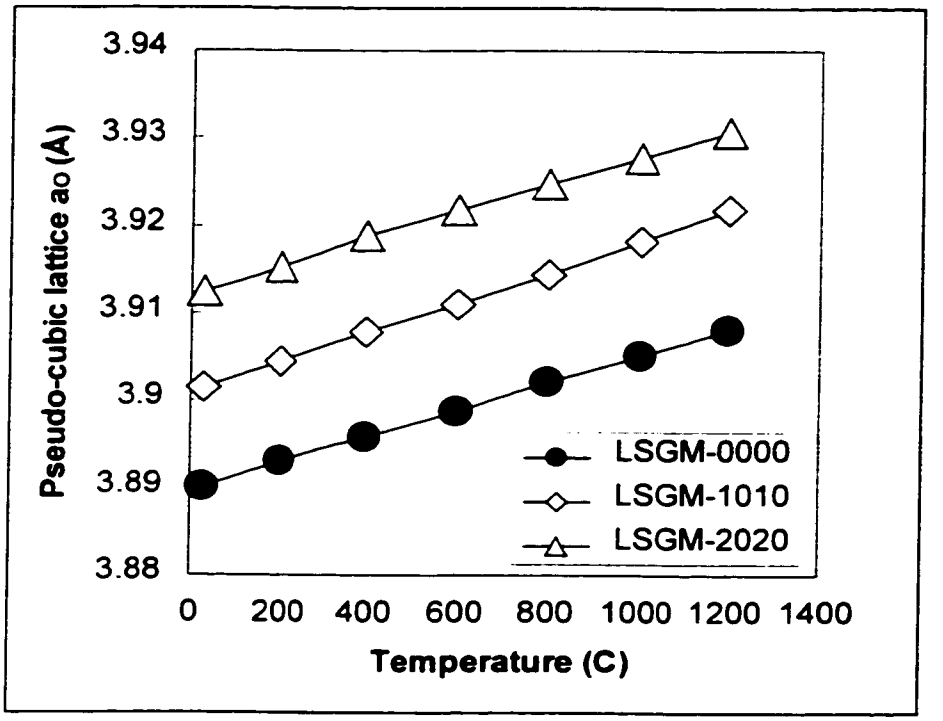

Fig. 6.10 The Pseudo-cubic Size Change as a Function of Temperature for LSGMs

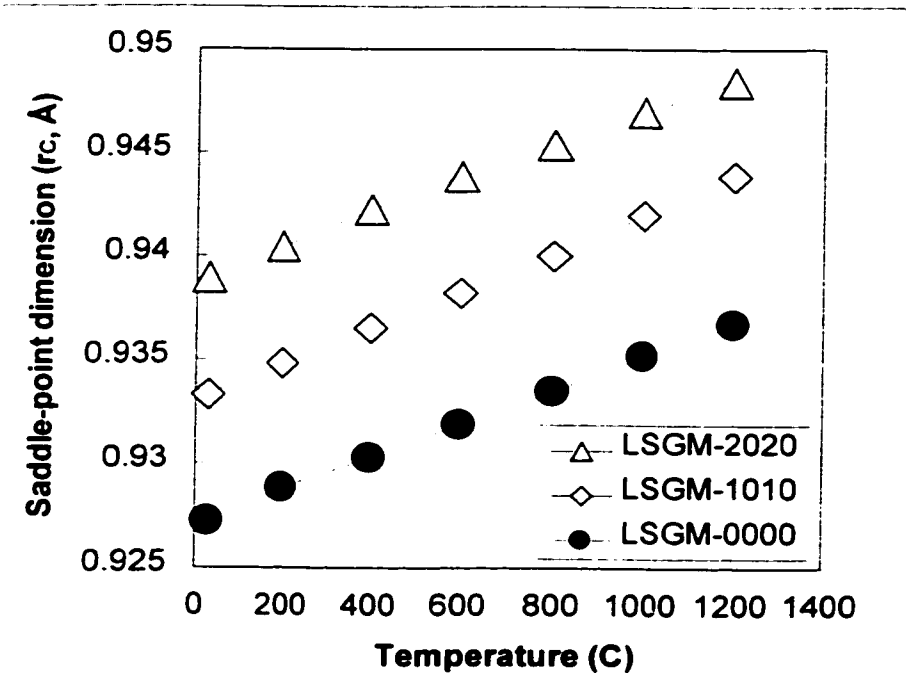

Fig. 6.11 The Saddle-point Size Change as a Function of Temperature for LSGMs

6.3 ATOM COORDINATES OF THE PEROVSKITES

Rietveld full-profile refinement[90] on room temperature X-ray diffraction data for stoichiometric LSGM-0000, LSGM-1010, and LSGM-2020 and high temperature neutron diffraction data for LSGM-1010 at 27, 300, 600, 900 and 1100°C were performed using GSAS (General Structure Analysis System, Los Alamos National Laboratory).[91] Literature data[61,84] were used as input for initial calculation to test the program and convergence was achieved but with large error. The lattice constants and atom positions were allowed to be refined later and the fitting improved significantly. The refined parameters are given in table 6.7 and 6.8. In these two tables, structural equivalent atom/ion positions are given as fraction in 3-dimentional Cartesian axes x, y, z. Site occupancy is assigned based on defect chemistry (as fraction). Space group is obtained by profile fitting. Lattice constants are labeled as a, b, c in Å. The numbers in brackets are calculated sigma as usual. The χ^2 is the term of goodness-of-fit, which indicates the quality of data analysis. In an ideal case, the χ^2 value should approach unity but a larger value (often above 3) is cited and reported in literature probably due to the difficulty of data fitting. In short, the GSAS program can produce many sets of results, depending on what we are looking for to decide how good χ^2 should be. The remaining parameters, such as size occupancy, lattice orientation, thermal coefficients, etc., are all assumed constant for simplicity.

Table 6.7 Refined Structural Parameters of LSGM from Room Temp. X-ray Data

Atom	Parameter	LSGM-0000	LSGM-1010	LSGM-2020
La/Sr	x	-0.003486	-0.002032	0.25
	y	-0.017094	0.003097	0.000049
	z	0.25	0.25	0
	Site occup.	1.0/0.0	0.9/0.1	0.8/0.2
Ga/Sr	x	0	0	0
	y	0.5	0.5	0.5
	z	0	0	0
	Site occup.	1.0/0.0	0.9/0.1	0.8/0.2
O1	x	0.275821	0.241910	0.467905
	y	0.274509	0.241750	0.691445
	z	0.531482	0.532250	0.356423
	Site occup.	1.0	1.0	1.0
O2	x	0.494513	0.444920	0.25
	y	0.071675	0.029120	0.502532
	z	0.25	0.25	0
	Site occup.	1.0	0.9	0.8
	a (Å)	5.524311(52)	5.537241(71)	7.817197(617)
	b (Å)	5.492413(62)	5.506648(80)	5.534872(840)
	c (Å)	7.774804(91)	7.803778(114)	5.535661(936)
	β(°)			89.89530(86)
	V ($Å^3$)	235.902(4)	237.950(5)	239.512(18)
	Space group	P b n m	P b n m	I 2/a
	$\chi 2$	1.805	1.630	2.262

Table 6.8 Refined Structural Parameters of LSGM-1010 (Neutron Diffraction)

Atom	Parameter	27°C	300°C	600°C	900°C	1100°C
La/ Sr	x	0.000049	0.002322	0.006011	0.001005	-0.000798
	y	-0.004505	-0.002185	0.003815	0.000121	0.001425
	z	0.25	0.25	0.25	0.25	0.25
	Site occup.	0.9/0.1	0.9/0.1	0.9/0.1	0.9/0.1	0.9/0.1
Ga/ Sr	x	0	0	0	0	0
	y	0.5	0.5	0.5	0.5	0.5
	z	0	0	0	0	0
	Site occup.	0.9/0.1	0.9/0.1	0.9/0.1	0.9/0.1	0.9/0.1
O1	x	0.259500	0.259465	0.248062	0.240736	0.243213
	y	0.259636	0.259756	0.244188	0.239895	0.243803
	z	0.534082	0.530484	0.526627	0.520202	0.511525
	Site occup.	1.0	1.0	1.0	1.0	1.0
O2	x	0.440335	0.444998	0.443187	0.450296	0.453264
	y	-0.001035	0.000178	0.012347	0.012097	0.018364
	z	0.25	0.25	0.25	0.25	0.25
	Site occup.	0.9	0.9	0.9	0.9	0.9
	a (Å)	5.53287(15)	5.54962(10)	5.56126(38)	5.57761(28)	5.58905(75)
	b (Å)	5.50300(14)	5.52570(10)	5.54166(36)	5.56533(26)	5.58569(64)
	c (Å)	7.79801(22)	7.82631(17)	7.85415(77)	7.87962(47)	7.89979(127)
	V ($Å^3$)	237.429(17)	239.998(6)	242.054(12)	244.593(7)	246.621(6)
	Space gp.	P b n m	P b n m	P b n m	P b n m	P b n m
	$\chi 2$	3.648	1.839	8.326	2.385	1.851

6.4 DEFECT CHEMISTRY OF THE PEROVSKITES

For an ionic crystal, charge neutrality is assumed. The doped LSGM perovskite is a pure ionic conductor[37,79] whereas the undoped $LaGaO_3$ is an insulator. A general formula for this material, taking account of the effect of dopants, should look like the following:

$$(La_{1-x}Sr_x)_A(Ga_{1-y}Mg_y)_B O_{3-\delta} \tag{6.5}$$

where x and y indicates the doping content in La- and Ga-site, respectively; A and B are the values of occupancy in the La- and Ga-site with a maximum of unity; δ is oxygen vacancy, which is restricted by charge neutrality. It is given by:

$$\delta = 3 - \frac{(3-x)A + (3-y)B}{2} = 3 - \frac{(3-x)(A+B)}{2} \tag{6.6}.$$

The second equality in Eq. (6.6) corresponds to the case where x = y. For most of the materials studied in this research, this was the case. The calculated δ value together with the percentage of oxygen vacancies for different LSGM compositions are listed in table 6.9 and plotted in Fig. 6.12. It can be seen that both the doping content and the A/B cation ratio have significant effect on creating oxygen vacancies, which is desired for increasing oxygen-ion conduction. However, a more general way of considering defect chemistry of LSGM perovskite is to link the oxygen vacancy to thermodynamics and to oxygen-ion conduction. Detailed discussion is given in Appendix III.

*Table 6.9 Oxygen Vacancy δ (and Vacancy Percentage) for Various LSGMs**

LSGM	A/B Cation Ratio				
Doping	0.95	0.98	1.00	1.02	1.05
0.0	0.075 (2.5%)	0.03 (1%)	0.0 (0%)	0.029412 (0.98%)	0.07142 (2.38%)
0.1	0.1725 (5.75%)	0.129 (4.3%)	0.1 (3.3333%)	0.128431 (4.281%)	0.169048 (5.6349%)
0.2	0.27 (9%)	0.228 (7.6%)	0.2 (6.6667%)	0.227451 (7.5817%)	0.266667 (8.8889%)

* *The oxygen vacancy in YSZ-10 is 2.5%.*

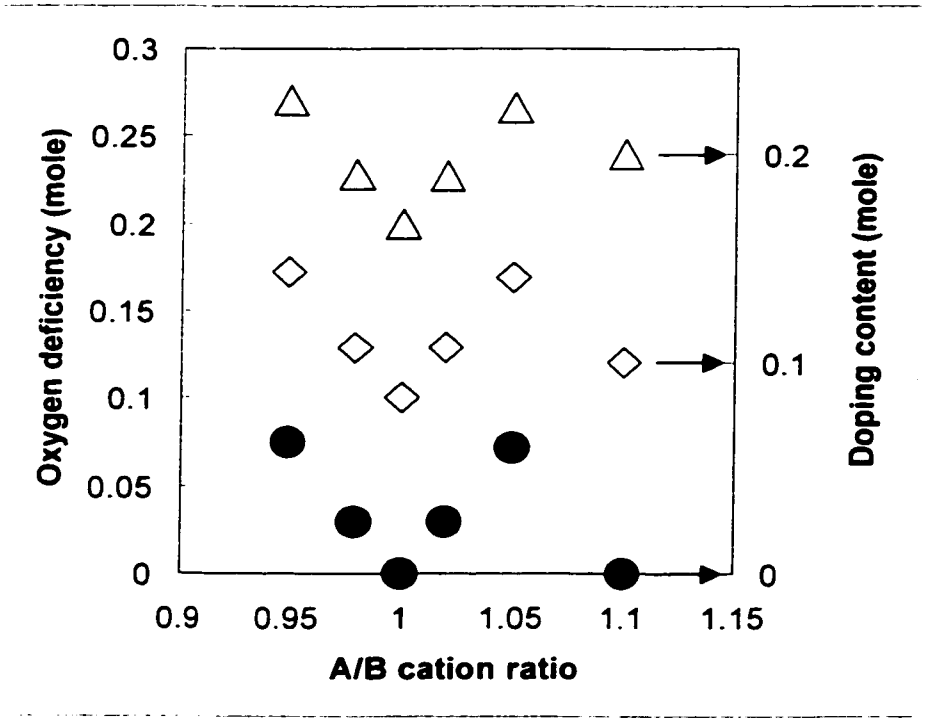

Fig. 6.12 The Calculated Oxygen Deficiency in the LSGM Perovskites

6.5 ELECTRICAL CONDUCTION OF THE LSGM PEROVSKITE

With the previously mentioned measurements and corresponding analysis and calculations, we are now in a position to answer why LSGM perovskites demonstrate superior oxygen ionic conduction and why they could be used as new electrolytes for SOFC. Prior to going into detail, it is worth reviewing the general concept of electrical conductivity.

Electrical conductance is defined as the inverse of electrical resistance. According to Ohm's law, conductance equals the current through an object divided by the applied voltage. The SI unit for conductance is Siemens ($S = 1/\Omega$). Conductance is proportional to the specific conductance, which has units of S/m (or commonly S/cm) and is called conductivity (Its equivalent engineering unit is $\Omega^{-1}cm^{-1}$).

The conductivity arises from the migration of charged species. The conductivity of each species (e.g. electron, hole or ion) is proportional to its charge, concentration, and mobility. The total conductivity is the sum of the individual (partial) conductivity.

Some materials are dominated by the charge transport of electrons. The electrons can either move in empty states in the conduction band or in holes in the valence band. For metals, these bands are overlapping and only partially filled. There is an 'ocean' of mobile electrons in metals. In semiconductors there is a band gap between the valence band and the conduction band. Thermal energy or doping is required to induce electrons in the conduction band or holes in the valence band. If the conductance was due to the electron

migration in the conduction band, the material is called n-type conductor; if it is due to hole in the valence band, it is a p-type conductor. The LSGM perovskites belong to p-type materials.

For an ionic material, whether doped or inherently non-stoichiometric, a considerable concentration of ionic defects, such as anion or cation vacancies and interstitials, is always present. These defects are essential to facilitate the migration of charge carriers (ions or holes) to produce conduction. Materials with mainly ionic conductivity can be used as solid electrolytes (e.g. YSZ and LSGM for SOFC), electrolyses (e.g. for water vapor electrolysis) and sensors (e.g. lambda-sensors for cars and sensors for gases in molten metals). Materials with mixed conduction (ionic and electronic) may find use as electrodes, electrocatalysts and oxygen-permeable gas separation membranes.

For the LSGM perovskites, measurement and analysis shows that both doping and off-stoichiometry increases lattice free volume (V_f) and doping also increases the saddle-point dimension (r_C) but decreases packing coefficient (c_i) (see section 6.1). It is reasonable to assure that the oxygen ionic conductivity will increase as V_f and r_C increase and c_i decreases. The temperature dependence of ionic conductivity is expressed by the Arrhenius relation:

$$\sigma T = A \exp(-E_a / kT) \tag{6.7}$$

where T is the absolute temperature, E_a is the activation energy for ionic conduction and A is a preexponential constant (contains entropy terms). Doping should increase A and decrease E_a. This can be interpreted by noting that doping creates oxygen vacancies and increase saddle-point size. The former leads to increase in entropy and therefore increases A value (c.f. Table 2.12). The latter provides easier diffusion path for oxygen-ion transport that lowers the activation energy of conduction. In addition, off-stoichiometry also increases the vacancy concentration and should further enhance A.

The free space is about one quarter of the lattice volume and the r_C is of ~ 0.93 to 0.94 Å (compared to r_O = 1.40 Å) at room temperature for LSGM perovskites. Upon heating, there is slight expansion in volume but the increase is small. The value of r_C is less than the size of oxygen ion. Consequently, the oxygen ion (r_O) can not migrate through the lattice opening (r_C) without extra (activation) energy — a conduction barrier (E_a) is presented. However, this barrier is expected to decrease with temperature. Differentiating and normalizing the size differences between the saddle-point dimension (the conducting path) and the oxygen-ion size (the conducting ion) would provide a geometrical method to quantify the conduction barrier. One possible way to do this is to calculate the difference between the conducting path opening (r_C) and the conducting ion radius (r_O). We have been able to phenomenological fit our data to the following expression:

$$\text{Conductivity Barrier} = \frac{1}{\textit{Ionic conduction}} \propto \left(\frac{r_O - r_C}{r_O} \right)^2 \qquad (6.8)$$

We will refer to this quantity as the conductivity barrier. This factor is reduced with doping content and temperature. Fig. 6.13 shows the calculated conductivity barrier change for the LSGM materials and the results explicitly show that the doped LSGM should have higher oxygen-ion conduction. At higher temperatures, the conduction should be higher due to the decrease in the barrier for oxygen ion migration. It is expected that the activation energy for ionic conductivity should be proportional to this conductivity barrier. Fig. 6.14 presents the measured activation energy[102] as a function of calculated conductivity barrier for varieties of perovskites. It is clear that this correlation holds. Further note that LSGM materials have a very low conductivity barrier and low activation energy.

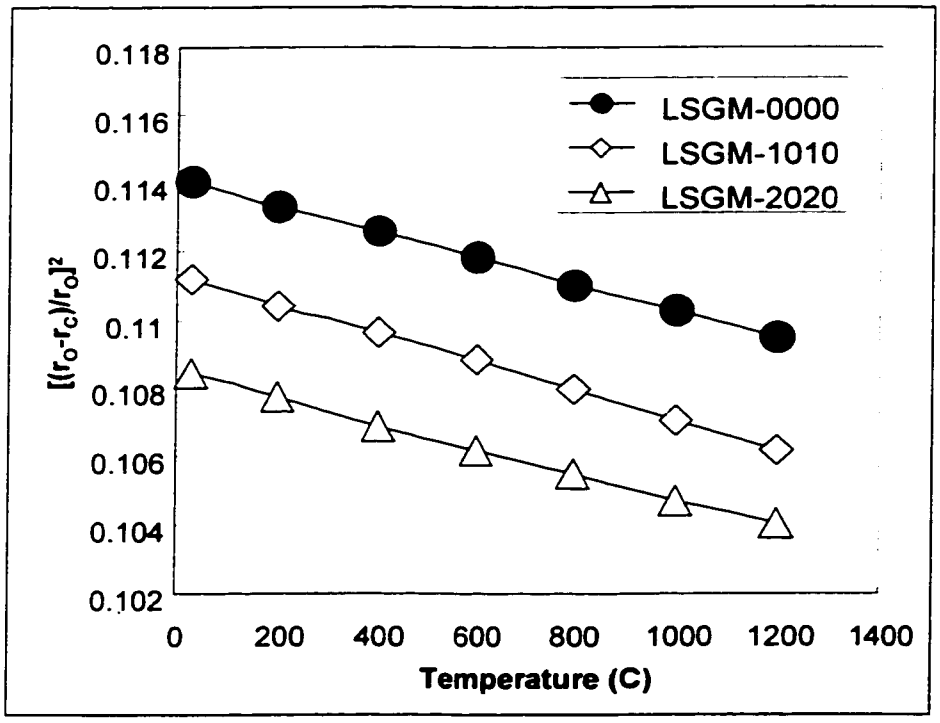

Fig. 6.13 The Oxygen-ion Conductivity Barrier as a Function of Temperature

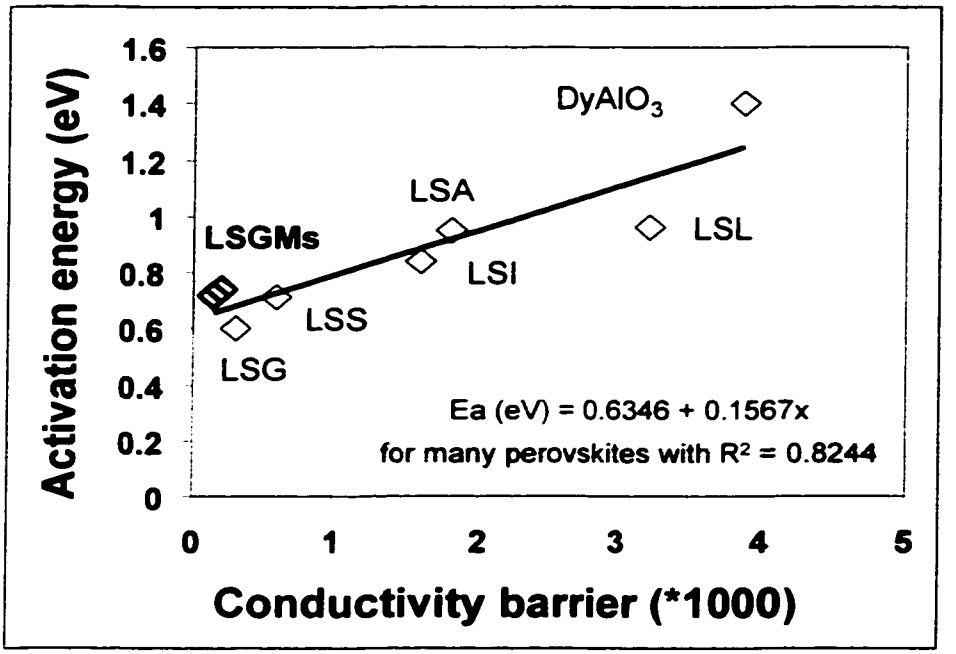

Fig. 6.14 The Correlation of Activation Energy and Conductivity Barrier

From structure analysis we have learned in LSGM system that doping leads to more defects (bigger δ which would enhance A term in Eq. 6.7) and larger saddle-point value (larger r_C would reduce E_a in Eq. 6.7). Similarly, off-stoichiometry leads to the creation of more defects with larger δ also. Both of them should facilitate higher oxygen ionic conductivity. However, the 4-point probe measurement did not show significant improvement in oxygen ionic conductivity due to the increase in doping (from 10 to 20 mol%, c.f. Table 5.4 & Fig. 5.13) and off-stoichiometry (from 0.90 to 1.02, c.f. Figs. 5.14 & 5.15). There could be two reasons for this. Firstly the formation of insulating minor phases could off-set the beneficial effect from doping and A/B ratio change. Another possible mechanism is the formation of some complicated defect clusters at high defect concentrations, which indicates an optimal doping and A/B ratio.

6.6 COMPARISON BETWEEN LSGM PEROVSKITES AND YSZ

The analysis (see Fig. 2.27 in section 2.5.3 for YSZ and section 6.5) provided so far would permit a qualitative comparison of the ionic conductivity between the conventional YSZ electrolyte with the new LSGM perovskites. Although the fluorite structured YSZ has a slightly larger saddle-point value and lattice free volume (or smaller conduction barrier), the LSGM perovskites accommodates larger percentages of oxygen vacancies (c.f. Table 6.9 & Fig. 6.12) while YSZ-10 only has 2.5% vacancies. So, LSGM perovskite has much larger preexponential factor A (c.f. Eq. 6.7). In addition, in LSGM perovskite, the charge carrier, oxygen ions, could have eight neighboring jump sites, while in YSZ fluorite only 4 of them are available. The overall influences result in the fact that the LSGM perovskites have superior oxygen-ion conductivity than that of YSZ (c.f. Fig. 2.28 in section 2.7 and Table 5.4 and Figs. 5.13 to 5.17 in section 5.2). Normalizing the conductivity of LSGM materials with respect to that of YSZ, it is useful to re- organize table 5.4 to provide a quantitative comparison among LSGMs and YSZ and these results are presented in table 6.10. It is clear that the LSGM perovskites can be used as electrolytes to lower SOFC operating temperature.

Table 6.10 Comparison of Electrical (Ionic) Conductivity among LSGMs and YSZ

	Conductivity (S/cm) at Indicated Temperatures & Normalized to that of YSZ							
Composition	@ 400°C	σ/σ_{YSZ}	@ 600°C	σ/σ_{YSZ}	@ 800°C	σ/σ_{YSZ}	@ 1000°C	σ/σ_{YSZ}
LSGM-1020	$3*10^{-3}$	3.75	$1.5*10^{-2}$	2.50	0.10	2.00	0.26	1.44
LSGM-1520	$4*10^{-3}$	5.00	$1.5*10^{-2}$	2.50	0.12	2.40	0.36	2.00
LSGM-2015	$5*10^{-3}$	6.25	$1.8*10^{-2}$	3.00	0.11	2.20	0.31	1.72
LSGM-2020	$4*10^{-3}$	5.00	$2.0*10^{-2}$	3.33	0.12	2.40	0.40	2.22
YSZ	$0.8*10^{-3}$	1	$0.6*10^{-2}$	1	0.05	1	0.18	1

6.7 SINTERING OF THE LSGM PEROVSKITES

The LSGM materials can be sintered to near full density between 1400 to 1500°C for 2 hours. Fig. 6.15 shows one set of sintering data collected from dilatometry study on samples calcinated at 650°C for 1 hour. The "green" samples begin to shrink when temperature reaches 650°C and undergoes fast and continuous dimension change during heating to 1500°C. When temperature is held constant at 1500°C for 2 hours, we only get less than 1% additional shrinkage. SEM micrographs showed that the sintered samples are close to full density with negligible porosity (less than 1 vol%). If sintering temperature is below 1500°C, significant amounts of minor phases are present (c.f Fig. 5.20). These minor phases are of tetragonal structure and behave as insulators and, therefore, their presence is undesirable in fuel cell applications. The effect of temperature

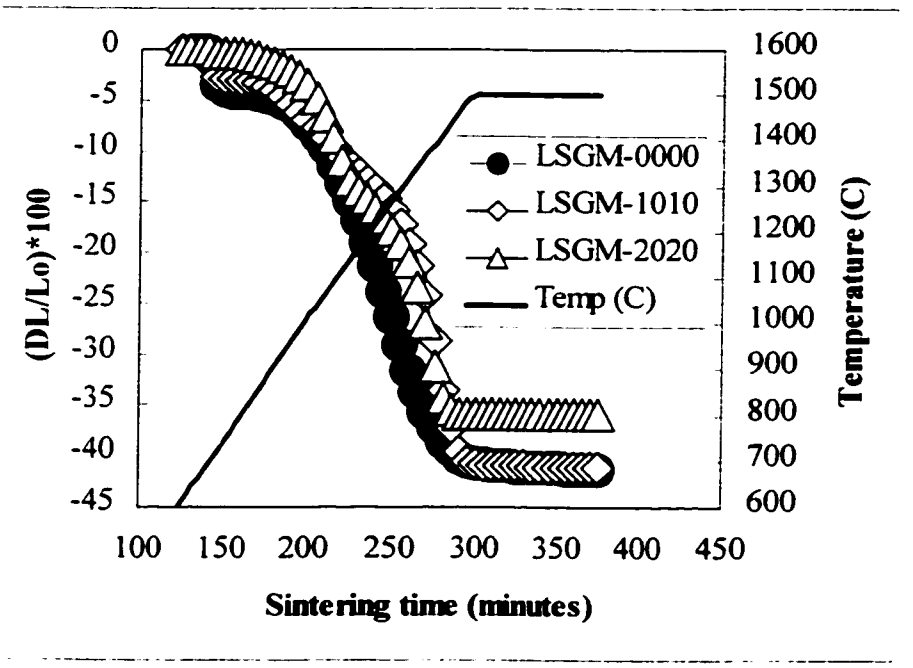

Fig. 6.15 Sintering Shrinkage Change as Function of Temperature and Time

on the grain size, presented in Figs. 5.17 to 5.19, shows that, the higher the temperature, the larger the grain size.

It is worth noting that the highest sintering temperature that can be used for LSGM materials is not only dependent on the temperature at which liquid phases form (which is reduced with increased doping content and for A/B < 1) but also limited by the volatilization of Ga_2O. At ambient pressure, Ga_2O is gaseous above 700°C.[103] In high-magnification SEM photos, we can see there are uniform grove-shapes that appear in thermally etched grain surfaces in doped LSGM samples while no such features were observed in pure undoped $LaGaO_3$ (see Fig. 6.15). The reason for this must be due to the change in homologous temperature (equals to the ratio of sintering temperature to melting point of the lowest melting constituent), since, according to phase diagram (c.f. Fig. 5.12), the melting temperature is lowered upon doping in the LSGM system. When firing all LSGM samples at either 1400 or 1500°C, the doped samples were at a higher homologous temperature. Based on this analysis, doped samples should have greater thermal driving force during sintering. Consequently, doped samples should have larger grain sizes and higher sintered density, providing the content of the minor phases is negligible. This is what we observed. We can see clearly from the change in shrinkage curves plotted in Fig. 6.15 where the doped samples reach near full density at lower temperature. The grove-shapes in Fig. 6.16 for doped samples also serve as the evidence that the homologous temperature is higher which allows for volatilization of Ga_2O.

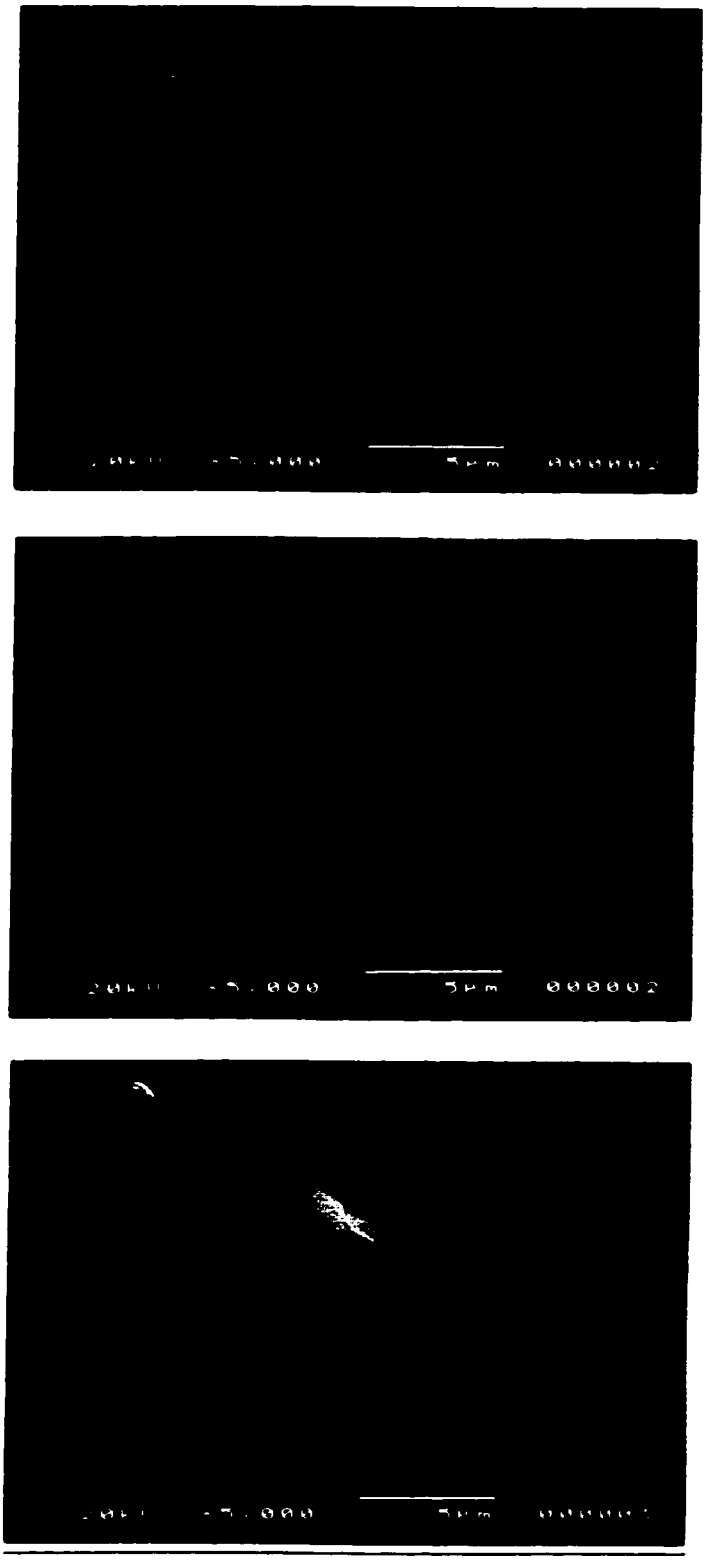

Fig. 6.16 Gaseous-phase Transport Paths (Doping ↑ from Top to Bottom) at 1500°C/2h

The change in A/B cation ratio affects the bulk properties (c.f. Eq. 6.3-6.6). Besides the beneficial defects induced by doping and varying the A/B ratio, undesirable minor phases form (see Chapter 5). Doping can alter the conduction paths of charge carriers (c.f. Eq. 6.2), while the change in A/B cation ratio often leads to the formation of minor phases (c.f. Table 5.2). The effect could be detrimental if the amount of minor phases were large (greater than a few wt%). It would be even worse if the minor phases were amorphous which could coat on the grain boundaries of the main perovskite phase.

Doping and varying A/B ratio also has impact on grain size. However, their roles are more complicated than that of temperature. In general, if no minor phases were involved, then the effect of doping behavior is similar to that of temperature such that the grain-size increases with doping content. Because the melting point of doped LSGM perovskite is lowered with doping content, doped materials are subjected to a higher homologous temperature (when sintered at the same temperature as undoped samples). The A/B ratio often limits grain growth by forming minor phases. The same goes for heavy doping when minor phases are formed. Minor phases pin the grain boundaries and prevent further grain growth leading to smaller grain size. These observations are valid for the case in which the minor phases are crystalline. This is what was observed when sintering was conducted at 1400°C. When higher sintering temperature was used, the grain size is increased with doping where the total amount of crystalline minor phases is negligible while the majority of them becoming liquid phase. It was the present of liquid minor phase that enhances sintering and gives rise larger grain size.

Temperature, doping and A/B ratio also effect sintered density. Their effects on density are dependent on the formation of minor phases. The sintered density is often reported with respect to the theoretical density. The theoretical density (ρ_{th}) of the LSGM materials is calculated according to:

$$Density = \frac{Unit\ cell\ atom\ weight}{Avogadros'\ number \times volume\ of\ one\ unit\ cell} \qquad (6.9)$$

utilizing the structure data of Table 6.2. The results are listed in table 6.11. It is clear that the maximum ρ_{th} is for pure, undoped $LaGaO_3$ and the value decreases with doping content and derivation of the A/B ratio.

It is now understood that minor phases have strong influence on sintered density (see Fig. 6.17). Consulting the phase diagram of the La_2O_3- Ga_2O_3 binary system (see Fig. 2.29), we note that there is a low eutectic temperature (1345°C) on the Ga_2O_3-rich side. This corresponds to A/B < 1 for undoped LSGM-0000. Sintering temperature of 1500°C is higher than this eutectic temperature. The observed Ga_2O_3 phase in LSGM-0000 at A/B =

*Table 6.11 Theoretical Density (ρ_{th}, g/cm^3) of the LSGM Materials**

LSGM	A/B Cation Ratio				
Doping (mole)	0.95	0.98	1.00	1.02	1.05
0.0	6.9965	7.1341	7.2259	7.1741	7.1002
0.1	6.6299	6.7614	6.8491	6.8007	6.7316
0.2	6.2824	6.4080	6.4918	6.4467	6.3822

** The cell volume was taken from table 6.2*

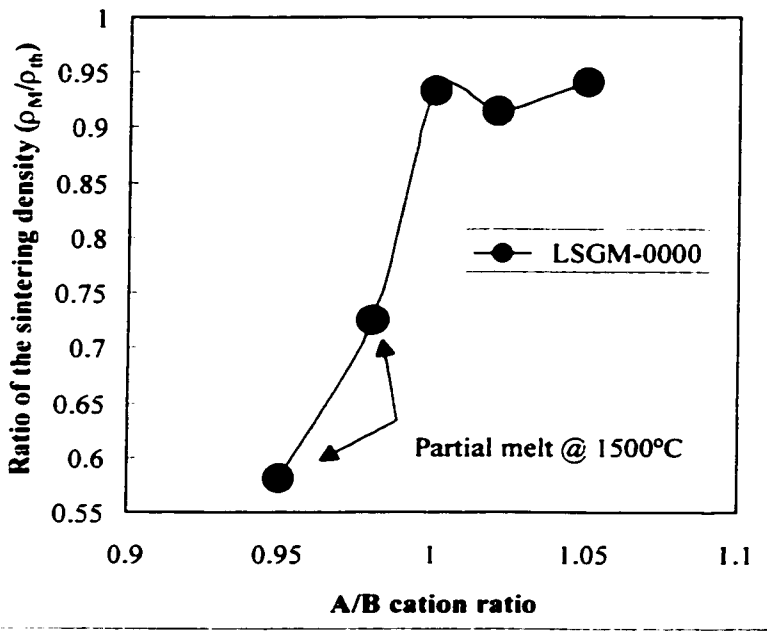

a) Undoped $LaGaO_3$ showing melting above 1345°C with A/B < 1

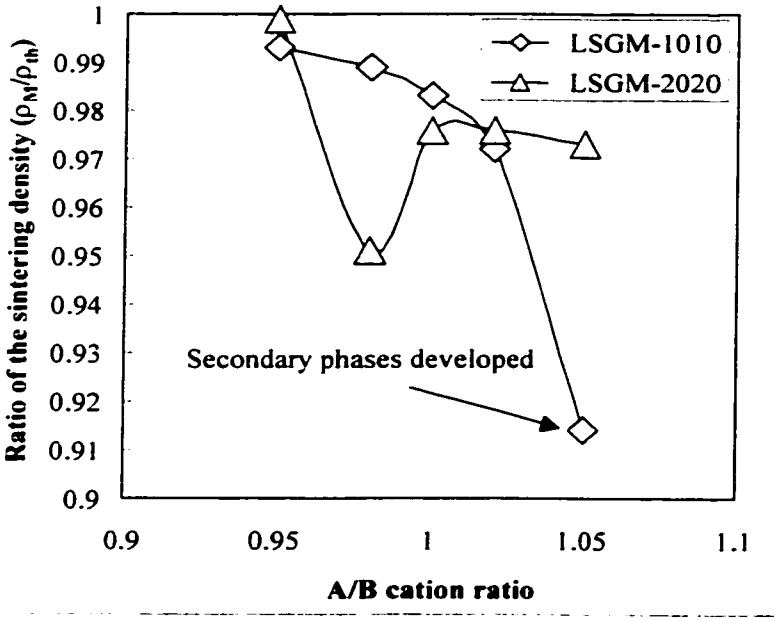

b) Minor Phases Developed in Doped LSGM

Fig. 6.17 Normalized Sintered Density as a Function of A/B Ratio for Samples Sintered at 1500°C for 9 Hours

0.95 and 0.98 indicated this low temperature eutectic phase was formed during sintering and these samples partially melted (marked on Fig. 6.17a) during sintering. As a result, holes and cracks developed in these samples. This is likely the reason why these samples have rather low density. When A/B > 1, the sample composition is located on the La_2O_3-rich side, the eutectic temperature is 1670°C, which is higher than the sintering temperature. Therefore, these samples did not melt and consequently they have a higher sintered density.

Doping creates oxygen vacancies, according to defect chemistry. It appears that doping enhances the solubility limit of perovskite such that we do not have the low temperature eutectic reaction. The combined effects of the creation of oxygen vacancies and the increased solubility assure relatively high sintered density for the doped samples (see Fig. 6.17b).

In summary, the presence of minor phase(s) plays a big role in densification and grain growth. The detailed effect depends on the doping level, the off-stoichiometry and the sintering temperature. The overall results from the sintering study are very promising. Most of the LSGM materials have been sintered to high density with ease (> 96% of the theoretical density). The high density is required to prohibit gas diffusion for electrolytes. Therefore, it is possible to define a suitable LSGM compositional window for SOFC application (c.f Table 5.2) which avoids compositions that do not sinter readily to high density.

CHAPTER 7

FUTURE WORK

All experimental evidence, from literature data and the data obtained in this study, have confirmed that the Sr and Mg doped $LaGaO_3$ (LSGM) perovskites show higher oxygen ionic conductivity compared to yittria stabilized zirconia (YSZ). From theoretical point-of-view, it is understood that the structure and distribution of defects determine the electrical conduction (and other material properties) of a material. Some of these aspects have been discussed in Chapter 6 for LSGM perovskites. There are intrinsic and extrinsic defects in a material. Intrinsic defects are governed by thermodynamics and their concentrations are determined by equilibrium conditions (composition and temperature). For ceramics used for electrical purposes (like electrolytes), the effect of intrinsic defects is negligible and many pure oxides (undoped $LaGaO_3$, for example) behave as insulators. Extrinsic defects, however, are more important in term of electrical conduction in solid oxides. Both doping and varying A/B cation ratio has significant influence on creating defects. This provides a sound means to control the material properties.

Qualitatively, we know that the tolerance factor, saddle-point dimension, lattice free volume, packing density and oxygen deficiency all affects electrical conduction in one way or another (c.f. Eq. 6-8 & Eq. 6.9) in LSGM materials. However, we can not quantify these inherent relations. An atomistic description of the crystal structure and distribution of defects is needed to furnish such a quantitative equation. To achieve this goal, some quantum mechanic based programs[103,104] would be of use. One of them is the

ab initial Pertubed Ion (*ai*PI) program[104-106] that allows the lattice energy (Madelung energy) and structure changes of ionic crystals (e.g. NaCl, CsCl, MgO, and LSGM of course) to be calculated, with respect to the influence of composition (doping and A/B ratio) and temperature. Starting from the change in Madelung energy, the contribution and effect of defects (from doping and A/B ratio variation) to many material properties can be determined numerically, providing sufficient knowledge of quantum mechanics and proper crystal structure information are available. For LSGM materials, the required crystal structure data are given in Chapter 5. Applying these structural data into the *ai*PI program (or other similar programs if available), the corresponding Madelung energy of the perovskite and the potential of its constituent ions can be computed. Based on the calculated energy data, further analysis should enable us to illustrate the energetic effect of defects (either single defect or the complex of various defect combinations) on electrical conduction (and other material properties).

More sintering study, especially constrained sintering of LSGM electrolyte with electrode materials, such as Sr doped $LaMnO_3$ (LSM), should greatly enhance our understanding of these materials for solid oxide fuel cell application.

The same methodology that was used in this study could be applied to research on other related materials.

BIBLIOGRAPHY

1. W.R. Grove, *On Voltaic Series and the Combination of Gases by Platinum*, Philos. Mag. **S. 3. 14**[86], 127-30 (1839).

2. W.R. Grove, *On a Gascous Voltaic Battery*, Philos. Mag. **S3. 21**[140], 417-20 (1842).

3. J.A.A. Ketelaar, *Chapter 1, History* in *Fuel Cell Systems*, Edited by Leo J.M.J. Blomen and Michael N. Mugerwa, Plenum Press, New York, 1993.

4. W.W. Jacques, Harpers Mag., **26,** 144-50 (1896), from Ref. 3.

5. J.H. Reid, *U.S. patent 736016,017 (1902) and USP 757,637 (1904),* from Ref. 3.

6. P.C.L. Noel, *Fr. patent 350,111 (1904),* from Ref. 3.

7. F. Haber, *Uber die Knallgaskette*, Z. Anorg. Allg. Chem., **51,** 245-88, 289-314, 356-68 (1906).

8. F. Haber, *Eneergie a. Kohle u. gasform. Brennstoffe, Osterr. Pat. 27,743 (1907,)* from Ref. 3.

9. I. Taitelbaum, *Studien Uber Brennstoffkentten*, Z. Elektrochem., **16,** 286-300 (1910). E. Baur, *Bemerkungen Zu Taitelbaums Abhandlung*: "*Studien Uber Brennstoffkentten*", **16,** 300-302 (1910).

10. W. Nernst, *Uber Die Elektrolytische Leitung Fester Korper Bei Sehr Hohen Temperaturen*, Z. Elektrochem., **6,** 41-43 (1899), 141 (1900).

11. W. Schottky, *Wiss. Veroff. Siemens Werke*, **14**[2], 1-90 (1935); Chem. Abstr. 20,5358 (1935).

12. E. Baur and H. Preis, *Uber Brennstoff-Ketter Mit Festleitern*, Z. Elektrochem., **43,** 727-32 (1937).

13. F. T. Bacon, *Fuel Cells, Past, Present and Future*, Elektrochem. Acta., **14**[7], 569-85 (1969).

14. K. Strasser, *The Design of Alkaline Fuel Cells*, Journal of Power Sources, **29**[3/4], 149-66 (1990).

15. S. Srinvasan, B.B. Dav, K.A. Murugesamoorthi, A. Parthasarathy, and A. J. Appleby, *Chapter 2, Overview of Fuel Cell Technology* in *Fuel Cell Systems*, dited by Leo J.M.J. Blomen and Michael N. Mugerwa, Plenum Press, New York, 1993.

16. D.S. Watkins, *Chapter 11, Research, Development, and Demonstration of Solid Polymer Fuel Cell Systems* in *Fuel Cell Systems*, Edited by Leo J.M.J. Blomen and Michael N. Mugerwa, Plenum Press, New York, 1993.

17. R.A. Lemons, *Fuel Cells for Transportation*, Journal of Power Sources, **29**[3/4], 251-64 (1990).

18. Supplement to J.W. Mellor's *"Comprehensive Treatise on Inorganic and Theoretical Chemistry"*, **Vol. VIII, Suppl. III**, 669-725, Longman Group Ltd, London, 1971.

19. R. Anahara, *Chapter 8, Research, Development, and Demonstration of Phosphoric Acid Fuel Cell Systems* in *Fuel Cell Systems*, Edited by Leo J.M.J. Blomen and Michael N. Mugerwa, Plenum Press, New York, 1993.

20. J.R. Selman, *Chapter 9, Research, Development, and Demonstration of Molten Carbonate Fuel Cell Systems* in *Fuel Cell Systems*, Edited by Leo J.M.J. Blomen and Michael N. Mugerwa, Plenum Press, New York, 1993.

21. N.Q. Minh, *High-Temperature Fuel Cells. Part I: How the Molten Carbonate Cell Works, and the Materials that Make it Possible*, CHEMTECH, **21**, 114-19 (1991).

22. E. Barendrecht, *Chapter 3, Electrochemistry of Fuel Cells* in *Fuel Cell Systems*, Edited by Leo J.M.J. Blomen and Michael N. Mugerwa, Plenum Press, New York, 1993.

23. J.R. Selman, *Motlen Carbonate Fuel Cells (MCFCs)*, Energy, **11**[1/2], 153-208 (1986).

24. K.A. Murugesamoorthi, S. Srinvasan, and A. J. Appleby,, *Chapter 10, Research, Development, and Demonstration of Solid Oxide Fuel Cell Systems* in *Fuel Cell Systems*, Edited by Leo J.M.J. Blomen and Michael N. Mugerwa, Plenum Press, New York, 1993.

25. N.Q. Minh, *High-Temperature Fuel Cells. Part II: The Solid Oxide Cell*, CHEMTECH, **21**, 120-26 (1991).

26. J. Weissbart and R.J. Ruka, *A Solid Electrolyte Fuel Cell*, J. Electrochem. Soc., **109**, 723-26 (1962).

27. D.H. Archer, R.L. Zahrandnik, E.F. Sverdrup, W.A. English, L. Elikan, and J.J. Alles, *Solid Electrolyte Batteries*, Proc. Power Sources Conf. 36-40 (1964).

28. N.Q. Minh, *Ceramic Fuel Cells*, J. Am. Ceram. Soc., **76**[3], 563-88 (1993).

29. F. Zheng, *Thermodynamics and Phase Behavior in Lanthanum Strontium Manganites*, Master Thesis, Washington State University, 1996.

30. J.A.M. Van Roosmalen and E.H.P. Cordfunke, *Chemical reactivity and interdiffusion of (La,Sr)MnO_3 and (Zr,Y)O_2 solid oxide fuel cell cathode and electrolyte*, Solid State Ionics, **52**, 303-312 (1992).

31. B.C.H. Steele, Oxygen Ion Conductors, in *High Conductivity Solid Ionic Conductors: Recent Trends and Applications*, edited by T. Takahashi, World Scientific, Singapore, 402-46 (1989).

32. N.Q. Minh and T. Takahashi, *Science and Technology of Ceramic Fuel Cells*, Elsevier Science B.V. 1995.

33. J.B. Goodenough, *Fast Ionic Conduction in Solids*, Proc. R. Soc. London, **A393**, 215-34 (1984).

34. T. Ishihara, H. Matsuda, and Y. Takita, *Doped $LaGaO_3$ Perovskite Type Oxide as a New Oxide Ionic Conductor*, J. Am. Chem. Soc., **116**, 3801-803 (1994); Proc. 2nd Intl. Symp. on Ionic and Mixed Conducting Ceramics, Electrochem. Soc., Pennington, NJ, **94-12**, 8593 (1994).

35. M. Feng and J. B. Goodenough, *A Superior Oxide-Ion Electrolyte*, Eur. J. Solid State Inorg. Chem., **31**, 663-72 (1994).

36. P.N. Huang and A. Petric, *Superior Oxygen Ion Conductivity of Lanthanum Gallate Doped with Strontium and Magnesium*, J. Electrochem. Soc., **143**[5], 1644-48 (1996).

37. J. W. Stevenson, T. R. Armstrong, L. R. Pederson, and W. J. Weber, *Processing and Electrical Properties of Alkaline Earth-Doped Lanthanum Gallate*, J. Electrochemical Society, **144**, 3613-20 (1997).

38. K.R. Kendall, C. Navas, J.K. Thomas, and H.Z. Loye, *Recent Developments in Perovskite-Based Oxide Ion Conductors*, Solid State Ionics, **82**, 215-23 (1996).

39. N. Imanaka and G.Y Adachi, *Rare Earth Contribution In Solid State Electrolytes, Especially in the Chemical Sensor Field*, Journal of Alloys and Compounds, **250**, 492-500 (1997).

40. I. Naray-Szabo, Publ. Univ. Tech. Sci., Budapest, **1**, 30 (1947).

41. S. Geller, *Crystallographic Studies of Perovskite-Like Compounds. IV. Rare Earth Scandates, Vanadites, Galliates, Orthochromites*, Acta Cryst. **10**, 243-248 (1957).

42. S. Gelller, and P.M. Raccah, *Phase Transitions in Perovskitelike Compounds of the Rare Earths*, Phys.Rev.B, **2**[4], 1167-72 (1970).

43. S. Geller, P.J. Curlander, and G.F. Ruse, *Perovskites-Like Rare Earth Gallium Oxides Prepared at Atmospheric Pressure*, Mat. Res. Bull. **9**, 637-644 (1974).

44. M. Mizuno, T. Yamada and T. Ohtake, *Phase Diagram of the System Ga_2O_3-La_2O_3 at High Temperatures*, Yogyo-Kyokai-Shi, **93**[6], 295-300 (1985).

45. M. Mizuno, T. Yamada, *Formation and Solidification Points of Binary Compounds in the Ln_2O_3-Ga_2O_3 System*, Yogyo-Kyokai-Shi, **93**[11], 686-91 (1985).

46. R. L. Sandstrom, E. A. Giess, W. J. Gallagher, A. Segmuller, E. I. Cooper, M. F. Chisholm, A. Gupta, S. Shinde, and R. B. Laibowitz, *Lanthanum Gallate Substrates for Epitaxial High-Temperature Superconducting Thin Films*, Appl. Phys. Lett., **53**, 1874-1876 (1988).

47. S. Miyazawa, *Surface Roughening Associated with ~ 140°C Transition of a $LaGaO_3$ Substrate for High T_C Superconducting Films*, Appl. Phys. Lett., **55**, 2230-32 (1989).

48 R. F. Belt and R. Uhrin, *Crystal Growth and Evaluation of Rare Earth Orthogallates for Laser Hosts*, SPIE Vol. **1104**. Growth, Characterization, and Applications of Laser Host and Nonlinear Crystals, 209-215 (1989).

49. E. A. Giess, R. L. Sandstrom, W. J. Gallagher, A. Gupta, S. L. Shinde, R. F. Cook, E. I. Cooper, E. J. M. O'Sullivan, J. M. Roldan, A. P. Segmuller, J. Angilello, *Lanthanide Gallate Perovskite-type Substrates for Epitaxial, High-T_C Superconducting $Ba_2YCu_3O_{7-d}$ Films*, IBM J. RES. DEVELOP, **34**[6], 916-26 (1990).

50. H. M. O'Bryan, P. K. Gallagher, G. W. Berkstresser, and C. D. Brandle, *Thermal Analysis of Rare Earth Gallates and Aluminates*, J. Mater. Res., **5**[1], 183-89 (1990).

51. G. Jasiolek and H. Dabkowska, *X-ray Emission Studies of Some $ReGaO_3$ Single Crystals*, J. the Less-Common Matals, **160**, 79-84 (1990).

52. A. M. Azad, R. Sudha, and O. M. Sreedharan, *Thermodynamic Stability of $LaGaO_3$ and Its Compatibility with $YBa_2Cu_3O_{7-X}$ for Sunstrate Application*, Mat. Res. Bull., **26**, 97-105 (1991).

53. S. Haussuhl, D. Mateika, *Elastic and Thermoelastic Properties of the Twinned Perovskite $LaGaO_3$ and the Cubic Untwinned Perovskite $La_{0.294}Sr_{0.706}Al_{0.647}Ta_{0.353}O_3$*, Cryst. Res. Technol, **26**[4], 481-483 (1991).

54. Y. Wang, X. Liu, G.-D. Yao, R. C. Liebermann, M. Dudley, *High Temperature Transmission Electron Microscopy and X-ray Diffraction Studies of Twinning and the Phase Transition at 145°C in $LaGaO_3$*, Mat. Sci. Eng., **A132**, 13-21 (1991).

55. G.-D. Yao, M. Dudley, Y. Wang, X. Liu, R. C. Liebermann, *Synchrotron X-ray Topography Studies of Twinning and the Phase Transition at 145°C in $LaGaO_3$ Single Crystals*, Mat. Sci. Eng., **A132**, 23-30 (1991).

56. G.-D. Yao, M. Dudley, Y. Wang, X. Liu, R. C. Liebermann, *Synchrotron Radiation Topography Studies of the Phase Transition in $LaGaO_3$ Crystals*, Nuclear Instruments and Methods in Physics Research **B56/57**, 405-408 (1991).

57. J. Kobayashi, Y. Tazoh, M. Sasaura, and S. Miyazawa, *Structure Analysis of Lanthanum Gallate*, J. Mater. Res., **6**[1], 97-100 (1991).

58. A. N. Morozov, O. Yu. Morozova, N. M. Ponimarev and S. N. knyazev, *Structure Perfection of $LaGaO_3$ Single Crystals -- A New Substrate Material for Growing High-T_C Superconducting Films*, Superconductivity, **5**[2], 386-96 (1992).

59. A. N. Morozov, O. Yu. Morozova, and N. M. Ponimarev, *Real Structure of Single Crystals of $LaGaO_3$ Grown by the Czochraski Method.*
I. X-ray Diffraction and X-ray Topographic Methods.
II. Refinement of Crystal System by Precision Measurements of Unit-Cell. Parameters by the Method of Bond.
III. High-Temperature Investigation, Crystallogr. Rep. **38**[3], 368-73, 374-76, 377-81 (1993).

60. I. K. Bdikin and I. M. Shmyt'ko, *Twinning of $LaGaO_3$ Single Crystals*, J. Appl. Cryst., **26**, 71-76 (1993).

61. W. Marti, P. Fischer, F. Altorfer, H. J. Scheel and M. Tadin, *Crystal Structures and Phase Transitions of Orthorhombic and Rhombohedral $RGaO_3$ (R = La, Pr, Nd) Investigated by Neutron Powder Diffraction*, J. Phys.: Condens. Matter, **6**, 127-35 (1994).

62. W. Marti, J. P. Rivera, F. Kubel, H. J. Scheel and H. Schmid, *Optical Studies of Ferroelastic Domain Structures of $LaGaO_3$ and $NdGaO_3$*, Ferroelectrics, **172**, 79 84 (1995).

63. W. Marti, P. Fischer, H. J. Scheel and F. Kubel, *Structures Characterization with Neutron Powder Data of $LaGaO_3$ and $NdGaO_3$ Based on X-ray Single-Crystal Data: Evidence for an Inversion Center*, Zeischrift fur Kristallographic, **211**, 891-94 (1996).

64. D. C. Dube, H. J. Scheel, I. Reaney, M. Daglish, and N. Setter, *Dielectric Properties of Lanthanum Gallate ($LaGaO_3$) Crystal*, J. Appl. Phys., **75**[8], 4126-30 (1994).

65. I. Utke, C. Klemenz, H. J. Scheel, P. Nuesch, *High-Temperature X-ray Measurements of Gallates and Cuprates*, J. Crystal Growth, **174**, 813-20 (1997).

66. T. Ishihara, H. Matsuda, Y. Takita, *Effects of Rare Earth Cations Doped for La Site on the Oxide Ionic Conductivity of $LaGaO_3$-Based Perovskite Type Oxide*, Solid State Ionics, **79**, 147-51 (1995).

67. T. Ishihara, Y. Hiei, Y. Takita, *Oxidative Reforming of Methane Using Solid Fuel Cell with $LaGaO_3$-Based Electrolyte*, Solid State Ionics, **79**, 371-75 (1995).

68. T. Ishihara, H. Minami, H. Matsuda, Y. Takita, *Application of the New Oxide Ionic Conductor, $LaGaO_3$, to the Solid Electrolyte of Fuel Cells*, **SOFC-IV**, 344-52 (1995).

69. T. Ishihara, H. Matsuda, M.A.B. Bustam, Y. Takita, *Oxide Ion Conductivity in Doped Ga Based Perovskite Type Oxide*, Solid State Ionics, **86-88**, 197-201 (1996).

35. M. Feng and J. B. Goodenough, *A Superior Oxide-Ion Electrolyte*, Eur. J. Solid State Inorg. Chem., **31**, 663-72 (1994).

70. J. B. Goodenough and M. Feng, *Improved Perovskite Oxide Ion Electrolytes*, Eur. J. Solid State Inorg. Chem., **31**, 663-72 (1994).

71. K. Huang, M. Feng, J. B. Goodenough, and M. Schmerling, *Characterization of Sr-Doped $LaMnO_3$ and $LaCoO_3$ as Cathode Materials for a Doped $LaGaO_3$ Ceramic Fuel Cell*, J. Electrochem. Soc., **143**[11], 3630-35 (1996).

72. K. Huang, M. Feng, and J.B. Goodenough, *Sol-Gel Synthesis of a New Oxide-Ion Conductor Sr- and Mg-Doped $LaGaO_3$ Perovskite*, J. Am. Ceram. Soc., **79**[4], 1100-104 (1996).

73. M. Feng, J.B. Goodenough, K. Huang, C. Milliken, *Fuel Cells with Doped Lanthanum Gallate Electrolyte*, J. Power Sources, **63**, 47-51 (1996).

74. K. Huang, M. Feng, and J.B. Goodenough, *Improvement on Sr- and Mg-doped $LaGaO_3$ Perovskite Solid Electrolyte*, Electrochemical Society Proceedings **96-27**, 7-18 (1997).

75. A. Petric, P. Huang and A. Skowron, *Characterization of the Conductivity and Structure of Lanthanide Gallate Perovskites*, Proc. of the 2nd European Solid Oxide Fuel Cell Forum, Edited by B. Thorstensen, European SOFC Forum, Oslo, Norway, 751-60 (1996).

76. W.T. Wang and E.E. Hellstrom, *Study of Chemical Compatibility and Interfacial Resistance Between Oxide Cathode Materials and A $LaGaO_3$-Based Electrolyte for Solid Oxide Fuel Cells*, Mat. Res. Soc. Symp. Proc. **411**, 261-66 (1996).

77. J. Drennan, V. Zelizko, D. Hay, F. T. Ciacchi, S. Rajendran and S. P. S. Badwal, *Characterisation, Conductivity and Mechanical Propertie of the Oxygen-Ion Conductor $La_{0.9}Sr_{0.1}Ga_{0.8}Mg_{0.2}O_{3-x}$*, J. Mater. Chem., 7[1], 79-83 (1997).

78. N.M. Sammes, M. Keppeler, H. Nafe, F. Aldinger and G.A.Tompsett, *The Mechanical Properties of Electrolyte Material*, **SOFC-VI**, 397 (1998).

79. J. W. Stevenson, T. R. Armstrong, L. R. Pederson, J. Li, C. A. Lewinsohn and S. Baskaran, *Effect of A-Site Cation Stoichiometry on Properties of Doped Lanthanum Gallate*, J. Electrochemical Society, 1998(preprint)

80. T. Berthold and B. Jobst, *Influence of Nd-Substitution on the Orthorhombic/Rhombohedral Phase Transition of $LaGaO_3$*, Materials Science Forum, **79-82** 703-708 (1991).

81. B. Jobst and T. Berthold, *Shift of the Phase Transition of $LaGaO_3$ above the Preparation Temperature of Superconductor Films*, High T_C Superconductor Thin Films, Ed. L. Correra, Elsevier Science Publishers B.V, 665-70 (1992).

82. P.R. Slater, J.T.S. Irvine, T. Ishihara, Y. Takita, *The Structure of the Oxide Ion Conductor $La_{0.9}Sr_{0.1}Ga_{0.8}Mg_{0.2}O_{0.285}$ by Powder Neutron Diffraction*, Solid State Ionics, **107**, 319-23 (1998).

83. P.R. Slater, J.T.S. Irvine, T. Ishihara, Y. Takita, *Structure of Lanthanum Gallate Electrolytes at High Temperatures*, **SOFC-VI**, 387-396 (1998).

84. P.R. Slater, J.T.S. Irvine, T. Ishihara, Y. Takita, *High-Temperature Powder Neutron Diffraction Study of the Oxide Ion Conductor $La_{0.9}Sr_{0.1}Ga_{0.8}Mg_{0.2}O_{0.285}$*, Journal of Solid State Chemistry, **139,** 135-43 (1998).

85. L.A. Chick, L.R. Pederson, G.D. Maupin, J.L. Bates, L.E. Thomas and G.J. Exarhos, *Glycine-nitrate Combustion Synthesis of Oxide Ceramic Powders*, Mat. Let. **10**[1,2], 6-12 (1990).

86. L.A. Chick, G.D. Maupin, G.L. Graff, L.R. Pederson, D.E. McCready and J.L. Bates, *Redox Effects in Self-sustaining Combustion Synthesis of Oxide Ceramic Powders*, Mat. Res. Soc. Symp. Proc. **249**, 159-164 (1992).

87. F. Zheng, *Thermodynamics and Phase Behavior in Lanthanum Strontium Manganites*, MS Thesis, Washington State University, 1996

88. L. Erdey, *Gravimetric Analysis*, Translated by Gyula Svehla, edited by Ilona Buzas, New York, Macmillan, 1963.

89. D.K. Schroder, *Semiconductor Material and Device Characterization*, John Wiley & Sons, Inc. 1998.

90. H.M. Rietveld, *A Profile Refinement Method for Nuclear and Magnetic Structures*, Journal of Applied Crystallography, **2**, 65-71 (1969).

91. A.C. Larson and R.B.V. Dreele, *GSAS -- General Structure Analysis System*, Los Alamos National Laboratory, (1994).

92. J.C. Russ, *Practical Stereology*, Plenum, New York, 1986.

93. P. Li, I.W. Chen and J.E. Penner-Hahn, *X-ray-absorption Studies of Zirconia Polymorphs. II. Effect of Y_2O_3 Dopant on ZrO_2 Structure*, Phy. Rev. **B 48**[14], 10074-81 (1993).

94. B.C.H. Steele, *Oxygen Ion Conductors and Their Technological Applications*, Materials Science and Engineering, **B13**, 79-87 (1992).

95. R.V. Kumar, *Application of Rare Earth Containing Solid State Ionic Conductors in Electrolytes*, J. Alloy and Compounds, **250**, 501-09 (1997).

96. V.M. Goldschmid, *Zusammenfassende Berichte: Konstruktion von Kristallen*, Zeitschr. f. Techn. Physik, **7**, 251-64 (1927).

97. R.D. Shannon, *Revised Effective Ionic Radii and Systematic Studies of Interatomic Distances in Halides and Chalcogenides*, Acta Cryst., **A32**, 751-67 (1976).

98. J.B. Goodenough and J.M. Longo, *Crystallographic and Magnetic Properties of Perovskite and Perovskite-related Compounds*, in Landholt-Bornstein Numerical Data and Functional Relationships in Science and Technology, Group III: Crystal and Solid State Physics, Volume 4: Magnetic and Other Properties of Oxides and Related Compounds, Springer, Berlin, Heidelberg, pp. 126-275 (1970).

99. J.K. Kilner, P.B. Barrow and R.J. Brook, *Electrolytes for the High Temperature Fuel Cell; Experimental and Theoretical Studies of the Perovskite $LaAlO_3$*, J. Power Sources, **3**, 67-80 (1978).

100. J.A. Kilner, *The Calculation of Defect Energies in the Perovskite Fluoride $KMnF_3$*, Phil. Mag. **A43**, 1473-82 (1981).

101. J.A. Kilner and R.J. Brook, *A Study of Oxygen Ion Conductivity in Doped Non-Stoichiometric Oxides*, Solid State Ionics, **6**, 237-52 (1982).

102. K. Nomura and S. Tanase, *Electrical Conduction Behavior in $(La_{0.9}Sr_{0.1})M^{III}O_{3-\delta}$ (M^{III} = Al, Ga, Sc, In, and Lu) Perovskites*, Solid State Ionics, 98, 229-236 (1997).

103. G.V. Samsonov, *The Oxide Handbook*, IFI/Plenum, New York, 1973.

104. K.K. Irikura and D.J. Frurip, *Computational Thermochemistry, Prediction and Estimation of Molecular Thermodynamics*, American Chemical Society, 1998.

105. V. Luana and L. Pueyo, Simulation of Ionic Crystals: *The ab initio Perturbed-ion Method and Application to Alkali Hydrides and Halides*, Phys. Rev. **B41**, 3800-3814 (1990).

106. V. Luana, M. Florez, E. Francisco, A.M. Pendas, J.M. Recio, M. Bermejo and L. Pueyo, *Quantum Mechanical Cluster Calculations of Solids: The ab initio Perturbed Ion Method, Cluster Models for Surface and Bulk Phenomena*, Edited by G. Pacchioni *et al.*, Plenum Press, New York, 605-618 (1992).

107. V. Luana, A. M. Pendas, J. M. Recio, E. Francisco, and M. Bermejo, *Quantum Mechanical Cluster Calculations of Ionic Materials: the ab initio Perturbed Ion (Version 7) Program*, Comput. Phys. Commun. 77, 107-34 (1993).

APPENDIX I

DIFFRACTION DATA FOR LSGM PEROVSKITES

Crystal structure analysis performed on all LSGM materials that were prepared and used in this study are based on room temperature and high temperature X-ray and neutron diffraction data. These raw data are presented in this Appendix in terms of doping content and temperature. Below is the figure captions for them.

Fig. AI-1 to AI-3 are room temperature X-ray diffraction spectra for LSGM-0000, LSGM-1010 and LSGM-2020 at various A/B ratios.

Fig. AI-4 to AI-8 are HTXRD spectra for LSGM-0000 from A/B = 0.95 to 1.05 at various temperatures.

Fig. AI-9 to AI-13 are HTXRD spectra for LSGM-1010 from A/B = 0.95 to 1.05 at various temperatures.

Fig. AI-14 to AI-18 are neutron diffraction spectra for stoichiometric LSGM-1010 at various temperatures.

Fig. AI-19 to AI-23 are HTXRD spectra for LSGM-2020 from A/B = 0.95 to 1.05 at various temperatures.

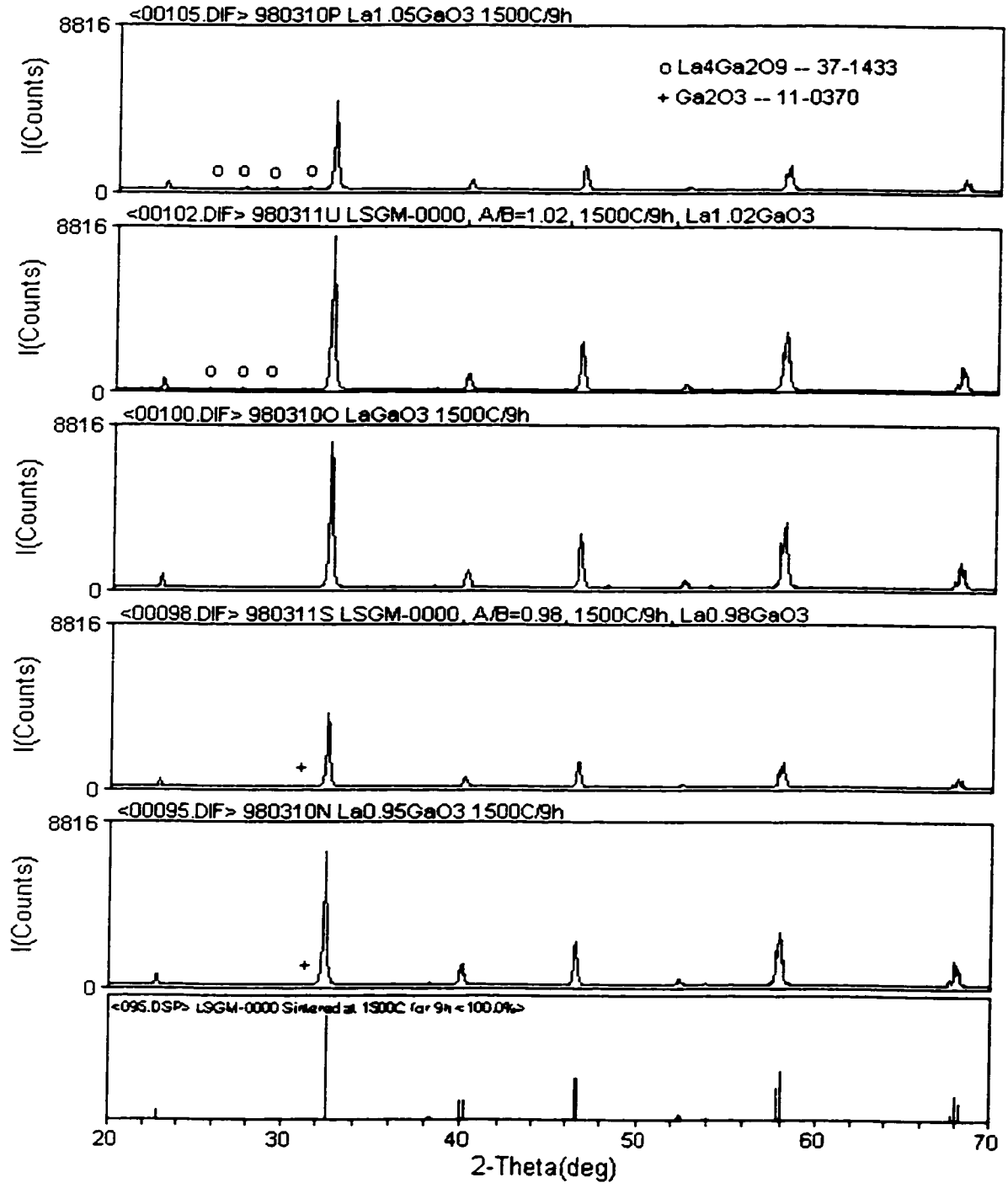

Fig. AI-1 X-ray spectra of LSGM-0000 with various A/B cation ratios

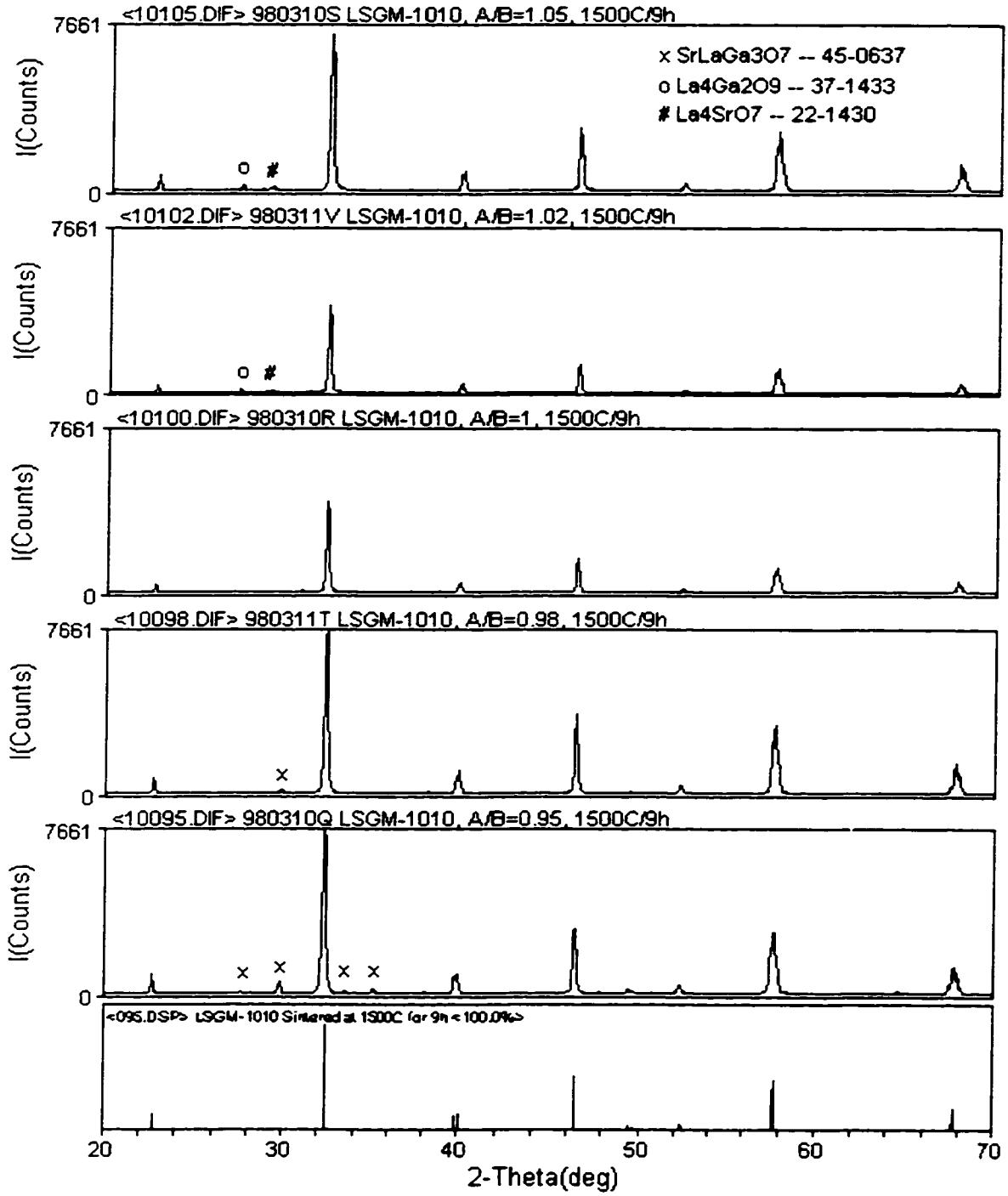

Fig. AI-2 X-ray spectra of LSGM-1010 with various A/B cation ratios

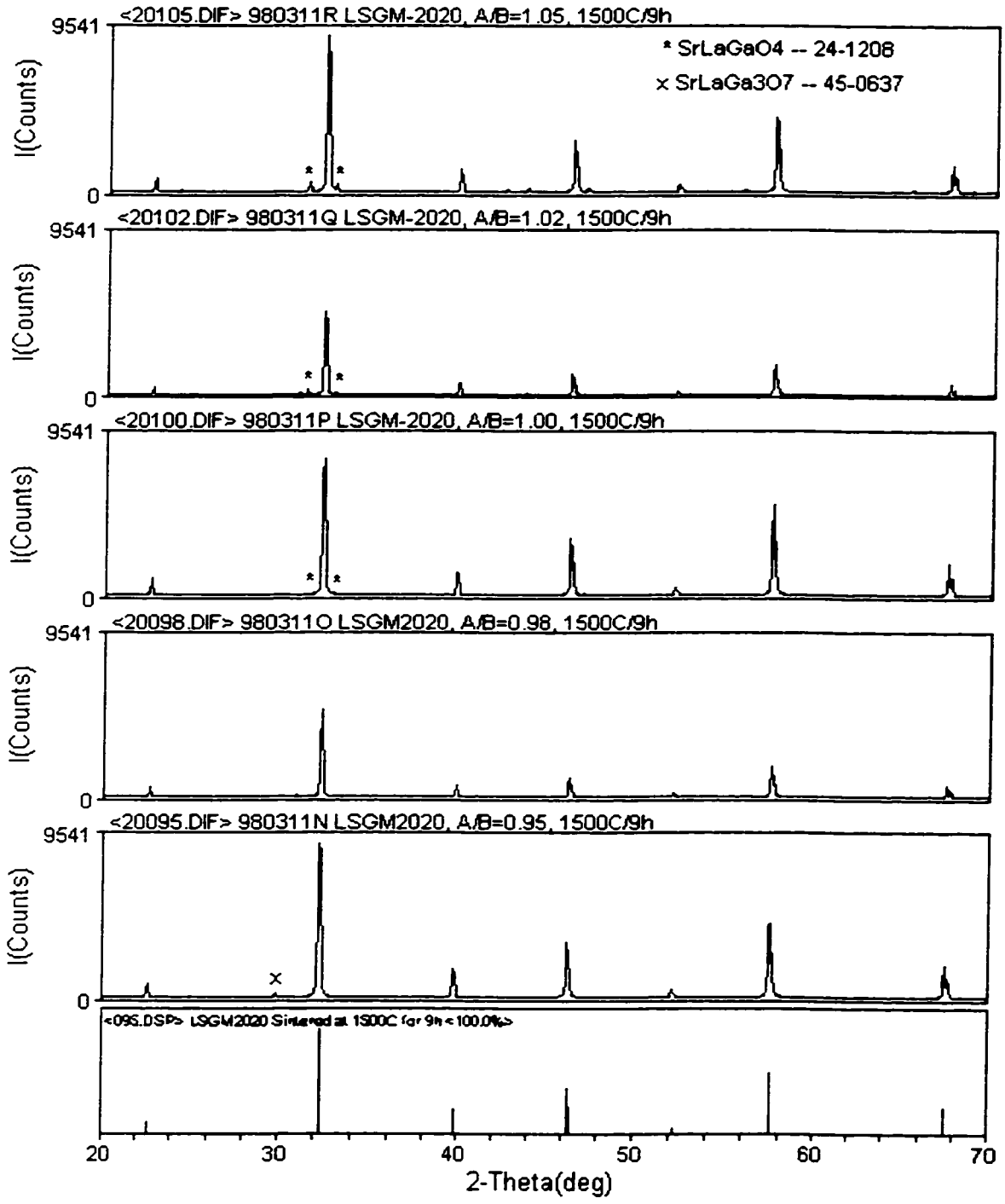

Fig. AI-3 X-ray spectra of LSGM-2020 with various A/B cation ratios

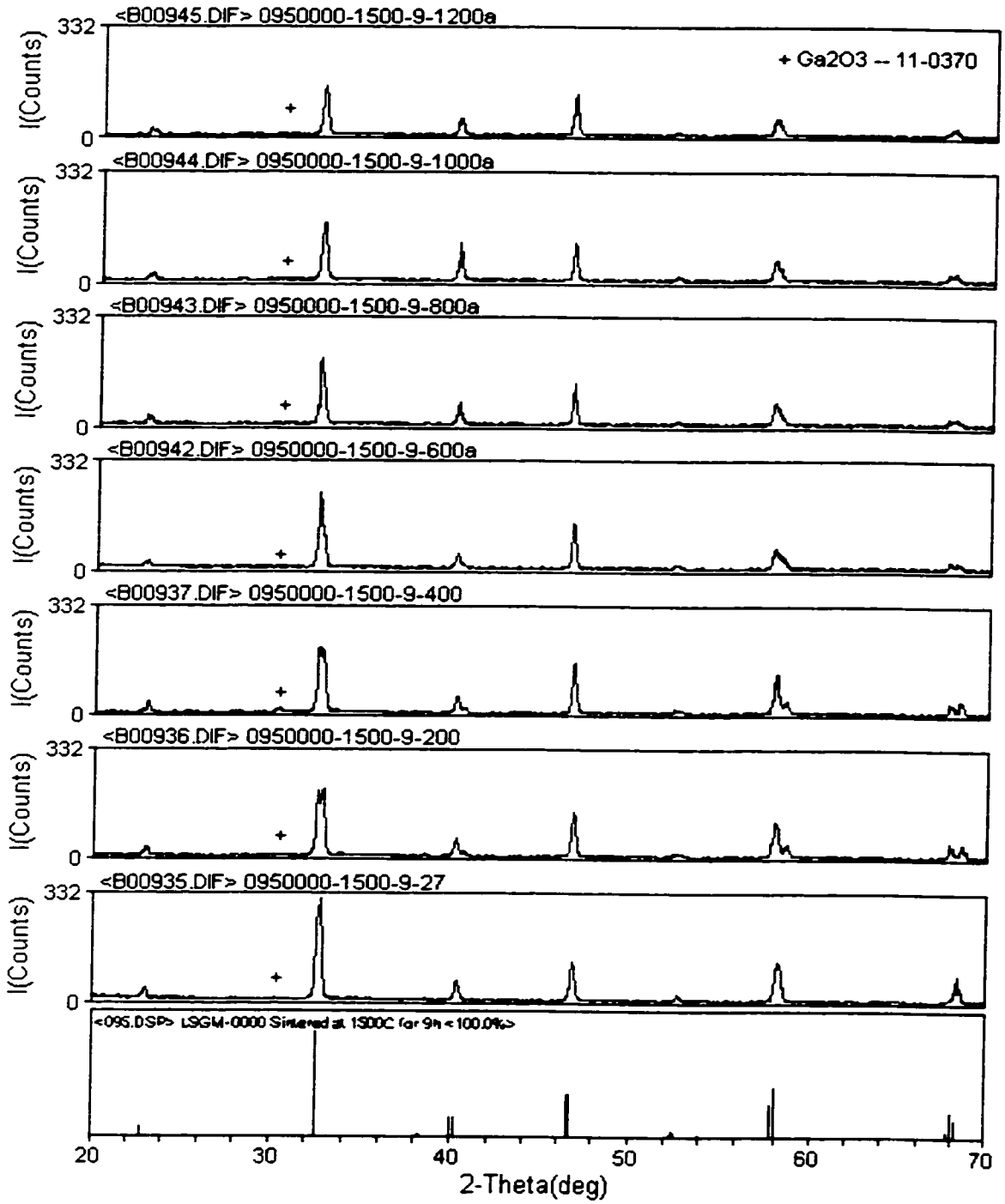

Fig. AI-4 HTXRD data for LSGM-0000 (A/B=0.95)

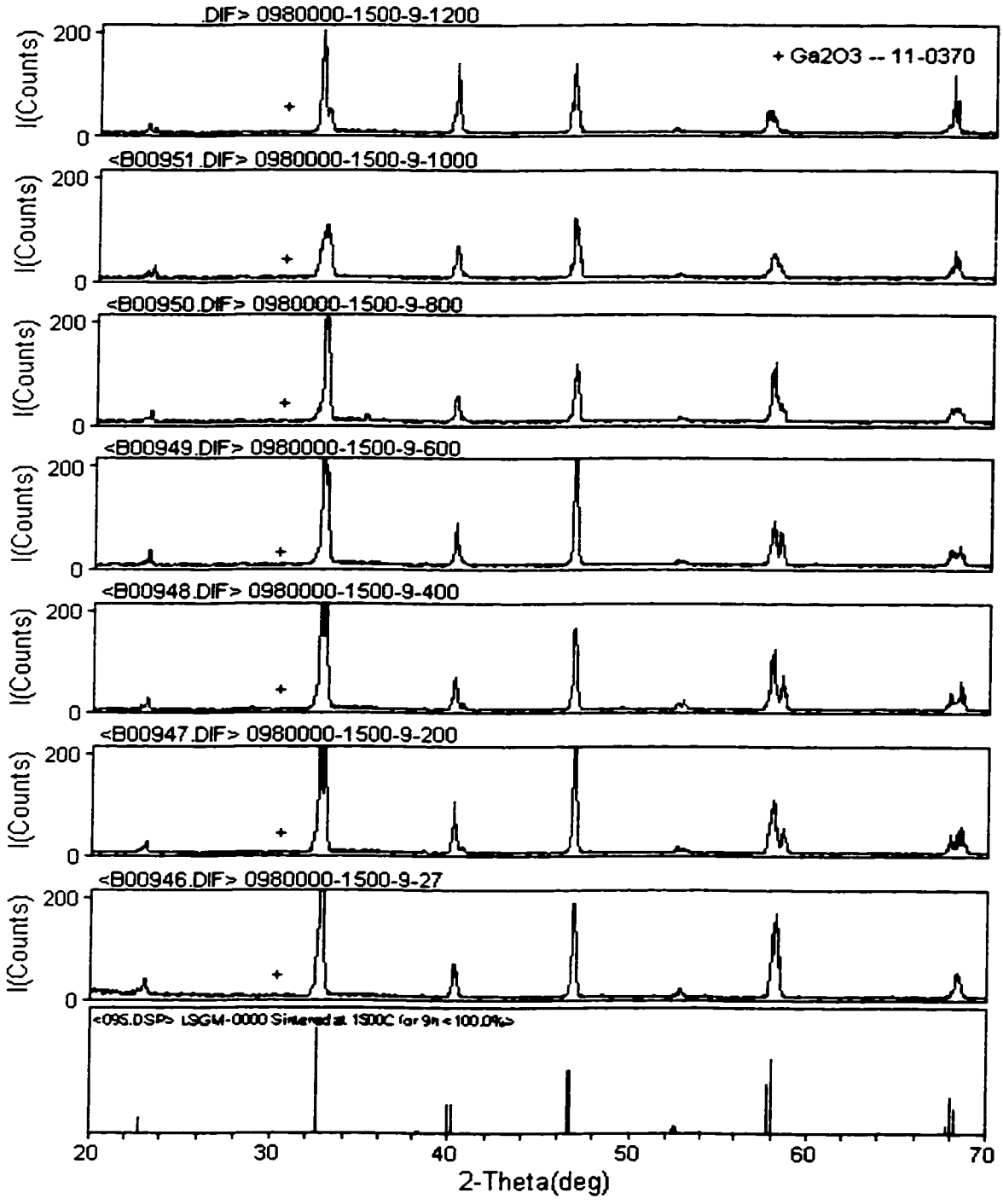

Fig. AI-5 HTXRD data for LSGM-0000 (A/B=0.98)

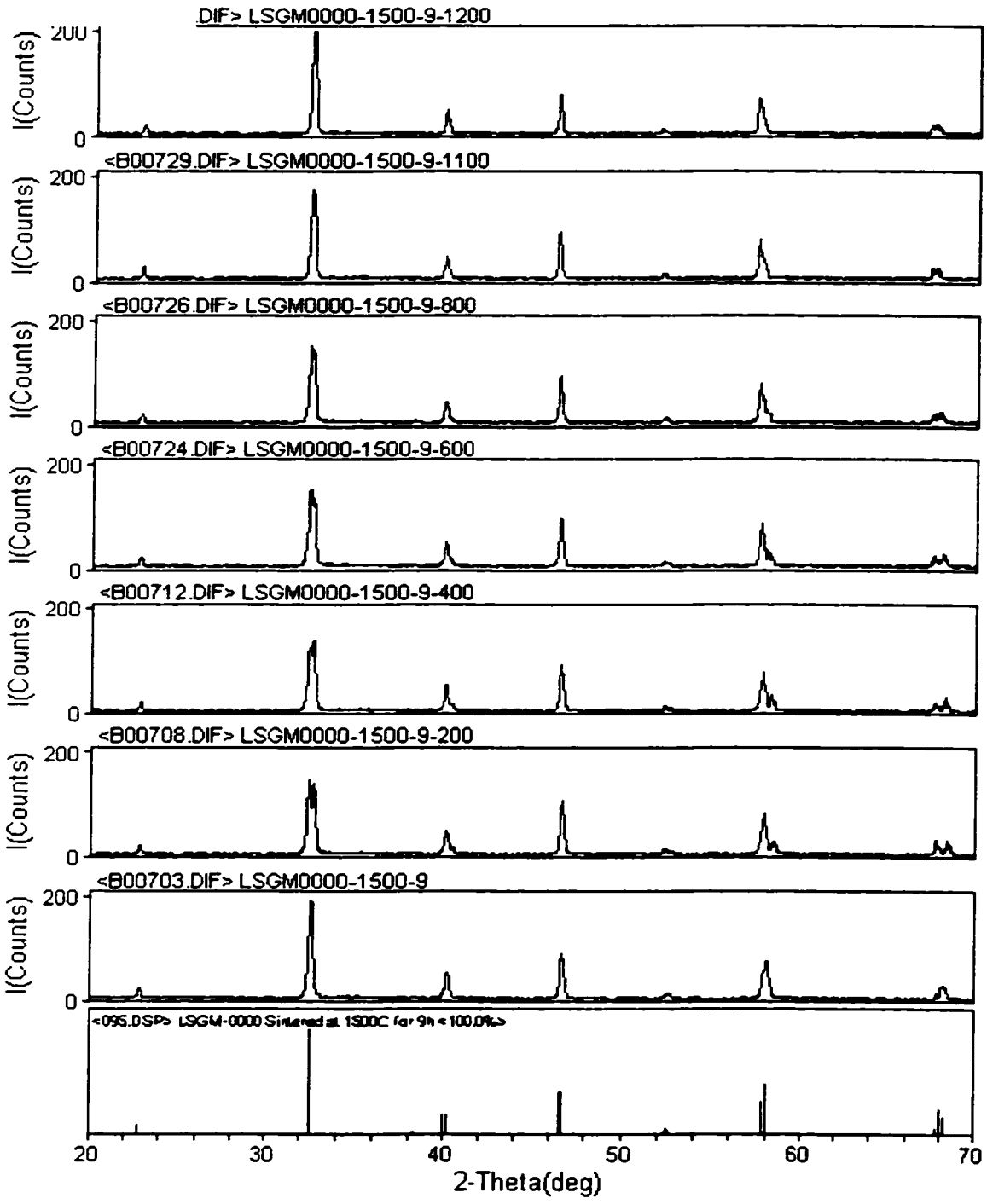

Fig. AI-6 HTXRD data for LSGM-0000 (A/B=1.00)

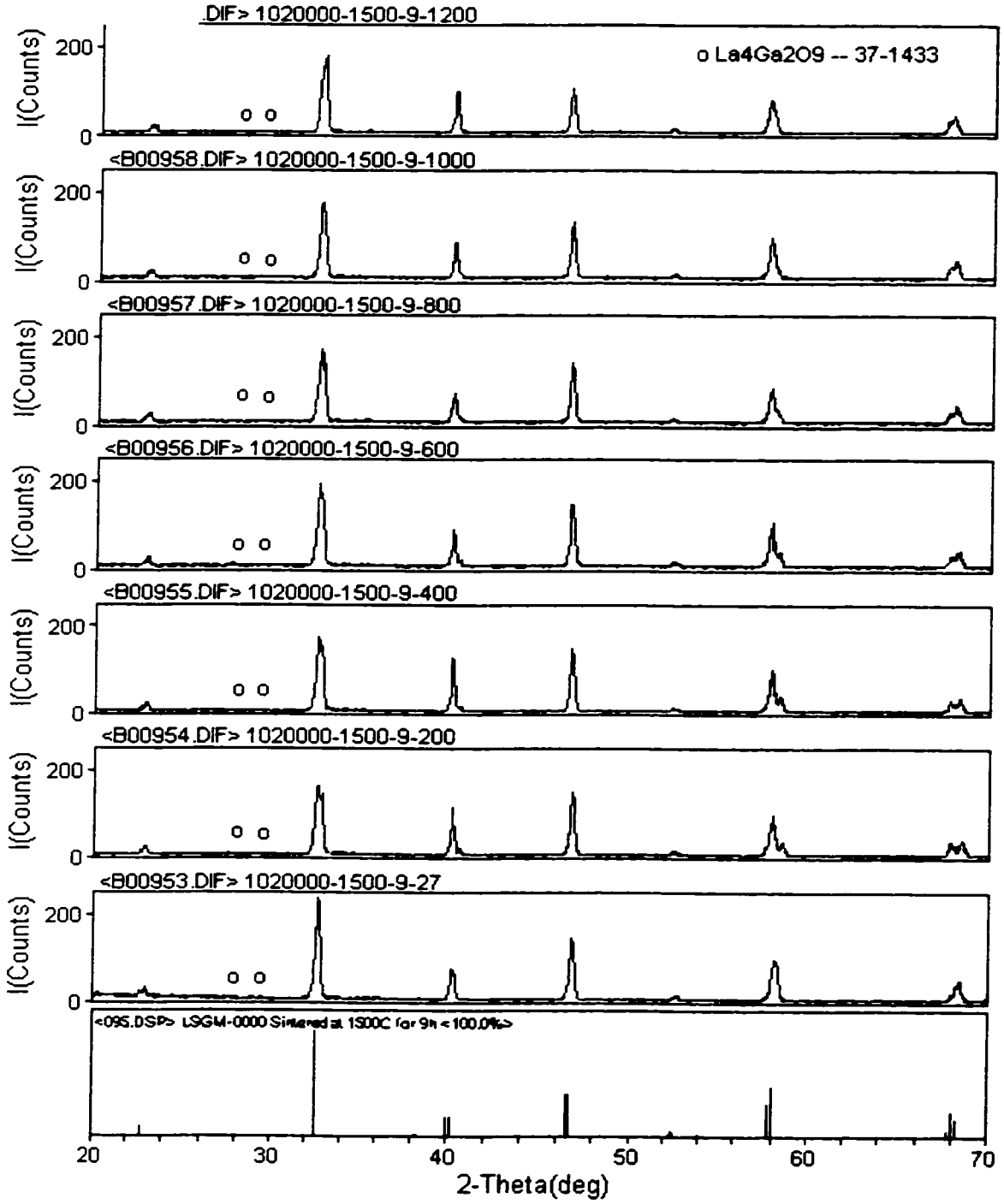

Fig. AI-7 HTXRD data for LSGM-0000 (A/B= 1.02)

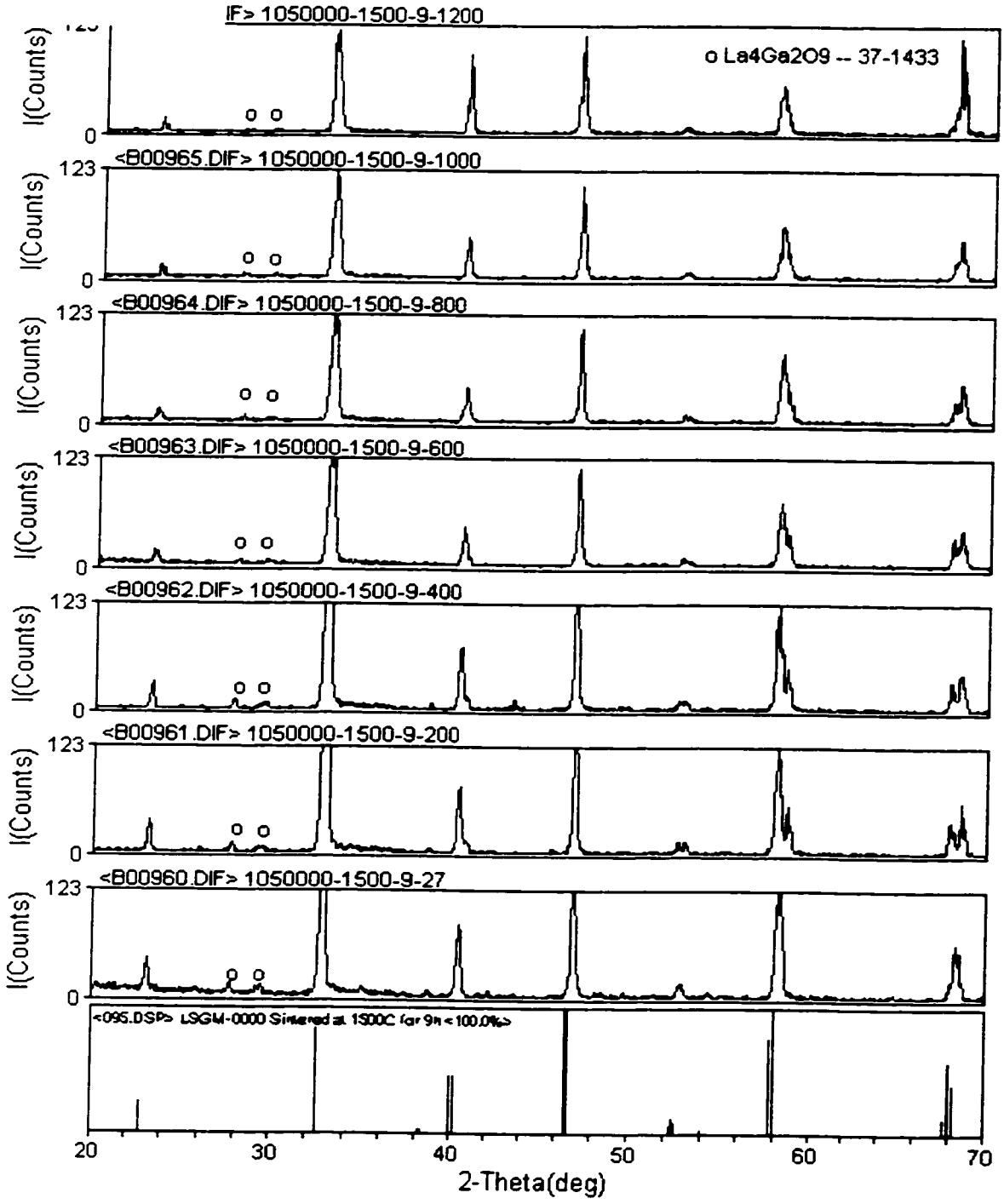

Fig. AI-8 HTXRD data for LSGM-0000 (A/B=1.05)

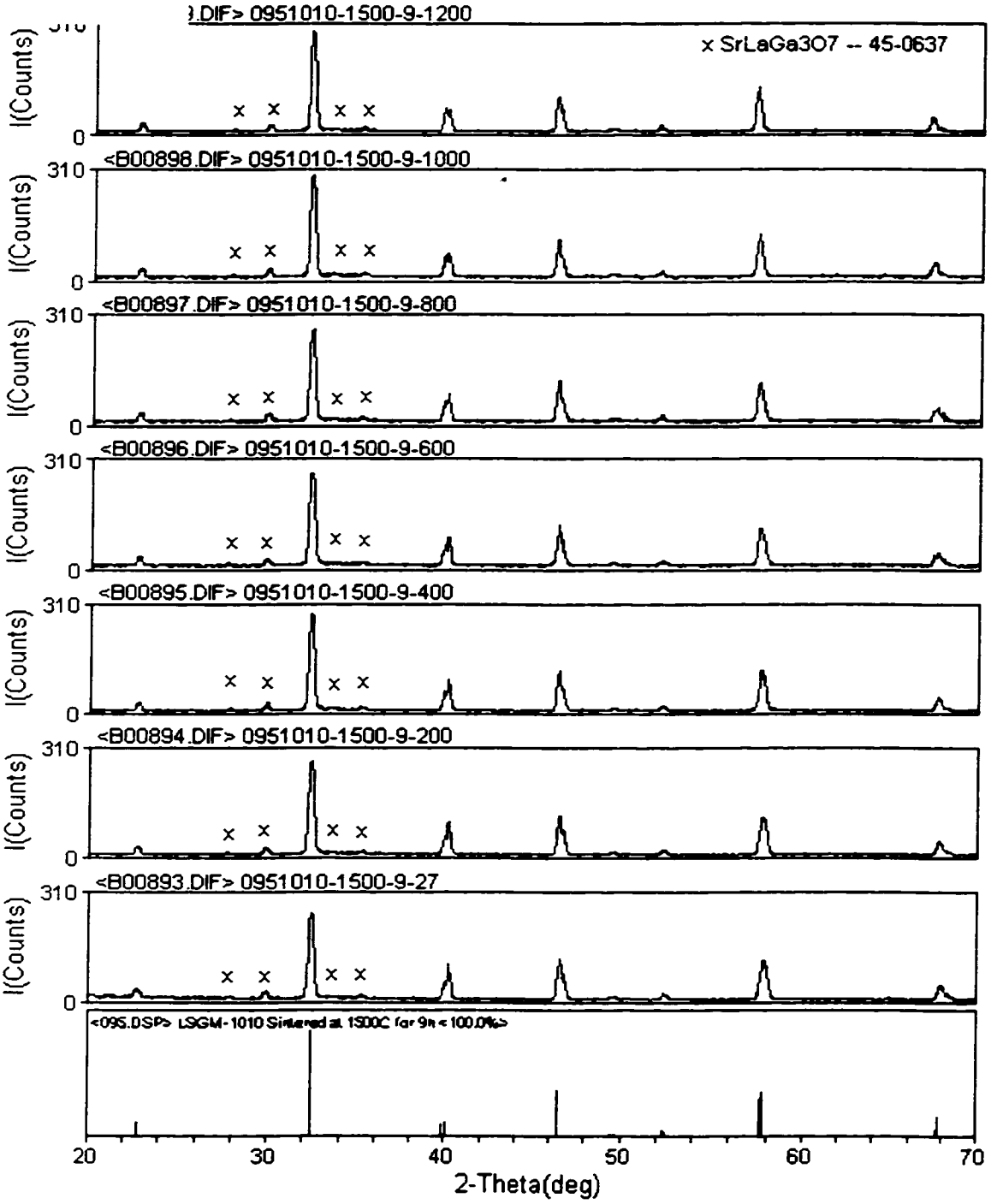

Fig. AI-9 HTXRD data for LSGM-1010 (A/B=0.95)

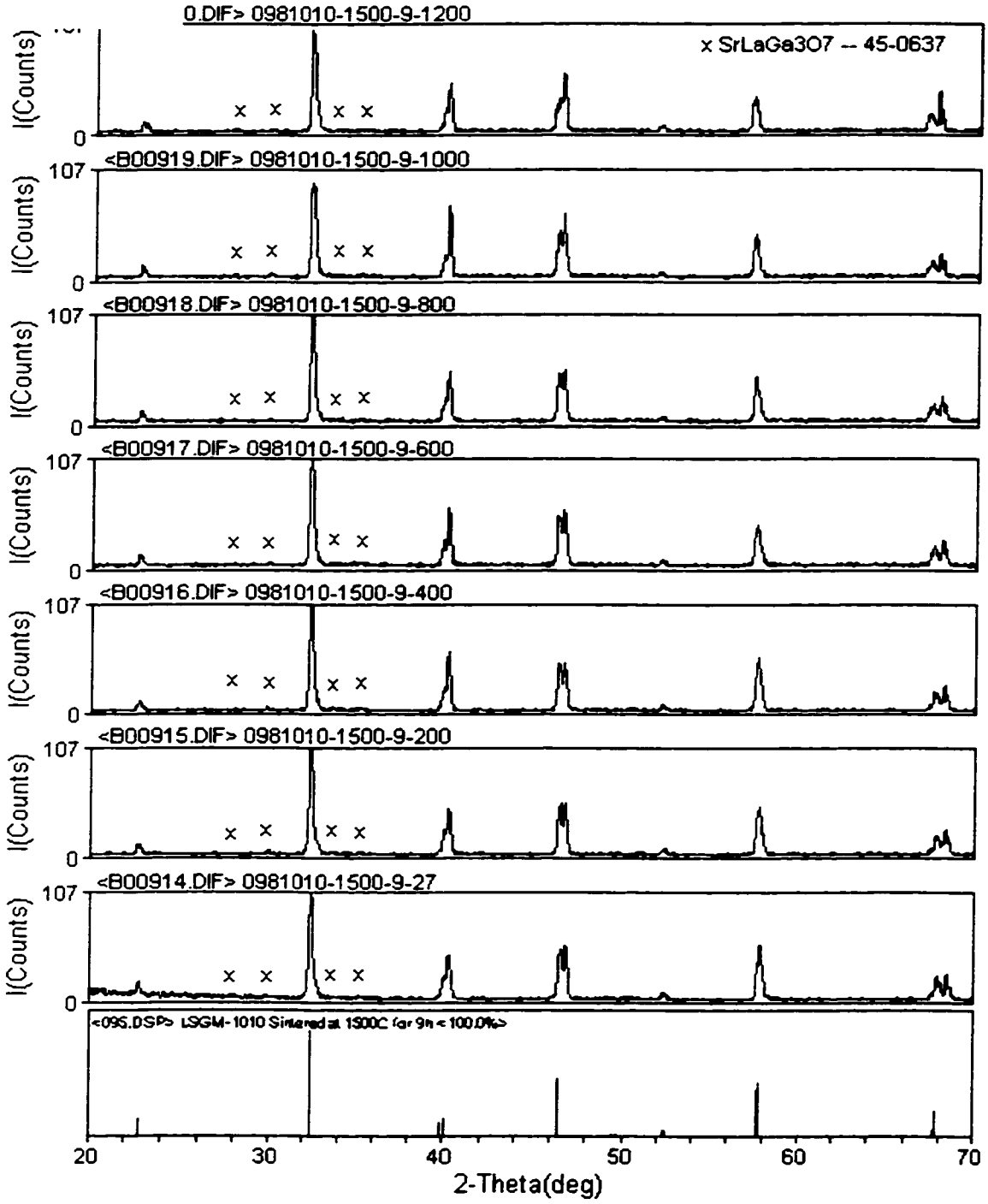

Fig. AI-10 HTXRD data for LSGM-1010 (A/B=0.98)

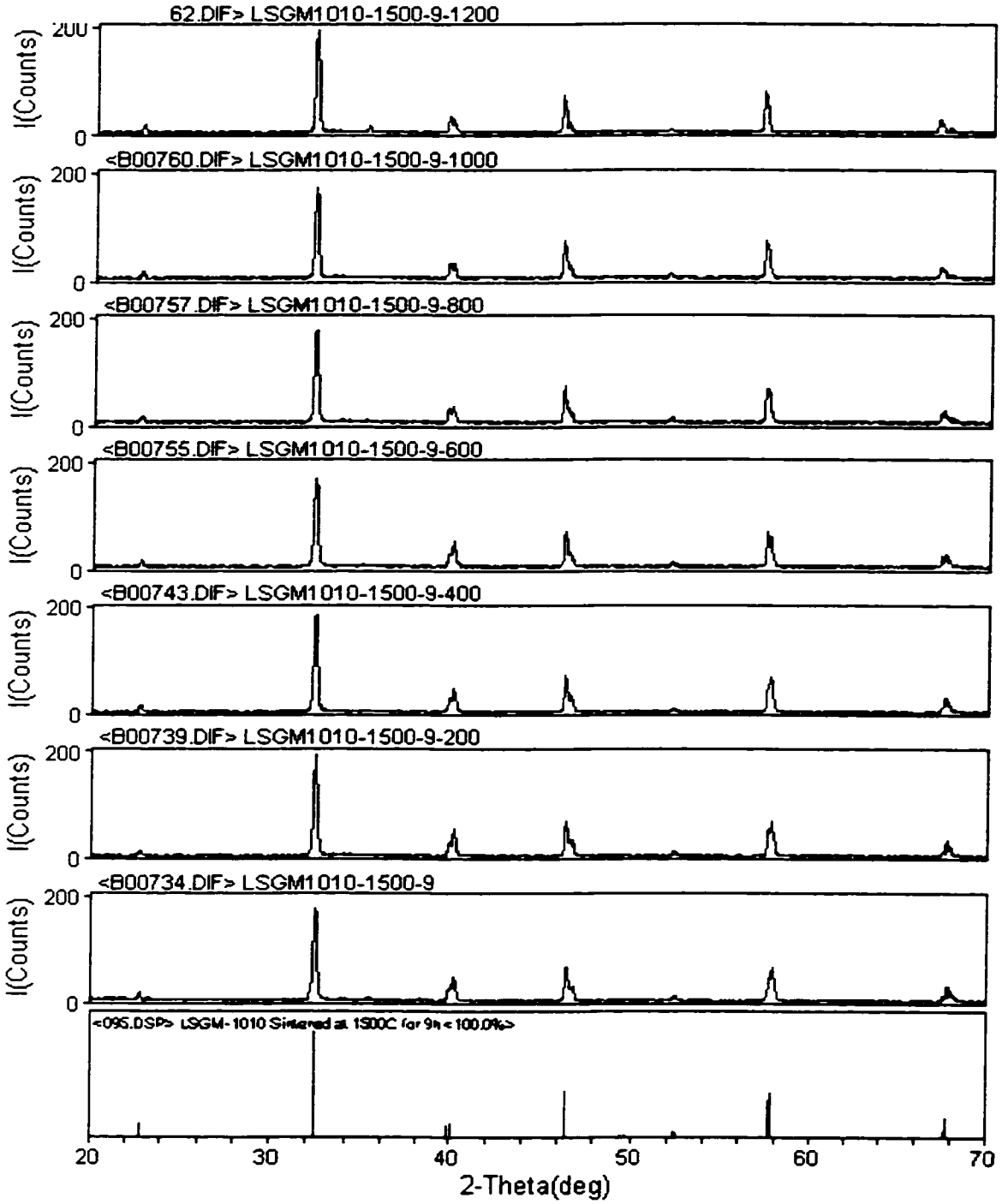

Fig. AI-11 HTXRD data for LSGM-1010 (A/B= 1.00)

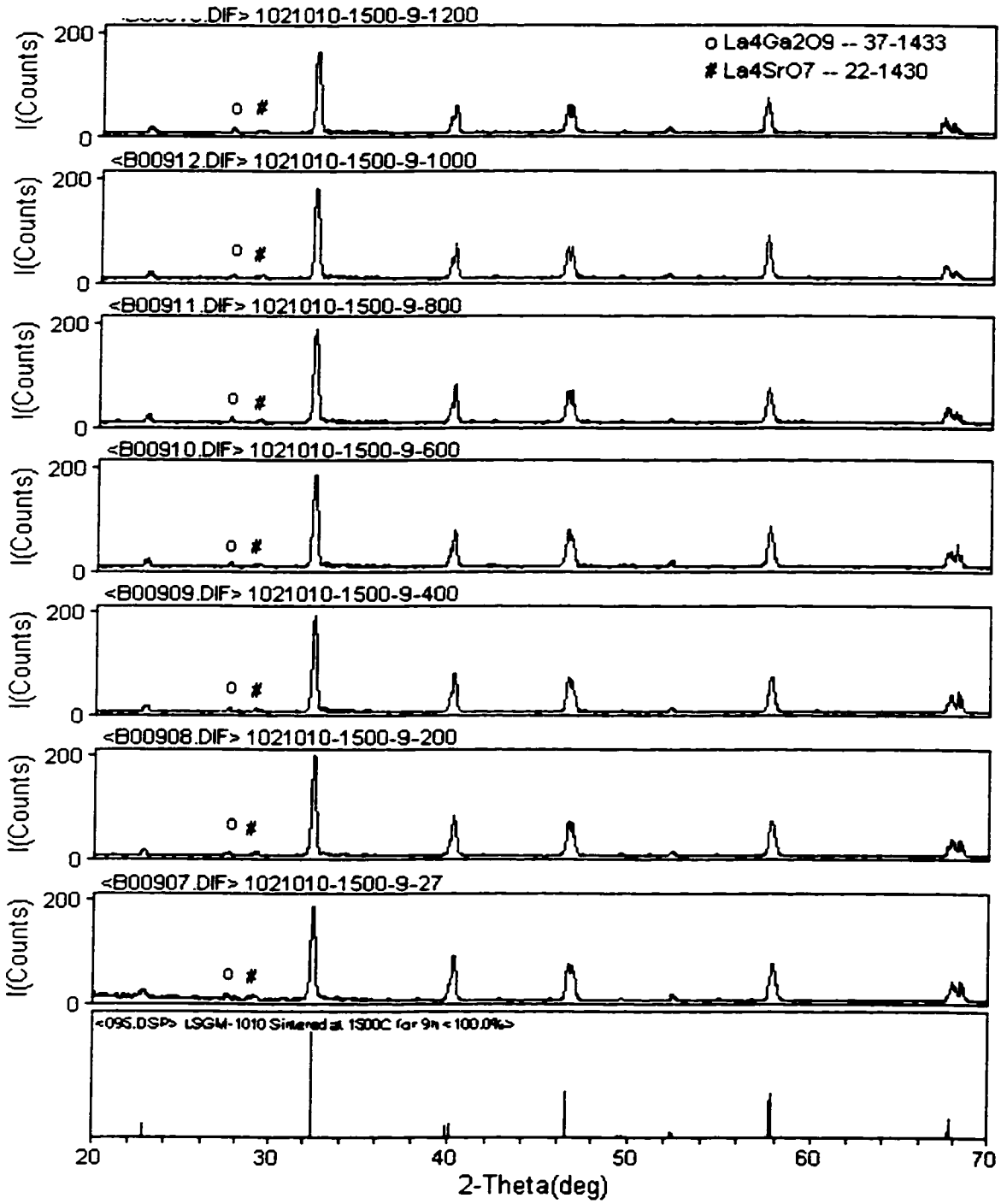

Fig. AI-12 HTXRD data for LSGM-1010 (A/B= 1.02)

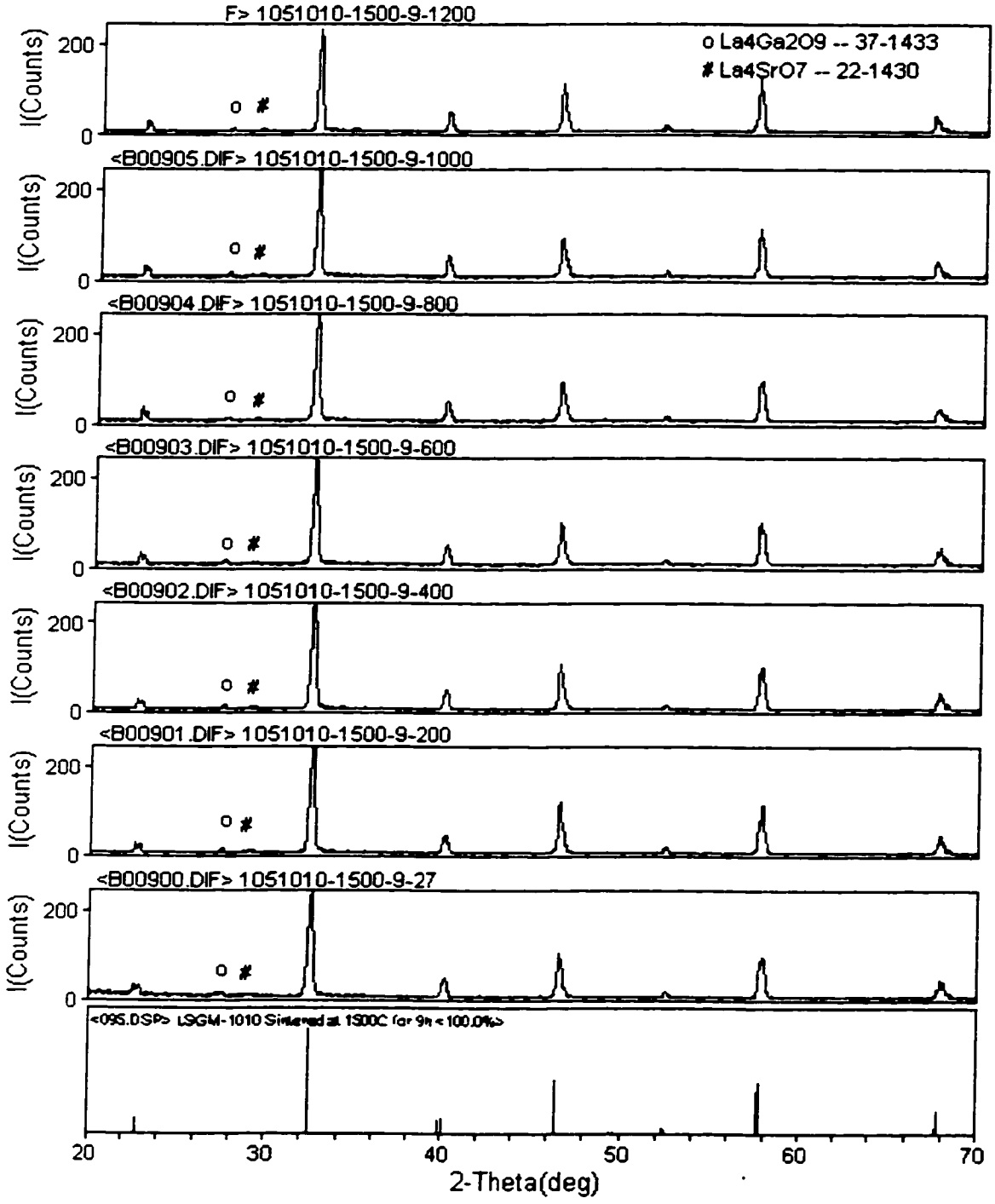

Fig. AI-13 HTXRD data for LSGM-1010 (A/B= 1.05)

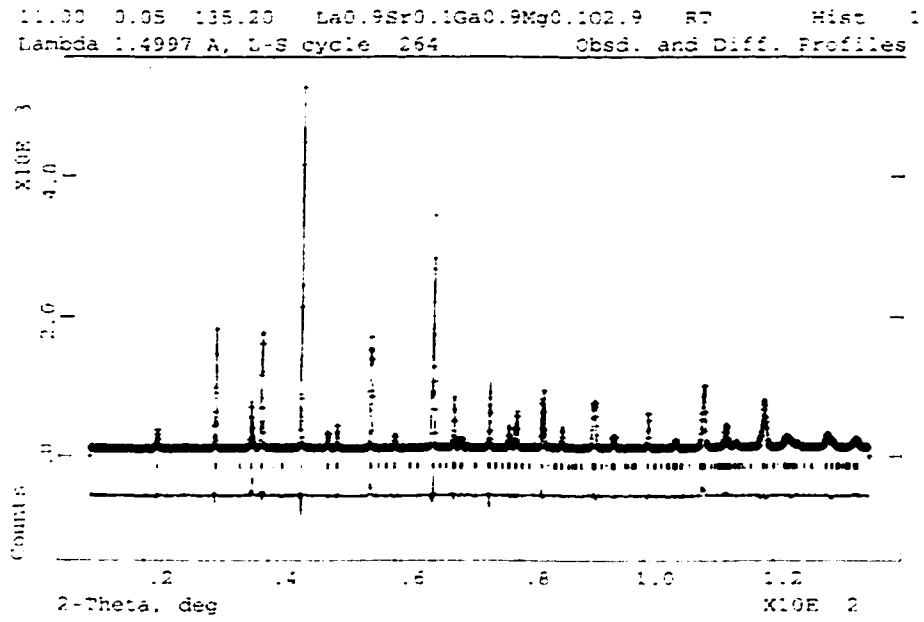

Fig. AI-14 Neutron diffraction data of LSGM-1010 (A/B= 1.00) at room temperature

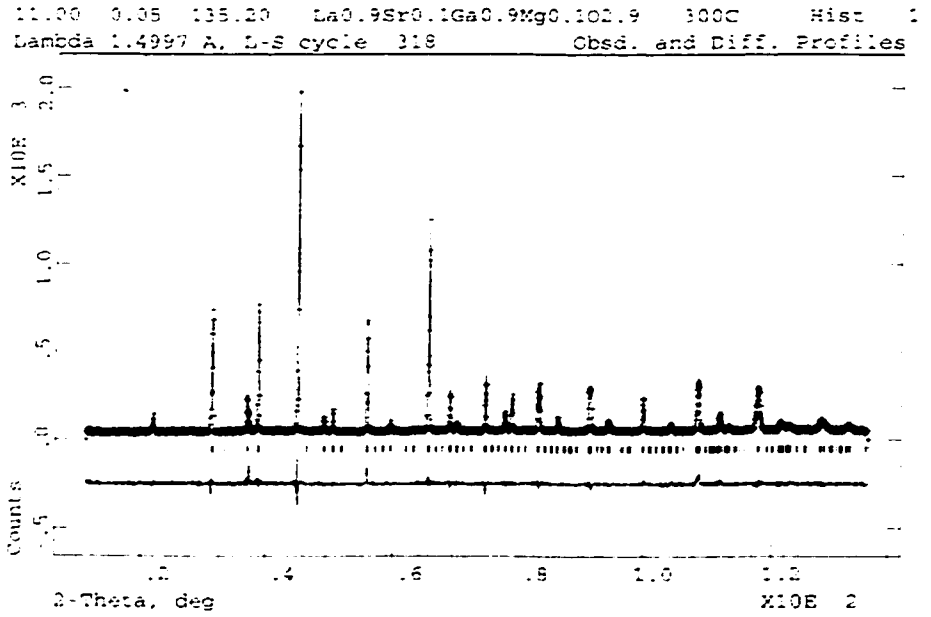

Fig. AI-15 Neutron diffraction data of LSGM-1010 (A/B= 1.00) at 300°C

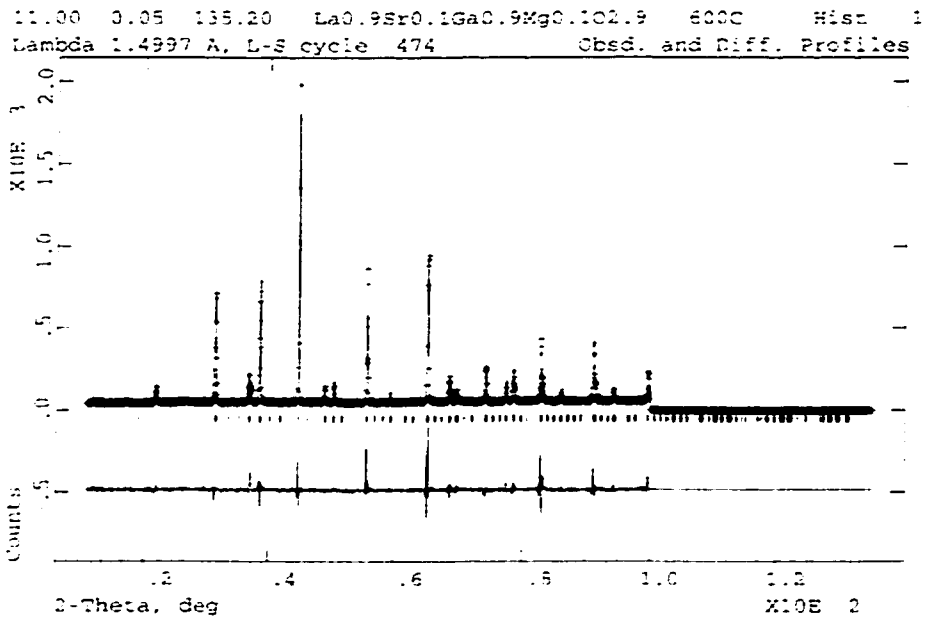

Fig. AI-16 Neutron diffraction data of LSGM-1010 (A/B= 1.00) at 600°C

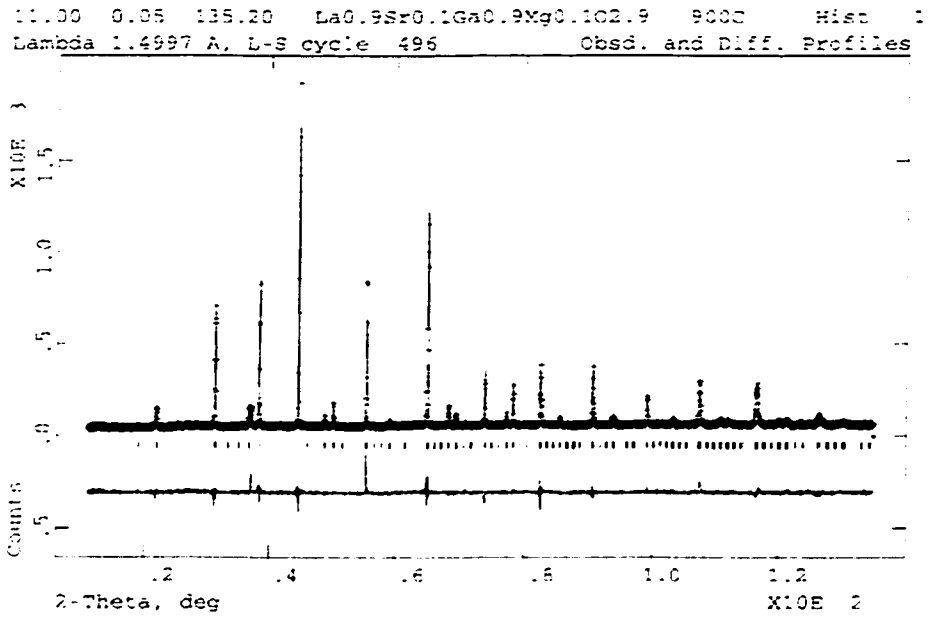

Fig. AI-17 Neutron diffraction data of LSGM-1010 (A/B= 1.00) at 900°C

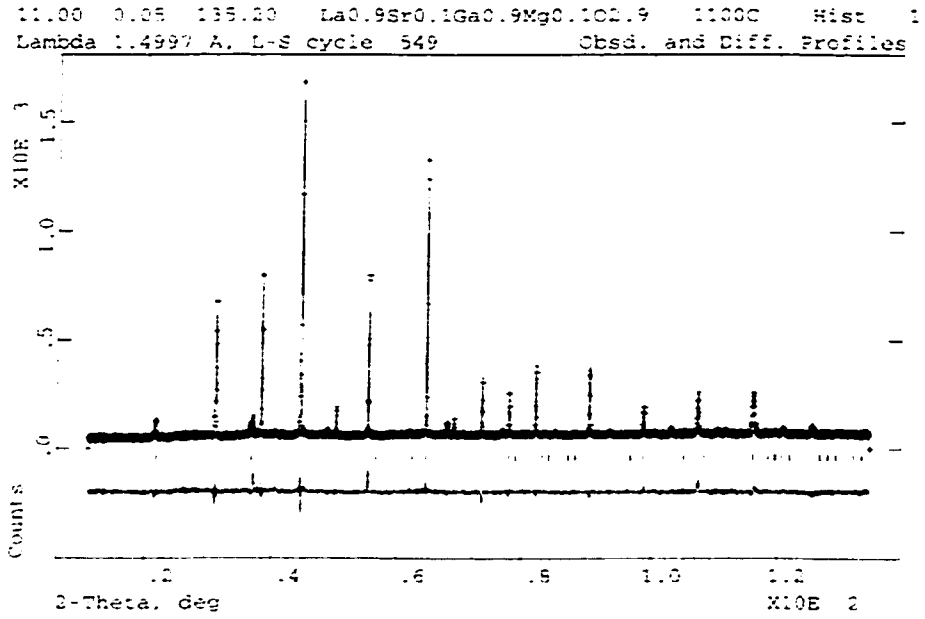

Fig. AI-18 Neutron diffraction data of LSGM-1010 (A/B= 1.00) at 1100°C

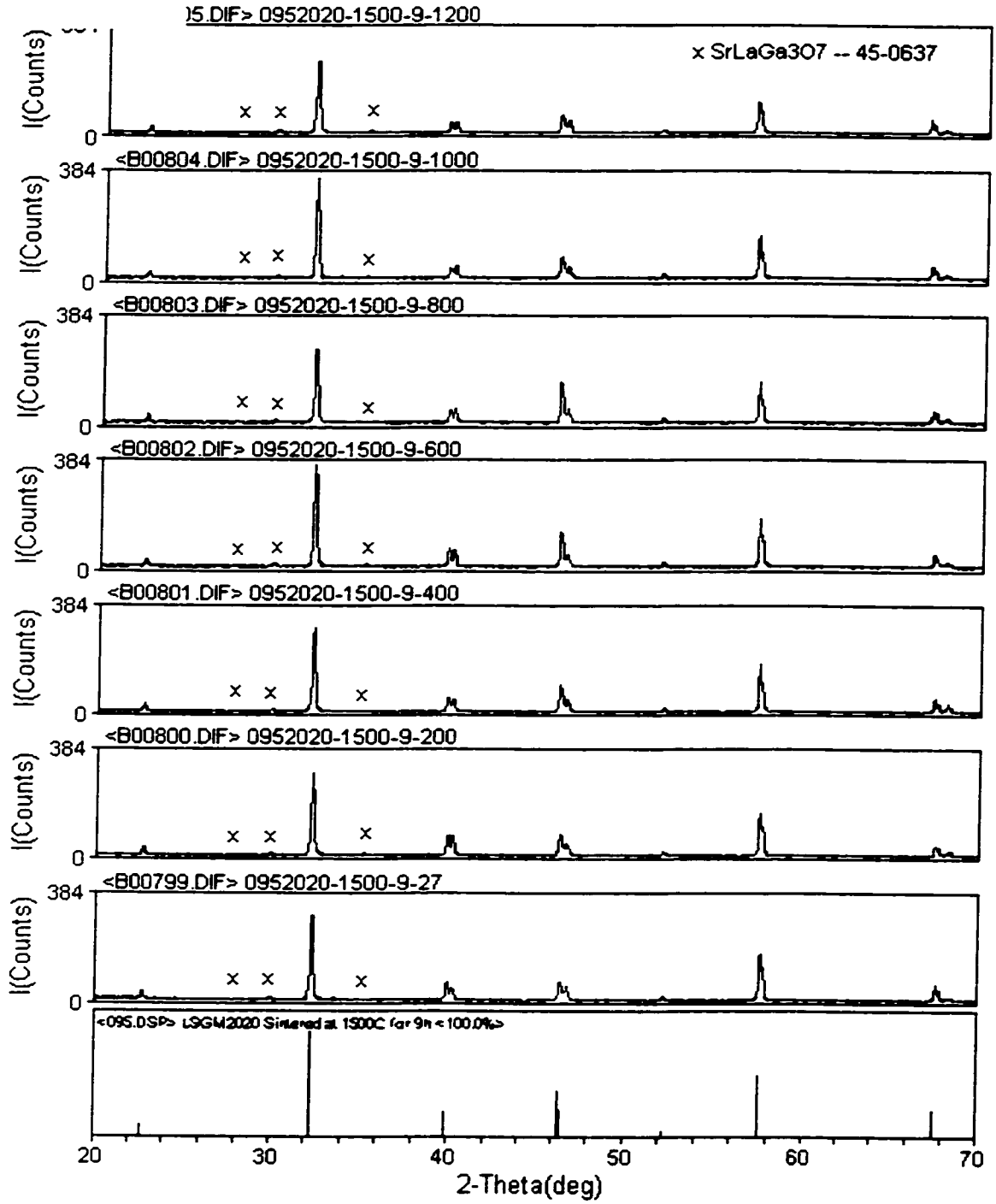

Fig. AI-19 HTXRD data for LSGM-2020 (A/B=0.95)

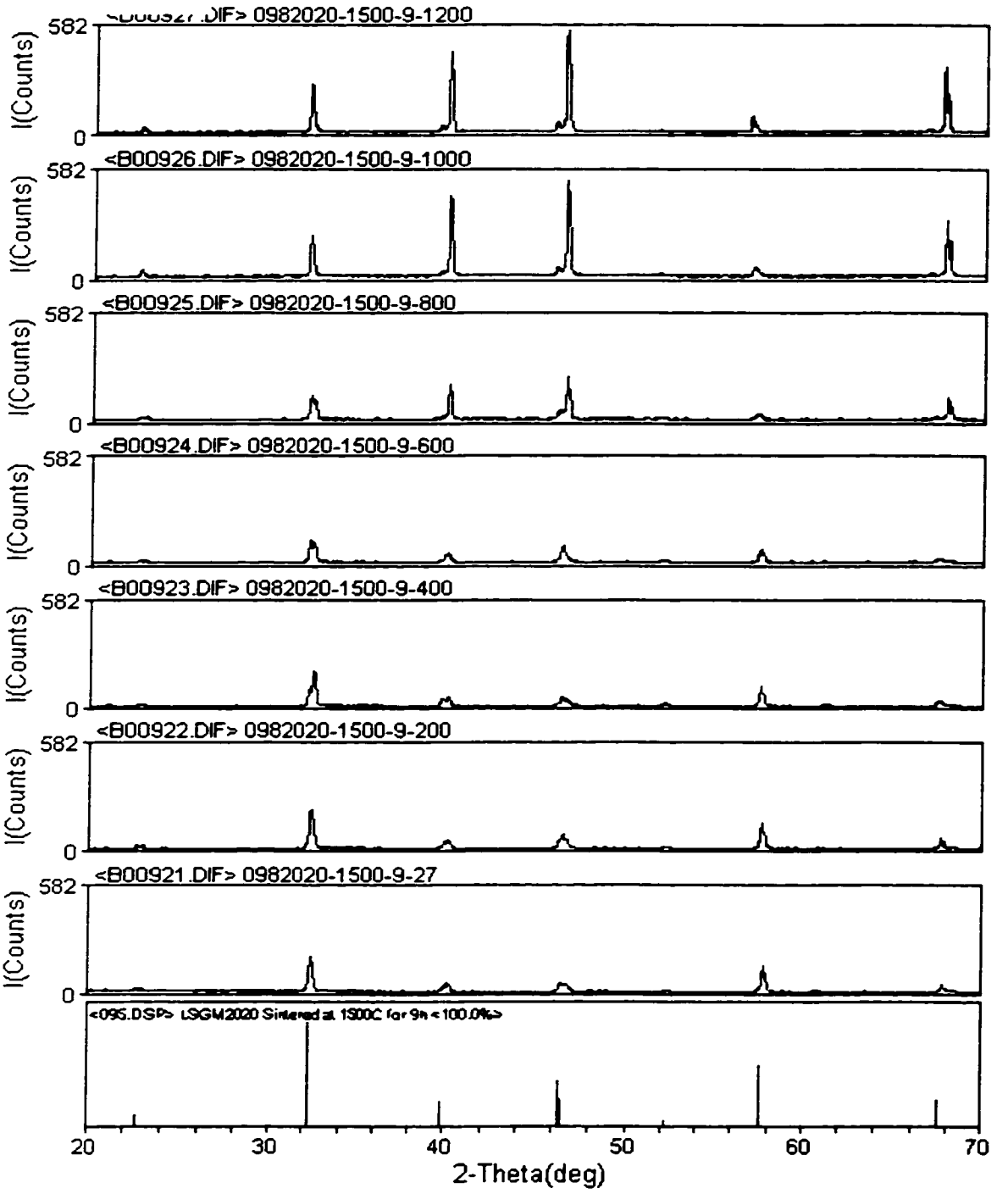

Fig. AI-20 HTXRD data for LSGM-2020 (A/B=0.98)

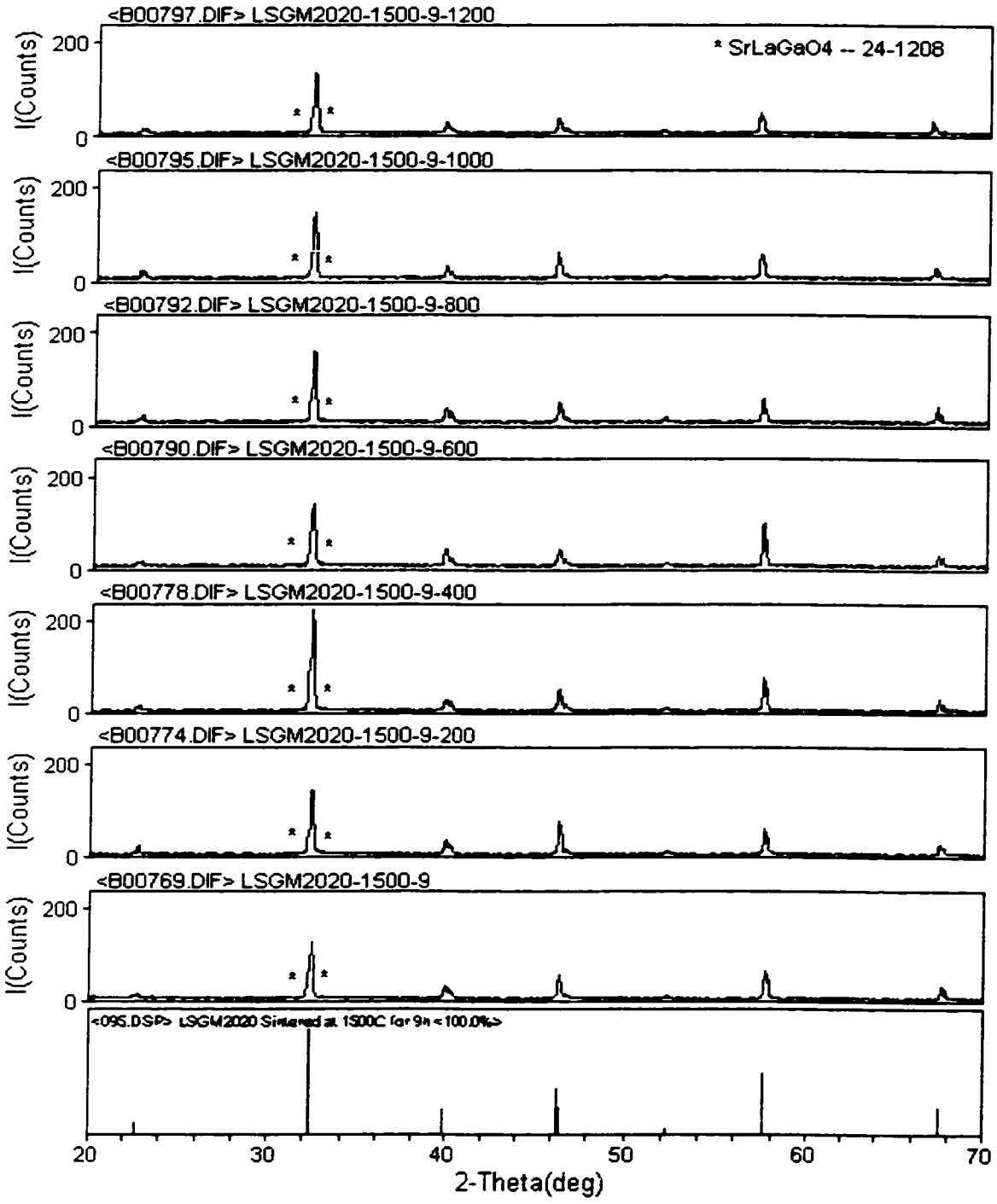

Fig. AI-21 HTXRD data for LSGM-2020 (A/B=1.00)

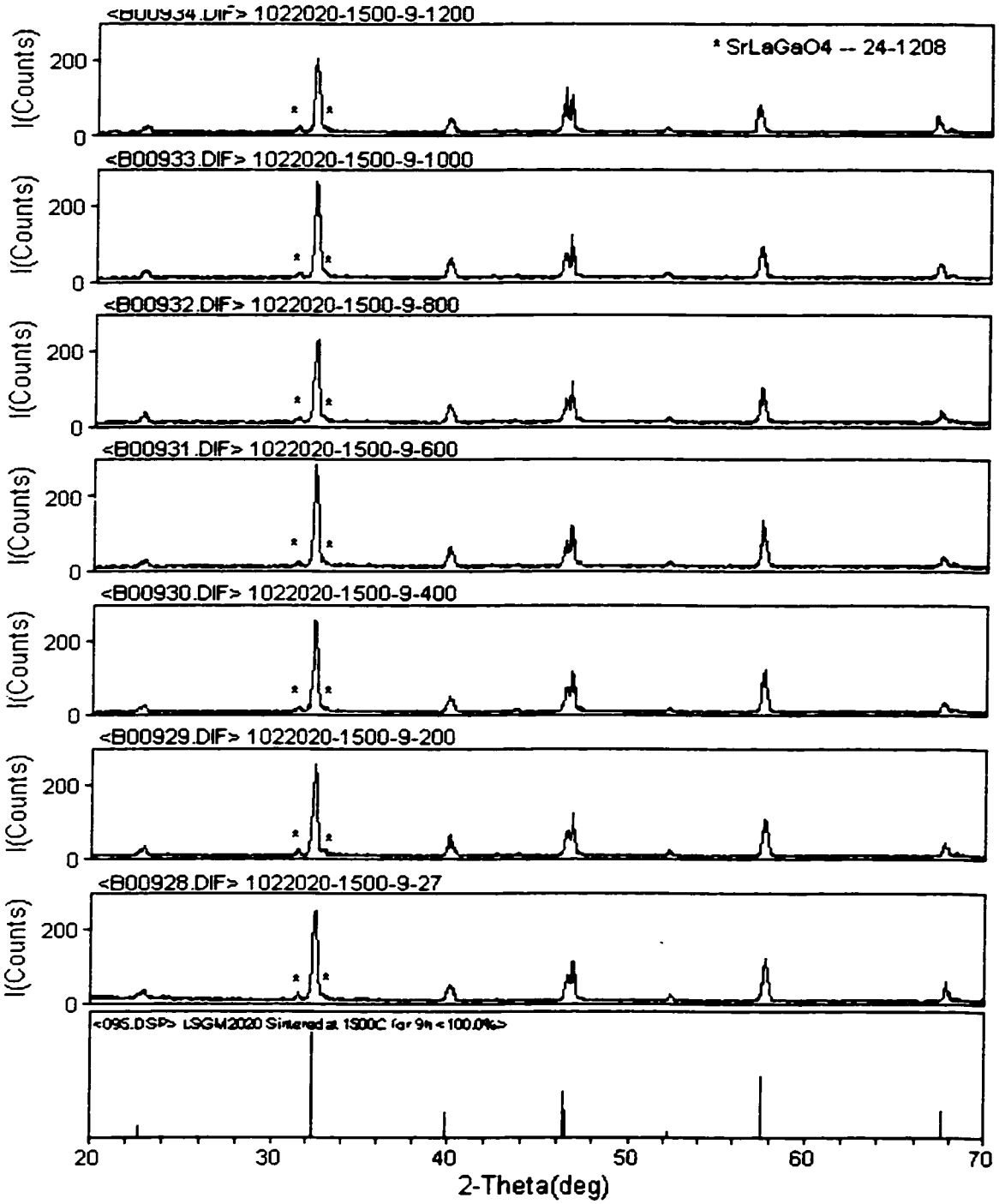

Fig. AI-22 HTXRD data for LSGM-2020 (A/B=1.02)

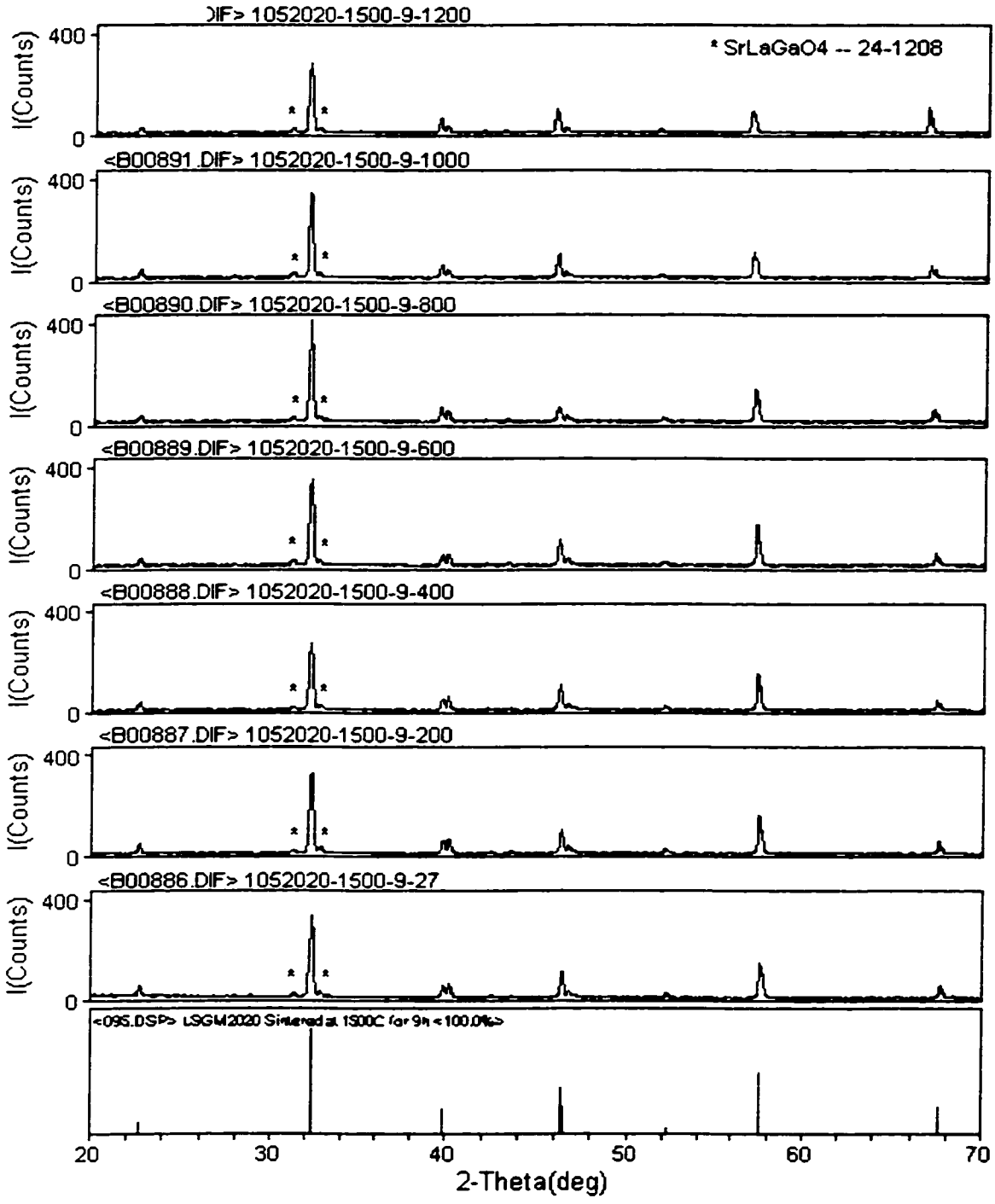

Fig. AI-23 HTXRD data for LSGM-2020 (A/B=1.05)

APPENDIX II

PHASE RELATIONSHIPS IN THE La-Sr-Ga-Mg-O SYSTEM

Most phase diagram information, if existed, was retrieved from the Phase Diagrams for Ceramists (PDC), published by The American Ceramic Society, Inc., between 1964 to 1996. The figure number used by PDC for a particular phase diagram was recorded for reference. Sources other than these from PDC will be cited as normal. A quaternary phase diagram of La_2O_3-SrO-Ga_2O_3-MgO system is proposed based on the available data from Powder Diffraction File (PDF) in JADE and the results of this study.

AII.1 THE BINARY SYSTEMS

AII.1.1 La_2O_3-Ga_2O_3 [PDC 340] System

Only two straight lines, representing the compositions of two binary compounds were adopted by PDC. That simple phase diagram remains widely used in the west since its publication in 1961. A high temperature phase diagram with much more information was published by Mizuno and co-workers in 1985.[AII-1] The phase diagram (see Fig. AII-1) is adopted in this study. The relevant phase information for the La_2O_3-Ga_2O_3 system is presented in Table AII-1.

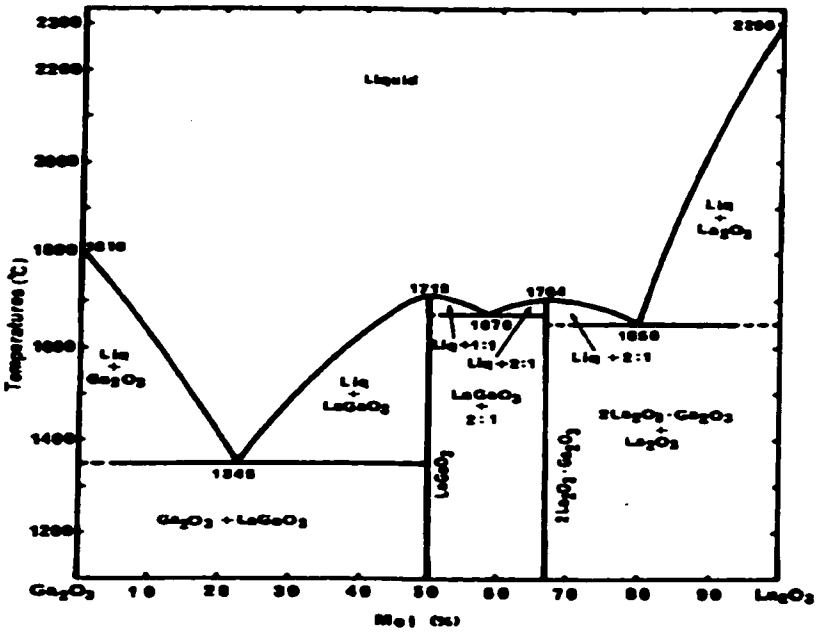

Fig. AII-1 Phase diagram of the system Ga_2O_3-La_2O_3 at high temperatures[AII-1]

Table AII-1 Phase presented at La_2O_3-Ga_2O_3 binary system[AII-1,2]

Phase	*melting point (°C)*	*PDF*	*notice*
La_2O_3	*2307*	*40-1284*	*congruent*
$La_4Ga_2O_9$	*1704±20*	*37-1433*	*congruent*
$LaGaO_3$	*1715±20*	*24-1102*	*congruent*
Ga_2O_3	*1900*	*11-0370*	*congruent*

AII.1.2 SrO-Ga_2O_3 [PDC 4359] System

There are five binary compounds in this binary in PDC version, where only one phase with composition $SrGa_2O_4$ melts congruently at 1580°C, the remaining melt incongruently (decomposed). The phase diagram is shown by Fig. AII-2. All available phase information is listed in Table AII-2 with proper PDC and PDF number indicates the source where the data comes from.

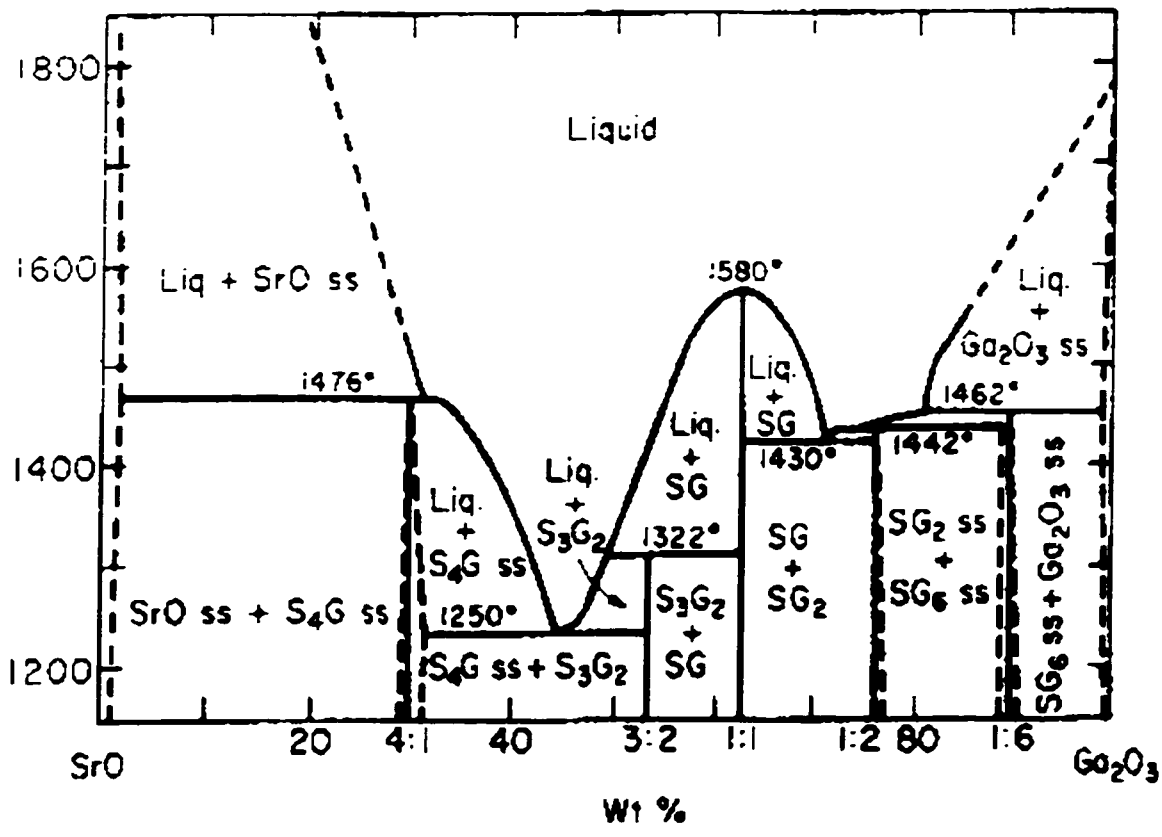

Fig. AII-2 The SrO-Ga_2O_3 phase diagram

Table AII-2 Phase presented at SrO-Ga_2O_3 binary system

phase	*melting point (°C)*	*PDF*	*notice*
SrO	*2430*	*06-0520*	*congruent*
$Sr_4Ga_2O_7$	*1476 (1540)*	*21-1181*	*incongruent*
$Sr_7Ga_4O_{13}$	*1490 PDC 10117*		*?*
$Sr_3Ga_2O_6$	*1230 PDC 10117*	*24-1200*	*decompose*
$Sr_3Ga_4O_9$	*1250* *1350 PDC 10117*	*31-1358*	*incongruent*
$SrGa_2O_4$	*1580* *1575 PDC 92-067* *1350 PDC 10117*	*22-0905*	*congruent*
$SrGa_4O_7$	*1442* *1440 PDC 92-067* *1490 PDC 10117*		*incongruent*
$SrGa_{12}O_{19}$	*1462* *1550 PDC 10117*	*26-0983*	*incongruent*
Ga_2O_3	*1900*	*11-0370*	*congruent*

AII.1.3 MgO-Ga_2O_3 System

PDC did not collect any phase diagram information for this system although Schmalzried[AII-1] has studied this binary in the subsolidus range. Fig. AII-3 shows the diagram proposed by Schmalzried.

The binary spinel phase of composition $MgGa_2O_4$ (PDF 10-0113), can be assumed of congruent melting character with a melting point much higher than 1600°C, referred to a ternary phase diagram of MgO-Al_2O_3-Ga_2O_3 [PDC 2522-3]. It is also assumed that MgO has large solubility in β-Ga_2O_3 and doping Mg in Ga-site at a level less than 40 mol% will not form new phase.

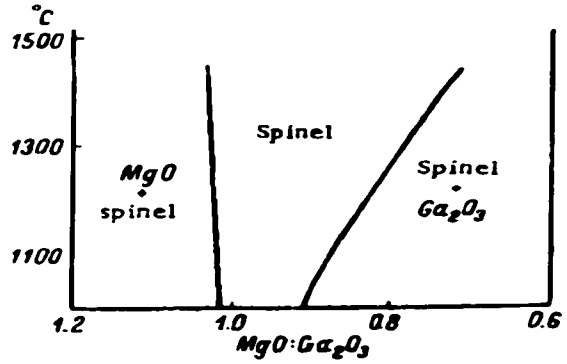

Fig. AII-3 Phase diagram of MgO- Ga_2O_3 in the subsolidus range [AII-3]

AII.1.4 La_2O_3-SrO [PDC 6429]

A partial of the quantitative diagram with SrO-content less than 10 mol% has been reported in early 70s[PDC 6429], where a rare earth oxide solid solution undergoes phase transitions from A-type hexagonal to H-type hexagonal and to X-type cubic structure at temperature above 2000°C. The oxide melted at temperature above 2275°C. The diagram from PDC 6429 is presented as Fig. AII-4.

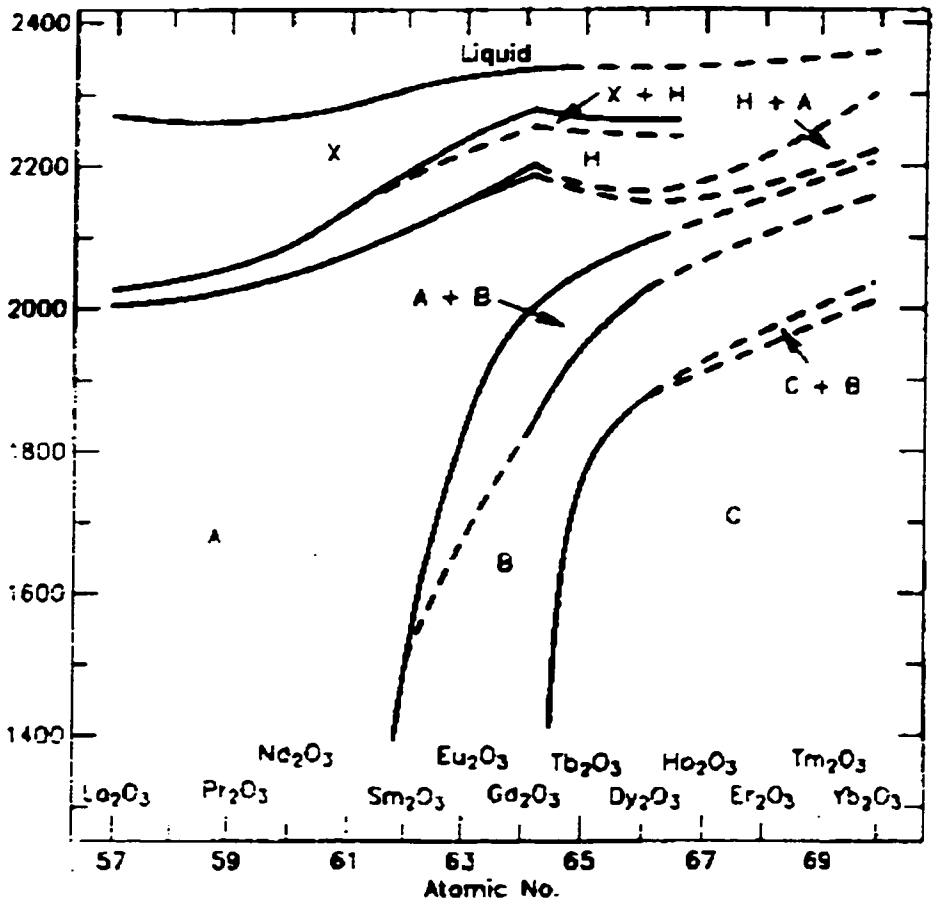

Fig. AII-4 Partial phase diagram of La_2O_3-SrO [PDC 6429]

Study on the composition being fully covered phase diagram of this binary was not available until 1994 when the author started work on the Sr doped $LaMnO_3$ system, where this binary is needed.[AII-4] Two binary compounds of La_4SrO_7 (PDF 22-1430) and $La_2Sr_2O_5$ (PDF 22-1431) were found and adopted for this study.

AII.1.5 La_2O_3-MgO System

There is no phase diagram data in PDC for this binary. However, Tresvyatskii and Lopato[AII-5] have studied this system by quenching technique. A simple eutectic reaction was reported at 28 mol% MgO at 2000±30°C. Their diagram is adopted as Fig. AII-5.

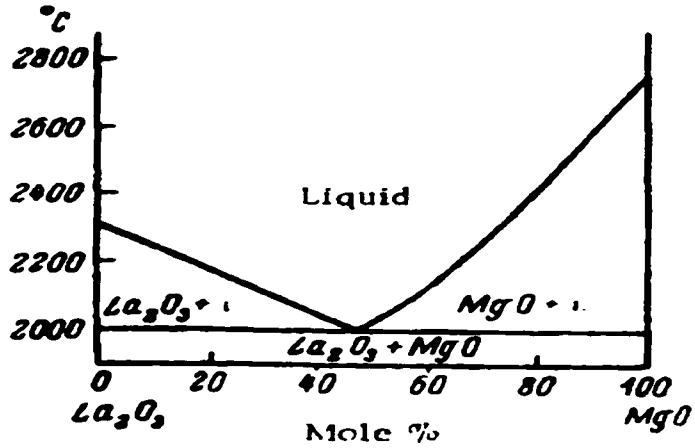

Fig. AII-5 Phase diagram of the MgO-La_2O_3 [AII-5]

Refers to MgO-La_2O_3-ZrO_2 [PDC 716] ternary phase diagram, similar results can be induced with liquidus temperature much higher than 1400°C and there is no solubility for both oxides.

AII.1.6 SrO-MgO [PDC 274]

A simple eutectic phase diagram was assumed with eutectic temperature above 1900°C at composition of about 45 mol% MgO. Fig. AII-6 shows the diagram from PDC 274.

AII.2 THE TERNARY SYSTEMS

AII.2.1 La_2O_3-SrO-Ga_2O_3 System

No ternary phase diagram is available besides three known ternary compounds of composition $LaSrGaO_4$ (PDF 24-1208), $LaSrGa_3O_7$ (PDF 45-0637) and $LaSr_2Ga_{11}O_{20}$ (PDF 45-0646). First two have been observed by XRPD in our preliminary studies as secondary phases in LSGM.

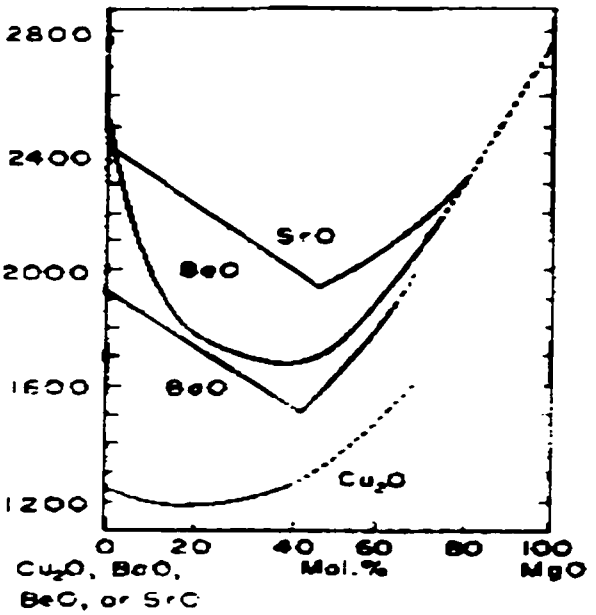

Fig. AII-6 The SrO-MgO phase diagram from PDC 274.

AII.2.2 La_2O_3-MgO-Ga_2O_3 System

There are three ternary compounds with composition of $LaGaMgO_7$, $LaGaMgO_4$ (PDF), and $LaGa_{11}MgO_{19}$ (PDF 26-0875) but none of them appeared in our study.

AII.2.3 La_2O_3-SrO-MgO System

No information on this ternary is available.

AII.2.4 Ga_2O_3-SrO-MgO System

No information on this ternary is available.

AII.3 The La_2O_3-SrO-Ga_2O_3-MgO Quaternary System

From the above available or predicted phase diagram information, plus the data from JADE (PDF files), a La_2O_3-SrO-Ga_2O_3-MgO quaternary phase diagram is predicted (see Appendix III for the detailed methodology for phase diagram prediction). The result is shown in Fig. AII-7.

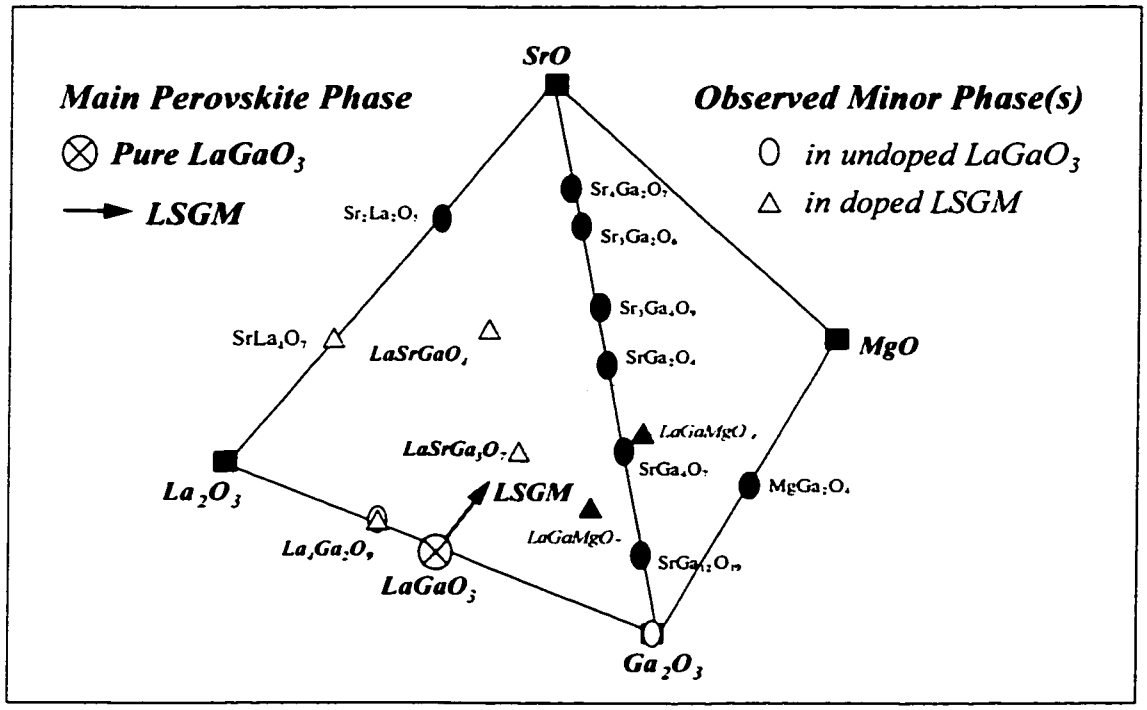

Fig. AII-7 The predicted La_2O_3-SrO-Ga_2O_3-MgO quaternary phase diagram

Reference:

*AII-1. M. Mizuno, T. Yamada and T. Ohtake, Phase Diagram of the System Ga_2O_3-La_2O_3 at High Temperatures, Yogyo-Kyokai-Shi, **93**[6], 295-300 (1985).*

*AII-2. M. Mizuno, T. Yamada, Formation and Solidification Points of Binary Compounds in the Ln_2O_3-Ga_2O_3 System, Yogyo-Kyokai-Shi, **93**[11], 686-91 (1985).*

*AII-3. H. Schmalzried, Zs. Phys. Chem., N.F., **28**[3/4], 203 (1961).*

AII-4. F. Zheng, Thermodynamics and Phase Behavior in Lanthanum Strontium Manganites, Master Thesis, Washington State University, 1996.

AII-5. S.G. Tresvyatskii and L.M. Lopato, New Applications of Rare Earth Elements in Technology, Moskva, Izdatel'stvo AN SSSR, 1964.

APPENDIX III

THERMODYNAMICS AND DEFECT CHEMISTRY OF LSGM

The electrical properties of an ionic material are dependent on the formation of defects. The high oxygen ionic conductivity of Sr and Mg doped $LaGaO_3$ (LSGM) perovskite is attributed to the defect created by doping and derivation of A/B cation ratio.

At very high oxygen partial pressure $p(O_2)$, the defect reaction in Sr and Mg doped $LaGaO_3$ (LSGM) system would look like the following:[AIII-1]

$$\frac{3}{2}O_2 \rightarrow V_{La}^{'''} + V_{Ga}^{'''} + 6h^{\bullet} + 3O_O^x \qquad \textit{(AIII-1)}$$

and the electrical neutrality requires:

$$3[V_{La}^{'''}] + 3[V_{Ga}^{'''}] = [h^{\bullet}] \qquad \textit{(AIII-2).}$$

Assuming:

$$[V_{La}^{'''}] = [V_{Ga}^{'''}] \qquad \textit{(AIII-3),}$$

then

$$K_{very-high} = [V_{La}^{'''}][V_{Ga}^{'''}][h^{\bullet}]^6 p(O_2)^{-3/2} = \frac{1}{36}[h^{\bullet}]^8 p(O_2)^{-3/2} = \text{constant} \qquad \textit{(AIII-4),}$$

which leads to

$$[h^{\bullet}] \propto p(O_2)^{3/16} \qquad \textit{(AIII-5).}$$

At high $p(O_2)$, the defect reaction in LSGM system would look like the following:

$$SrO + MgO + \frac{1}{2}O_2 \xrightarrow{LaGaO_3} Sr_{La}^{'} + Mg_{Ga}^{'} + 2h^{\bullet} + 3O_O^x \qquad \textit{(AIII-7)}$$

and the electrical neutrality requires:

$$[Sr_{La}^{'}] + [Mg_{Ga}^{'}] = [h^{\bullet}] \qquad \textit{(AIII-8).}$$

Assuming:

$$[Sr_{La}^{\cdot}] = [Mg_{Ga}^{\cdot}] \qquad \textit{(AIII-9)},$$

then

$$K_{high} = [Sr_{La}^{\cdot}][Mg_{Ga}^{\cdot}][h^{\bullet}]^2 p(O_2)^{-1/2} = \frac{1}{4}[h^{\bullet}]^4 p(O_2)^{-1/2} = \text{constant} \qquad \textit{(AIII-10)},$$

which leads to

$$[h^{\bullet}] \propto p(O_2)^{1/8} \qquad \textit{(AIII-11)}.$$

At medium $p(O_2)$, the defect reaction in LSGM system would look like the following:

$$SrO + MgO \xrightarrow{LaGaO_3} Sr_{La}^{\cdot} + Mg_{Ga}^{\cdot} + V_O^{\bullet\bullet} + 2O_O^x \qquad \textit{(AIII-12)}$$

and the electrical neutrality requires:

$$[Sr_{La}^{\cdot}] + [Mg_{Ga}^{\cdot}] = 2[V_O^{\bullet\bullet}] \qquad \textit{(AIII-13)}.$$

Assuming:

$$[Sr_{La}^{\cdot}] = [Mg_{Ga}^{\cdot}] \qquad \textit{(AIII-14)},$$

then

$$K_{medium} = [Sr_{La}^{\cdot}][Mg_{Ga}^{\cdot}][V_O^{\bullet\bullet}] = [V_O^{\bullet\bullet}]^3 = \text{constant} \qquad \textit{(AIII-15)},$$

which leads to

$$[V_O^{\bullet\bullet}] = \text{constant} \qquad \textit{(AIII-16)}.$$

At low $p(O_2)$, the defect reaction in LSGM system would look like the following:

$$O_O^x \rightarrow \frac{1}{2}O_2 + V_O^{\bullet\bullet} + 2e^{\cdot} \qquad \textit{(AIII-17)}$$

and the electrical neutrality requires:

$$[e^{\cdot}] = 2[V_O^{\bullet\bullet}] \qquad \textit{(AIII-18)},$$

then

$$K_{low} = p(O_2)^{1/2}[V_O^{\bullet\bullet}][e^{\cdot}]^2 = 4p(O_2)^{1/2}[V_O^{\bullet\bullet}]^3 = \text{constant} \qquad \textit{(AIII-19)},$$

which leads to

$$[V_O^{\bullet\bullet}] \propto p(O_2)^{-1/6} \qquad \textit{(AIII-20)}.$$

For SOFC application, a quasi-chemical equation may be used to express the formation of double charged oxygen vacancies, $V_O^{\bullet\bullet}$, in the Sr and Mg doped perovskite $LaGaO_3$ — $(La_{1-x}Sr_x)_A(Ga_{1-y}Mg_y)_BO_{3-\delta}$ as the follows:

$$SrO + MgO + O_O^x \xrightarrow{LaGaO_3} Sr_{La}^{\cdot} + Mg_{Ga}^{\cdot} + V_O^{\bullet\bullet} + \tfrac{1}{2}O_2 \qquad \textit{(AIII-21)}$$

Using the law of mass action, the equilibrium constant for the formation of $V_O^{\bullet\bullet}$ is:

$$K_{V_O^{\bullet\bullet}} = [Sr_{La}^{\cdot}][Mg_{Ga}^{\cdot}][V_O^{\bullet\bullet}]p(O_2^{1/2}) \qquad \textit{(AIII-22)}.$$

To maintain the electrical neutrality, we have:

$$[Sr_{La}^{\cdot}] + [Mg_{Ga}^{\cdot}] = 2[V_O^{\bullet\bullet}] \qquad \textit{(AIII-23)}.$$

The defect concentrations are related to the doping contents according to the following:

$$[V_O^{\bullet\bullet}] = \frac{(x+y)/2}{3} \qquad \textit{(AIII-24a)},$$

$$[Sr_{La}^{\cdot}] = x \qquad \textit{(AIII-24b)},$$

$$[Mg_{Ga}^{\cdot}] = y \qquad \textit{(AIII-24c)},$$

To simplify the problem, let $x = y$, then:

$$[V_O^{\bullet\bullet}] = \frac{(x+y)/2}{3} = \frac{x}{3} \qquad \textit{(AIII-25a)},$$

$$[Sr_{La}^{\cdot}] = x \qquad \textit{(AIII-25b)},$$

$$[Mg_{Ga}^{\cdot}] = y = x \qquad \textit{(AIII-25c)}.$$

So,

$$K_{V_O^{\bullet\bullet}} = [V_O^{\bullet\bullet}][Sr_{La}^{\cdot}][Mg_{Ga}^{\cdot}]p(O_2^{1/2}) = \frac{x^3}{3}p(O_2^{1/2}) = \text{constant} \qquad \textit{(AIII-26)},$$

Or

$$K_{V_O^{\bullet\bullet}} = [V_O^{\bullet\bullet}][Sr_{La}^{\cdot}][Mg_{Ga}^{\cdot}]p(O_2^{1/2}) = 9[V_O^{\bullet\bullet}]^3 p(O_2^{1/2}) = \text{constant} \qquad \textit{(AIII-27)}.$$

For the formation of $V_O^{\bullet\bullet}$, the composition (x or $[V_O^{\bullet\bullet}]$) of the oxide thus depends on the oxygen partial pressure according to:

$$x \propto p(O_2)^{-1/6} \text{ or } [V_O^{\bullet\bullet}] \propto p(O_2)^{-1/6} \qquad \textit{(AIII-28)}.$$

The relative partial free energy of oxygen $\Delta\overline{G}_{O_2}$, with regards to doping content x, is equal to:[AIII-2]

$$\Delta\overline{G}_{O_2} = RT\ln p(O_2) \propto -6RT\ln x \qquad \textit{(AIII-29)}.$$

Since

$$\Delta\overline{G}_{O_2} = \Delta\overline{H}_{O_2} - T\Delta\overline{S}_{O_2} \qquad \textit{(AIII-30)},$$

so,

$$\Delta\overline{H}_{O_2} = \frac{\partial(\Delta\overline{G}_{O_2}/T)}{\partial(1/T)} \qquad \textit{(AIII-31)},$$

and

$$\Delta\overline{S}_{O_2} = -\frac{\partial\Delta\overline{G}_{O_2}}{\partial T} \qquad \textit{(AIII-32)}.$$

The Gibbs energy of the formation of vacancy can be expressed as:[AIII-3]

$$\Delta G_v = n\left(\Delta H_v - T\Delta S_v^{vib}\right) + kT\left[N\ln\left(\frac{N}{N+n}\right) + n\ln\left(\frac{n}{N+n}\right)\right] \quad \textit{(AIII-33)},$$

and

$$\frac{\partial G}{\partial n} = \Delta H_v - T\Delta S_v^{vib} + kT\left[-\frac{N}{N+n} + \ln\frac{n}{N+n} + \frac{N}{N+n}\right] = \Delta H_v - T\Delta S_v^{vib} + kT\ln\frac{n}{N+n} \quad \textit{(AIII-34)}$$

Let $\frac{\partial G}{\partial n} = 0$, *we have the equilibrium vacancy concentration as:*

$$\frac{n}{N+n} = x_v = \exp\left(-\frac{\Delta H_v}{kT}\right)\exp\left(\frac{\Delta S_v^{vib}}{R}\right) = \exp\left(-\frac{\Delta G_v}{kT}\right) \quad \textit{(AIII-35)}.$$

For oxygen vacancy,

$$\Delta G_{V_O^{\bullet\bullet}}^o = \Delta H_{V_O^{\bullet\bullet}}^o - T\Delta S_{V_O^{\bullet\bullet}}^{vib} = -RT\ln K_{V_O^{\bullet\bullet}} \quad \textit{(AIII-36)}$$

and

$$K_{V_O^{\bullet\bullet}} = \exp\left(-\frac{\Delta H_{V_O^{\bullet\bullet}}^o}{RT}\right)\exp\left(\frac{\Delta S_{V_O^{\bullet\bullet}}^{vib}}{R}\right) \quad \textit{(AIII-37)}.$$

Compared Eq. (AIII-26) to Eq. (AIII-37), we have:

$$\frac{x^3}{3}p\left(O_2^{1/2}\right) = \exp\left(-\frac{\Delta H_{V_O^{\bullet\bullet}}^o}{RT}\right)\exp\left(\frac{\Delta S_{V_O^{\bullet\bullet}}^{vib}}{R}\right) \quad \textit{(AIII-38a)},$$

$$p\left(O_2^{1/2}\right) = \frac{3}{x^3}\exp\left(-\frac{\Delta H_{V_O^{\bullet\bullet}}^o}{RT}\right)\exp\left(\frac{\Delta S_{V_O^{\bullet\bullet}}^{vib}}{R}\right) \quad \textit{(AIII-38b)},$$

$$\frac{1}{2}\ln p\left(O_2\right) = \ln 3 - 3\ln x - \frac{\Delta H_{V_O^{\bullet\bullet}}^o}{RT} + \frac{\Delta S_{V_O^{\bullet\bullet}}^{vib}}{R} \quad \textit{(AIII-38c)},$$

$$RT\ln p\left(O_2\right) = 2RT\ln 3 - 6RT\ln x - 2\Delta H_{V_O^{\bullet\bullet}}^o + 2\Delta S_{V_O^{\bullet\bullet}}^{vib} \quad \textit{(AIII-38d)},$$

or

$$\Delta\overline{G}_{O_2} = -2\Delta H^o_{V_O^{\bullet\bullet}} + T\left(2\Delta S^o_{V_O^{\bullet\bullet}} - 6R\ln x + 2R\ln 3\right) \qquad \textit{(AIII-39).}$$

Thus

$$\Delta\overline{H}_{O_2} = -2\Delta H^o_{V_O^{\bullet\bullet}} \qquad \textit{(AIII-40),}$$

and

$$\Delta\overline{S}_{O_2} = -2\Delta S^o_{V_O^{\bullet\bullet}} + 6R\ln x - 2R\ln 3 \qquad \textit{(AIII-41).}$$

If we assume the defects, i.e., the oxygen vacancies ($V_O^{\bullet\bullet}$), in oxygen-deficient oxides are randomly distributed and there are no interactions between them, then the derivations obtained above can be used to discuss the general thermodynamic properties for LSGM materials. The relative partial enthalpy $\Delta\overline{H}_{O_2}$ should be independent of composition and it is directly proportional to the enthalpy of formation of oxygen vacancy ($V_O^{\bullet\bullet}$). It is however believed that the interactions among certain defects are much more pronounced and their effects should not be excluded in real world. Nevertheless, Eq. (AIII-40) is still a good approximation. The vibration entropy is independent of composition and the compositional dependence of relative partial entropy $\Delta\overline{S}_{O_2}$ can be expressed as:

$$\frac{\partial\Delta\overline{S}_{O_2}}{\partial\ln x} = 6R \qquad \textit{(AIII-42).}$$

Reference:

AIII-1. F.A. Kroger and H.J. Vink, Solid State Physics, Ed. by F. Seitz and D. Turnbell, Academic Press, New York, 1956.

AIII-2. P. Kofstad, Nonstoichiometry, Diffusion, and Electrical Conductivity in Binary Metal Oxides, John Wiley & Sons, Inc., 1972.

AIII-3. R.A. Swalin, Thermodynamics of Solids, John Wiley & Sons, Inc., 1972.

VITA

Feng Zheng

June 26, 1962
Mayang, Hunan, China

Education:	*10/96-06/00*	Ph.D. *University of Washington (UW)*, USA
	08/94-07/96	M.S. *Washington State University (WSU)*, USA
	09/79-07/83	B.S. *The Central-South University of Technology (CSUT)*, PRC
Work Experiences:	*01/00-06/00*	Teaching/Research Assistant at *University of Washington*, USA
	08/94-12/99	Lab Research Student at *Battelle PNNL*, USA
	11/92-01/94	Visiting Staff at the *University of Sheffield*, UK
	02/92-10/92	Visiting Staff at *Davy International Sheffield*, UK
	08/83-01/92	Instructor at *Anshan Iron & Steel School*, PRC
	(09/85-07/86	*Visiting Staff at Beijing University of Science & Technology)*
	(09/83-02/84	*Visiting Staff at Anshan Institute of Iron & Steel Technology)*

Awards:

Associated Western Universities Incorporated Fellowship Recipient of 1994-99
Graduate Student Fellowship Recipient of the American Ceramic Society 1998

Research Involved By Material Systems:

1. **Ceramics**
   - 1.1 Sr and Mg Doped $LaGaO_3$ *(Ph.D. Project, UW, PNNL & ORNL, 96-00)*
   - 1.2 Cu-Si-O-P-B System *(Work Done in UW, 97-98)*
   - 1.3 Ti-Si-C System *(Work Done in UW, 96-98)*
   - 1.4 Sr Doped $LaMnO_3$ *(MS Project, WSU and PNNL, 94-96)*
   - 1.5 Leucite-Fayalite-Silica System *(Work Done in PRC, 85-86)*
   - 1.6 CaO-MgO-Al_2O_3-SiO_2 System *(Work Done in PRC, 83-85)*
2. **Metallurgy**
   - 2.1 Alloy Systems
     - 2.1.1 Fe-Cr-Mo-V-C System *(Work Done in Sheffield, UK, 92-94)*
     - 2.1.2 Strain-stress Modeling of Hot Rolling Processing *(Work Done in Sheffield, UK, 92)*
     - 2.1.3 Modeling of the Run-out Table Cooling System *(Work Done in Sheffield, UK, 92)*
     - 2.1.4 Analysis of the Failure Behavior of Welded Tubing *(Work Done in PRC, 87-88)*
     - 2.1.5 Fe-Mo-C System *(B.S. Project, Changsha, PRC, 83)*
   - 2.2 Non-ferrous Systems
     - 2.2.1 Mg-Pb-Sn System *(Work Done in PRC, 87-88)*
     - 2.2.2 Mg-Cu-Pb System *(Work Done in PRC, 85-86)*
     - 2.2.3 Pb-Sn-Bi-Sb System *(Work Done in PRC, 83-85)*

Special Skills:

1. Qualified Radiological Worker I of US Department of Energy (DOE)
2. Experience in the Use of R/HTXRD, TEM, SEM and Thermal Analysis Software and Equipment
3. Experience with Computational Skills in Phase Diagram Calculations and Lattice Energy Calculations

Journal and book papers in English:

1. F. Zheng, R.K. Bordia and L.R. Pederson, *Phase Distribution in Sr and Mg Doped $LaGaO_3$ Perovskites*, submitted for publication.
2. F. Zheng, R.K. Bordia, L.R. Pederson, E.A. Payzant and C.J. Rawn, *Phase Stability of Sr and Mg Doped $LaGaO_3$*, submitted for publication.
3. C.-S. Park, F. Zheng, S. Salamone and R.K. Bordia, *Processing of Composites in the Ti-Si-C System*, Journal of Materials Science, in print.
4. F. Zheng, B.B. Argent and J.F. Smith, *Thermodynamic Computation of the Mo-V Binary Phase Diagram*, Journal of Phase Equilibria, **20**[4], 370-373 (1999).
5. F. Zheng and L.R. Pederson, *Phase Behavior of the Lanthanum Strontium Manganites*, Journal of Electrochemical Society, **146**[8], 2810-2816 (1999).
6. F. Zheng and L.R. Pederson, *Thermodynamic Properties of the La-Sr-Mn-O System*, Journal of Electrochemical Society, **146**[8], 2817-2820 (1999).
7. F. Zheng and T.G. Stoebe, *Letter to the Editor*, Journal of Electrochemical Society, **146**(3) 1238-1240 (1999).
8. Jin Zhanpeng, Gan Weiping, Zheng Feng and Wei Shuling, *On the Formation of Carbide Layers in Diffusion Couples Consisting of Mo and the Fe-C Alloys*, 'Phase Diagrams' Edited by Jin Zhanpeng (in English), pp178-184, Central South Univ. of Tech., Changsha, 1987.